

Universidad de Alcalá

Departamento de Electrónica

Programa de Doctorado en Electrónica: Sistemas Electrónicos
Avanzados. Sistemas Inteligentes



Optimization of passive ultrafast fiber lasers
based on indium nitride for novel applications

TESIS DOCTORAL

Autor

Laura Monroy Lafuente

Directores

Dr. Miguel González Herráez

Dr. Fernando B. Naranjo Vega

Alcalá de Henares

2022

Agradecimientos

Este trabajo está dedicado a aquellas personas que me han apoyado durante todos estos años y me han animado a continuar con mi pasión por la física del láser. Me gustaría agradecer en primer lugar a todos los profesores tanto del colegio como de la Universidad que contribuyeron a mi formación e impulsaron mi interés por el mundo de la ciencia, con especial mención a María Jesús, Gabriel Álvarez Galindo, Gemma Piquero, o Alfredo Luis Aina. También quiero agradecer a todos aquellos profesores del máster de Ingeniería Fotónica quienes me introdujeron en el maravilloso mundo de la investigación científica.

En primer lugar, me gustaría expresar mi más sincero agradecimiento hacia Fernando Naranjo Bernabé y Miguel González Herráez por la oportunidad que me han brindado para continuar mis estudios de doctorado en la UAH. Gracias por vuestra paciencia, calma y confianza, así como todos vuestros conocimientos los cuales me han ayudado durante estos años. También me gustaría darle las gracias a Óscar Esteban y Sonia Martínez por su tiempo resolviendo mis infinitas dudas en el laboratorio, y a Ana de Andrés y Sirona Valdueza por dejarme participar en sus clases.

Me gustaría darle las gracias a todos mis compañeros del grupo GRIFO del departamento de Electrónica de la UAH, en el he que podido desarrollar mi tesis doctoral todos estos años: Miguel Soriano, Andrés, Luis, Regina, Javier Nuño, Rosario, Hugo, Pedro, Pablo, Camilo y Michael, y a mis compañeros de despacho, Javier, Edel, Daniel y Adrián por esas risas y momentos frikis durante las comidas. Quiero agradecer especialmente a mi antecesor y mi maestro Marco, quien no solo me enseñó todo lo que había que saber sobre láseres y absorbentes saturables y el estresante mundo de la burocracia en la investigación, sino también con quien he tenido el privilegio de compartir risas, estrés, o lo que se terciara. Gracias por tu ayuda y tu incansable positivismo y sobre todo por ser un auténtico amigo.

Además, esta tesis ha sido posible gracias a la colaboración de increíbles investigadores que tuve el privilegio de conocer durante mis estancias de doctorado en el Instituto de Óptica “Daza de Valdés” del CSIC: Pedro Corredera, Juan Diego Ania Castañón, Conchi Pulido, y a mis compañeras de doctorado Francesca Gallazzi e Inés Cáceres quienes tanto me ayudaron durante todas esas horas de pruebas de laboratorio. A Eva Monroy, del instituto CEA, IRIG-PHELIQS (IRAC) en la Universidad Grenoble-Alpes, por sus valiosos e instructivos comentarios durante las épocas de correcciones de artículos y su amplio conocimiento del mundo de los materiales. Así como a nuestros coautores y colaboradores de la Universidad de Arizona del James C. Wyant College of Optical Science, a Khanh Kieu gracias por aceptar mi estancia con su grupo de investigación y permitirme usar su laboratorio y enseñarme a utilizar los distintos tipos de fibra, a Josh Magnus, mi compañero de doctorado, gracias por tu paciencia y tu ayuda inestimable para llevar a cabo las medidas experimentales.

Quisiera también agradecer a las distintas fuentes de financiación, a la universidad de Alcalá y al ministerio de educación por las becas FPI y FPU, al ministerio de ciencia, Innovación y Universidades, la Comunidad de Madrid, así como a la Universidad de Arizona.

Esta tesis no tendría lugar sin el apoyo incondicional de mi familia. A mis padres por haberme facilitado aprender siempre lo que he querido y por su ayuda, con la que no habría llegado a donde estoy ahora. A mi hermana, por su optimismo y por estar siempre ahí y su apoyo con pompones. Y a mi hermanastra Elima, por creer en mí sin reservas. También le quiero agradecer en especial a Álvaro, lo eres todo para mí, gracias por estar siempre apoyándome y alegrándome en los momentos difíciles, aguantando mis llores y agobios y por tu confianza ciega en mí, no sería quien soy sin ti. Gracias por todo, te quiero. No quisiera olvidar a mis amigos, Bea, mi otra hermana, quien me ha acompañado todos estos años desde que íbamos al colegio, gracias por tu confianza y tu eterna amistad, y a mis amigos del barrio, gracias por esas risas y momentos rocambolescos.

Por último, a los miembros del tribunal por revisar este trabajo y su tiempo, y a ti lector, por tu valentía para leer este trabajo fruto de años de estudio y esfuerzo, espero que te sea útil y sobre todo leve. Un último chiste antes de que empiece los serio.

What's a poorly measured 5 femtosecond pulse?
A 10 femtosecond pulse

Laura Monroy Lafuente

Resumen

Los láseres ultrarrápidos en fibra constituyen una de las fuentes de luz más utilizadas actualmente debido a su fiabilidad y flexibilidad, convirtiéndose en la pieza clave de múltiples aplicaciones, como las comunicaciones ópticas, el procesamiento de materiales o la espectroscopía. Entre ellos, los láseres en fibra anclado en modos basados en el uso de absorbentes saturables demuestran características superiores de estabilidad, simplicidad y bajo coste, capaces de emitir pulsos ultracortos con potencias extremadamente altas en un amplio rango espectral. En las últimas décadas, se han probado varios absorbentes saturables, donde los materiales de semiconductor destacan por su amplia profundidad de modulación, su elevada absorción no lineal y su baja intensidad de saturación. Sin embargo, presentan algunas limitaciones como un estrecho ancho de banda y un bajo umbral de daño. Por tanto, en este trabajo se propone el uso de un semiconductor de InN en un láser todo en fibra anclado en modos para la generación de láseres ultrarrápidos de alta potencia en la región del infrarrojo cercano. Esta configuración ha demostrado trenes de pulsos Gaussianos en el rango de los femtosegundos mediante un sistema sencillo y de bajo coste.

El objetivo de esta tesis es optimizar las características de un láser de fibra anclado en modos basado en un absorbente saturable de InN, y desarrollar un novedoso dispositivo espectroscópico para aplicaciones de detección. Primeramente, se estudia la mejora de las propiedades del absorbente saturable de semiconductor mediante un mayor control del dopaje residual así como del crecimiento de material, demostrando el máximo comportamiento no lineal para este tipo de absorbentes saturables en un láser en fibra. También se discute cómo estas características podrían mejorarse mediante el desarrollo de un nuevo diseño de láser totalmente en fibra, capaz de contrarrestar las limitaciones actuales de ruido y pérdidas de inserción dentro de la cavidad láser. De este modo, se demuestra la duración de pulso más corta y la máxima potencia óptica, conservando una configuración sencilla, lo que allana el camino hacia el desarrollo de sistemas láser comerciales en aplicaciones de alta potencia.

A continuación, se introducen nuevas aplicaciones potenciales del sistema láser de fibra: en la detección de gases, mediante la generación de supercontinuo del pulso láser ultrarrápido en fibras monomodo capaces de cubrir espectros de absorción más amplios; y en la caracterización de moléculas biológicas mediante el uso de una novedosa estructura espectroscópica SF-CARS conectada a la fuente láser totalmente en fibra. Además, se exponen las implicaciones del chirp-matching en el rendimiento de la medición de la absorción, y el impacto de la dispersión y los efectos no lineales generados por diferentes fibras ópticas en la compresión y el ensanchamiento de los pulsos de fibra ultrarrápidos. La configuración láser propuesta supera la máxima resolución medible y la cobertura espectral, las limitaciones más importantes a las que se enfrenta la espectroscopía moderna.

Finalmente, se resumen los objetivos alcanzados en esta tesis, evaluando el potencial de las aplicaciones propuestas, así como futuras líneas de investigación basadas en dichos hallazgos.

Abstract

Ultrafast fiber lasers are currently a very predominant research field due to their advantageous properties of reliability, compactness and flexibility, which have become the key to multiple applications, such as optical communications, material processing, spectroscopy, etc. Among them, mode-locked fiber lasers incorporating saturable absorbers demonstrate superior characteristics of simplicity, low cost and stability, capable of emitting short pulses in the femtosecond range with extremely high optical powers in a wide spectral range. In the last decades, several saturable absorbers have been tested, with semiconductor materials standing out due to their extensive modulation depth, high nonlinear saturable absorption, and low saturation intensity. However, some limitations such as a narrow working bandwidth and a low damage threshold level are also present. In this sense, we propose in this work the use of an InN semiconductor saturable absorber in a polarization independent mode-locked ring fiber laser for ultrafast high power laser generation in the near-infrared region. This configuration has proven to generate femtosecond trains of Gaussian pulses in a desirably simple implementation.

In this work, we aimed to optimize the laser performance of a mode-locked fiber laser based on an InN saturable absorber, and develop a novel spectroscopic device for sensing applications. We report the improvement of the semiconductor saturable absorber properties by a higher control of the residual doping as well as the material deposition during the fabrication process, demonstrating the maximum nonlinear behavior and damage threshold achieved by this type of saturable absorber in a ring fiber laser. We also discuss how these characteristics might be increased by developing a new all-fiber laser design to counteract the current limitations of noise and insertion losses within the laser cavity. In doing so, we demonstrate the shortest pulse duration and maximum optical power, while retaining a simple set-up, paving the way toward commercial laser systems in high power applications.

Afterwards, we develop potential applications employing the fiber laser system: in gas sensing, by exploiting the supercontinuum generation of the ultrafast laser pulse in standard single-mode fibers capable of covering the broadest absorption spectra of the sample under study; and in the characterization of biological molecules by using a novel SF-CARS spectroscopic structure embedded in the all-fiber laser source. We discuss the implications of chirp-matching on the performance of the absorption measurement, and the impact of dispersion and nonlinear effects generated by different optical fibers in the compression and broadening of ultrafast fiber pulses. The proposed laser configuration overcomes two of modern spectroscopy's most significant limitations: maximum resolution and spectral coverage.

The objectives achieved in this thesis are finally summarized, evaluating the viability of the proposed applications, as well as commenting on open lines of research originating from the findings.

Contents

Agradecimientos	III
Resumen	V
Abstract	VI
List of Figures	X
1 Introduction	1
1.1 Motivation	2
1.2 Objectives	3
1.3 Structure of the thesis	4
2 Fundamentals of optical fibers	7
2.1 Introduction to optical fibers	8
2.1.1 Historical context	8
2.1.2 Optical properties of fibers	9
2.2 Propagation of light in silica fibers	11
2.2.1 Maxwell equations	12
2.2.2 Linear effects in optical fibers	14
2.3 Nonlinear propagation of light in silica fibers	18
2.3.1 Nonlinear optical effects	18
2.3.2 NLSE	22
2.4 Solitons	23
2.4.1 Dispersion-managed solitons	25
2.4.2 Higher-order effects	25
3 Light-matter interaction	27
3.1 Linear optical effects	28
3.1.1 Transmission, reflection and absorption	29
3.1.2 Optical transitions	30
3.2 Nonlinear optical effects	32
3.2.1 Second harmonic generation (SHG)	32
3.2.2 Third harmonic generation (THG)	34
3.2.3 Nonlinear absorption effects	35
3.2.4 Stimulated Raman scattering	39

4	Ultrafast fiber lasers	43
4.1	Introduction to fiber lasers	44
4.1.1	Fundamentals of fiber lasers	44
4.1.2	Generation of ultrashort pulses in fiber lasers	46
4.2	Passive mode-locked fiber lasers	49
4.2.1	Mode-locking technique	49
4.2.2	Saturable absorbers	51
4.3	InN as SESAM	55
4.3.1	Growth of III-nitrides	55
4.3.2	Structural properties	56
4.3.3	Optical properties	60
4.4	InN-based ultrafast mode-locked fiber laser	63
4.4.1	Experimental set-up	63
4.4.2	Optical characteristics of the InN-based ML-fiber laser	65
4.4.3	Numerical simulations	68
4.5	Conclusions	73
5	Optimization of ultrafast InN based fiber laser	75
5.1	Improvement of InN semiconductors	77
5.1.1	Introduction of a buffer layer	79
5.1.2	Deposition control	87
5.2	Improvement of the laser system	97
5.2.1	All-fiber configuration	98
5.2.2	High-power ultrafast all-fiber laser	105
5.3	Conclusions	110
6	Sensing applications of ultrafast InN based fiber lasers	113
6.1	Gas sensing	114
6.1.1	Supercontinuum generation	115
6.1.2	Experimental set-up	117
6.1.3	Preliminary results	118
6.1.4	Discussion of results	120
6.2	Biomedical sensing	121
6.2.1	Pulse compression for high-power laser systems	122
6.2.2	Design of the “all-fiber” spectroscopy laser source	123
6.2.3	Numerical simulations	128
6.3	Conclusions	140
7	Conclusions	141
7.1	Conclusions and main contributions	142
7.2	Future perspectives	144
7.3	Author’s publications	146
	Bibliography	164

List of Figures

2.1	Structure of step-index and graded-index refractive profiles in MMFs	10
2.2	Transversal Gaussian distribution for a step-index SMF	11
2.3	Attenuation spectrum of a SMF	16
2.4	Dispersion on a Gaussian pulse propagating in SMF	17
2.5	SPM-induced broadening of an initially unchirped Gaussian pulse	21
2.6	Temporal evolution of a $N = 2$ soliton propagating through a SMF	24
2.7	Higher-order dispersion on a Gaussian pulse propagating in SMF	26
3.1	Bandgap energy level structure of semiconductors.	29
3.2	Nonradiative transitions in semiconductors	31
3.3	Radiative transitions of semiconductors	32
3.4	Phase matching in SHG	33
3.5	TPA and SA absorption effects in direct bandgap semiconductors	37
3.6	Scattering spectrum produced by elastic and inelastic processes	40
3.7	Spontaneous and stimulated Raman scattering processes.	42
4.1	Basic components of a laser oscillator	45
4.2	Representation of different ultrashort pulse generation mechanisms	46
4.3	Optical properties of ultrashort pulses	48
4.4	Passive mode-locking mechanism in a resonator laser cavity	50
4.5	Properties of a saturable absorber	51
4.6	Real saturable absorption evolution along time	54
4.7	Classification of the III-V binary semiconductor compounds	55
4.8	Hexagonal symmetry of wurtzite structures	57
4.9	InN energy band gap structure	59
4.10	Nonlinear transmission characteristics of InN-based SESAM	64
4.11	Fiber laser set-up in reflection configuration	65
4.12	Oscilloscope trace for a fundamental mode-locked fiber laser cavity	66
4.13	Optical spectrum and AC traces for a passively mode-locked fiber laser	67
4.14	Ultrafast Gaussian pulse simulation	69
4.15	Symmetrized split-step Fourier method	70
4.16	Simulation of pulse propagation through different fibers	71
4.17	Pulse evolution in a fiber laser cavity	72
4.18	Stability of the simulated fiber ring laser cavity	73
5.1	Structural morphology of InN layers	80
5.2	Transmittance measurement of the InN samples	81
5.3	Experimental Z-scan schematic representation	82
5.4	Nonlinear transmission measurement of the InN-GaN sample	83
5.5	Laser set-up with the InN with the buffer layer semiconductor	84

5.6	ESA of the output laser with the InN as saturable absorber	84
5.7	Characterization of the output laser pulse of the InN-GaN SA	85
5.8	Tauc's plot of samples S0, S0', S1 and S2	89
5.9	Nonlinear transmission change of samples S0, S0', S1 and S2	90
5.10	Experimental set-up of an InN-based SA in an ultrafast ML fiber laser	92
5.11	Optical laser characterization of samples S0, S1 and S2	94
5.12	Schematic structure of the GRIN-to-SESAM coupling device	99
5.13	All-fiber Er-doped laser set-up	100
5.14	Optical characterization of the output laser pulse	101
5.15	Average power continuous monitoring measurement	101
5.16	Fiber laser optical characterization of the GRIN-to-SESAM device	103
5.17	Set-up of the expanded GRIN-to-fiber laser	106
5.18	Characterization of long fiber laser cavities	108
6.1	SC generation simulation of a Gaussian pulse.	117
6.2	SC generation in 2.3 km of SSMF	118
6.3	SC spectrum after the interaction with the gas molecules	119
6.4	Absorption spectrum of the three different gas molecule samples	120
6.5	All-fiber laser source scheme for spectroscopic applications	125
6.6	Grating pair compression scheme of the 1 μm pulse	127
6.7	Schematic of the spectroscopic imaging system	127
6.8	Spectral focusing CARS spectroscopy scheme	129
6.9	Spectral resolution and spectral coverage calculation	130
6.10	Simulation of the CARS signal and spectral coverage evaluation	132
6.11	CARS simulated results of the laser set-up	134
6.12	CARS laser set-up using the InN fiber cavity	136
6.13	Pump and Stokes simulation based on the results of Section 5.2	137
6.14	CARS spectroscopy simulation from the output laser pulses of 5.2	138

List of Acronyms

AC Autocorrelation.

AS Anti-Stokes.

ASE Amplified spontaneous emission.

CARS Coherent anti-Stokes Raman scattering.

CNT Carbon nanotubes.

CW Continuous wave.

DCF Dispersion-compensating fiber.

DSF Dispersion-shifted fiber.

EDF Erbium-doped fiber.

EDFA Erbium-doped fiber amplifier.

ESA Electrical spectrum analyzer.

FFT Fast Fourier transform.

FROG Frequency-resolved optical gating.

FT Fourier transform.

FWHM Full width half maximum.

FWM Four wave mixing.

GDD Group delay dispersion.

GNLSE Generalized nonlinear Schrödinger equation.

GRIN Graded-index lens.

GVD Group velocity dispersion.

HNLF High nonlinear fiber.

IFD Instantaneous frequency difference.

MI Modulation instability.

ML Mode-locking.

MQW Multiquantum wells.

NIR Near infrared.

NLSE Nonlinear Schrödinger equation.

OSA Optical spectrum analyzer.

PAMBE Plasma-assisted molecular beam epitaxy.

PCF Photonic crystal fiber.

PM Power meter.

PM980 Polarization maintaining fiber.

RSA Reverse saturable absorption.

SA Saturable absorber.

SC Supercontinuum generation.

SESAM Semiconductor saturable absorber mirror.

SF Spectral focusing.

SHG Second harmonic generation.

SMF Single mode fiber.

SNR Signal to noise ratio.

SPM Self-Phase modulation.

SRS Stimulated Raman scattering.

TBP Time-bandwidth product.

THG Third harmonic generation.

TOD Third order dispersion.

TPA Two photon absorption.

UN3 Single-clad fiber.

VOA Variable optical fiber attenuator.

WDM Wavelength division multiplexing.

XPM Cross-phase modulation.

YDFA Ytterbium-doped fiber amplifier.

Chapter 1

Introduction

Contents

1.1	Motivation	2
1.2	Objectives	3
1.3	Structure of the thesis	4

1.1 Motivation

In the last decades, the importance of developing detection systems capable of measuring live and direct molecules has grown considerably along with the progress of technology, as industrial settings become more complex while emitting harmful exhaust fumes. Having access to this information can prove to be essential to the modern world, since it can provide us with information regarding physical processes, thus enabling us to predict and react to specific situations. In addition to monitoring and studying natural phenomena, these spectroscopic measurements can also be used to prevent industrial system failures such as gas exposure, thus enhancing prevention and safety techniques. Also, these devices contribute to improving productivity, security, and sustainability in the context of a multitude of applications, enabling the development of smart technologies for security and control purposes. Nevertheless, molecular sensing devices can be considered the cornerstone of environmental monitoring of exhaust fumes which contribute to the greenhouse effect on our planet as well as becoming the main cause of breast diseases and cancer that affect modern society. In addition to physics and chemistry, optical spectroscopy has also been employed in other fields, such as medicine, to provide an accurate diagnosis.

In order to be able to distinguish between different molecules, and thus discriminate the damaging compounds, a considerable amount of research effort has been focused on developing techniques for sensing and measuring physical parameters while covering the maximum range for a single measurement. Fast acquisition performances are of great importance due to the rapid biological processes related to living materia. In order to obtain high spatial and temporal resolution in the imaging system, spectroscopic devices require reliable and stable light sources that can reach high power levels. As such, ultrashort laser sources are the ideal solution to fulfill this requirement.

During the last few decades, laser sources capable of producing ultrafast optical pulses have advanced considerably since they were introduced as essential tools for a multitude of industrial, military, and medical applications. Due to their inherent properties, including low costs, environmental robustness, and alignment-free operation, ultrafast fiber laser technologies have recently drawn considerable attention. A growing number of sophisticated sensing techniques have been developed using optical fibers. With the inherent qualities of fused silica, optical fibers have become a popular alternative to traditional electrical wires and are used in a wide range of engineering applications. Optical fibers offer many advantages over traditional sensors, such as immunity to electromagnetic interference, small dimensions, and functionality in difficult-to-reach locations. Fiber lasers with broad spectral bandwidths and high optical powers are a promising candidate to study fast molecular dynamics, because of their advantages in high optical resolution and fast acquisition rates, while producing high-quality, strong pulses in the picosecond and femtosecond range due to their malleability and stability.

Mode-locked all-fiber laser sources based on passive saturable absorbers, are considered the simplest and most effective laser technology to monitor complex and large ranges of absorption spectra of molecules, providing a reliable and stable ultra-

fast train of pulses. Semiconductor saturable absorbers are one of the most potential materials for ultrashort pulse generation, due to their characteristics of high modulation depth and saturation intensity. Semiconductor saturable absorbers are therefore widely implemented in optical mode-locked fiber lasers, with emissions varying from the ultraviolet to the infrared region. However, the lack of semiconductors with ideal saturable absorber properties, such as thermal and electrical resistance, high saturable absorption, low saturation fluence and high modulation depth, for reliable ultrashort pulse emission is still a challenging task.

In order to counteract these limitations, a semiconductor saturable absorber belonging to the III-nitride group is employed. The proposed InN semiconductor material demonstrates superior properties with higher modulation depth and saturable absorption coefficients, thermal and electrical stability; and a higher damage threshold level. These properties permit its use in fiber lasers with a mode-locking configuration, assessing the limitations of optical power and time duration for ultrashort pulse generation, accomplishing the industrial requirements, as demonstrated in the previous thesis developed in the Photonics Engineering Group of Alcalá [184]. This system's potential is not fully optimized so far, where emerging applications could benefit from the development and use of highly-powered lasers. A few improvements are still needed for the laser system in terms of stability and ultra-short pulse duration performance, considering the high resolution requirements of recent sensing applications. This statement becomes the starting point of this thesis.

On this matter, the objectives of this thesis are to improve the laser performance of the InN-based mode-locked fiber laser system, particularly in what concerns the saturable absorber and the fiber laser design, envisioning the forthcoming challenges of resolution and spectral coverage of spectroscopic devices, as well as exploiting the capabilities of ultrafast fiber laser sources for sensing and high powered applications.

1.2 Objectives

Based on the above motivation, the research project developed for this thesis had the following set of objectives:

- Development of algorithms and methods to address and overcome current limitations of fiber-based passive laser ring cavities for sensing applications.
- Devise methods for the optimization of the laser structure based on their quality of performance.
- Analyze the viability of these methods in a laboratory setting.
- Identify and develop new sensing methods tailored to meet specific application needs.

This work has been accomplished in the framework of the following research projects:

- Community of Madrid projects: SINFOTON (S2013/MIT-2790) and SINFOTON2 by AEI/FEDER funds (S2018/NMT-4326).
- Ministerio de Ciencia, Innovación y Universidades projects: ANOMALOS (TEC2015-71127-C2-2-R), ECOSYSTEM (RTI2018-097957-B-C31).
- Alcalá University projects: Solar simulator AAA class for characterization of electrical devices.
- University of Arizona: Stimulated Raman Spectroscopy (SRS) for microbe ID (IDSEP160030).
- University of Alcalá grant for PhD: FPI-2018 (November 2018-November 2020).
- Spanish government grant for PhD: FPU-2019 (November 2020-April 2023).

1.3 Structure of the thesis

The present dissertation has been structured according to the objectives enumerated above.

- **Chapter 2: “Fundamentals of optical fibers”**

In the next chapter, we briefly introduce the fundamentals of fiber optics technology. It presents the basics of light propagation in fiber waveguides, as well as the description of intrinsic phenomena such as attenuation, dispersion and nonlinear effects present in optical fibers. In addition, a summary of the soliton formalism involved in laser generation is introduced.

- **Chapter 3: “Light-matter interaction”**

A brief review of the working principles of the main optical effects based on light-matter interaction is presented. We focus in particular on the predominant nonlinear phenomena which are required to understand the exposition of the following chapters. Also, the fundamental theory of Raman scattering is summarized, together with some of the spectroscopy techniques employed in this thesis.

- **Chapter 4: “Ultrafast fiber lasers”**

Chapter 4 introduces passively mode-locked ultrafast fiber lasers to the reader, going from a short introduction of the underlying principles behind ultrashort pulse generation in mode-locked fiber lasers, to a review of the state-of-the-art focused on the most relevant passive saturable absorbers (SAs) with the aim of devising a femtosecond fiber laser, employing a semiconductor saturable absorber mirror (SESAM) as the passive element. An overview of the main characteristics of the employed InN material as SA is then presented, before starting to describe the experimental laser configuration used in this thesis. Finally, an in-depth simulation of the laser system has been performed, denoting its limitations and improvements. This chapter covers the fundamental topics necessary to understand the following chapters.

- [Chapter 5: “Optimization of ultrafast InN based fiber laser”](#)

In this chapter, we propose a set of strategies and optimization techniques to mitigate the limitations of the ultrafast fiber laser system. Specifically, we demonstrate the optimization of the InN semiconductor characteristics, using improved mechanical and fabrication processes, showing as well how these materials can improve the ultrafast laser performance when applied in all-fiber configurations. This chapter corresponds to the work that led to the publication of references [153,160,167].

- [Chapter 6: “Sensing applications of ultrafast InN based fiber lasers”](#)

In chapter 6, we explore potential applications of the systems reported in Chapter 5, based on performing highly-sensitive absorption measurements with ultrafast fiber lasers. We demonstrate the detection of gas concentration with supercontinuum laser sources in optical fibers. A preliminary demonstration of molecular detection for biomedical sensing applications is also explored. The results here obtained were published in references [171,174].

- [Chapter 7: “Conclusions”](#)

The main conclusions of the work developed over the doctoral program are summarized in this chapter, as well as the possible future open-lines of research. Finally, a list of the work published by the author is included.

- [Bibliography and appendices](#)

The references cited in this document have been listed in order of their appearance in the bibliography.



Chapter 2

Fundamentals of optical fibers

Contents

2.1	Introduction to optical fibers	8
2.1.1	Historical context	8
2.1.2	Optical properties of fibers	9
2.2	Propagation of light in silica fibers	11
2.2.1	Maxwell equations	12
2.2.2	Linear effects in optical fibers	14
2.3	Nonlinear propagation of light in silica fibers	18
2.3.1	Nonlinear optical effects	18
2.3.2	NLSE	22
2.4	Solitons	23
2.4.1	Dispersion-managed solitons	25
2.4.2	Higher-order effects	25

This introductory chapter provides an overview of the characteristics of optical fibers, which are essential for developing fiber lasers as discussed in later chapters. In Section 2.1 a historical view of the fiber's background and its main characteristics is introduced. Section 2.2 briefly introduces the theoretical principles behind optical fiber technology, explaining the fundamentals of light propagation through the fiber, while Section 2.2.2 presents a description of the relevant phenomena that affect light along fiber propagation. Finally, a brief explanation of the soliton development will be described in Section 2.4. This chapter sets the basis for the following chapters, including the principles of fiber lasers as well as the work presented in this Ph.D. Thesis.

2.1 Introduction to optical fibers

In the last decades, optical fibers have become the principal technology in optical communications thanks to their advantageous properties compared to electrical cables, such as low losses, high data rate operation and electromagnetic immunity. Nowadays, optical fibers combined with optical lasers have led to a new era of communications, where almost every long-distance communication system relies on optical fiber cables.

2.1.1 Historical context

Light has been used as a communication tool over the last two centuries. Most ancient civilizations used simple systems, such as fire signals or mirrors to transfer elemental information. Light and optics became popular in ancient Greece, where philosophers such as Pythagoras, Euclid, and Aristotle developed theories on the nature of light [1–3].

In the following centuries, better communication systems arose with the development of the telephone in the late XIX century and the creation of coaxial cables [4]. However, despite the increase in communication capacity, their use was limited to mobile and short communication links. In order to solve these problems, coherent electromagnetic radiation sources at radio frequencies were first applied in 1897 with the invention of the radio communication system [5]. These electromagnetic sources, although capable of travelling long distances, are also limited in the amount of information transmitted at each frequency.

In 1960, the first laser system was discovered [6], yielding monochromatic, coherent, and highly directional radiation sources at optical frequencies with high-power levels, along with the discovery of new optical effects such as harmonic generation [7] and frequency mixing [8]. Hence, new optical systems were rapidly developed in the following years [9]. The invention of optical fibers as an optical communication system in 1966 by Kao and Hackmann [10], was viewed as a replacement for electrical wires, since fibers were able to convey information over larger distances. However, initial tests demonstrated high attenuation and splicing issues in the fiber cables. Ever since, the transmission and distance capabilities of optical fibers have increased exponentially until these days, with attenuation levels as low as 0.1484 dB/km in the wavelength window of 1570 nm, while covering distances of hundreds of kilome-

ters [11, 12]. As a result, data transmission using optical fibers is now ubiquitous throughout the world's telecommunications network and used for many applications, including optical sensing, imaging, and other fields.

2.1.2 Optical properties of fibers

The use of optical carrier waves guided along optical fibers for communication is an extremely attractive technique due to its numerous outstanding advantages over conventional electrical communication systems. In addition, optical fibers are generally manufactured by optical components with lifetimes of 20-30 years with very small diameters and high tensile strengths, allowing bends and twists without damage. Therefore, optical fibers are also superior in relation to handling, transportation, storage and installation compared to electrical wires, as well as in maintenance time and costs. Furthermore, optical fibers, which are commonly fabricated from glass, are electrical insulators, and thus unaffected by external electrical noise and crosstalk (negligible optical interference between fibers since optical fibers do not radiate to the external surroundings). Finally, and as it was mentioned before, optical fibers with low attenuation ($< 0.15\text{dB/km}$) and superior information-carrying capacity (50000-bandwidth improvement over coaxial cables) have replaced copper cables in long-haul telecommunication applications. The fundamental principles of optical fibers resulting in these enhanced performance capabilities are described in the following sections.

Optical fibers are essentially cylindrical threads of glass that confine light within their core, enabling its transmission over large distances with low propagation losses and immunity to external electromagnetic disturbances. Usually, these waveguides are composed of an internal glass tube (core, n_1) with dimensions ranging from $5\text{ }\mu\text{m}$ to $50\text{ }\mu\text{m}$, and covered by a glass cylinder (cladding, n_2) with different refractive index and a diameter of hundreds of μm . An additional polymer jacket is used for external protection (with an extension double to the cladding), preventing the fiber from moisture and abrasion [13]. In order to guide light waves, these threads are engineered based on the total internal reflection principle [14], i.e., the refractive index n_2 of the cladding layer is slightly lower than the core refractive index n_1 . Typically, optical fibers are made of fused silica (SiO_2) glass due to its low cost and low propagation losses. The addition of specific dopants to the silica glass during the fabrication process, increases the core refractive index (e.g. Germanium oxide) or decreases the cladding refractive index (e.g. Fluor oxide). In addition, by doping the waveguides with other ions such as rare-earths, optical fibers can also be used as powerful fiber amplifiers [15], as we will explain in Chapter 4, enabling the transmission of weak signals without additional external electro-optical devices, hence increasing their transmission capacity compared to electrical cables.

In the last decades, significant progress has been made in the fabrication of customized optical fibers with different materials, shapes, and sizes, which play an important role in multiple applications, such as optical communications, material processing, or biomedical sensing. The production of application-specific optical fibers requires numerous technological processes, tailored to their specific use [16]. An optical fiber is characterized by two main parameters: the transverse refractive index profile and the number of modes.

- Depending on the relative core-cladding index difference, different types of guiding structures can be constructed. The most common configuration, known as the step-index profile, is based on the introduction of a well-defined interface between the core and cladding refractive indices. Other configurations, such as graded-index profiles, have a gradual increase of the core refractive index from the boundaries of the core (matching the value of the cladding refractive index) to the center, providing lower propagation losses. Therefore, more sophisticated refractive index profiles yield better transmission capabilities. A diagram of the two fiber configurations is depicted in Fig. 2.1.

However, guiding is not always achieved by single core-cladding optical fiber configurations. Some special structures, such as hollow core fibers [17], multicore fibers [18], or geometrically asymmetric refractive index profiles based on the introduction of high birefringence or nonlinear properties within the guiding region [19], have been successfully applied for, e.g., fiber sensing applications [20]. Nevertheless, most of the fibers applied in the telecommunication infrastructure are based on standard step-index silica glass optical fibers due to their simplicity and low manufacturing cost.

In this work, we will be centered on the use of standard optical fibers, though some of these microstructured fibers may be used in this thesis for certain applications, as we will see in Chapter 6.

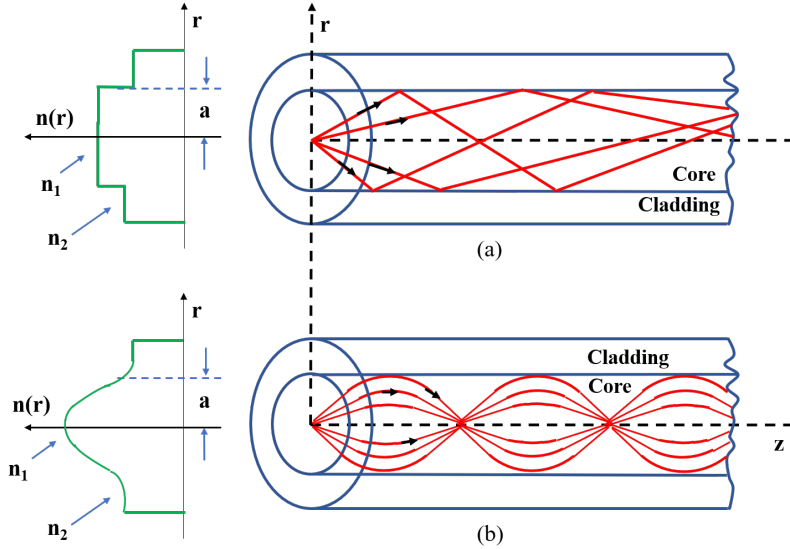


Figure 2.1: Schematic of refractive index profiles (left) in standard multimode optical fibers and its corresponding propagation modes (right), (a) with a step-index structure (top), (b) with a graded-index architecture (bottom). Reproduced figure from [12].

- An important characteristic of optical fibers is the number of modes supported by the fiber core, which may be described as a function of the V parameter:

$$V = \frac{2\pi}{\lambda} a \sqrt{n_1^2 - n_2^2}, \quad (2.1)$$

where λ is the optical wavelength of the transmitted light and a represents

the core radius of the optical fiber. The transverse modes of the fiber constitute an optical distribution of the electromagnetic field transmitted along the propagation direction's perpendicular plane, as seen in Figs. 2.1 and 2.2. For single-mode operation, step-index fibers require $0 \leq V \leq 2.405$, which for usual refractive index differences implies a core radius a of less than $5\mu\text{m}$. In comparison to single-mode fibers (SMF), multimode fibers enable the propagation of hundreds of modes through large cores, with typical values of 25-30 μm core radius.

The term optical fiber in this text, unless otherwise specified, is referred to as single-mode fiber since nonlinear effects are generally associated with them. We will mostly use standard SMFs over this thesis.

For different refractive-index profiles, different transversal mode distributions can be obtained (see Fig. 2.1). The main property that characterizes the transversal distribution profile is the mode-field diameter. Since we are employing standard step-index single-mode optical fibers, a single fundamental Gaussian mode distribution can be approximated [21]. In this case, the mode-field diameter (MFD) corresponds to the distance between the $1/e$ amplitude field points in relation to the maximum field within the mode distribution, as depicted in Fig. 2.2. The spot size w_0 , defined as the half-width of the transversal mode, can be measured as $w_0 = \text{MFD}/2$. It must be noticed that the MFD in most refractive index profiles does not coincide with the fiber core diameter (in the case of SMFs, the MFD value is slightly larger than the core diameter).

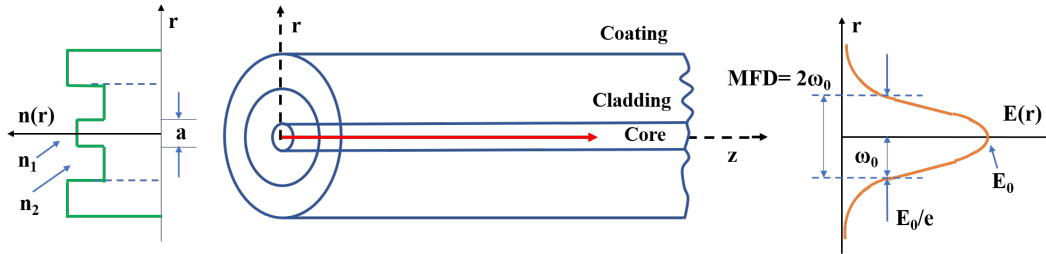


Figure 2.2: Visual representation of the transversal Gaussian mode distribution (right) for a standard step-index single-mode optical fiber (left). $E(r)$ corresponds to the electric field amplitude, E_0 is the maximum value of the amplitude, and w_0 is the half-width of the Gaussian mode measured when the electromagnetic field decays at $1/e$. Reproduced figure from [12].

In the following section, we will introduce a brief description of the fundamentals of light propagation in the optical fiber, and an analysis of the phenomena that affect light within the optical fiber, laying the foundations for the following chapters and the work developed in this thesis.

2.2 Propagation of light in silica fibers

For single-mode optical fibers, in which a single fundamental mode propagates through a core size comparable to the guided wavelength, the analysis of the wave evolution must be studied according to electromagnetic theory.

2.2.1 Maxwell equations

Despite being a fundamental constant of the universe, the speed of light will vary with the optical density of the propagation medium. For a given medium, this “optical density” is quantified through its refractive index and associated with the speed of light as ($n = c/v_p$, where v_p refers to the propagation velocity within the medium). The refractive index is traditionally interpreted as an oscillator model of bound charges, whose stored electromagnetic radiation is emitted at the same frequency as the input light but with a certain delay.

As with many other electromagnetic phenomena, light can be understood as an electromagnetic wave whose propagation can be described by Maxwell’s equations [22]. In the case of dielectric media, i.e., in the absence of free charges (zero conductivity), the propagation of electromagnetic waves is governed by two coupled vector relationships, which can be expressed by an electric field E , a magnetic field H , and their corresponding flux electric and magnetic densities D and B respectively, in the form:

$$\vec{\nabla} \cdot \vec{D} = 0 \quad , \quad (2.2a)$$

$$\vec{\nabla} \cdot \vec{H} = 0 \quad , \quad (2.2b)$$

$$\vec{\nabla} \times \vec{E} = -\frac{\partial \vec{B}}{\partial t} \quad , \quad (2.2c)$$

$$\vec{\nabla} \times \vec{H} = \frac{\partial \vec{D}}{\partial t} \quad . \quad (2.2d)$$

The propagation of light in optical fibers can be represented as the superposition of incident light with all the optical fields produced by the medium. Material polarization is the result of the generation of a dipole moment created by the separation of positive and negative charges due to the application of an external field. Therefore, the relation between the flux electric and magnetic densities and the applied external fields can be written as,

$$\vec{D} = \varepsilon_0 \vec{E} + \vec{P} = \varepsilon \vec{E} \quad , \quad (2.3a)$$

$$\vec{B} = \mu_0 \vec{H} + \vec{M} = \mu \vec{H} \quad , \quad (2.3b)$$

where \vec{P} and \vec{M} are the electric and magnetic polarizations, the latter of which is equal to zero in the case of dielectric media such as in optical fibers. The refractive index is determined by a material’s response to a transient electromagnetic field and related by the electrical permittivity ε and magnetic permeability μ of the material;

$$n = \sqrt{\frac{\varepsilon}{\varepsilon_0} \frac{\mu}{\mu_0}} \quad . \quad (2.4)$$

Therefore, the propagation velocity of the electromagnetic wave in the optical fiber can be defined as $v_p = \frac{1}{\sqrt{\mu\varepsilon}}$.

In order to obtain a solution of the electric field, \vec{D} and \vec{B} can be substituted into Eq. (2.2c) and Eq. (2.2d) giving:

$$\vec{\nabla} \times \vec{\nabla} \times \vec{E} = -\mu\varepsilon \frac{\partial^2 \vec{E}}{\partial t^2} , \quad (2.5a)$$

$$\vec{\nabla} \times \vec{\nabla} \times \vec{H} = -\mu\varepsilon \frac{\partial^2 \vec{H}}{\partial t^2} . \quad (2.5b)$$

However, by applying the divergence conditions ($\vec{\nabla} \times \vec{\nabla} \times \vec{\psi} = \vec{\nabla}(\vec{\nabla} \cdot \vec{\psi}) - \vec{\nabla}^2 \vec{\psi}$) on Eq. (2.5a) and Eq. (2.5b), where the divergence, $\vec{\nabla} \cdot \vec{\psi}$, can be neglected because of the absence of free charges, we can obtain the nondispersive wave equations of the propagation of light in optical fibers:

$$\vec{\nabla}^2 \vec{\psi} = \frac{1}{v_p^2} \frac{\partial^2 \vec{\psi}}{\partial t^2} , \quad (2.6)$$

where ψ may refer to both the \vec{E} or \vec{H} electromagnetic fields. This equation, also known as the Helmholtz equation, describes the propagation of light through optical fibers. Since the electric component of the electromagnetic field dominates in most light-matter interactions, the propagation in optical fibers will henceforth be described in terms of E for sake of brevity [23].

By expressing Eq. (2.6) in polar coordinates and applying separation of variables, the basic solution of the wave equation can be represented as a sinusoidal monochromatic, uniform, plane wave with a certain frequency (ν or $\omega = 2\pi\nu$), or wavelength (associated with the frequency by $\lambda = v_p/\nu$) and a propagation direction given by the wavevector \tilde{k} (related to $|k| = 2\pi/\lambda = \omega/c$):

$$\vec{E}(\vec{r}, t) = \frac{1}{2} \{ A(\vec{r}, t) F(r) e^{i(k\vec{r} - \omega_0 t + \varphi(t))} + c.c. \} . \quad (2.7)$$

The solution of Eq. (2.7) represents the real electric field generated by a radiation source that propagates in an optical fiber, being $A(\vec{r}, t)$ the electric pulse envelope (amplitude) and $F(r)$ is the mode distribution in the optical fiber, represented by the Bessel function, and $\varphi(t)$ is the optical phase in the time domain. The “c.c.” term corresponds to the complex conjugate of the electric field. As it was mentioned before, a good approximation for the fundamental fiber mode function is a Gaussian distribution (see Fig. 2.2) in the form:

$$F(r) \approx e^{(-r^2/w^2)} , \quad (2.8)$$

where w corresponds to the half-width of the mode distribution.

For simplicity, the complex conjugate term is omitted, since only the real part of the electric field has a physical meaning:

$$\vec{E}(\vec{r}, t) = \text{Re} \{ A(\vec{r}, t) e^{i(k\vec{r} - \omega_0 t + \varphi(t))} \} = A(\vec{r}, t) \cos \left(k\vec{r} - \omega t + \varphi(t) \right) . \quad (2.9)$$

Nevertheless, the parameter measured in this thesis is the intensity, determined by the quadratic module of the amplitude of the electric field $I(t) \approx |\vec{A}|^2$ and

detected by an optical photodiode. The optical intensity can be defined therefore as the power per unit area and is expressed in W/cm^2 units.

The Fourier transform (FT) of the electric field allows for a representation of this field in the frequency domain which can be written as,

$$\vec{E}(\omega) = \int_{-\infty}^{+\infty} \vec{E}(t) e^{i\omega t} dt . \quad (2.10)$$

Therefore, we can define a spectral electric field with a wavevector $k(\omega)$

$$\vec{E}(r, \omega) = \{ A(\omega) F(r) e^{[i n k(\omega) \vec{r}]} \} , \quad (2.11)$$

where \vec{r} is the direction of propagation, and $A(\omega)$ is the amplitude of the spectral electric field. The factor $n k(\omega)$ is known as the wavenumber constant (β), which for narrowband optical fields can be expressed in terms of a Taylor expansion around the central frequency ω_0 [24]:

$$\beta(\omega) = n(\omega) k_0 = \beta_0 + \beta_1(\omega - \omega_0) + \frac{\beta_2}{2}(\omega - \omega_0)^2 + \dots , \quad (2.12)$$

being m and integer, denoting the order of the Taylor expansion. The parameters β_0 , β_1 and β_2 provide information about the phase and group velocity (v_p and v_g , respectively) as it will be explained in the next section.

Analogously to the temporal domain, the amplitude of the pulse in the frequency domain (A) is related to the spectral intensity $I(\omega)$. The amplitude of the electric field can be represented in terms of the spectral carrier envelope with the inverse Fourier transform:

$$A(\vec{r}, t) = \frac{1}{2\pi} \int_{-\infty}^{+\infty} A(\vec{r}, \omega - \omega_0) e^{[-i(\omega - \omega_0)t]} d\omega . \quad (2.13)$$

For a complete explanation of the mathematical assumptions, see [24].

2.2.2 Linear effects in optical fibers

We will derive the main effects involved in the propagation of optical waveforms within optical fibers in this section. Initially, a first-order approximation of the fiber response is assumed, analyzing the fiber losses and chromatic dispersion effects.

2.2.2.1 Fiber losses

In a first-order approximation, the polarization of the material can be written as a function of the electric field as [23]:

$$P_i = \varepsilon_0 \sum_{ij} \tilde{\chi}_{ij} E_j , \quad (2.14)$$

where i, j are the Cartesian coordinates x, y and z , and $\tilde{\chi}_{ij}$ is the electric susceptibility tensor, which is related to the permittivity of the dielectric material by the relation:

$$1 + \chi = \frac{\varepsilon}{\varepsilon_0} = \varepsilon_r , \quad (2.15)$$

being ε_r the medium's relative permittivity. This electric susceptibility is a complex parameter, which is usually employed in the frequency domain. The separation of the electric susceptibility into its real and imaginary components, denotes two physical quantities, the refractive index (n) and the attenuation (α) of the optical pulse in the dielectric medium:

$$n(\omega) = 1 + \frac{1}{2} \operatorname{Re} [\chi(\omega)] , \quad (2.16a)$$

$$\alpha(\omega) = \frac{\omega}{n c} \operatorname{Im} [\chi(\omega)] . \quad (2.16b)$$

Attenuation describes the transmission loss of the optical intensity of light when propagating through an optical medium. Fiber losses originate from multiple physical mechanisms, which can be derived from intrinsic phenomena, such as material absorption or scattering, or from extrinsic lossy events like material impurities within the optical fiber or mechanical defects (microbending losses, mode coupling radiation losses or splicing losses, among others).

The global effect of fiber losses (usually expressed in dB/km units) can be represented as a logarithm relationship between the input power P_0 and the transmitted optical power P_L at a given distance L [25],

$$\alpha_{dB} = \frac{-10}{L} \log \left(\frac{P_L}{P_0} \right) . \quad (2.17)$$

The origin of the material absorption losses stems from the material composition and fabrication process of the optical fiber, or from impurities within the fused silica glass.

In the first case, since the attenuation parameter changes in terms of the resonance frequencies of the material, two major absorption bands corresponding to the ultraviolet region and the far infrared region can be measured, leading to the generation of a low absorption window that covers a spectral range from 0.8 and up to 1.7 μm [11].

On the other hand, the extrinsic losses are related to material impurities, dominated by the absorption of water (OH^- ion) in the silica glass. The absorption peaks of water are centered at 0.72, 0.95 and 1.4 μm , creating narrow windows of low attenuation around 1.3 and 1.5 μm wavelengths [26].

Within the low absorption bands, the predominant intrinsic loss mechanism in optical fibers is Rayleigh scattering, created by small inhomogeneities of the refractive index. This causes part of the beam to diverge in other propagation directions from the initial one. Due to its $1/\lambda^4$ dependency, this intrinsic process dominates at the low-wavelength absorption window, and particularly at short wavelengths [27].

Therefore, the total attenuation in the optical fiber is minimized for light at around $1.55 \mu\text{m}$ with a total attenuation value of 0.2 dB/km , as shown in Fig. 2.3. Therefore, optical pulses generated in the near-infrared region will be the only ones considered for this dissertation.

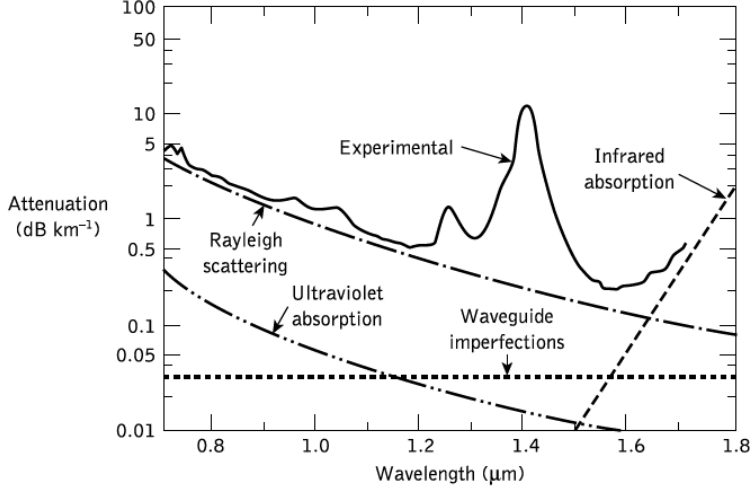


Figure 2.3: Attenuation spectrum of a single-mode optical fiber, with the corresponding absorption and scattering loss mechanisms [11].

2.2.2.2 Chromatic dispersion

The phenomenon of chromatic dispersion refers to the interplay of light with bound electrons in the dielectric material (optical fiber) causing the dependency of the refractive index with the optical frequency [28]. A monochromatic lightwave propagating along an optical fiber travels at a phase velocity (v_p). However, light is generally composed of a combination of multiple plane waves, what is called a wave packet. The velocity of propagation of the wave packet (optical pulse), is designated as group velocity $v_g(\omega)$. The phase and group velocities of an optical pulse travelling in an optical fiber are almost coincident with a value of $v = 2 \cdot 10^8 \text{ m/s}$, and can be extracted from the zero and first-order terms in Eq. (2.12),

$$v_p(\omega_0) = \frac{\omega}{k(\omega)} = \frac{c}{n(\omega)} = \frac{\omega_0}{\beta_0} , \quad (2.18a)$$

$$v_g(\omega_0) = \left. \frac{d\omega}{dk} \right|_{\omega=\omega_0} = \frac{c}{n(\omega_0 + \omega_0 \frac{dn}{d\omega})} = \frac{1}{\beta_1} . \quad (2.18b)$$

In Fig. 2.4 (a), a schematic representation of the phase and group velocities of two different pulses is depicted. It must be noted that even if each of the wavepackets has a different phase velocity (Δv_p), the group velocity coincides in accordance with the above explanation.

As mentioned before, chromatic dispersion refers to the variation of v_g with the optical frequency, a phenomenon that generates the broadening (or potentially also compression) of the travelling pulse in the optical fiber. This term, also known as

Group Delay Dispersion (GDD), is related to the group velocity as:

$$\beta_2 = \frac{d\beta_1}{d\omega} = \frac{d}{d\omega} \left(\frac{1}{v_g} \right) = \frac{1}{c} \left[2 \frac{dn(\omega)}{d\omega} + \omega \frac{d^2\omega}{d\omega^2} \right]. \quad (2.19)$$

Nevertheless, in most literature, chromatic dispersion is represented per unit length, referred to as Group Velocity Dispersion (GVD) in units of s^2/m .

In practice, it is also common to express the dispersion effect as a function of the dispersion parameter D in units of s/m^2 , connected to the GVD coefficient by the following equation:

$$D = -\frac{2\pi c}{\lambda^2} \beta_2. \quad (2.20)$$

The frequency value where the dispersion coefficient vanishes is known as the zero-dispersion wavelength (λ_D). In SMF optical fibers, this value is close to $1.3 \mu\text{m}$. However, changes in the refractive index profile in optical fibers generate a shift of the zero-dispersion wavelength in the vicinity of $1.55 \mu\text{m}$, creating the well-known dispersion-shifted fibers (DSF). Another example are dispersion-compensating fibers (DCF), in which the zero-dispersion wavelength is higher than $1.6 \mu\text{m}$, thus the β_2 exhibits a large positive value.

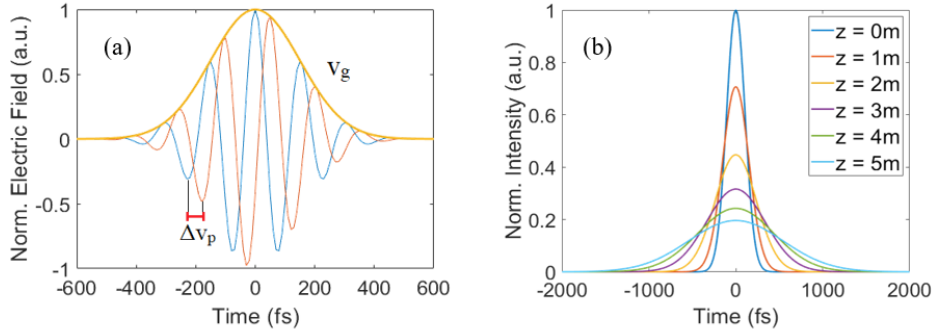


Figure 2.4: Dispersion effect on a Gaussian 250 fs optical pulse propagating in a 5 m SMF, (a) representation of the phase (v_p) and group velocities (v_g) in two different wavepackets, (b) broadening effect of the second-order chromatic dispersion coefficient $\beta_2 = -20 \text{ ps}^2/\text{km}$.

Depending on the sign of the dispersion parameter, two different regimes can be defined. For optical wavelengths such that $\lambda < \lambda_D$ or $\beta_2 > 0$, the medium has what is called normal dispersion, that is low frequencies (red-shifted) travel faster in an optical fiber than high frequency (blue-shifted) components. On the other hand, if the wavelength of the light exceeds that of zero-dispersion ($\lambda > \lambda_D$), the medium displays anomalous dispersion or the dispersion coefficient becomes negative $\beta_2 < 0$, i.e., red-shifted components travel slower than blue-shifted ones [24]. An optical pulse can be widened or shortened while propagating through the optical fiber, depending on the sign of the GVD coefficient and its own frequency chirp. The most common optical fibers that present normal and anomalous dispersion at $1.55 \mu\text{m}$ are, respectively, the erbium-doped fiber (EDF) and the single-mode fiber (SMF), which will be described in Chapter 4. The effect of GVD in a 250 fs Gaussian optical pulse propagating through 5 m of SMF with a second-order dispersion coefficient of

$\beta_2 = -20 \text{ ps}^2/\text{m}$ is shown in Fig. 2.4 (b), corresponding to a dispersion coefficient of $D = 17 \text{ ps/nm km}$.

2.3 Nonlinear propagation of light in silica fibers

In the following section, a complete discussion of the nonlinear effects that affect the propagation of pulses within optical fibers is presented.

2.3.1 Nonlinear optical effects

As explained in the latter section, polarization depends on the electric field by the expression defined in Eq. (2.14). The polarization parameter is proportional to the electric field under the assumption of low optical intensities [29]. However, when the optical intensity of the input electric field is too high, nonlinear effects appear and the polarization vector can no longer be considered linear. Hence, the total polarization of a system must be expressed as [30]:

$$\begin{aligned} P(t) = & \varepsilon_0 \int_{-\infty}^{\infty} \chi^{(1)}(t') \cdot E(t-t') dt' \\ & + \varepsilon_0 \int \int_{-\infty}^{\infty} \chi^{(2)}(t', t'') \cdot E(t-t') E(t-t'') dt' dt'' \\ & + \varepsilon_0 \int \int \int_{-\infty}^{\infty} \chi^{(3)}(t', t'', t''') \cdot E(t-t') E(t-t'') E(t-t''') dt' dt'' dt''' + \dots \end{aligned} \quad (2.21)$$

Each χ^i corresponds to the i -order susceptibility tensor; $\chi^{(1)}$ is the first-order electric susceptibility, which is related to the linear refractive index, and second-order susceptibility $\chi^{(2)}$ leads to some nonlinear effects, such as second harmonic generation (SHG), among others. The third-order susceptibility $\chi^{(3)}$ is related to nonlinear effects such as third harmonic generation (THG) and Kerr effect [24]. As a result of the symmetry of fused silica materials, the second-order term is equal to zero [31] and hence, only third-order effects should be considered.

Therefore, an expression for the linear and nonlinear terms of the polarization vector can be obtained as a function of the first and third order susceptibilities [30] $P = P_L + P_{NL}$ where:

$$P_L(\vec{r}, t) = \varepsilon_0 \int_{-\infty}^{+\infty} \chi^{(1)}(t-t') E(\vec{r}, t') e^{i\omega_0(t-t')} dt' , \quad (2.22a)$$

$$P_{NL}(\vec{r}, t) = \varepsilon_0 \chi^{(3)} : E(\vec{r}, t) E(\vec{r}, t) E(\vec{r}, t) . \quad (2.22b)$$

Note that, in a first approximation, the Kerr third-order susceptibility effect has been considered instantaneous.

The total polarization of the material propagating for instance in the x direction of the optical fiber can be expressed as [29]:

$$P_0 = \varepsilon_0 \left(\chi_{xx}^{(1)} + \frac{3|E_0|^2}{4} \chi_{xxxx}^{(3)} \right) E_0 = \varepsilon_0 \chi_{eff} E_0 , \quad (2.23)$$

where $\chi_{xx}^{(1)}$ and $\chi_{xxxx}^{(3)}$ are the first and third order x-direction component susceptibilities, respectively, and χ_{eff} is the effective susceptibility of the dielectric material. From this equation, it will be derived its main consequences, i.e. the Kerr effect and the nonlinear phase modulation in optical fibers.

2.3.1.1 Kerr effect

The phenomenon of Kerr effect refers to the nonlinear dependence of the refractive index on the incident optical intensity for high-power optical pulses. Thus, the refractive index can be expressed from the material susceptibility χ_{eff} as [29]:

$$n^2 = 1 + \chi_{\text{eff}} = 1 + \chi_x^{(1)} + \frac{3|E_0|^2}{4} \chi_{xxxx}^{(3)} = n_0^2 \left(1 + \frac{3|E_0|^2}{4n_0^2} \chi_{xxxx}^{(3)} \right) \quad (2.24)$$

where $|E_0|^2$ corresponds to the intensity of the optical pulse and n_0 is the linear term of the refractive index ($n_0 = 1 + \chi_x^{(1)}$). Using a first-order Taylor expansion, assuming that the index dependency with intensity is small, Eq. (2.24) can be expressed as a function of the optical intensity:

$$n = n_0 + n_2 I, \quad (2.25)$$

where n_2 is the nonlinear term of the refractive index, being $n_2 \ll n_0$ and equal to $3\chi_{xxxx}^{(3)}/8n_0$. The parameter n_2 is also known as the Kerr coefficient [32]. Particularly, the Kerr coefficient for single-mode fused silica fibers has a value of $n_2 = 2 \cdot 10^{-20} \text{ m}^2 \text{ W}^{-1}$, which becomes of particular importance in high-power optical pulses and/or long fiber distances [24].

2.3.1.2 Phase modulation and nonlinear spectral broadening

The nonlinear dependency of the refractive index leads to the generation of a temporal phase-shift of an optical pulse along its propagation through the optical fiber. Two different phenomena can be distinguished, self-phase modulation, and cross-phase modulation, as described below.

- The intensity dependence of the refractive index produces a self-induced temporal phase-shift in the optical wave [33]. This nonlinear effect, named as Self-Phase Modulation (SPM), can be expressed as a function of the nonlinear refractive index by:

$$\varphi = \frac{2\pi}{\lambda_0} n(I) L = (n_0 + n_2 I) k_0 L, \quad (2.26)$$

where L is the fiber length and k the wavenumber. Therefore, the phase-shift can be expressed as a small perturbation of the refractive index ($\Delta n = n_2 I$) as follows:

$$\Delta\varphi = \frac{2\pi L}{\lambda_0} \Delta n = \frac{2\pi n_2 L}{\lambda_0} \frac{P}{A_{\text{eff}}}. \quad (2.27)$$

In Eq. (2.27), the optical intensity has been substituted by the expression

$I = P/A_{eff}$ being P the incident power and A_{eff} is the area of the transversal mode distribution. By assuming a Gaussian mode distribution propagating through the optical fiber (see Fig. 2.2), the nonlinear coefficient of the phase-modulation term is:

$$\gamma = \frac{\Delta\varphi}{P \cdot L_{eff}} = \frac{n_2\omega_0 L_{eff}}{c A_{eff}} = \frac{4n_2 L_{eff}}{\lambda_0 w^2} , \quad (2.28)$$

being w the beam radius of the mode distribution, and ω_0 the angular frequency of the optical pulse and L_{eff} the effective length of the interaction region defined by $\pi w^2/\lambda$ for the case of Gaussian beams with a typical value of $80 \mu\text{m}^2$ for SMF propagation at $1.55 \mu\text{m}$.

Therefore, the expression of the electric field of an optical pulse with SPM while propagating in a SMF fiber is [24],

$$E(L, t) = E_0(0, t) e^{[i\varphi_{NL}(L, t)]} , \quad (2.29)$$

being $E_0(0, t)$ the electric field amplitude at the origin.

Due to the nonlinear dependency of the refractive index, the temporal phase of the optical pulse can be expanded into its nonlinear terms [34]:

$$\varphi(t) = \varphi_L(t) + \varphi_{NL}(t) , \quad (2.30)$$

$$= \varphi_0 + \varphi_1 t + \frac{1}{2}\varphi_2 t^2 + \frac{1}{6}\varphi_3 t^3 + \dots , \quad (2.31)$$

where φ_i is the i -th order of the optical pulse's nonlinear temporal phase. The zeroth-order of the temporal phase is related to the phase of the central frequency ω_0 of the optical pulse. The linear variation of the phase with time, φ_1 , can be related to the instantaneous frequency of the optical pulse as:

$$\omega_{inst} = \omega_0 + \Delta\omega = \omega_0 - \frac{\partial\varphi}{\partial t} . \quad (2.32)$$

Thus, a change in frequency $\Delta\omega$ can be understood as a variation of the phase as a function of time. This implies that, depending on the sign of the linear phase coefficient, a frequency shift to shorter or larger frequencies can be introduced.

Substituting this frequency variation in Eq. (2.27), it can be obtained an expression for the frequency change as a function of the nonlinear refractive index and thus related to the optical intensity.

$$\Delta\omega = \frac{2\pi n_2 L}{\lambda_0} \frac{dI}{dt} . \quad (2.33)$$

Finally, the quadratic term of the temporal phase φ_2 , is connected to the variation of the instantaneous frequency with time. This effect is usually referred to as linear chirp. For a positive increase of ω_{inst} with time, a positive chirp is introduced, while in the opposite case, a negative chirp is generated. A nega-

tive Gaussian chirped pulse with a temporal width of 250 fs and a nonlinear phase (chirp parameter) of $\varphi_2 = 400 \text{ rad/fs}^2$ has been plotted in Fig. 2.5 (a).

In summary, the SPM effect introduces a modification (broadening) of the pulse spectrum due to the time dependence of the nonlinear phase-shift [34]. An example of pulse broadening in 5-m of SMF with a 250 fs Gaussian optical pulse due to the effect of SPM with a nonlinear coefficient of $\gamma = 1.3 \text{ W}^{-1}\text{km}^{-1}$ is depicted in Fig. 2.5(b).

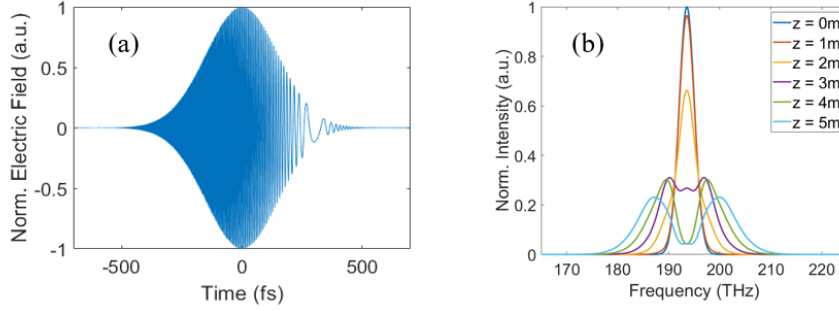


Figure 2.5: SPM-induced broadening of an initially unchirped 250 fs Gaussian pulse with a SPM parameter of $\gamma = 1.3 \text{ W}^{-1}\text{m}^{-1}$ while propagating through 5 m of SMF.

- Cross-Phase Modulation (XPM) refers to the nonlinear phase-shift generated in a pulse due to the interaction with other co-propagating pulses with different wavelengths, directions or polarizations within an optical fiber [35]. The variation of the intensity of one of the pulses, modulates the refractive index of the fiber (Kerr effect), generating a phase modulation on the overlapping optical fields. Analogously to SPM, this phase modulation can be understood as a crosstalk mechanism between channels, creating a frequency modulation and thus, a spectral broadening in the optical pulse. However, in contrast with electric crosstalk, no energy transfer is produced between co-propagating channels. The XPM effect becomes stronger with an increase in the number of channels or a reduction in the channel spacing. Nevertheless, in most practical cases, this effect is weakened since overlapping of optical pulses with different wavelengths or polarizations cannot be maintained for long fiber distances due to the group velocity mismatch [36].

2.3.1.3 Modulation Instability

Modulation Instability (MI) is a nonlinear process that leads to phase and amplitude modulation of an optical beam due to the interplay of both dispersion and nonlinear effects [37]. In the context of optical fibers [38], small variations of the incident intensity generate a variation of the refractive index (Kerr effect), leading to a time-varying nonlinear phase-shift, and thus producing a frequency chirp on the optical perturbation as explained in the previous section. This introduces a red-shift of the leading edge of the perturbation, whereas the trailing edge is shifted towards the blue-components of the optical spectrum [39]. In anomalous dispersion, this effect reinforces the perturbation (leading and trailing edge tend to meet) and therefore the effect increases exponentially (the negative chirp stretches the optical

pulse, generating an instability of the steady state). In the case of normal dispersion ($\beta_2 > 0$), a temporal broadening of the optical pulse is produced due to the generation of a positive chirp, hence leading to a reduction of the perturbation. In other words, MI only exists in anomalous dispersion. This phenomenon underlies the working principle of ultrashort pulsed laser generation in single-mode optical fibers developed and studied in this dissertation.

2.3.2 NLSE

The equation described in Eq. (2.6) corresponds to the general representation of the wave equation. Nevertheless, the propagation of optical pulses with a width below 10 ns and intensities >10 GW/cm² in optical fibers is influenced by dispersion and nonlinear effects, thus affecting their spectrum and shape [40]. Taking into account the nonlinear component of the polarization vector, the wave equation is written as:

$$\vec{\nabla}^2 \vec{E} - \mu\epsilon_0 \frac{\partial^2 \vec{E}}{\partial t^2} = \mu \left[\frac{\partial^2 \vec{P}_L}{\partial t^2} + \frac{\partial^2 \vec{P}_{NL}}{\partial t^2} \right] , \quad (2.34)$$

where P_L and P_{NL} correspond to the linear and nonlinear polarization components. Therefore, transforming Eq. (2.34) to the frequency domain [31]:

$$\vec{\nabla}^2 \vec{E} + (n(\omega)k_0)^2 \vec{E} + k_0^2 \vec{P}_{NL}(\omega) = 0 , \quad (2.35)$$

where $\vec{P}_{NL}(\omega)$ corresponds to the nonlinear polarization parameter in the frequency domain. The factor $n(\omega)k_0$ and the wavenumber constant β are no longer linear parameters but include both the dispersion and nonlinear effects as:

$$\tilde{\beta}(\omega) = \beta(\omega) + \Delta\beta , \quad (2.36)$$

where the term $\Delta\beta$ represents the fiber losses and nonlinearities of the optical pulse [24]. By substituting Eq. (2.11) into Eq. (2.35), we can obtain the nonlinear amplitude of the electric field in the temporal domain [24]:

$$\frac{\partial A(z, t)}{\partial z} = -\beta_1 \frac{\partial A(z, t)}{\partial t} - i \frac{\beta_2}{2} \frac{\partial^2 A(z, t)}{\partial t^2} + i \Delta\beta A(z, t) , \quad (2.37)$$

For the sake of simplicity, the wavenumber is expanded up to $m = 2$. It must be noticed that higher-order dispersion and nonlinear coefficients should be treated as small perturbations of the P_L component, which are negligible in a first-order approximation [31]. Taking these effects into consideration, Eq. (2.37) can be expanded as:

$$\frac{\partial A(z, t)}{\partial z} + \beta_1 \frac{\partial A(z, t)}{\partial t} + i \frac{\beta_2}{2} \frac{\partial^2 A(z, t)}{\partial t^2} + \frac{\alpha}{2} A(z, t) = i \gamma |A|^2 A(z, t) , \quad (2.38)$$

being β_1 and β_2 the first and second-order dispersion coefficients, α corresponds to the fiber losses, and γ is the nonlinear coefficient of the optical fiber and related to the Kerr effect explained in section 2.3.1.2. The $|A|^2$ term represents the optical power of the pulse, which is assumed to be normalized for this equation. Eq. (2.38),

also known as the nonlinear Schrödinger equation (NLSE), represents the optical pulse propagation in a single-mode optical fiber by taking into consideration fiber losses, nonlinearities and dispersion effects. As it will be discussed in Chapter 4, if the optical fiber has a gain medium [24], Eq. (2.37) must include a gain coefficient term (g) as $\tilde{\alpha} = \alpha - g$. However, these effects can be counteracted, so a stable pulse can be obtained, as explained in the next section.

2.4 Solitons

The term soliton, mentioned for the first time in 1965 [41], refers to the formation of a particular optical wave by nonlinear dispersion compensation, in which the spectral broadening induced by the nonlinear chirp in SPM balances the temporal broadening generated by the GDD. When acting independently, these broadening effects reduce the propagation distance of the optical pulse. However, the balance of these phenomena at a critical pulse intensity enables the propagation of optical waves over large distances without any distortion of their temporal or spectral shape. This feature becomes important in the application field of high-speed optical fiber communications [42].

Optical soliton propagation can be theoretically described by the NLSE obtained in Eq. (2.38). In order to study these soliton waves, it is useful to normalize the NLSE equation by introducing some variables [24],

$$U = \frac{A}{\sqrt{P_0}}, \quad \xi = \frac{z}{L_D}, \quad \tau = \frac{T}{T_0}, \quad (2.39)$$

where T is connected to the time vector and group velocity as $T = t - z/v_g$, T_0 corresponds to the temporal width of the optical pulse, P_0 is the peak power, z is the propagation direction, and L_D is the dispersion length and defined by $T_0^2/|\beta_2|$. Using these parameters, Eq. (2.38) can be expressed as,

$$i \frac{\partial U}{\partial \xi} = -\frac{1}{2} \frac{\partial^2 U}{\partial \tau^2} - N^2 |U|^2 U. \quad (2.40)$$

This equation constitutes the NLSE equation for soliton propagation in the anomalous dispersion regime (assuming $\text{sgn}(\beta_2) = -1$) as for SMF optical fibers [43]. The N parameter is referred to as the soliton order and can be expressed by:

$$N^2 = \frac{L_D}{L_{NL}} = \frac{\gamma P_0 T_0^2}{|\beta_2|}, \quad (2.41)$$

where $L_{NL} = (\gamma P_0)^{-1}$ is the nonlinear length. The N parameter can be suppressed on the previous equation by substituting the amplitude of the electric field by $u = N U$,

$$i \frac{\partial u}{\partial \xi} = \frac{1}{2} \frac{\partial^2 u}{\partial \tau^2} - |u|^2 u. \quad (2.42)$$

It must be noted that the N parameter determines the importance of the SPM or GVD effects in the pulse propagation along the optical fiber: for values $N \gg 1$, the

SPM effect dominates, while dispersion governs for $N \ll 1$. Nevertheless, for $N = 1$, pulse evolution is equally affected by the SPM and GVD effects, corresponding to the first-order soliton [44]. This optical wave can also be called the fundamental soliton since the shape of the optical pulse remains stable during its propagation, unaffected after a collision with another soliton. On the other hand, a higher-order solitons integer ($N > 1$), exhibit a periodic (or breathing) evolution as the pulse propagates along the optical fiber, i.e., the pulse is stretched in time until it is divided in separate pulses, and then recombined with its original shape for a length of z_0 [24],

$$z_0 = \frac{\pi}{2} \frac{T_0^2}{|\beta_2|} . \quad (2.43)$$

An example of a higher-order ($N = 2$) soliton propagation in SMF with a dispersion and nonlinear coefficients of $\beta_2 = -1\text{ps}^2/\text{km}$ and $\gamma = 1\text{W}^{-1}\text{km}^{-1}$ over a soliton period z_0 is represented in Fig. 2.6.

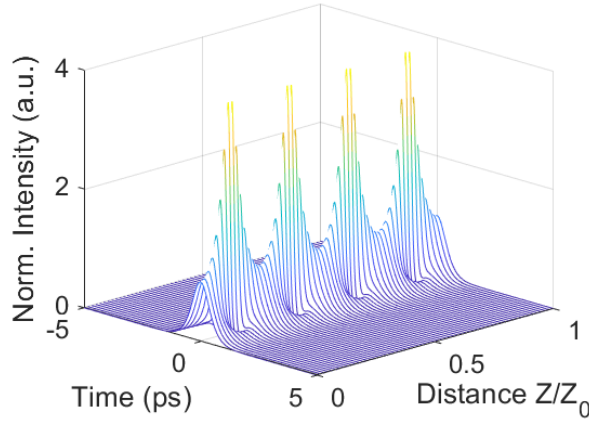


Figure 2.6: Temporal evolution of a 250 fs, second-order soliton propagating through a SMF fiber over a soliton period (z_0) with $\gamma = 1\text{W}^{-1}\text{km}^{-1}$ and $\beta_2 = -1\text{ps}^2/\text{km}$ for the nonlinear and dispersion coefficients, respectively.

The NLSE equation of soliton propagation can give multiple solutions, determined by the dispersive and nonlinear properties of the optical fibers. In its simplest form ($N=1$), a hyperbolic secant pulse can be obtained as an analytical solution to Eq. (2.40).

$$U(z, t) = \sqrt{P_0} \text{sech} \left(\tau \sqrt{\frac{\gamma P_0}{\beta_2}} \right) e^{i \frac{\gamma P_0}{2} z} . \quad (2.44)$$

The number of solitons propagating through an optical fiber may depend on the initial's pulse shape (Gaussian, sech^2 , etc.) and its intensity [30].

Due to the presence of periodic disturbances related to the optical fiber losses or its dispersion and nonlinear coefficients during the propagation of solitons, a co-propagating dispersive wave can be generated, where the soliton ejects any excess energy. Consequently, narrow peaks appear in the optical spectrum, known as Kelly sidebands, which provide information about the chromatic dispersion of the optical fiber. These sidebands are also associated with the minimum pulse duration achievable by the soliton pulse. When the energy of the optical pulse is increased,

Kelly sidebands become more perceptible. However, since strong Kelly sidebands may lead to unstable soliton generation. Dispersion compensation or pulse energy reduction can be introduced to mitigate this effect.

However, when the dispersion or nonlinear properties of the optical fiber are modified, other kinds of solitons can be obtained, such as dark solitons [45], dispersion-managed solitons [46] or dissipative solitons [47]. The next section introduces the fundamentals of dispersion-managed solitons, laying the foundations for the ultrafast fiber lasers employed in this work that will be considered in the following chapters.

2.4.1 Dispersion-managed solitons

The technique of dispersion management is usually employed in the deployment of fiber-optic communication systems. This technique consists of the introduction of fibers with different dispersion parameters, whose net sum leads to a low average GVD coefficient in the optical system, compared to its local and independent values. For instance, two different types of fibers with an opposite sign of the dispersion parameter, (such as EDF and SMF), can be employed to reduce the total dispersion coefficient. The optical solutions of the NLSE equation for this type of systems, have a pulse-like periodic shape, that presents some characteristics different from those described in fundamental solitons. In dispersion-managed solitons, the amplitude and phase oscillate periodically, while the frequency varies within the optical pulse, generating chirped-pulses. Besides, the optical shape is similar to a Gaussian profile instead of the sech^2 distribution characteristic of fundamental solitons [24, 46]. Hence, dispersion management is a very useful technique for the generation of ultrafast pulses in fiber laser cavities. An example of a dispersion-managed fiber laser resonator will be studied in Chapter 4.

2.4.2 Higher-order effects

For ultrashort pulses with a temporal width below 1 ps and high optical intensities, higher-order dispersion and nonlinear effects must be considered. Among them, third-order dispersion (TOD), self-steeping and Raman scattering will be taken into account in this work.

Although the second-order pulse-broadening factor of the dispersion parameter dominates in the case of ultrashort pulses, it is required to add the third-order term (β_3), also known as TOD, for specific configurations. The third-order dispersion is related to the asymmetric oscillation structure that occurs at the edges of the optical pulse. Hence, when $\beta_3 > 0$, the oscillations occur at the trailing edge of the pulse, while in the opposite case, the leading edge of the optical pulse develops the oscillations [28]. This term becomes the dominant factor when the optical wavelength of the pulse nearly coincides with the zero-dispersion wavelength of the optical fiber. In Fig. 2.4 is represented the effect of TOD with a dispersion coefficient of $\beta_3 = 0.1 \text{ ps}^3/\text{km}$ in 5 m of SMF on a 250 fs Gaussian pulse, where we can observe the oscillations on the trailing edge of the optical wave.

On the other hand, in the case of higher-order nonlinear effects, self-steeping [48],

is a nonlinear process that generates an asymmetry in the spectral broadening of ultrashort pulses produced by the SPM due to the dependency of the group velocity with the optical intensity. In this sense, the frequency components at the center of the pulse travel at a lower speed than those located at the wings of the optical pulse. Thus, the optical pulse's peak is shifted towards its trailing edge, generating an asymmetric pulse as it propagates through the optical fiber. Furthermore, self-steeping can also introduce a modification on the spectral width of the SPM-induced pulse, i.e., the blue-side of the optical pulse suffers a larger spectral broadening than the red-side due to the asymmetry of the pulse shape, creating a non-uniform distribution of the optical intensity. In addition, intrapulse Raman scattering (T_R) [49, 50], is a phenomenon in which the blue components of the optical pulse transfer energy to the redder part of the spectra. A typical value of $T_R \approx 3$ fs is measured for optical pulses propagating in SMF fibers centered at $1.55 \mu\text{m}$ [51].

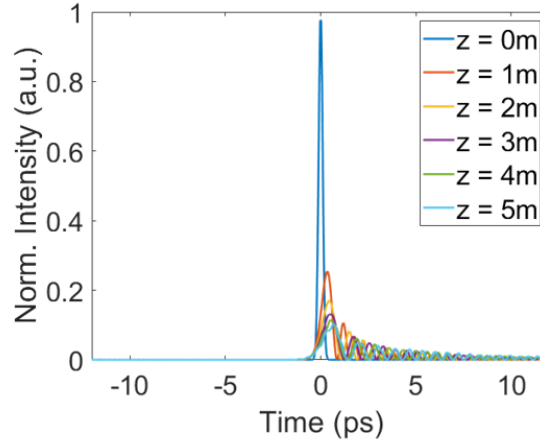


Figure 2.7: Higher-order dispersion effect on a Gaussian 250 fs optical pulse propagating in a 5 m SMF with a positive TOD contribution $\beta_3 = 0.1 \text{ ps}^3/\text{km}$.

The NLSE equation can be expanded to include losses, TOD, self-steeping and Raman scattering, denoted as the Generalized Nonlinear Schrödinger Eq. (GNLSE), where a constant and linear polarization along the propagation through the optical fiber is assumed for simplification.

$$\begin{aligned}
 \frac{\partial u}{\partial \xi} + \frac{\alpha}{2} L_D u - \frac{1}{2} \frac{\partial^2 u}{\partial \tau^2} - \overbrace{\frac{\beta_3}{6|\beta_2|T_0} \frac{\partial^3 u}{\partial \tau^3}}^{\text{TOD}} \\
 = i \left(|u|^2 u + \underbrace{i \frac{1}{\omega_0 T_0} \frac{\partial}{\partial \tau} (|u|^2 u)}_{\text{self-steeping}} - \underbrace{\frac{T_R}{T_0} u \frac{\partial |u|^2}{\partial \tau}}_{\text{Raman scattering}} \right), \quad (2.45)
 \end{aligned}$$

This equation has been employed in the simulation of the optical pulse and its propagation through the fiber laser cavity, as it will be described in Chapter 4.

Chapter 3

Light-matter interaction

Contents

3.1	Linear optical effects	28
3.1.1	Transmission, reflection and absorption	29
3.1.2	Optical transitions	30
3.2	Nonlinear optical effects	32
3.2.1	Second harmonic generation (SHG)	32
3.2.2	Third harmonic generation (THG)	34
3.2.3	Nonlinear absorption effects	35
3.2.4	Stimulated Raman scattering	39

Over the past few decades, optical fibers have played an increasingly important role in the generation of sophisticated sensing techniques. Because of the inherent qualities of fused silica, optical fibers have become a popular alternative to traditional electric wires and are employed in multiple engineering applications. In comparison with traditional sensors, optical fibers have many attractive features, such as immunity to electromagnetic interference, small dimensions, and the ability to be placed in difficult-to-reach areas. Optical fibers are one of the most attractive devices to measure the linear and nonlinear effects of optical materials. Nonlinear phenomena soon gained increasing popularity as a powerful method of characterizing photonic materials as well as finding applications in numerous fields, with a significant impact on industrial applications and information technology [52]. Measurement of nonlinear effects such as high-harmonic generation or FWM is essential for molecular identification, as well as the basic mechanism of autocorrelation measurements, among others.

In order to fully comprehend this progress and potential future applications, the linear and nonlinear effects in optical materials must be explored in more detail. Therefore, this chapter presents a description of the basic physical principles of light-matter interaction, essential for the analysis and characterization of molecular properties. Practical considerations are highlighted in order to illustrate the utility of these effects and demonstrate some of their applications. Finally, selected applications of nonlinear material effects are discussed, setting up the foundations of ultrafast fibers lasers presented in Chapter 4.

This chapter is organized as follows. In the next section, we introduce several basic theoretical concepts related to the structure of matter and its linear optical properties when interacting with light. Section 3.2 is dedicated to an overview of the nonlinear effects essential for the complete characterization of molecules, and for the understanding of the working principles of lasers, explained in Chapter 4, and the basis for molecular detection systems described in Chapter 6.

3.1 Linear optical effects

Matter is composed of electric charges, which interact with light. Electromagnetic fields stimulate atoms, molecules and solids, causing them to vibrate and emit light. Due to its energy level configuration, determined by quantum electrodynamics, matter exhibits different behaviors depending on its structure (atoms, molecules, or solids) [53]. An individual molecule can be recognized by the vibrations of its molecular bonds, producing its signature, or fingerprint. Whereas in solids, atoms or groups of atoms are gathered in a regular and periodic crystalline structure, whose energy levels can be described by the band theory [54]. In this thesis, we are only going to focus on semiconductors, due to their inherent properties in laser configurations, as it will be explained in Chapter 4. In the case of semiconductors, electrons are located in a fundamental energy band, denoted as the valence band. When the electrons interact with light, constituted by the photons, they “jump” to an upper energy level, named as conduction band, as depicted in Fig. 3.1. These two bands are separated by a forbidden band, known as energy bandgap (E_g), which constitutes the principal parameter for the material identification. At 0 K temperature, the va-

lence band in semiconductors is fully occupied, whereas no electrons can be found in the conduction band. However, as the temperature rises, the probability of electron transitions from the valence band to the conduction band increases. Depending on the bandgap structure, different semiconductors can be described [34]. When the maximum point of the valence band and the minimum value of the conduction band are centered at the same position in reciprocal space, the semiconductor is said to have a direct optical band gap. In this case, only photons can be involved in the optical transition of electrons between the valence and conduction bands (see Fig. 3.1 (a)). On the other hand, if the relative positions of the maximum and minimum values of the conduction and valence bands respectively are not coincident, the semiconductor presents an indirect bandgap structure, as represented in Fig. 3.1 (b). The optical transitions of indirect materials can only be explained by the introduction of the phonon particles [54]. Nevertheless, in this thesis, we are only going to focus on direct bandgap semiconductors.

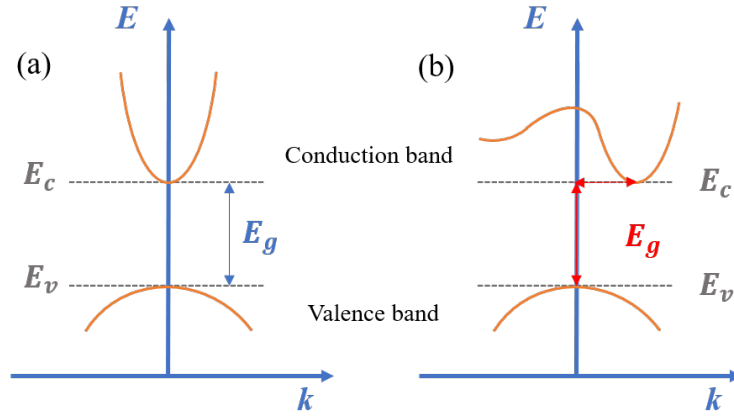


Figure 3.1: Diagram of the energy levels of semiconductors with (a) direct bandgap structure, and (b) indirect bandgap structure.

The properties of an optical wave propagating through an optical medium (power, frequency, phase, etc.) can be modulated due to the interaction with the charges of the material. This modulation is determined by the type of material and the energy level structure. The characteristics of the medium can be obtained and interpreted by measuring this modulation [34].

As it was explained in Chapter 2, linear optical effects can be represented by a linear dependency of the electric field with the polarization vector. The velocity of the pulse, while propagating through a medium, is slower than in vacuum due to the refractive index of the medium (n). Nevertheless, this refractive index is a complex parameter, whose dependence on the optical wavelength can explain most of the linear optical effects of materials.

3.1.1 Transmission, reflection and absorption

When light interacts with matter, a fraction of the incident light intensity passes through the material without any alteration, this is known as optical transmittance and denoted as $T(\lambda)$. Nevertheless, two more linear effects can occur within the

medium, where part of the optical intensity can be deviated in another direction within the incident medium, creating the reflectance of the incident light $R(\lambda)$, or it can be absorbed $A(\lambda)$ by the medium [55]. Nevertheless, transmission, reflection and absorption are optical parametric processes, that is the energy and phase of the propagation wave are conserved. Thus, an expression connecting the transmittance, reflectance and absorbance can be described in:

$$T(\lambda) + R(\lambda) + A(\lambda) = 1 . \quad (3.1)$$

As it was mentioned before, the refractive index can be expressed as a complex coefficient which depends on the optical wavelength as,

$$\bar{n}(\lambda) = n(\lambda) - i \kappa(\lambda) , \quad (3.2)$$

where $\kappa(\lambda)$ is the extinction coefficient, and related to the absorption of the medium, denoted as $\alpha(\lambda)$,

$$\alpha(\lambda) = 4 \pi \frac{\kappa(\lambda)}{\lambda} . \quad (3.3)$$

Thus, the electric field of Eq. (2.9) can be expressed as a function of the complex refractive index and propagating in the z direction as,

$$\vec{E}(t) = E_0 e^{-\frac{2\pi\kappa z}{\lambda}} e^{i(\omega t - kz)} \quad (3.4)$$

where E_0 is the amplitude of the electric field, and k the propagation vector (in this case along the z direction). Therefore, the optical intensity of the propagating pulse is attenuated in terms of the absorption coefficient and the distance covered by the optical wave within the medium. This effect can be expressed by the Beer-Lambert's equation as,

$$I_L(\lambda) = I_0 e^{-\alpha(\lambda) L} , \quad (3.5)$$

where I_0 and I_L correspond to the input and output optical intensities respectively and L is the material thickness. Taking into account this equation, the transmission parameter can be expressed as the decay of the intensity as a function of distance as $T \sim I/I_0$. These processes are the basis of most optical effects in solids as it will be explained in the next sections.

3.1.2 Optical transitions

In this section, an overview of the principal quantum transitions of direct semiconductors is described, with a special emphasis on the absorption and emission processes, responsible for the operation of modern photonic devices, such as optical amplifiers and laser diodes.

During light-matter interaction, a photon can be absorbed by the medium, imparting energy to the electrons, thus generating the excitation of electrons in the valence band. In order to excite electrons from the valence band to the conduction band, only external electromagnetic fields with an energy greater than the forbidden band can interact with the medium, $h\nu \geq E_g$ [56]. On the contrary, the medium is

said to be transparent to the spectral region of the incident electromagnetic field.

The excitation of an electron from the valence band to the conduction band by the absorption of a photon generates an empty state in the valence band, known as a hole, creating what is called an electron-hole pair, and then altering the electrical properties of the semiconductor (Fig. 3.2(a)). After a time delay known as relaxation time (τ), the electron tends to decay to its fundamental state, leading to the recombination of the electron-hole pair in the valence band. This mechanism is responsible for the operation of most photodetectors. The relaxation can be produced by different transition processes [57].

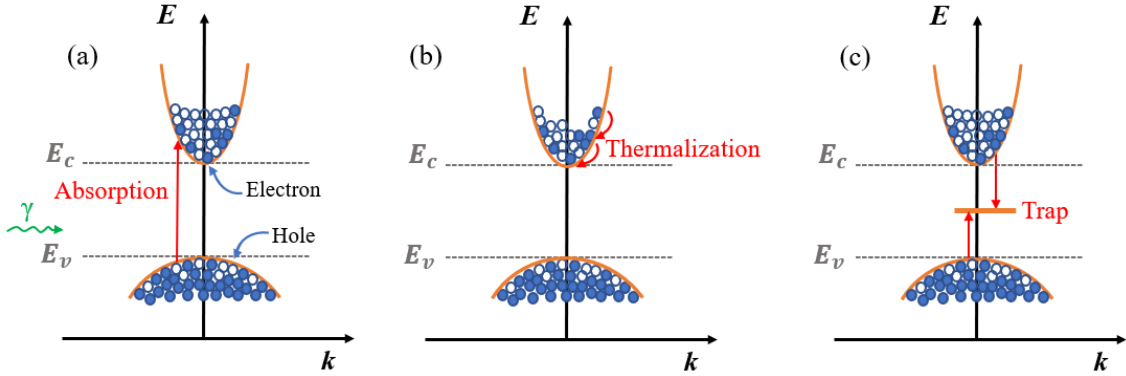


Figure 3.2: Photon absorption and nonradiative recombinations in semiconductors, (a) after the absorption of a photon, (b) the electron loses its accumulated energy by thermalization, emitting a phonon, in free-carrier transitions, or (c) an electron and a hole are trapped in an energy level within the forbidden band due to defects in the medium leading to impurities transitions.

- The energy of an incident photon can be transferred to free electrons or to lattice vibrations, creating phonons and thus giving some energy to the crystal lattice, leading to an increase of the material's temperature. An example of this is the thermalization process, which results in the relaxation of the electron to the bottom of the energy band. In addition, the recombination of the electron-hole pair can be generated by the emission of phonons by an acceptor/donor center trap. These traps, located at energy levels within the forbidden band, are associated with defects and impurities of the semiconductor medium. These processes are known as nonradiative recombinations [34]. A schematic figure for these processes can be found in Fig. 3.2(b) and (c).
- On the contrary, radiative recombinations refer to the processes in which the energy released by the electron can take the form of a photon with an energy $h\nu$. This desexcitation process of the electron-hole pair is better known as spontaneous emission, constituting the main working principle of light-emitting diodes. However, after the excitation of the electron by an incident photon to the upper energy state, the electron-hole pair may be induced to emit another photon. When the material is pumped by a photon with certain energy above the forbidden bandgap, with a specific frequency, propagation direction and polarization, it stimulates the relaxation of a previously excited electron, releasing a duplicate photon with the same properties as the incident one. This process, known as stimulated emission, is the phenomenon

that describes the operation of lasers and amplifiers, as it will be discussed in Chapter 4. A representation of a radiative recombination process based on spontaneous emission is depicted in Fig. 3.3 (a), whereas radiative processes such as stimulated emission are shown in Fig. 3.3 (b).

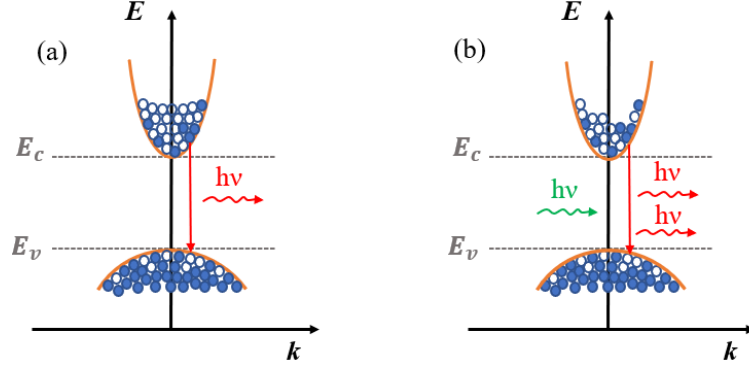


Figure 3.3: Radiative recombinations in semiconductors by (a) spontaneous emission, (b) stimulated emission.

3.2 Nonlinear optical effects

In the following pages, some nonlinear effects in optical materials related to variations of absorption or refractive index are explained. Although nonlinear optical effects can be found in any material, each material exhibits them at a given power level. This is ascertained by the nonlinear coefficients of the material, which depend on its internal structure and composition. In the last chapter, we saw how the nonlinear response of a material, under the influence of an intense external source, can induce an anharmonic motion of the bound electrons [58]. This can be translated into a nonlinear dependency of the polarization with respect to the incident electric field due to the nonlinear susceptibilities. These processes can be classified as second or third order nonlinear effects, depending on whether second-order susceptibility or third order susceptibility is present.

3.2.1 Second harmonic generation (SHG)

The second-order susceptibility is negligible in an isotropic medium, as it was in the case of optical fibers. Nevertheless, this effect becomes important for the study of biological samples.

Sum-frequency generation (SFG) [31], is a second order nonlinear optical process founded on the generation of a photon at frequency ω_3 due to the annihilation of two incident photons described by the frequencies ω_1 and ω_2 . This effect is a parametric process, in which the total energy is conserved,

$$\hbar\omega_3 = \hbar\omega_1 + \hbar\omega_2 . \quad (3.6)$$

Second-harmonic generation (SHG) discovered by Franken et al. in 1961 [59], is a special case of SFG, in which $\omega_1 = \omega_2$. In this sense, by considering an incident

electric field propagating at frequency ω_0 , and from Eq. (2.20), we find that the second-order contribution of the nonlinear polarization vector can be expressed as:

$$\vec{P}^{(2)}(t) = \epsilon_0 \chi^{(2)} \vec{E}\vec{E} = \frac{1}{2} \epsilon_0 \chi^{(2)} \tilde{E}_0 \tilde{E}_0^* + \frac{1}{4} \epsilon_0 \chi^{(2)} \tilde{E}_0^2 e^{2i\omega_0 t} + \dots, \quad (3.7)$$

where the first component, independent of time, is related to the nonlinear effect of optical rectification [60], generating a steady polarization in the optical material. Whereas, the second term, with an optical frequency of $2\omega_0$, corresponds to the second-harmonic generation. As a consequence, two electric fields are measured after the interaction with the medium oscillating at frequencies ω_0 and $2\omega_0$ respectively. Hence, the total second-harmonic intensity will be a superposition of all these waves. This principle holds well for short lengths. Nevertheless, for long distances, due to the difference in the respective refractive indices, the fundamental and second harmonic waves will propagate at different speeds. Thus, the output intensity would be maximum for constructive interference, i.e. the two waves arrive in phase. This condition is known as phase matching [24]. The net distance at which the phase matching condition is fulfilled is the coherence length, which can be described by:

$$L_{coh} = \pi / \Delta k, \quad (3.8)$$

where Δk corresponds to the phase mismatch parameter, and related to the difference between the corresponding wavevectors of the fundamental and second harmonic waves. Thus, for optimum efficiency, the phase mismatch between the fundamental and second harmonic waves should be equal to zero. A figure denoting the phase-matching (a) and non-phase matching (b) conditions is shown in Fig. 3.4.

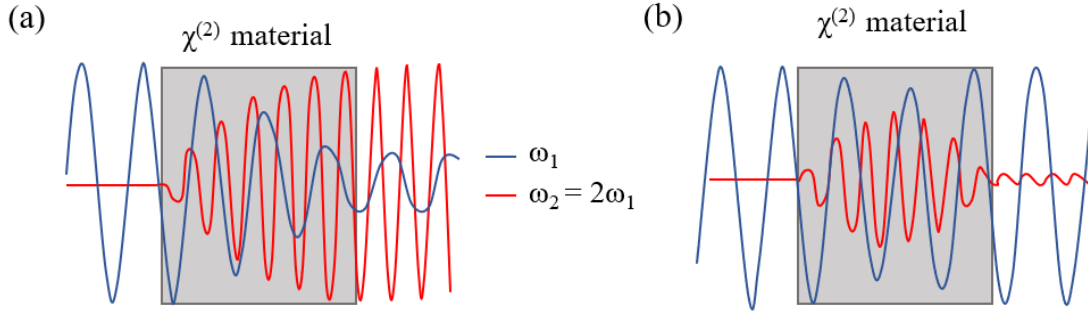


Figure 3.4: SHG generation of a nonlinear optical material with (a) phase matching condition, and (b) non-phase matching.

SHG was employed for the first time in 1982 as a spectroscopic technique to probe the adsorption of molecular monolayers in optical surfaces [61]. Thus, SHG can be used in material science as a microscopy technique for the characterization of nanostructured materials, revealing information about the orientation of molecules, and the symmetry of material surfaces and interfaces, i.e., discriminating non-centrosymmetric crystals and determining their structural purity [62]. In the medical field, SHG is employed to measure the presence of collagen cells, which determine the structure of many tissues such as skin, arteries, bones, etc., becoming the main structural protein in mammals [63]. SHG can also be used in multiple industrial applications, such as in the generation of 532 nm green lasers from 1064 nm

laser sources. Furthermore, SHG constitutes the basic principle in the operation of autocorrelation systems, applied for measuring the widths of ultrashort pulses [64]. These applications employ optical materials such as lithium iodate or Barium Borate (BBO) [65].

3.2.2 Third harmonic generation (THG)

The interaction between electromagnetic fields in nonlinear mediums may become relevant in high intensity and long distance configurations. Similarly to SHG, three photons can interact between them, creating a fourth photon with an optical frequency three times greater than the incident one. Therefore, a similar expansion for the third order polarization vector can be obtained,

$$\vec{P}^{(3)}(t) = \epsilon_0 \chi^{(3)} \vec{E} \vec{E} \vec{E} = \frac{3}{8} \epsilon_0 \chi^{(3)} \tilde{E}_0 \tilde{E}_0^* e^{i\omega_0 t} + \frac{1}{8} \epsilon_0 \chi^{(3)} \tilde{E}_0^3 e^{3i\omega_0 t} + \dots \quad (3.9)$$

The first term in the expansion is related to the nonlinear component of the refractive index and the corresponding Kerr effect, as explained in Eq. (2.25). Whereas the second term describes an electric field at frequency $3\omega_0$, and related to the third harmonic generation (THG).

THG was discovered in 1965 by Maker et al. from a direct third order nonlinear effect generated in a crystalline material [66]. Nevertheless, this process is difficult to be found in nature due to the small $\chi^{(3)}$ parameter in optical media. Thus, frequency tripling is usually constructed as a combination of $\chi^{(2)}$ processes such as SHG and SFG.

A special case of THG is four-wave mixing (FWM) [67]. In this third order nonlinear process, three different frequencies generate a fourth frequency component, described by the following relation $\omega_4 = \omega_1 \pm \omega_2 \pm \omega_3$. In order to accomplish the phase matching condition, the relation between the wavevectors should be [68],

$$\Delta k = k_3 + k_4 - k_1 - k_2. \quad (3.10)$$

In molecular microscopy, THG allows the study of 3D biological samples, detecting their heterogeneities and interfaces [69]. Furthermore, due to the dependency of the nonlinear refractive index on the $\chi^{(3)}$ parameter, THG is also employed for the detection of refractive index mismatches within the interface of the biological specimen [70]. In the medical field, THG detects the hemoglobin protein, enabling the characterization of blood vessels and the blood flow velocity, and thus the detection of the heart rate and the pulse velocity curve in small arteries, essential in the prevention of heart diseases [71]. FWM also finds applications in the industrial field as the basic process for optical phase conjugation, parametric amplification, or in supercontinuum generation, as it will be described in Chapter 6. Besides, FWM is responsible for the generation of ultraviolet 355-nm light by frequency tripling of a laser source with 1064 nm, as employed in microresonators based on frequency comb generation, such as Nd:YAG or Nd:YVO4 lasers [72]. Optical materials such as BBO or lithium triborate (LBO) can be used for THG.

3.2.3 Nonlinear absorption effects

As it was mentioned before, third order nonlinearity plays an important role in optoelectronics. FWM has found applications in any media from liquids, gases or solids [73–75], including semiconductors [76], molecules and polymers [77], nanostructured materials [78], and graphene [79]. Distinguishing between the real and the imaginary part of the third order nonlinear coefficient $\chi^{(3)}$, may lead to applications such as supercontinuum generation, pulse compression, and soliton generation, as well as pulsewidth measurement and spectroscopy, among others. Both of these factors are crucial to determining the behavior of optoelectronic devices.

For the real part of the susceptibility, and following the Eq. (2.24), the nonlinear refractive index can be described as a function of the third order susceptibility,

$$n_2^2 = 1 + \chi^{(1)} + \chi^{(3)} \frac{3I}{2c\epsilon_0 n_0} , \quad (3.11)$$

By using the Taylor expansion, $(1 + \chi^L + \chi^{NL})^{1/2} \approx n_0 (1 + \chi^{NL}/2n_0^2)$, the nonlinear refractive index can be expressed as [31],

$$n_2 = \frac{3}{4n_0^2 \epsilon_0 c} \text{Re} [\chi^{(3)}] . \quad (3.12)$$

When high intensity beams propagate through a nonlinear material, the induced refractive index changes lead to self-focusing or defocusing effects [80]. In this process, the strong wave alters the optical characteristics of the material in such a way that the optical wave is focused or de-focused within the optical medium depending on the sign of n_2 . In the case of $n_2 > 0$, if the intensity of the optical beam is maximum at the focal point, the variation of the refractive index becomes greater at the center of the optical beam, while decaying on the periphery, causing the beam to be concentrated in the material, and modifying its propagation direction via the material medium's nonlinear response. Thus, the material behaves as a graded-index medium, introducing a nonuniform phase-shift, and thereby generating a curvature on the optical wavefront. Thereby, the optical medium can act as a positive lens, whose focal length depends on the value of the incident power. As the wave travels through the medium, the intensity of the self-focused region increases until defocusing effects or medium damage interrupt this process. The self-focusing condition occurs for incident powers greater than the critical power, defined by [81],

$$P_{cr} = \varphi \frac{\lambda_0^2}{4\pi n_0 n_2} , \quad (3.13)$$

where φ is a constant determined by the initial spatial distribution of the optical beam.

When the self-focusing effect is compensated by the optical diffraction, the optical beam propagates with a constant diameter within the medium. This effect, known as self-trapping, is essential in multiple applications in the laser field, such as Kerr-lens mode-locking, parametric generation, and self-compression of ultrashort laser pulses [82, 83]. However, for $P \gg P_{cr}$, the polichromatic optical beam is de-

composed in multiple components, yielding to the break-up of the incident wave. This process is associated with the generation of imperfections within the optical medium due to the FWM effect.

Analogously to the nonlinear refractive index defined in Eq. (2.24), the imaginary part of the third order susceptibility is related to the absorption coefficient, which can be written in the form,

$$\alpha(I) = \alpha_0 + \alpha_2 I , \quad (3.14)$$

where α_0 is related to the losses introduced by the impurities of the material (as explained in Section 2.2.2.1), and α_2 corresponds to the nonlinear absorption coefficient which can be expressed as,

$$\alpha_2 = \frac{3\pi}{\lambda n_0^2 \epsilon_0 c} \text{Im} [\chi^{(3)}] . \quad (3.15)$$

Thus, an increase in the absorption parameter with the incident light intensity, leads to a positive value of the nonlinear absorption coefficient $\alpha_2 > 0$. The nonlinear refractive index n_2 and the nonlinear absorption coefficient α_2 , are the two main parameters required to determine the third order nonlinear optical parameters of materials.

Just like the case of nonlinear refractive index, intense monochromatic radiations from an electromagnetic light source can induce a change in the transmission of the material and thus in its absorption properties. Optical manifestations of this phenomenon include the increase of the photons to be absorbed by the material (TPA), or the reduction of the absorption of the material (SA), among others. These effects have resulted in numerous scientific and technological applications within multiple areas, such as nonlinear spectroscopy and optical limiting [84]. A more detailed explanation of these two processes is given below.

- If the intensity of light (photon density) is high enough, the probability of an electron absorbing more than one photon before going to the excited state can be significantly increased. In its simplest form, two photons can be absorbed simultaneously from an incident radiation field generating the transition from the fundamental level to an upper energy state in an optical medium. This process, known as two-photon absorption (TPA), can be generated by either two photons from the same electric field with equal frequency ω , or by two different optical fields described by the frequencies ω_1 and ω_2 respectively. The bandgap of the optical material must therefore be lower than the sum of the incident frequencies. An example of this is shown in Fig. 3.5(a).

Therefore, the optical absorption of the material and thus the number of photons absorbed depend on the instantaneous optical intensity. Following Eq. (3.5) and Eq. (3.14), the total absorption of the medium can be described by the nonlinear absorption, related to the square of the optical intensity as,

$$\frac{dI}{dz} = -\alpha_0 I - \alpha_2 I^2 , \quad (3.16)$$

where z is the propagation direction. By assuming the beam to be linearly polarized and a centrosymmetric medium, we can integrate Eq. (3.16) as a

function of the material thickness L ,

$$I(L) = I_0 \frac{e^{-\alpha_0 L}}{1 + \alpha_2 I_0 L_{eff}}, \quad (3.17)$$

being L_{eff} the length of the material related exclusively to the absorption losses contribution and defined as,

$$L_{eff} = \frac{(1 - e^{-\alpha_0 L})}{\alpha_0}. \quad (3.18)$$

From Eq. (3.18), three different cases can be studied. In most light-matter interaction scenarios where $\alpha_0 > 0$, the total length of the material L , is usually greater than the effective length. However, for very thick materials ($L \rightarrow \infty$), the effective length of the material can be simplified to $L_{eff} = 1/\alpha_0$. Finally, for lossless materials $\alpha_0 = 0$ (materials with such a small value of linear absorption that can be considered negligible), the effective length is equal to the total length L of the material.

However, these equations can be generalized if an arbitrary number of photons is absorbed [84]. During this process, referred to as multiphoton absorption, n photons are absorbed from a single electric field or multiple electric fields simultaneously. Multiphoton microscopy (MPM) is a technique that has been used to image living, intact biological tissues from the molecular level to the whole organism [85]. MPM offers many advantages over similar optical imaging techniques, such as better penetration depth and lower photodamage, when imaging living tissues over long periods of time with minimal invasion. As a perfect technology for imaging living and intact tissues, MPM has been rapidly adopted by researchers, resulting in a proliferation of commercially available systems.

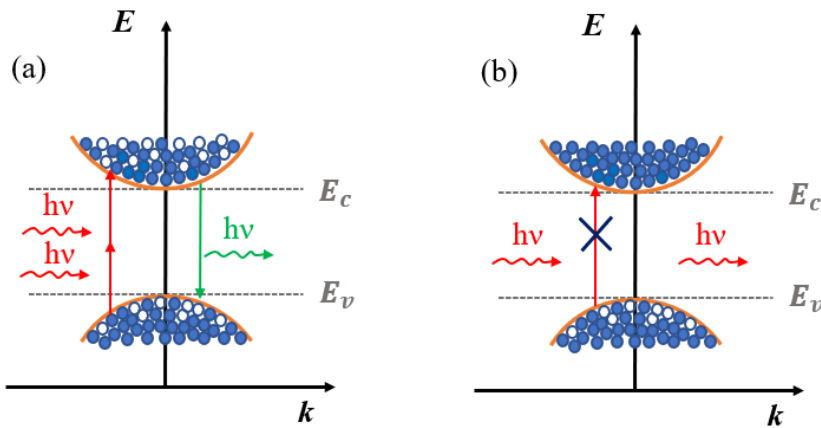


Figure 3.5: Direct bandgap semiconductor nonlinear absorption effects with (a) two-photon absorption (TPA) or (b) saturable absorption (SA).

- On the other hand, in certain materials such as semiconductors, the absorption coefficient can be reduced or even saturated when pumped with high incident powers [84]. The photons of the incident electric field excite the electrons in

the ground state to upper energy levels, thereby depleting the fundamental state. Thus, most of the electrons from the valence band are excited in a time period shorter than the spontaneous decay time, leading to the saturation of the conduction band (the system cannot absorb as much incident light as it could at low intensity). The energy redistribution of the electron population generates a reduction of the subsequent absorption processes, and thus producing an increase in the optical transmission of the high-intensity beam through the material. The net change of the absorption coefficient with the incident intensity will then have a negative value $\Delta\alpha < 0$. This effect is called saturable absorption. Fig. 3.5 (b) shows a diagram of the absorption saturation process in a direct bandgap semiconductor.

The absorption rate $\alpha(I)$ is in this case determined by the incident optical intensity I as follows,

$$\alpha(I) = \frac{\alpha_0}{1 + I/I_{sat}} , \quad (3.19)$$

where I_{sat} corresponds to the saturation intensity. This parameter is related to the absorption probability rate, and the lifetime of the excited state.

Nevertheless, in most literature, the optical absorption of the medium can be represented as a function of the optical fluence, related to the intensity $I(t)$ in a certain period of time t as,

$$F = \int_0^t I(t) dt . \quad (3.20)$$

Substituting this equation in Eq. (3.19) we obtain the absorption as,

$$\alpha(I) = \frac{\alpha_0}{1 + F/F_{sat}} . \quad (3.21)$$

where F_{sat} can be approximated to $I_{sat} \cdot \Delta\tau$ being $\Delta\tau$ the FWHM temporal duration of the optical pulse.

Analogously to Eq. (3.16) and Eq. (3.19), the intensity decay (optical loss) of the medium can be defined in terms of the nonlinear absorption coefficient and the material thickness by the Lambert's law as,

$$\frac{dI}{dz} = - \frac{\alpha_0 I}{1 + I/I_{sat}} . \quad (3.22)$$

Therefore, the intensity distribution will permit us to obtain an approximation of the saturation intensity/fluence of the material. A further detailed discussion of the saturable absorption and intensity distribution can be found in Chapter 4.

Thus, through the redistribution of population due to intense laser fields, interesting interactions can be induced, such as absorption, stimulated emission, and the creation of free carriers in complex molecular systems. The processes of TPA, which constitutes a special case of reverse saturable absorption (RSA), and SA, have led to the development of multiple applications in science and technology [86], and are

especially employed as spectroscopic tools [84]. In 1967, Giuliano and Hess demonstrated, for the first time, the spectroscopic properties of complex molecules in terms of saturable absorption [87]. Since then, a considerable interest in using saturable absorption started to emerge as a high-resolution nonlinear tool for the study of the structure of matter in spectroscopic devices.

Furthermore, these properties introduce the theoretical principles of self-pulsation behind semiconductor optical fiber laser technology, where saturable absorption constitutes the crucial effect at the basis of passive Q-switching and mode-locked ring cavities [88].

3.2.4 Stimulated Raman scattering

During the propagation of light, direct interactions between the incident light and the guiding medium result in the scattering phenomenon. Since most optical materials present small inhomogeneities of the refractive index, known as scattering centers, light can be reflected in multiple directions. These scattering phenomena are essential for the complete understanding of fiber optic technology, since optical scattering not only corresponds to the main loss mechanism in optical fibers, but also can be employed in sensing applications. Optical scattering can be divided into two different processes, elastic (Rayleigh and Mie) and inelastic (Brillouin and Raman) scattering [89].

In elastic processes, the energy of the incident photon during the interaction between the incident light and the material is conserved, thus no change in the optical frequency nor electronic transitions is observed. In the presence of a transient electric field, the medium vibrates into a ground state, as well as emitting a secondary wave proportional to the power of the incident wave. Elastic scattering processes can be categorized depending on the size of the defect that causes the optical effect. The elastic process is said to present Rayleigh scattering if the radius of the defect is lower than $\lambda/15$, otherwise the material has Mie scattering. This latter effect, negligible in most optical fibers and wavelength independent, is usually attributed to defects generated during the fabrication process. Contrary to this, Rayleigh scattering is the dominant scattering interaction in fiber optics, with a strong wavelength dependency (following a $1/\lambda^4$ relation), due to its contribution to the attenuation of light within the telecommunication band.

If the lightwave transfers energy to the surrounding material after the interaction, the scattering process is said to be inelastic. In this sense, a photon is absorbed by the material under the excitation of an incident electric field, leading to a transition to a high energy state. The desexcitation of the photon is produced to a lower energy level excluding the fundamental state, thus the energy of the emitted photon ($\hbar\omega_s$) does not coincide with the energy's excitation photon ($\hbar\omega_p$). When the lower state has larger energy than the ground state, the emitted photon has a longer wavelength than the excitation photon, creating a phonon with a frequency determined by the difference between the two energy levels ($\hbar\omega_p - \hbar\omega_s$). This is known as Stokes shifted scattering. On the other hand, if the incident photon absorbs energy from a thermally-active photon, thus increasing its energy from the fundamental state to an upper energy level (vibrational state), and emitting a shorter-wavelength light than compared to the incident light, while annihilating the phonon, resulting in

anti-Stokes shifted scattering with energy $\hbar\omega_a$. A representation of the energetic transitions for each case is depicted in Fig. 3.6(a). The difference between the incident and emitted light can be used to determine the relative positions of the energy levels in the material. Depending on the type of phonon employed in the inelastic process, two different scattering effects can be distinguished, Raman (optic) and Brillouin (acoustic) [31].

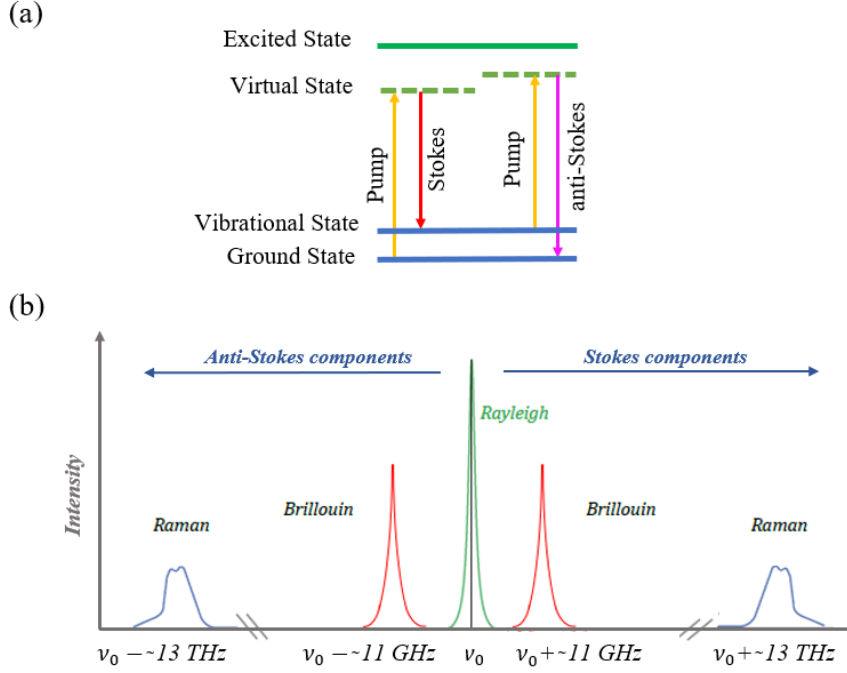


Figure 3.6: Stokes and Anti-Stokes energetic transitions due to inelastic scattering phenomena and (b) schematic spectrum of scattering effects produced by elastic and inelastic processes.

The generation or destruction of an acoustic phonon, i.e. a pressure wave, during the energy transfer of the interaction between the optical material and the photon, is referred to as Brillouin scattering. Acoustic phonons are produced due to the creation of electrostrictions in the medium, and thus generating refractive index changes related to photoelasticity. The frequency of the produced acoustic phonons is typically 11GHz for silica, with a peak power as high as half the intensity of the incident pulse. In addition, Brillouin scattering can only occur in the opposite direction from the pump light (counterpropagating).

On the other hand, the interaction results in Raman scattering when the energy transfer between the photon and the material creates or annihilates an optical phonon (molecular vibrational or rotational modes). In this case, optical phonons are related to the polarization changes in the material medium. Optical phonons are centered around 13 THz with a peak power 100 times smaller than in Brillouin scattering. However, as opposed to Brillouin scattering, Raman can propagate in a copropagating or counterpropagating direction with respect to the excitation. Due to their intrinsic dependence on the current material state, both phenomena can be used for sensing applications [89]. A visual representation of the spectrum produced by the different scattering phenomena is represented in Fig. 3.6(b).

The scattering effects in optical fibers are typically spontaneous, but the effects can also be stimulated if the light power is high enough to alter the local properties of the material. Since molecular vibrational information is specific to the chemical bonds and symmetry of molecules, Raman scattering will only be considered in this thesis for spectroscopic applications [90].

Spontaneous Raman scattering is a very weak second-order radiative process, that requires a long integration time. However, a high intensity optical wave can excite molecular vibrations, thus causing molecules to emit reduced energy photons (a Stokes wave), to which most of the pump energy is transferred. This interaction is known as stimulated Raman scattering (SRS) [91]. A schematic representation of the spontaneous and stimulated Raman processes is depicted in Fig. 3.7.

Due to the phonon population dependency of the anti-Stokes signal, the energy transfer from the pump beam to the Stokes beam is more efficient than in the anti-Stokes scattering. Therefore, in SRS, two excitation fields are employed, denoted as pump, with a frequency of ω_p , and the Stokes beam centered at ω_s . The pump beam generates the excitation of the vibrational mode, while the Stokes beam stimulates the emission of a second photon with frequency ω_s . When the frequency difference $\omega_p - \omega_s$ is resonant with a Raman active molecular vibration, this transition is resonantly enhanced (see Fig. 3.7(b)).

Since SRS is a third order nonlinear effect, four simultaneous coherent Raman processes will occur, namely stimulated Raman gain (SRG) at frequency ω_s , stimulated Raman loss (SRL) with a frequency of ω_p , coherent Stokes Raman scattering at the frequency $(\omega_s - \omega_p) + \omega_s$, and coherent anti-Stokes Raman scattering (CARS) with the new frequency of $\omega_p + (\omega_p - \omega_s)$, as shown in Fig. 3.7(b). In SRG and SRL, due to the energy transition between the incident optical wave and the molecular vibrational mode, the Stokes beam experiences an intensity gain, while the pump beam has an intensity loss. On the other side, due to the FWM process, a new frequency component is generated apart from the input beams, where the CARS signal is accompanied by a nonresonant signal generated by electronic contributions to the FWM process.

Therefore, the interaction between the pump (in continuous-wave (CW) conditions) and the Stokes beam can be described by [30]:

$$\frac{dI_p}{dz} = \frac{\omega_p}{\omega_s} g_p I_p I_s - \alpha_p I_p , \quad (3.23)$$

$$\frac{dI_s}{dz} = g_R I_p I_s - \alpha_s I_s , \quad (3.24)$$

where I_p and I_s are the pump and Stokes optical intensities respectively, g_R is the Raman gain coefficient, and α_p and α_s the corresponding medium loss coefficients of pump and Stokes waves.

By assuming that the intensity of the pump beam is greater than the Stokes intensity, an expression of the Stokes pulse as a function of the pump intensity and effective length (see Eq. (3.18)), can be obtained as,

$$I_s(L) = I_s(0) e^{g_R I_p(0) L_{eff,p} - \alpha_s L} . \quad (3.25)$$

Thus, the Stokes beam can be enhanced if $g_R I_p(0) L_{eff,p} > \alpha_s L$, whose maximum value would be for a frequency shift of 13 THz, which corresponds to the maximum value of g_R .

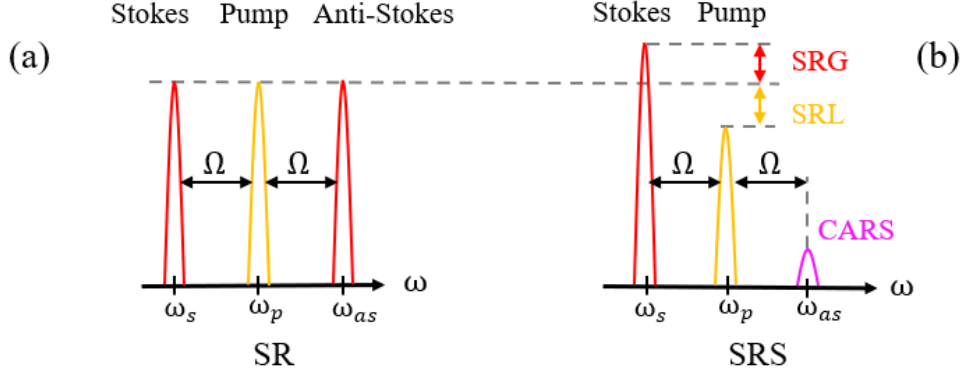


Figure 3.7: Comparison of the spontaneous (left) and stimulated Raman scattering processes (right) in terms of electronic energetic transitions.

In molecular spectroscopy, both SRS and coherent Raman spectroscopy are widely employed in various applications from a wide variety of fields, such as in material composition analysis, in the study of molecular conformational structures, as a non-invasive label-free imaging in living tissue, or in ultrafast microscopy [92]. Among its properties, SRS provides background free nonresonant spectral signals that are nearly identical to those obtained from spontaneous Raman spectroscopy. Moreover, the SRS is linearly dependent on the molecular concentration under investigation within the sample, while CARS signals are proportional to the square of sample concentration. In this thesis, an example of a CARS spectroscopic system has been constructed for the analysis of living cells, as it will be discussed in Chapter 6.

Chapter 4

Ultrafast fiber lasers

Contents

4.1	Introduction to fiber lasers	44
4.1.1	Fundamentals of fiber lasers	44
4.1.2	Generation of ultrashort pulses in fiber lasers	46
4.2	Passive mode-locked fiber lasers	49
4.2.1	Mode-locking technique	49
4.2.2	Saturable absorbers	51
4.3	InN as SESAM	55
4.3.1	Growth of III-nitrides	55
4.3.2	Structural properties	56
4.3.3	Optical properties	60
4.4	InN-based ultrafast mode-locked fiber laser	63
4.4.1	Experimental set-up	63
4.4.2	Optical characteristics of the InN-based ML-fiber laser	65
4.4.3	Numerical simulations	68
4.5	Conclusions	73

Ultrafast fiber laser technologies have recently attracted extensive attention owing to their inherent properties, including low cost, environmental robustness and alignment-free operation. Due to their flexibility and stability, these sources can produce high-quality, powerful pulses in the picosecond and femtosecond ranges. Aside from the reliability and sensitivity that optical measurements offer, fiber lasers have other specific advantages. The most advantageous properties of optical fiber lasers are their simplicity and reduced costs in fabrication, installation and maintenance, while being immune to external electromagnetic interference. Nonetheless, the most interesting features are the optical tunability of the laser frequency and power consumption, enabling remote and high performance sensing capabilities.

In the following chapter, we will review the state-of-the-art in optical fiber lasers, emphasizing on mode-locked ultrafast fiber lasers, and especially on the employment of saturable absorbers as the passive element for ultrafast pulse generation. We will conclude with an in-depth description of the laser source developed in this work, based on an InN-based ultrafast mode-locked fiber laser.

4.1 Introduction to fiber lasers

Lasers have revolutionized the way we study and explore light. Prior to the 1950s, only incoherent light sources were available. Nowadays, the laser can generate monochromatic, coherent, and highly directional radiation. With the advent of optical fibers, optical lasers soon replaced electrical systems as the most promising alternative due to their inherent properties in communication systems.

4.1.1 Fundamentals of fiber lasers

The optical laser is a device that amplifies light due to the stimulated emission process. This amplification, in conjunction with an optical cavity, provides the formation of a standing electromagnetic wave that may generate a monochromatic and highly coherent output light.

In general, most fiber laser cavities, also known as resonator cavities, are constituted by a power supply (pump), normally an external diode light source that pumps a gain medium. The central frequency of the laser is dictated by the operating range of the gain medium. Optical fibers can be used as the gain medium when doped by rare-earth ions such as erbium (Er), neodymium (Nd) and ytterbium (Yt) [93]. Nevertheless, with the discovery of other dopants such as holmium, samarium and thulium, fiber lasers can nowadays operate in a wide wavelength range from 0.4 to 4 μm . Among them, Er-doped fiber lasers have been extensively investigated since these lasers are capable of generating optical pulses in the optical communications range (C-band window) at 1.55 μm , which coincides with the region with the lowest attenuation in optical fibers (see Fig. 2.3) [34]. Finally, an optical feedback (propagation material) is necessary to reintroduce part of the emitted light of the laser again into the laser cavity. Optical fibers can also be employed as optical feedback by using fiber couplers (the output power is determined by the power coupling ratio [94]). Laser cavity schemes based only on optical fibers are known as all-fiber cavities. A schematic representation of a laser oscillator is shown in Fig. 4.1.

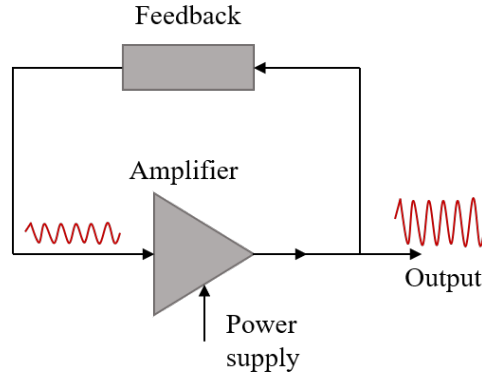


Figure 4.1: Basic components of a laser oscillator.

Lasers operate in what is called continuous wave mode (CW) when they emit monochromatic plane waves with a constant amplitude. As a result, the associated spectrum in the Fourier domain may correspond to an approximate Dirac-delta peak centered at frequency ω_0 . This type of laser source is employed in multiple applications in the telecommunication field, playing an important role in laser printers, optical disc drives, and was introduced as the basis for the development of internet technology [95].

However, lasers can sometimes be operated in a pulsed mode, since the optical peak power can be greatly increased by reducing the optical pulse duration [96]. Pulsed lasers can produce optical pulses with durations as little as a few femtoseconds, which can be compressed up to the attosecond regime. Thus, optical lasers operating in the high-power regime, must be performed in pulsed mode since CW operation cannot be maintained.

As compared to CW operation, the energy of pulsed lasers is stored within the optical resonator in the form of light, and released periodically by an optical modulator. This mechanism can be understood as an on-off operation process of the laser itself, in which the energy is collected in the off-time while otherwise the energy is permitted to escape. The on-off duration time will be designated by means of an internal modulation process, which can be produced by four different methods [34, 97].

- A direct approach to internal modulation is by controlling the laser pump intensity. This method, known as gain switching, consists of turning the pump laser periodically on and off for short periods of time designated by an external electrical current. In these periods, the loss coefficient is smaller than the gain coefficient during on-times, thus emitting laser light. A schematic figure of the gain switching mechanism has been depicted in Fig. 4.2 (a).
- On the contrary, Q-switching is related to the modulation of the optical losses of the resonator cavity, where no light is emitted by the laser when the optical resonator's losses are increased (the energy is accumulated within the cavity during the off-times and released when the losses are reduced). In Fig. 4.2 (b), it is represented as the gain-loss balance that occurs in a Q-switching laser.
- A special case of Q-switching, known as cavity dumping, consists of the alter-

ation of the transmittance of the optical mirrors in a free-space configuration of the laser cavity. During a period of time, photons are collected in the cavity without the possibility of escaping, thus increasing the optical power inside the laser cavity. Afterwards, one of the mirrors is “removed”, liberating the accumulated photons during the on-times. This process can be understood as the opposite case of gain switching as plotted in Fig. 4.2 (c).

- However, the most important modulation method for the generation of ultrashort laser pulses is known as mode-locking. This process consists of coupling the longitudinal modes of a laser inside a resonator cavity by locking together their optical phases. The coupling of the oscillating waves can be performed by modulating the losses of the resonator cavity. Thus, the constructive interference of multiple longitudinal modes generates a periodic train of ultrashort pulses with timewidths in the range of picoseconds and femtoseconds. An extensive description of the mode-locking regime will be discussed in the next section.

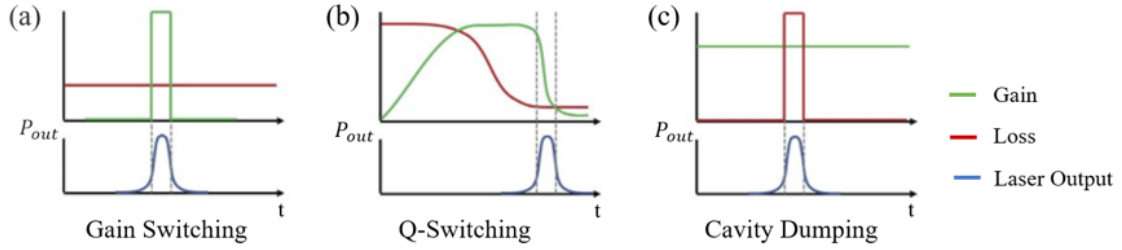


Figure 4.2: Representation of different ultrashort pulse generation mechanisms: (a) gain switching, (b) Q-switching and (c) cavity dumping [97].

4.1.2 Generation of ultrashort pulses in fiber lasers

The principal characteristics that define an ultrafast pulse are listed below [1, 12].

- Within a resonator cavity, the number of standing optical waves is determined by the length of the optical cavity (L). Therefore, there exists an integer number (m) of optical frequencies (ν) spanning the region between the fiber ends, which can be defined as

$$m = \frac{2nL\nu_m}{c} . \quad (4.1)$$

where n is the refractive index of the medium. When the temporal phase of these frequencies is a multiple of 2π (due to the boundary conditions), the standing waves are known as longitudinal modes, separated by a constant frequency difference defined by,

$$\nu_F = \frac{c}{2nL} , \quad (4.2)$$

where ν_F is the free spectral range.

The electric field of the output signal propagating in the z direction within an optical medium will be defined as a combination of the longitudinal modes,

$$E(z, t) = \sum_m E_{0,m} e^{i 2\pi \nu_m (t - z/v_g)} , \quad (4.3)$$

where $E_{0,m}$ is the amplitude of the signal for each longitudinal mode with frequency ν_m . This frequency ν_m can be expressed as a function of the central frequency of the optical pulse as,

$$\nu_m = \nu_0 + m\nu_F , \quad (4.4)$$

Therefore, for $m = 0$, the frequency of the mode coincides with the central frequency of the pulse. From this point, the term optical frequency will be related to the optical pulse's central frequency, which coincides with the longitudinal frequency with maximum electrical amplitude, unless otherwise specified for simplification purposes.

At the output of the laser cavity, since all the longitudinal modes have the same phase at the output, a pulse train of ultrashort waves is obtained, whose temporal spacing between consecutive pulses can be defined by a measurable parameter known as repetition period T_{rep} . As a result, the pulse period is inversely related to the number of emitted pulses per second, defining the frequency of the output pulse train $f_{rep} = 1/T_{rep}$. Note that f_{rep} and ν_F are usually related.

In optical fiber lasers, the repetition rate can be controlled by the length of the fiber laser cavity. The distance between consecutive pulses in time typically coincides with the roundtrip period of light when propagating through the total fiber resonator length, hence $f_{rep} \approx \nu_F$. However, if the energy inside the laser cavity is high enough, multiple pulses may be present within the cavity with equal spacing. This is known as harmonic generation. Fiber lasers may present a wide range of repetition frequencies, varying from 1 to 100 MHz for typical laser cavities.

- As it was mentioned before, the temporal pulsewidth of ultrashort pulses, also known as pulse duration ($\Delta\tau$), is defined as the time duration of the temporal intensity of an optical pulse at a half width full maximum (FWHM). Generally, ultrashort pulses have temporal durations in the range of ps or fs.

Within this dissertation, a Gaussian distribution will be considered as the temporal pulse profile (E_0) of an ultrafast pulse. Thus, the Gaussian pulse shape, defined by the envelope of the amplitude of the optical pulse is represented as [24],

$$E_{0,Gauss}(t) = \frac{A_{Gauss}}{\sqrt{2\pi} \tau_{Gauss}} e^{\left(\frac{t-t_0}{2\tau_{Gauss}}\right)^2} , \quad (4.5)$$

where A_{Gauss} is the amplitude of the Gaussian electric field and τ_{Gauss} is the temporal duration of the optical pulse when the amplitude decays $1/e$, and related to the FWHM with the relation,

$$\tau_{Gauss} = \frac{\Delta\tau}{2\sqrt{2\ln 2}} = 0.425 \Delta\tau . \quad (4.6)$$

The principal properties of a Gaussian pulse in the temporal domain have been represented in Fig. 4.3 (a).

- Analogously to the time width, the spectral bandwidth ($\Delta\lambda$) denotes the FWHM of the optical spectrum of the pulse obtained from the expression of the electric field in the frequency domain, as explained in Eq. (2.10). This parameter is usually measured in nm and related to the frequency bandwidth as $\Delta\lambda = c \Delta\nu / (\nu^2)$. For transform-limited pulses, the linewidth of the optical pulse is related to the time duration by the expression $\Delta\nu \simeq \frac{1}{\tau_p}$ and to the number of modes by $\Delta\nu = \Delta m \nu_F$.

In ultrafast fiber lasers, an important parameter that denotes the quality and stability of ultrashort pulses is the time-bandwidth product (TBP). The TBP value can be obtained as a product of both the time and frequency FWHM variables as,

$$\Delta\tau \cdot \Delta\nu \geq \kappa \quad (4.7)$$

where κ represents the quality of the optical pulse, and related to the minimum optical width achievable for a specific pulse. The pulse is said to be in transform-limited condition if TBP is equal to κ , otherwise, the pulse is chirped (closely linked to dispersion and nonlinear broadening effects). For Gaussian pulses, the TBP value can be as low as 0.44 [98].

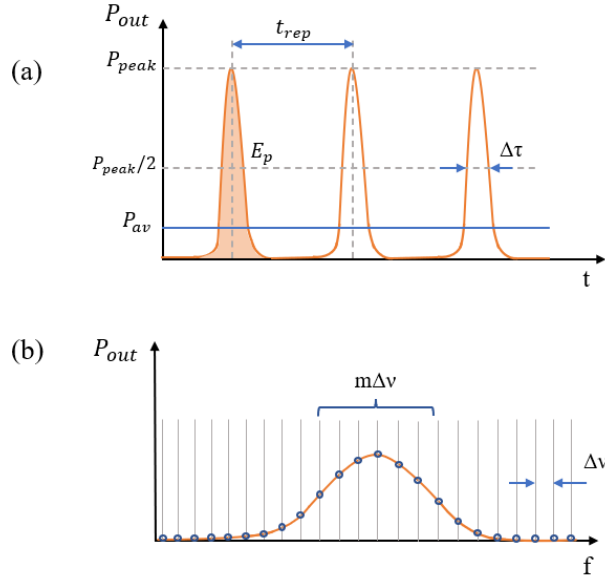


Figure 4.3: Schematic representation of the main characteristics of ultrashort pulses, where t_{rep} refers to the repetition rate, P_{av} and P_{peak} are the average and peak powers and $\Delta\tau$ is the temporal pulsewidth at FWHM.

- The average power circulating in one roundtrip in the resonator cavity is simply the pulse energy averaged over a given period of time. The pulse energy can be defined as the total energy within a single pulse. Whereas the maximum power of the optical pulse, denoted as peak power, can be related to the pulse energy by the pulse duration as,

$$P_{peak} \simeq \frac{E_p}{\Delta\tau} \quad (4.8)$$

The peak power can also be expressed in terms of the average power. Nevertheless, this relationship should be corrected by a constant factor C , related to the pulse shape. Most common pulse profiles are square, solitonic or Gaussian pulses with a C value of 1, 0.88 and 0.94 respectively [99], hence:

$$P_{peak} = C \frac{P_{avg}}{f_{rep} \Delta\tau} . \quad (4.9)$$

Experimentally, both the energy and peak power cannot be obtained with a direct measurement, but can be estimated from the average power, pulse duration and repetition rate with the corresponding pulse shape correction factor.

4.2 Passive mode-locked fiber lasers

In the following pages, in order to contextualize the topic of this thesis, we will provide an overview of passively mode-locked fiber lasers. Firstly, we will describe in detail the mechanism of mode-locking, focusing mainly on the passive approximation, and specifically on the use of saturable absorbers as internal modulators. An in-depth description of the state-of-the-art semiconductor saturable absorbers is presented, since it is the mode-locking approach adopted in this work.

4.2.1 Mode-locking technique

In order to describe the mechanism of passive mode-locking, a single pulse will be assumed to be circulating within the resonator cavity for simplification purposes. During the mode-locking process, a pulse is initiated by a weak modulation of the circulating radiation in the resonator cavity that is synchronized with the roundtrip time. At each roundtrip, the optical pulse hits the saturable absorber, saturating its absorption and thus reducing the optical losses in a short period of time equivalent to the temporal pulse duration. The optical losses of the laser cavity are reduced to a level below the optical gain provided by amplification sources such as rare-earth doped optical fibers, permitting the transmission of the incident light. In contrast, any incident light with a lower intensity that interacts with the saturable absorber at different times, is not sufficient to compensate for the reduced losses. In this way, the saturable absorber not only suppresses additional pulses of light propagating through the laser cavity, but also attenuates the CW background components within the resonator. Consequently, the saturable absorber may also attenuate the leading and trailing wings of the optical pulse, since these components have a weaker intensity than those frequencies placed at the center of the optical pulse. As a result, the saturable absorber tends to shorten the pulse duration, which can be compensated by other effects such as chromatic dispersion and nonlinear effects that may lengthen the pulse when propagating through the optical fiber resonator cavity [100]. The temporal evolution of an optical pulse in a passively mode-locked laser is depicted in Fig. 4.4. The intensity modulation of the saturable absorber is represented as the balance between the losses and gain contributions within the resonator cavity, represented in grey and red lines respectively.

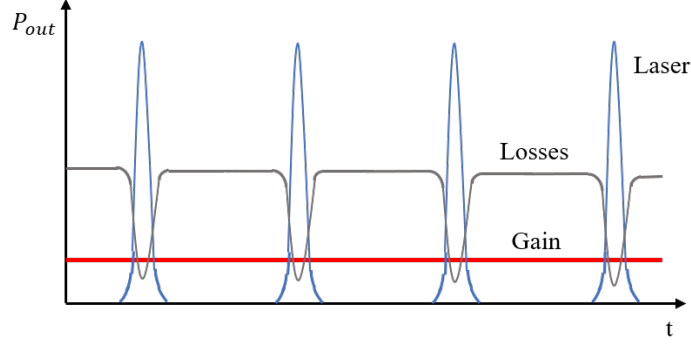


Figure 4.4: Pulse generation (blue line) by the gain-losses compensation (red and grey lines) mechanism, generated by a saturable absorber in a passive mode-locked laser cavity.

The dynamics of the laser cavity are dominated by the gain coefficient, as it can be seen in Fig. 4.4. As above described, the gain is saturated when the optical power of the laser cavity is greater than a certain average power. Therefore, the gain coefficient as a function of the incident power can be expressed as,

$$g(T) = \frac{g_0}{1 + \frac{P(T)}{P_{sat}}} \quad (4.10)$$

where the gain at small signal is represented by g_0 , $P(T)$ is the average power denoted by the pulse energy and the roundtrip time as $P(T) = E_p(T)/T_R$, and P_{sat} is the saturation power of the gain medium.

However, after the interaction with the incident light, the SA has a certain recovery time. The absorption of a SA decreases, becoming saturated, as the intensity of the incident light increases. This absorption is then restored from saturation to its original level by intraband desexcitation processes, such as thermal relaxation, with a time duration of tens or hundreds of femtoseconds, followed by a recombination process, which lasts from a few hundred to thousands of picoseconds. The time duration of these two processes represents the recovery time of the saturable absorber, which can be divided into two categories. When the saturable absorber recovery time is shorter than the time duration of the optical pulse, it is considered a fast absorber [101]. However, when the recovery time is comparable or greater, it is considered a slow absorber [102].

In general, mode-locked fiber lasers start in a CW mode after switching on the pump source, with noise fluctuations of the laser power working as a seed for the mode-locking process. The generation of ultrashort pulses can also be initiated with an additional process, such as vibrating mirrors or nonlinear effects in optical components. It is known as self-starting mode locking when the laser begins generating pulses automatically after switching on the laser [103]. Self-starting is usually achieved by passive mode-locking systems, where slow saturable absorbers are found to be more suitable than fast saturable absorbers. At the output, a single pulse remains within the laser cavity and is stabilized by the SA. Nevertheless, multiple effects such as chromatic dispersion or parasitic intracavity reflections may inhibit the self-starting process [104]. Therefore, a careful design of the laser cav-

ity, preventing undesired reflections within the resonator, must be considered for high-quality, reliable and stable fiber lasers.

4.2.2 Saturable absorbers

4.2.2.1 Characteristics of saturable absorbers

The main properties that characterize a saturable absorber have been represented in Fig. 4.5, which can be classified in [105]:

- Linear transmission (T_{lin}): A low-powered optical pulse is attenuated after the propagation through a SA because of its linear absorption parameter. This intrinsic loss is known as linear losses and can be presented both in transmission (T_{lin}) or reflection configurations (R_{lin}).
- Nonlinear transmission (T_{ns}): for high pulse energy fluences, the saturable absorber is bleached, reaching a maximum transmission or reflection value (T_{ns} or R_{ns}).
- Modulation depth (MD): The maximum change of the transmission or reflection achievable by the SA is defined as the modulation depth related to the linear and nonlinear transmission as $MD = T_{ns} - T_{lin}$.

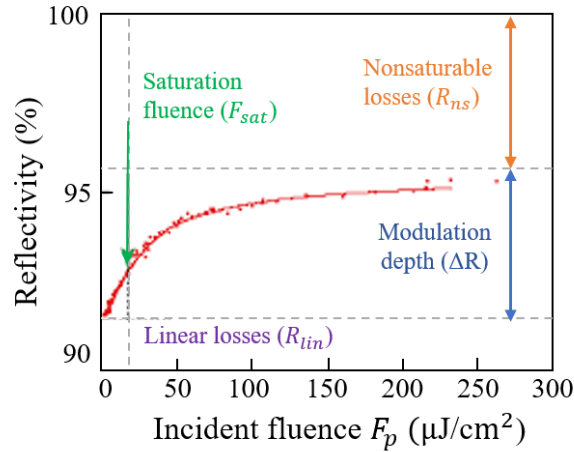


Figure 4.5: Properties of a saturable absorber in reflection configuration [105].

- Recovery time: The average decay time described by the desexcitation of the bound electrons from the excited to the ground state is denoted as recovery time (τ_{rec}).
- Saturation fluence (F_{sat}): The amount of energy required to saturate the SA with a saturation value of $1/e$ is called saturation fluence. The saturation intensity (I_{sat}), defined as the saturation fluence divided by the mode area, is a frequency-dependent inherent property of the optical material which varies with the penetration depth in the SA. The mode-locking regime will be therefore stabilized when the SA is considered as fully saturated (optical bleaching).

- **Damage threshold:** The maximum level of SA operation above which the material may incur damage is indicated as damage threshold. This parameter can be expressed in terms of optical intensities or fluences.

4.2.2.2 Classification of saturable absorbers

Generally, the longitudinal modes within a laser cavity oscillate independently, with uncoupled phase. Thus, a resonator cavity can be understood as a conjunction of independent lasers emitting individual light waves with slightly different frequencies and with unfixed phases that change randomly due to the thermal fluctuations of the material that generates the laser radiation. The interference of these modes can generate a near-constant output intensity, whose amplitude may vary depending on the number of modes.

However, if a large number m of longitudinal modes is coupled together oscillating with a fixed phase, the laser will no longer emit a random constant output intensity but an intense pulse of light. The oscillating waves within the laser cavity will interfere constructively with each other, producing a giant number of photons being reflected back and forth in the resonator. When the optical gain of the resonator is greater than the optical losses, the photons are allowed to escape in the form of a giant narrow pulse with a spectral width of $\Delta\nu$. Each of these pulses is emitted with a repetition period of t_{rep} dependent on the cavity length L and as a (sub)-multiple of the time taken by the light to make a complete roundtrip around the resonator. In these conditions, the laser is said to be working in the fundamental mode-locking regime when only one pulse at a time is propagating through the laser cavity [106].

By employing an active or passive modulator located inside the laser cavity, it is possible to lock the phase of the longitudinal modes.

- Active mode locking consists of the use of an amplitude or phase modulator, usually in the form of an electro-optic or acousto-optic modulator, which modulates the losses of the resonator and is synchronized with the cavity roundtrip time. The most common active ML technique modulates the optical field with a sinusoidal amplitude. This modulation can be interpreted as a light shutter (switch), changing the attenuation of the output light intensity. The laser emits light radiation when the shutter is opened (maxima of the sinusoidal modulation signal), while enclosing it when the shutter is closed (minimum values of the sinusoidal). The emission of optical pulses will be achieved when the inverse of the roundtrip time coincides with the frequency of the modulator. Any other field distribution will be partially or totally blocked by the optical switch. Mode-locked laser emission will only occur when the modes are equally phase-shifted [107].
- On the contrary, passive mode-locking refers to those techniques that do not require external modulation to generate ultrashort pulses, e.g., nonlinear devices that modulate the losses of the light within the laser cavity. These optical devices, known as saturable absorbers (SA), vary their transmission as a function of the incident intensity of the optical pulse, as it was explained in

Chapter 3. In passive mode-locking, the wings of the optical pulse are attenuated by the saturable absorber, corresponding to the components with low intensity, but permits the transmission of the high-intensity components at the peak of the pulse. The pulse duration is determined by the saturable absorber, the amplification source, the cavity dispersion and the optical nonlinearities within the laser cavity [108]. Shorter pulses (with a temporal duration below 1 ps) can be generated with this mechanism compared to active mode-locking.

Two basic types of saturable absorbers can be categorized depending on their mechanism. Real SAs are based on optical materials that exhibit a nonlinear decrease of the absorption coefficient with increasing light intensity. On the contrary, artificial SAs do not rely on saturable absorption but introduce a reduction of optical losses as the incident intensity increases.

- Among artificial passive mode-locking devices, a particularly simple solution consists of the use of a nonlinear amplifying loop mirror (NALM), with a figure-of-eight fiber laser set-up [109]. This mechanism is based on the interference of two counter-propagating pulses with different phases due to the location of the amplification stage within the laser cavity. The phase of the interfering pulses will be matched at the pulse peak and non-matched in the wings, leading to a reduction in the pulse duration at the output. An optical pulse with a time duration as short as 300 fs and in the pJ energy range can be obtained by this method [110]. Further dispersion and nonlinear compensation yield pulse durations below 50 fs and 0.5 nJ [111].

In addition to NALM, another kind of artificial saturable absorber is the nonlinear polarization rotator (NPR). In this technique, the transmittance of a polarized pulse varies as a function of the SPM and XPM effects, while propagating through the optical fiber and multiple optical polarizers by tuning their transfer function, and thus narrowing its pulse duration, simulating the effect of a saturable absorber. By adjusting the net dispersion of the optical cavity, a pulse as short as 77 fs and 70 pJ can be obtained [112]. However, polarization states can be modified due to environmental external fluctuations, for instance temperature variations, leading to unstable laser pulses. Additional devices such as Kerr lens, nonlinear mirrors or nonlinear fibers can also be employed as artificial SAs.

- Natural saturable absorbers have been employed for pulse generation since the invention of the laser itself. Optical dyes and colored glass filters were used for the first time in 1964 for CW mode-locking laser operation [113]. Nevertheless, the achievement of high-power ultrashort pulses remained challenging until the development of semiconductor saturable absorbers in 1990 [114]. Because of their inherent properties (low saturation intensity, for instance), semiconductor saturable absorbers quickly became the most relevant technology for generating ultrafast mode-locked high-energy pulses from fiber lasers. However, they also have some limitations, such as a high cost of fabrication and narrow operating bandwidths. Novel materials for SA applications are being developed to address these limitations. Among them, nanomaterials are of particu-

lar interest such as multiquantum dots and multiquantum well (MQW) heterostructures [115, 116] or carbon nanotube (CNT) quantum wires have demonstrated ultrashort pulse generation with a time width as low as 74fs [117]. Most recently, 2D materials such as topological insulators [118], transition dichalcogenides [119], and black phosphorus [120], have drawn the attention of researchers due to their advantages, including controllable bandgap energy and ease of fabrication. An overview of the most important natural saturable absorbers that have been discovered since their invention in 1964 is represented in Fig. 4.6.

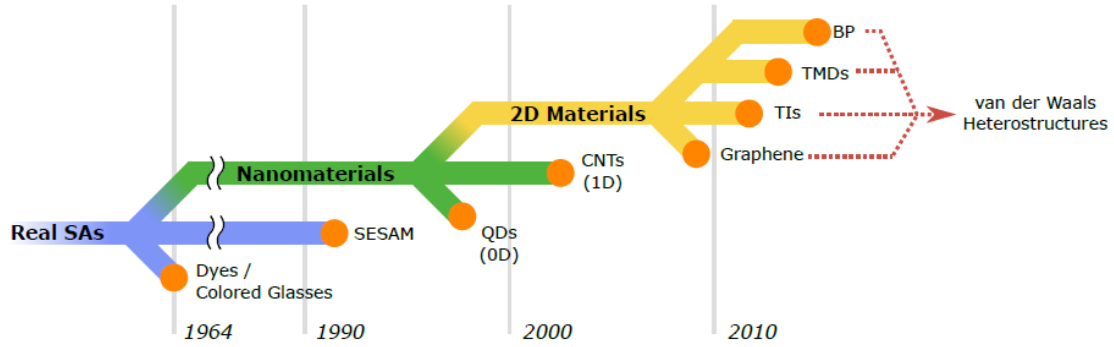


Figure 4.6: Historical evolution of natural saturable absorbers since its discovery in 1964 to the present day [121].

In the next section, semiconductor saturable absorbers will be introduced, since they are the basis of the fiber laser employed in this work.

4.2.2.3 Semiconductor saturable absorbers

Most of the semiconductor materials used as SAs for ultrashort pulse generation in mode-locked fiber lasers correspond to the III and IV columns of the periodic table. The combination of an element in column III, for instance aluminum (Al), gallium (Ga) or indium (In), with other elements belonging to column V, including nitrogen (N), phosphorus (P), arsenic (As) or antimony (Sb) yields semiconductor materials that can be used as light sources, such as in light-emitting diodes or lasers, or as optical detectors [34]. Among the binary semiconductors, gallium arsenide (GaAs), was the first to be used in photonic devices as a saturable absorber in a passive mode-locked titanium-sapphire laser. Throughout the past few years, III-nitride research has gained a great deal of attention thanks to the wide range of possible applications of these semiconductors; where aluminum-nitride (AlN) is commonly used as a saturable absorber in lasers emitting in the mid-ultraviolet region. Another possibility would be gallium-nitride (GaN) which is usually found as the basic component in some electronic devices due to its high temperature resistance. Finally, indium-nitride (InN) can be developed for lasers emitting at longer wavelengths (near-infrared region) due to its lower bandgap value [122, 123].

A complete classification of the semiconductor materials has been represented in Fig. 4.7 in terms of bandgap energy, wavelength and lattice constant (constant distance between unit cells in a crystal lattice).

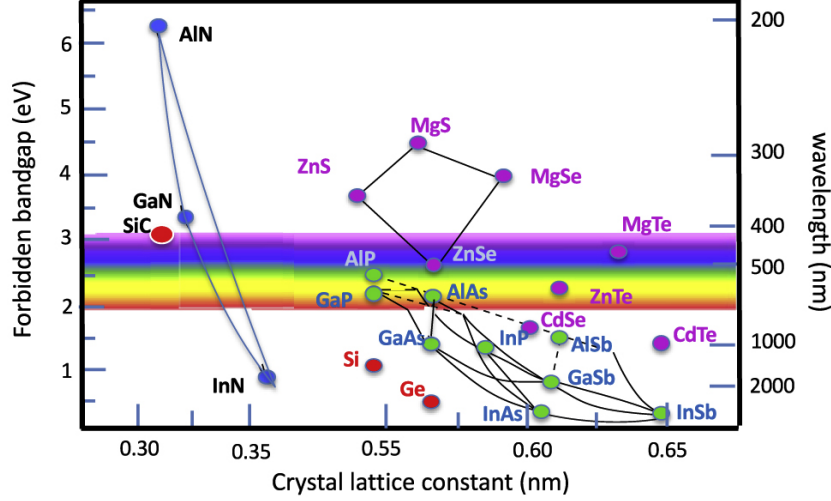


Figure 4.7: Classification of the III-V binary semiconductor compounds as a function of the bandgap energy, the emission wavelength, and its lattice constant [124].

With regard to this thesis, a novel non-commercial semiconductor saturable absorber based on InN has been developed and tested. A full explanation of the fabrication methods of InN, as well as its structural and optical characteristics, can be found in the next section.

4.3 InN as SESAM

In this section, a brief description of the growth principles, characteristics and applications of the fabrication technology for thin-film deposition of III-nitrides employed in this thesis is introduced, i.e., molecular beam epitaxy. Subsequently, a full explanation of the structural and optical characteristics of III-nitrides and especially on InN materials will be discussed.

4.3.1 Growth of III-nitrides

Multiple deposition techniques for material formation can be found in the literature, which are classified into four different categories as evaporation methods, glow-discharge technologies or gas and liquid-phase chemical processes [125]. The selection of the growth technique can have a significant impact on the properties of thin films. Among them, it is highlighted the technique of plasma-assisted molecular beam epitaxy (PAMBE), due to its advantages in the generation of high-quality crystals with greater control of dopant concentration as well as the material layer thickness. These properties are essential for the development of binary III-nitrides with bulk or heterostructure composition. A general overview of the deposition of III-nitrides using PAMBE is given in this section for InN thin films which have been used in the course of this thesis within ultrafast passive mode-locked fiber lasers.

Plasma-assisted molecular beam epitaxy (PAMBE) is based on the fabrication of single-crystal epitaxial films in a highly-controlled vacuum environment with a pressure of up to 10^{-11} mBar. The III-group semiconductor elements (e.g. Al, Ga, In)

are introduced in the vacuum chamber from effusion cells. The excitation and dissociation of the N_2 molecules produced by a radio frequency plasma process, generate an atomic flux that interacts with the evaporated metal elements or molecules. The evaporated atoms of N and III-group metals are deposited epitaxially on a heated substrate. The composition, thickness, and dopant concentration of each layer can be controlled by the use of shutters within the vacuum chamber. Furthermore, material parameters such as growth rate, mobility or atomic flux arriving at the substrate may lead to different growth regimes, including Frank-Van der Merwe [126], based on a uniform layer growth, Volmer-Weber [127] or a pyramidal construction and Stranski-Krastanow [128], which consists of a combination of the latter two. Among them, the method of Frank-Van der Merwe is important due to its use in the fabrication of bulk and MQWs structures. Due to the low temperature requirement for InN epitaxial deposition, the PAMBE technique has been employed for the fabrication of the InN-based SESAMs used in this thesis. The MBE InN samples studied in this work were grown by Dr. Eva Monroy in the INAC-SP2M laboratories in CEA-Grenoble.

4.3.2 Structural properties

Semiconductor materials are widely known for their highly symmetric and simple atomic arrangements. The crystal structure is determined and thus classified by the symmetry of these arrangements.

In relation to the crystalline lattice structure, the binary III-group of semiconductor nitrides AlN, GaN and InN can have three different structural phases, including α -phase, or wurtzite, based on a hexagonal close-packed lattice (HCP), whereas β -phase and γ -phase, also known as zinc-blende and rock-salt structures, are described by a face-centered cubic lattice morphology. Among them, III-nitrides are usually found in the wurtzite structure, since it is the most thermodynamically stable phase at room temperature. However, group-III nitrides can also occur in the zinc-blende structure and less frequently in the rocksalt structure, which is only achieved at extremely high pressures. This thesis will focus only on wurtzite nitrides.

The lattice structure of nitrides can be characterized by three different parameters that describe its hexagonal morphology: the length of the hexagonal base side, defined in Fig. 4.8 as a , the height of the hexagonal prism denoted as c , and the distance between the nitrogen-metal atoms indicated by the parameter u . Depending on the nature of the metal element in the nitride compound, the nitride structure may present some deviations from their ideal hexagonal morphology, characterized by the relations $u/c = 0.375$ and $c/a = 1.633$. The hexagonal structure of an ideal wurtzite crystal is depicted in Fig. 4.8 (a). Among the binary III-nitride group, InN presents the most approximate values to the ideal case with a $u/c = 0.377$ and $c/a = 1.612$ ratios [129].

The hexagonal structure can be described by the projection of four crystallographic directions, based on the Miller notation. The lattice cell is therefore constituted by the parameters above defined and represented as $\vec{a}_1, \vec{a}_2, \vec{a}_3, \vec{c}$, where the vectors \vec{a}_1, \vec{a}_2 , and \vec{a}_3 denote the basal plane (hkl), and \vec{c} the height of the hexagonal prism, perpendicular to the basal plane and indicated with the Miller-Bravais notation [130]. These basal vectors can be related with the equation $\vec{a}_3 = -(\vec{a}_1 + \vec{a}_2)$,

while the height c is connected to the base by the interplanar distance d_{hkl} as,

$$\frac{1}{d_{hkl}^2} = \frac{4}{3} \frac{h^2 + k^2 + hk}{a^2} + \frac{l^2}{c^2} . \quad (4.11)$$

The wurtzite structure can be decomposed into two HCP sublattices (tetrahedrons) separated by the ratio $3/8c$ in the direction $[0001]$, as represented in Fig. 4.8. In the Hermann-Mauguin notation, this structure is denoted as a dihexagonal-pyramidal crystal (6mm type) with a hexagonal symmetry, which will be important for nonlinear behavior as it will be explained in the next section. In general, binary nitrides are grown in the $[0001]$ direction leading to advantageous properties, and thermal and chemical stability.

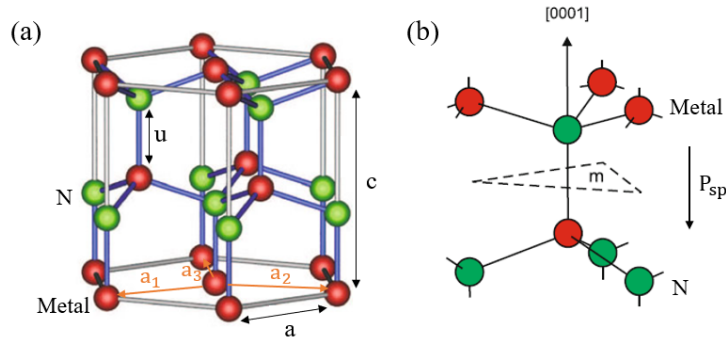


Figure 4.8: Hexagonal symmetry of wurtzite structures. (a) Principal lattice parameters of wurtzite structures with hexagonal morphology, and (b) Spontaneous polarization effect within a small section of the wurtzite structure due to the electronegativity properties of tetragonal structures. In this case, metal polarity is shown with the metal compounds on top of the bilayer along the growth direction $[129]$.

4.3.2.1 Polarization properties of III-group nitrides

Due to the absence of inversion symmetry along the c -axis in uniaxial anisotropic materials, wurtzite possesses two different polarity configurations. This polarity configuration will be determined by the difference in the electronegativity parameters between the metal and nitrogen elements that constitute the hexagonal material. In each tetrahedron, nitrogen atoms attract the electrons from the metal atoms due to their higher electronegativity (3.0) than the atoms Al, Ga or In (1.6-1.8), thus inducing an electrostatic dipole. The sum of each tetrahedron polarity generates a macroscopic dipole defining a spontaneous polarization vector denoted as P_{sp} . An example of the electronegative tendency of wurtzite structures is represented in Fig. 4.8 (b). Depending on the growth direction, two different material polarity structures can be defined, named as metal-polarity (or positive) when the material grows in the $[0001]$ planar direction with the Al, Ga or In face at the top of the bilayer. On the contrary, the material is said to have nitrogen polarity, that is negative polarity, when N atoms are located at the top of the bilayer in the $[000-1]$ axis. The direction of the spontaneous polarization vector will therefore be from the metal to the N-atoms surface, coinciding with the direction from the least to

the most electronegative atom of the material. This spontaneous polarization is found to be -0.034 C/m^2 , -0.090 C/m^2 and -0.042 C/m^2 for GaN, AlN and InN materials [131].

The growth process in which the crystal film is deposited on a lattice-matched crystal substrate with the same material is known as homoepitaxial deposition. However, due to the absence of III-group nitrides as suitable substrates, the growth of nitride layers is predominantly heteroepitaxial on substrates with similar thermal properties such as sapphire (Al_2O_3), silicon carbide (SiC), or silicon (Si), among others.

However, heteroepitaxial growth induces strain effects throughout the layer during the growth process due to the lattice mismatch of the different materials. The mechanical stress applied to the tetrahedrons (σ_{ij}) may induce a distortion in the total dipole, leading to a strain of the hexagonal structure (ε_{ij}) and thus the appearance of a piezoelectric polarization component P_{pz} .

Nevertheless, as the growth of the nitride material on a substrate with a different lattice constant is generally made in the $[0001]$ axis, the stress is zero in this direction ($\sigma_{zz} = 0$), introducing a uniform in-plane stress in the x-y axis ($\sigma_{xx} = \sigma_{yy}$). Thus, deformations are only induced in three directions, i.e., along the c direction (ε_{zz}), as well as along the perpendicular plane (0001) ($\varepsilon_{xx}, \varepsilon_{yy}$). Furthermore, because of the wurtzite morphology of nitrides, the piezoelectric polarization vector will only affect the c -axis direction, defined as,

$$\vec{P}_{pz}^Z = 2 \varepsilon_{xx} e_{31} - \varepsilon_{zz} e_{33} , \quad (4.12)$$

where e_{ij} are the piezoelectric coefficients related to the corresponding stress directions within the hexagonal structure. Therefore, the strain directions ε_{xx} and ε_{zz} can be represented as a function of the lattice parameters as:

$$\varepsilon_{xx} = \frac{a - a_0}{a_0} \quad (4.13a)$$

$$\varepsilon_{zz} = \frac{c - c_0}{c_0} \quad (4.13b)$$

where a, c correspond to the lattice parameters of the material under mechanical stress, and a_0, c_0 are related to the ones in the relaxed state with a value of 3.545 \AA and 5.703 \AA , respectively.

In the case of binary III-group nitrides, the e_{31} and e_{33} parameters have a value of -0.50 and 1.79 C/m^2 for AlN, -0.35 and 1.27 C/m^2 for GaN, and -0.57 and 0.97 C/m^2 for InN respectively [131].

The sum of the spontaneous and piezoelectric polarizations defines the total polarization P_{tot} of the material, and thus the generation of an internal electric field, related to the polarization vector by the equation described in Eq. (2.38).

The InN semiconductors employed in this thesis as SAs for ultrafast pulse generation in a mode-locked fiber laser demonstrate polarization independence when the incident pump is launched in the z direction. The spontaneous polarization can be screened as it is produced at the interfaces of the material, whereas the piezoelectric

polarization becomes the dominant factor in nitride-strained nanostructures.

The structural characterization of InN semiconductor materials has been conducted in previous theses of our group [132,133] by atomic force microscopy (AFM) and field-emission scanning electron microscopy (FESEM) techniques.

Therefore, a sapphire layer, which is also described by a hexagonal structure, has been employed as the material substrate. In this thesis, an InN material deposited on a GaN-on-sapphire template has been used as the semiconductor saturable absorber. The sapphire material has a refractive index lower than the InN semiconductor, and it is transparent in the near-infrared range.

4.3.2.2 Bandgap structure of binary III-nitrides

The bandgap energy structure of semiconductors can be classified depending on the energy level. In this case, the band with higher energy corresponds to the conduction band, while the lower energy band, known as the valence band, is separated into the heavy-hole (HH), the light-hole (LH) and the split-off hole or crystal field band (CH) states, respectively.

A direct optical band gap is present in all wurtzite binary III-nitrides (AlN, GaN, InN). Therefore, the maximum value of the valence band coincides with the minimum point of the conduction band centered in the Brillouin zone (Γ point). A schematic representation of the bandgap structure of InN and GaN compounds is depicted in Fig. 4.9.

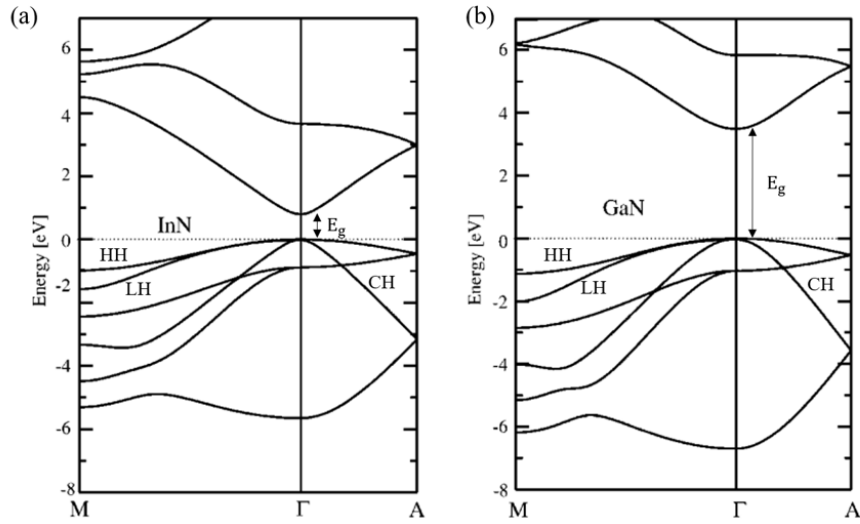


Figure 4.9: Energy bandgap structure of a wurtzite InN and GaN semiconductor materials centered in the Brillouin zone Γ [134].

Nevertheless, the bandgap energy structure of semiconductors can be varied by an external perturbation, such as temperature, as demonstrated by Varshni et al. [135]. At high temperatures, the shift in the relative positions of the valence and conduction bands increases linearly with the temperature. Whereas at low temperatures, the dilatation of the band structure follows a nonlinear dependency.

The energy bandgap of the binary III-group semiconductor materials varies from the ultraviolet region, 6.2 eV or 200 nm in the case of AlN, to the infrared region, 0.65 eV or 1900 μm corresponding to the InN compound. However, the bandgap energy of InN semiconductors has been a matter of controversy in the last decades due to its wide range of values under different growth processes. A direct bandgap energy value of 1.9 eV was measured for an InN semiconductor grown by RF-sputtering on a glass substrate at room temperature [136]. Soon afterward, Davydov et al. found a 0.9 eV bandgap energy in high-quality InN polycrystalline films [137]. Nevertheless, in the last few years, molecular beam-epitaxy (MBE) has enabled the generation of good-quality InN crystals, resulting in an optical band gap energy of only 0.64 eV at room temperature [138]. Therefore, larger bandgap energy structures in the range of 1.6 to 1.9 eV can be related to poor-quality crystalline layers and higher free carrier concentrations, which may lead to the appearance of the Burstein-Moss effect, associated with the presence of dopants within the layers of the material, as it will be explained in Chapter 5.

In relation to electronic properties, such as the concentration of carriers and mobility, these determine the performance and efficiency of III-nitrides-based devices. The mobility of carriers in semiconductors is affected by several factors, including temperature, electrical field, material quality and doping concentration. In this sense, the mobility of carriers within the semiconductor is low when the lattice mismatch between the semiconductor and substrate layers is large.

As for the thermal and chemical properties, III-nitrides have a high melting point, chemical stability and mechanical strength due to the strong chemical bonding between the atoms of the material. Moreover, the strong bonding of III-nitrides makes them resistant to electrical degradation caused by high electrical currents and radiation damage. Thus, III-nitride-based devices are capable of working in hostile environments, due to their high thermal resistance and good thermal conductivity properties. The principal thermal and electrical properties of binary III-group nitrides are listed in Table 4.1.

Properties	AlN	GaN	InN
Bandgap energy (eV)	6.20	3.39	0.65
Thermal conductivity ($\text{W cm}^{-1}\text{K}^{-1}$)	2.0	1.3	0.8
Melting point ($^{\circ}\text{C}$)	>3000	>2500	>1100
Effective electron mass (m_o)	0.48	0.2	0.06
Electron mobility ($\text{cm}^2\text{V}^{-1}\text{s}^{-1}$)	300(T) /426(E)	1000(T) /900(E)	14000(T) /3980(E)
Electron concentration (cm^{-3})	$<10^{16}$	$\sim 10^{17}$	$>10^{17}$

Table 4.1: Thermal and electrical properties of wurtzite III-nitrides AlN, GaN and InN [139]. The (T) and (E) notation of the electron mobility correspond to the theoretical and experimental values for each compound.

4.3.3 Optical properties

In order to determine the optical characteristics of an III-nitride device, several factors must be taken into account, including the refractive index, absorption and

transmission coefficients of the materials. Depending on the value of the optical intensity of the incident light source, it can be differentiated between linear and nonlinear optical properties.

4.3.3.1 Linear characteristics

In relation to the linear transmission and reflection properties, the material can be characterized by the measurement of the collected energy from a light source after passing through the sample. Usually, the light source consists of a white lamp emitting from the ultraviolet to the near-infrared region, thus the transmission behavior of the material can be studied for the whole spectral range. The optical power is collected by an optical lens and focused on a photodetector, from which the data is analyzed. A Sellmeier approximation can be used to estimate the real part of the refractive index from the transmittance measurements [140]. The refractive indices of binary III-nitrides are found to be $n_0 = 2.16$ for AlN, $n_0 = 2.36$ for GaN and $n_0 = 2.95$ for InN when illuminated by a laser source with an optical wavelength centered at $1.55 \mu\text{m}$ [141]. Some preliminary results of the transmission coefficient in InN semiconductors have been carried out in [142].

On the other hand, the linear absorption coefficient α_0 can be estimated from the linear transmission coefficient as $\alpha_0(\lambda) = \ln[T(\lambda)]/l$, being l the layer thickness of the material [143]. Depending on the incident energy, the total absorption coefficient can be expressed as,

$$\alpha(E) = \frac{\alpha_0}{1 + e^{(E_{g,eff} - E/\Delta E)}} , \quad (4.14)$$

where $E_{g,eff}$ is the effective bandgap energy of the III-nitride and ΔE corresponds to the absorption edge broadening. Thus, from the measurement of the linear transmission and absorption coefficients, the value of the bandgap energy of the material can be estimated.

Through the representation of the magnitude $(\alpha E)^n$, being n a constant parameter that depends on the structure of the material ($n = 1/2$ for direct bandgap structures and $n = 1$ for indirect structures), in terms of the incident energy E , it can also be determined the bandgap energy of the semiconductor. In this representation, also known as Tauc's plot [144], the crossing point between the linear fit of the $(\alpha E)^n$ curve and the x-axis E will correspond to the approximate experimental bandgap energy value of the material.

In the case of InN semiconductor materials, Jimenez et al. [145], measured an energy bandgap of 0.8 eV (when excited with a laser source at $1.55 \mu\text{m}$) and a linear absorption coefficient of $\alpha_0 = 1.4 \cdot 10^4 \text{ cm}^{-1}$ with the material used in this thesis.

4.3.3.2 Nonlinear characteristics

When the optical intensity of the incident light source is high enough, nonlinear effects govern the transmission and absorption processes of materials. Due to the 6 mm type hexagonal wurtzite structure of III-nitrides mentioned in the previous section, the second-order nonlinear effects generated when impinging in the z direction within the material can be considered negligible [31]. Therefore, in this case, the study of the nonlinear properties of III-nitrides is based on the measurement of the

nonlinear refractive index (n_2) and nonlinear absorption (α_2) parameters, related to the third-order susceptibility $\chi^{(3)}$.

To do this, a high-power radiation source is focused on the material sample by an optical lens. The sample is translated in the z-axis propagation direction in order to obtain the maximum intensity transmission value, which coincides with the focal point of the lens. The output energy is collected by another lens and collimated on a photodetector. The transmission curve in terms of the position of the sample in the propagation direction z measured by this technique, known as z-scan, can be approximated by the equation,

$$T(z) = 1 - \frac{1}{2\sqrt{2}} \frac{\alpha_2 I_0 L_{eff}}{1 + x^2} \quad (4.15)$$

where x is the ratio of the position of the sample z and the focal point z_0 , while L_{eff} is the effective thickness of the material defined in Eq. (3.18). If the transmission curve decreases as the sample is moved along the z-direction, i.e., a valley is obtained at the focal point ($\alpha_2 > 0$), the material is said to have reverse saturable absorption (RSA), whereas if the transmission increases when the sample is moved closer to the focal point with a peak at its center ($\alpha_2 < 0$) the material presents saturable absorption (SA).

In the case of binary III-nitrides, a TPA behavior was observed for bulk AlN with a nonlinear absorption coefficient of $\alpha_2 = 13 \text{ cm/GW}$ and $n_2 = -1.9 \cdot 10^{-13} \text{ cm}^2/\text{GW}$ when illuminated with a light source centered at 355 nm (3.5 eV) at room temperature [146]. For GaN semiconductors, TPA processes were also measured at room temperature with a nonlinear absorption value of $\alpha_2 = 1500 \text{ cm/GW}$ and $n_2 = -2.9 \cdot 10^{-12} \text{ cm}^2/\text{GW}$ for an incident wavelength of 362 nm (3.42 eV) [147]. Nevertheless, these materials do not exhibit significant nonlinear behavior in the infrared region. Regarding InN materials, the nonlinear absorption coefficient was found to be of $\alpha_2 = -3500 \text{ cm/GW}$ and $n_2 = -2.5 \cdot 10^{-11} \text{ cm}^2/\text{GW}$ for a bulk wurtzite InN structure when excited with a 1.55 μm laser source, thus demonstrating a large SA performance [148]. Therefore, InN materials demonstrate relatively large nonlinear effects over other semiconductor devices when excited with a light source near their bandgap energy, thus becoming the perfect candidate as saturable absorbers in ultrafast pulse generation in fiber lasers.

This process can also be repeated as the intensity of the light source increases (a figure with the transmission value for each incident power can be obtained). From this image, the main parameters of a saturable absorber material can be calculated, i.e., the linear and nonlinear transmission losses, the maximum change in transmittance, also known as modulation depth, as well as the saturation fluence and the maximum bearable optical intensity (damage threshold) characteristics, defined previously in Fig. 4.5. The transmission variation as a function of the incident fluence can be expressed in terms of these coefficients by the equation [149]:

$$T(F) = T_{ns} \frac{\text{Ln} \left[1 + \frac{T_{lin}}{T_{ns}} (e^{F/F_{sat}} - 1) \right]}{F/F_{sat}} e^{-F/F_{sat}} . \quad (4.16)$$

In terms of modulation depth and saturation fluence, AlN and GaN semicon-

ductors do not demonstrate high nonlinear effects: less than 4% for GaN materials, whereas a 15% maximum transmission change and a saturation intensity of $0.27 \mu\text{J}/\text{cm}^2$ in GaN/AlN MQWs at $1.55 \mu\text{m}$ have been measured in [150].

An extensive study of the optical properties of InN wurtzite semiconductors was carried out in previous studies [142], where a linear and non-saturable transmission of $T_{lin} = 28\%$ and $T_{ns} = 45\%$ were measured with a saturation fluence of $F_{sat} = 315 \mu\text{J}/\text{cm}^2$. Therefore, these materials constitute the perfect candidate for saturable absorption in mode-locked fiber lasers at the $1.55 \mu\text{m}$.

4.4 InN-based ultrafast mode-locked fiber laser

In this section, an overview of the laser configuration used in this work will first be presented. The optical properties, including time duration and optical power, are also discussed. Finally, numerical simulations of the laser cavity are developed, denoting the advantages and disadvantages of InN-based mode-locked fiber lasers and the introduction of possible solutions for the enhancement of the fiber laser cavity and its optical properties.

4.4.1 Experimental set-up

An experimental ring fiber laser cavity was constructed with the aforementioned InN saturable absorbers in reflection configuration for mode-locked operation. To do this, an optical aluminium mirror has been placed on the bottom face of the InN sample, creating what is called a SESAM device. To do this, an ATC ORION-3-HV sputtering chamber was used, and placed in Grupo de Ingeniería Fotónica (GRIFO) facilities at Universidad de Alcalá in Madrid. These Al-mirrors are approximately 300 nm thick, and have been deposited at a deposition rate of 240-250 nm/h, at room temperature with a flux of Ar of 2sccm. The power applied to the Al target during deposition was 75 W, and the chamber pressure was maintained at 5 mTorr. The SESAM is constituted by a $1 \mu\text{m}$ InN thin layer deposited on a GaN-on-sapphire template of $4 \mu\text{m}/350 \mu\text{m}$ thickness, by a PAMBE technique whose fabrication characteristics can be summarized in a growth temperature and growth rate of 450°C and 280 nm/h respectively with nitrogen interruptions every 5 min. The reflection of the aluminum layer was measured to be $\sim 96\%$, whereas the linear transmission of the InN sample was calculated at 23% for an incident source centered at $1.56 \mu\text{m}$, as shown in the inset of Fig. 4.10. In relation to the absorption, it has been measured at a value of $\alpha_0 = 1.4 \cdot 10^4 \text{ cm}^{-1}$ and $\alpha_2 = -3.5 \cdot 10^3 \text{ cm/GW}$ for the linear and nonlinear coefficients. In this case, the saturable and non-saturable transmission coefficients are 27.8% and 44.5%, corresponding to a modulation depth (MD) of 16.7%, whereas the maximum nonlinear change, calculated as T_{ns}/T_{lin} , is set to 160%. A figure of the SESAM sample nonlinear transmission features is represented in Fig. 4.10.

The resonator cavity comprises an on-off operation gain medium, based on an off-the-shelf Er-doped fiber amplifier (EDFA Accelink TV-series), operating at a constant and non-adjustable saturation output power of 24 dBm during the on-

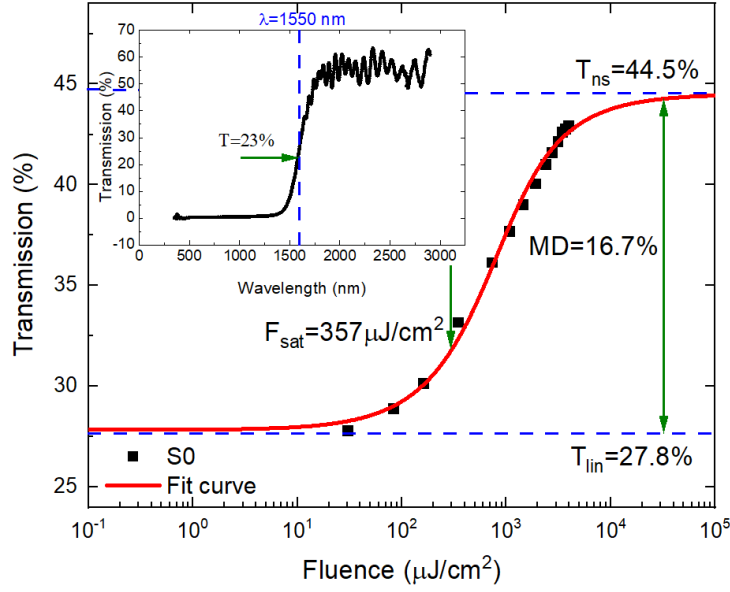


Figure 4.10: Experimental nonlinear optical transmission of the InN-based SESAM sample S0 as a function of the incident fluence (black dots). The red line represents the nonlinear fit of the transmission curve described by Eq. (4.16) obtaining the principal optical characteristics of a saturable absorber, i.e., the linear (T_{lin}) and non-saturable transmission (T_{ns}), modulation depth (MD) and saturation fluence (F_{sat}). The inset figure shows the linear transmission of the InN sample under the excitation of a light source with a variable wavelength from 350 to 3000 nm, obtaining a 23% when illuminated at 1550 nm.

times. The amplification operation is introduced along 16 m of EDF with a group velocity dispersion coefficient of $GVD=0.016 \text{ ps}^2/\text{m}$ similar to the one reported in reference [151], generating a total dispersion of 0.256 ps^2 . This value is an estimation taken from similar EDF samples as the ones used in the EDFA, since the gain medium is a commercial EDFA, and the company has not provided the authors with the real value.

The rest of the optical cavity is constituted by 22 m of SMF, with an estimated GVD coefficient of $+18 \text{ ps}^2/\text{nmkm}$ which at 1560 nm corresponds to a dispersion of $-0.021 \text{ ps}^2/\text{m}$, corresponding to a total dispersion of -0.462 ps^2 . The net dispersion coefficient of the laser cavity, with a total length of 38 m, can be calculated as the sum of the EDF and SMF dispersion coefficients, with a value of -0.206 ps^2 (working in the anomalous regime), since the InN SESAM dispersion effect can be considered as negligible. This can be explained by the enormous difference in length between the fibers (tens of meters) and the saturable absorber, which in this case has a thickness of $1 \text{ }\mu\text{m}$, i.e., a difference of 7 orders of magnitude. Note that in this case, the vast majority of the transmission through the semiconductor is made in a single round-trip, i.e., the multiple internal reflections within the bulk structure are relatively small in comparison with the direct single-pass transmission. This is also evidenced by the relatively small Fabry-Pérot oscillating spectral features in the transmission measurement in the inset of Fig. 4.10, denoting the small dispersion coefficient of the saturable absorber.

Once the gain medium is switched on, a CW noisy and random power radiation is sent to the SESAM, propagating through standard single-mode fiber (SMF28). Thus, a self-starting operation is generated by the saturable absorber, leading to the emission of an ultrashort $1.56 \mu\text{m}$ optical pulse train. When the radiation source impinges on the SESAM sample in the z-axis propagation direction, no polarization dependency is observable because of the wurtzite morphology of the InN material, thus no polarization controller has been included within the laser cavity.

As it was mentioned in Chapter 2, the laser does not emit pure soliton pulses, but should be considered as a dispersion-managed soliton laser with a low net anomalous dispersion. The optical pulse is stretched and compressed temporally (optical breathing) as it propagates through each optical fiber, passing from normal to anomalous dispersion regions. Thus, after multiple round-trips a stable pulse train is emitted. The complete laser set-up of the resonator cavity is plotted in Fig. 4.11.

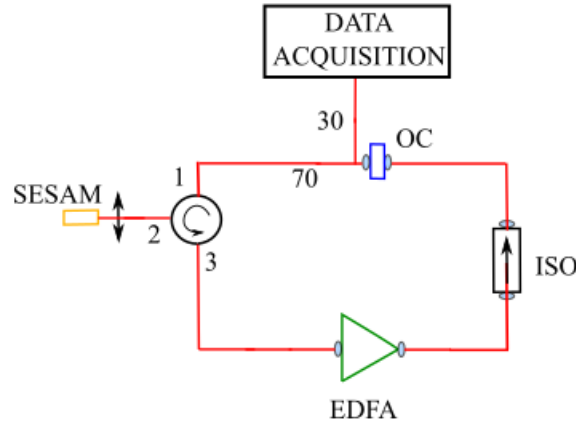


Figure 4.11: Reflective fiber laser set-up based on the use of an EDFA amplification system and SMF optical fibers, controlled by an isolator and variable attenuator, where the SESAM-InN sample is located in reflection configuration [152].

4.4.2 Optical characteristics of the InN-based ML-fiber laser

In order to measure the optical characteristics of the fiber laser, a 70/30 optical fiber coupler is introduced within the laser cavity, in which a 30% of the optical power is extracted, whereas the remaining 70% of the optical power is recirculated for the purpose of maximizing the mode-locking operation within the resonator cavity [142].

- **Transversal mode:** In Chapter 2, the transversal mode profile of an optical pulse propagating through an optical fiber was described by a Gaussian distribution (see Fig. 2.2). In this case, a knife-edge technique has been used for the characterization of the spatial intensity distribution at the output of the passively mode-locked fiber laser in terms of the beam waist and the Rayleigh distance. An experimental value of $\omega_0 = 8.5 \mu\text{m}$ and $z_R = 223.2 \mu\text{m}$ have been obtained for the beam waist and the Rayleigh distance, respectively.
- **Repetition rate:** As explained in Section 4.1, a train of pulses is generated at the output of a passively mode-locked laser, with a time separation between consecutive pulses given the cavity round-trip time.

The repetition period T_{rep} can be measured by the use of a photodetector connected to an oscilloscope. In this case, we employ an optical 100 MHz-photodetector (PDB410CAC, Thorlabs) and an oscilloscope with an optical bandwidth of 4 GHz (Keysight Technologies MSO9404A) with 40 GSa/s. An experimental figure of the time period of a fiber laser cavity with a length of 38 m is depicted in Fig. 4.12. A time interval of 178.5 ns has been estimated between consecutive pulses, operating in the fundamental mode.

Nevertheless, this repetition rate can also be obtained by using an electrical spectrum analyzer (ESA) but in the frequency domain (f_{rep}). In our case, a repetition rate of 5.6 MHz was estimated for a 38 m fiber laser cavity with a 32 GHz RF-spectrum analyzer (Agilent N9010A).

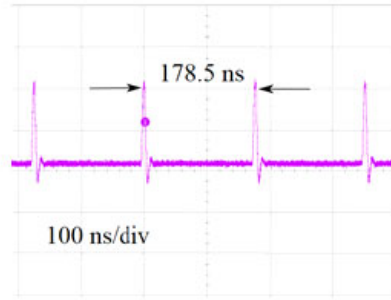


Figure 4.12: Oscilloscope trace for a fundamental mode-locked fiber laser cavity with a 178.5 ns (5.6 MHz) repetition rate [153].

- **Optical spectrum:** The spectrum of an ultrafast pulse can be obtained by connecting an optical spectrum analyzer (OSA) to the output port of the laser. In this work, we use a Yokogawa AQ-6215B device to measure all the experimental pulse spectra. An example of the spectrum is represented in Fig. 4.13(a). The optical spectrum can be adjusted to a Gaussian pulse shape, typical of strongly dispersion-managed cavities. By applying a Gaussian fitting curve (red line) to the experimental data (solid black dots), the FWHM of the optical pulse can be determined. In this case, a 3 dB bandwidth of 19.2 nm has been measured centered at 1564 nm. It must be noted the absence of Kelly-sidebands in the optical spectrum, denoting the distance from the pure soliton laser operation [46]. Furthermore, the spectrum does not present any visible noise from the EDFA.
- **Pulse duration:** the fiber laser output is driven to the autocorrelator (AC) for the characterization of the temporal width of the emitted ultrafast pulse. As explained in Chapter 2, the autocorrelation device is based on the SHG principle, measuring what is called the ACF [154].

Nevertheless, in 1993 Rick Trebino et al. [154], discovered a new technique capable of measuring both the amplitude and phase of the optical pulse. This device, known as frequency-resolved optical gating (FROG), gives a complete description of the incident electric field, thus the chirp parameter of the optical pulse can also be determined. With this method, the quality of the laser pulse can be monitored continuously [155].

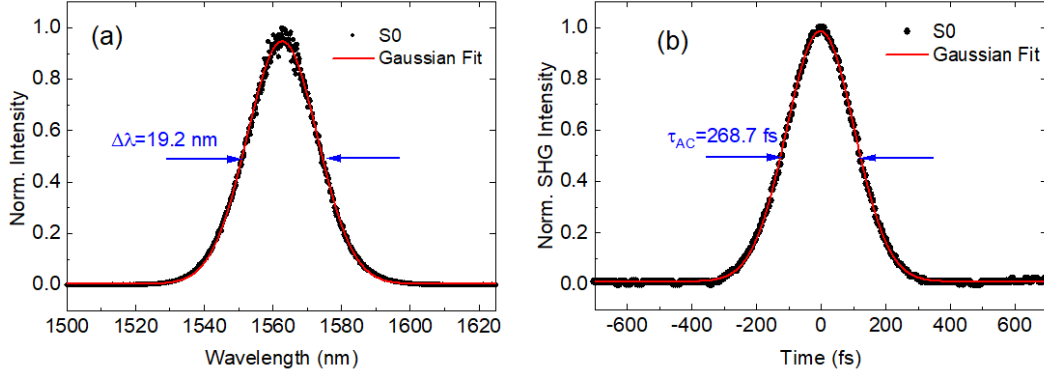


Figure 4.13: Optical spectrum (a) and autocorrelation (b) traces for a passively mode-locked fiber laser using a 1 μm InN SESAM sample as saturable absorber. The red lines correspond to the Gaussian fit curves to the experimental data (black dots).

In this thesis, a commercial APE Mini PulseCheck autocorrelator is employed for the characterization of the pulse duration in the temporal domain of the mode-locked fiber laser with a temporal resolution as low as 5 fs and a delay resolution of 0.05 fs. The autocorrelation trace of the 38 m fiber laser cavity output laser pulse is depicted in Fig. 4.13(b). A Gaussian fit has been applied to the autocorrelation traces, represented with a solid red line. Therefore, the temporal duration of the optical pulse (τ_p) can be obtained by the FWHM measurement of the ACF (τ_{AC}) multiplied by a constant corrector parameter, whose value depends on the shape of the pulse profile [156]. In the case of Gaussian pulses, this factor corresponds to $\tau_{AC}/\tau_p = 0.707$, whereas for sech^2 pulses it varies to $\tau_{AC}/\tau_p = 0.648$. In this sense, the temporal pulsewidth has been measured to be 268.7 fs calculated from the Gaussian fitting curve of Fig. 4.13(b). It is worth noting that no pedestal has been observed in the autocorrelation function, analogous to the absence of Kelly sidebands in the optical spectrum. This feature is usually found in optical lasers operating in the pure soliton mode and associated to a sech^2 pulse profile. Therefore, the Gaussian shape indicates the dispersion-managed operation of this mode-locked fiber laser. Furthermore, no secondary peaks are observed in the ACF pulse profile.

As discussed in Section 4.1, the TBP parameter can be calculated from the product of the temporal and spectral pulsewidth (in the frequency domain) as described in Eq. (4.7), with a value of 0.445, working close to the Gaussian range for the transform-limited condition (0.44).

- **Average power:** In order to measure the power of a train of pulses at the output of the fiber laser, a power-meter (Thorlabs, PM100USB) is connected to the output port. As it was mentioned before, the peak power and pulse energy are estimated from the average power, repetition rate and pulsewidth in the temporal domain. In this sense, an average power of 28 mW has been measured at the output of the laser cavity, which corresponds to 24 kW and 4.5 nJ for the peak power and pulse energy respectively, based on the repetition rate and temporal pulsewidth previously measured.

Therefore, taking into account the 70/30 fiber coupler within the laser cavity, the average power hitting the saturable absorber material scales up to 70 mW. This implies an optical fluence of 9 mJ/cm² within the InN layer. No optical damage has been observed for the maximum gain provided by the EDFA medium (24 dBm) in the SESAM sample. Accordingly, these results indicate that InN can be utilized for high-energy applications more effectively than popular materials working at 1.5 μ m, such as InGaAs SESAMs, whose damage thresholds are below the 2 mJ/cm² range.

4.4.3 Numerical simulations

In this section, some simulations related to the ring fiber laser cavity have been performed in MATLAB® in order to study the stability of the pulse within the resonator, as well as its limitations and possible improvements. To do this, we will firstly introduce the simulation of an ultrafast Gaussian optical pulse and its spectral representation. In a 2nd section, the propagation of the optical pulse through an optical fiber is explained by the split-step Fourier method. Afterwards, a complete simulation of the laser cavity is performed incorporating the simulation of the saturable absorber. Finally, we study the stability of the pulse while propagating through the resonator.

- **Gaussian Pulse**

An ultrashort pulse comprises only a few cycles of a sine wave. Our expression for an ultrashort pulse will be the product of a sine wave and a pulse envelope function, which in this case will take the form of a Gaussian shape, as above described. Therefore, to simulate the Gaussian pulse envelope, we will follow the equation represented in Eq. (4.5), whereas the complete electric field can be expressed with:

$$E(t) = \sqrt{P_{peak}} e^{\left(\frac{t-t_0}{2\tau_{Gauss}}\right)^2} e^{i\omega_0 t} \quad (4.17)$$

where t_0 corresponds to the initial time, usually centered in zero, and ω_0 is the central angular frequency of the pulse. In this case, a wavelength of 1560 nm is assumed, which implies an angular frequency of $1.2 \cdot 10^{15}$ rad/s. Moreover, the pulse duration τ_{Gauss} is related to the FWHM by Eq. (4.6).

In order to simulate the complete Gaussian electric field, it is necessary to describe a time window (T) big enough to achieve the desired resolution. This time window will depend on the number of points (N) and the time separation between them (dt), following the Nyquist-Shannon theorem. Nevertheless, this also implies processing a huge number of data, which will derive in time-consuming computational systems.

Consequently, the electric field must be defined both in the temporal and frequency domains. To do this, the MATLAB program has a software packet based on the FT algorithm, named as fast Fourier transform (FFT), setting the number of points N as a power of 2. As a result, it is usually employed a number of points in the range of 2^{13} to 2^{16} .

An example of a Gaussian pulse with a peak power of 30kW and a temporal duration of 270 fs has been represented in Fig. 4.14(a) by 2^{12} points in a time window of 10 ps. This pulse has also been represented in the frequency domain/wavelength range after applying the FFT function in the MATLAB code (b) and (c).

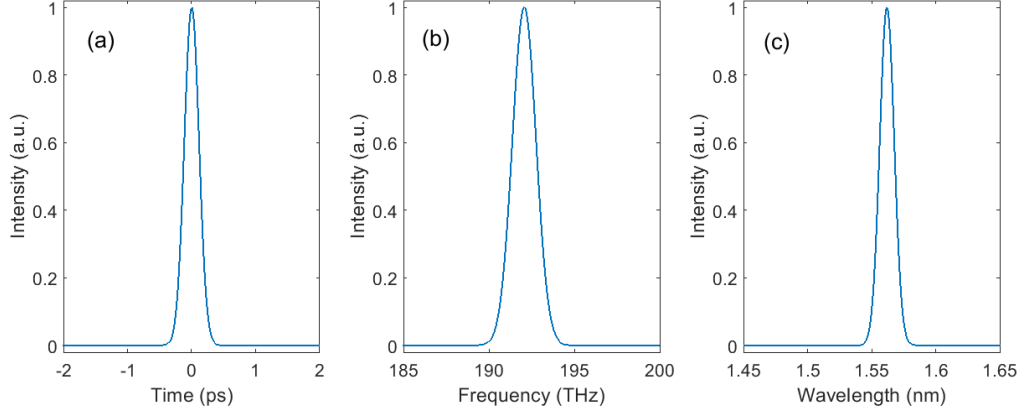


Figure 4.14: Simulation of an ultrafast 30 kW-Gaussian pulse with a pulsewidth of 270 fs represented by a time window of 10 ps with 2^{12} points and a time spacing of $dt = 0.0917$ ps (a) and its representation in the frequency domain (b) and wavelength region (c) when applying the FFT algorithm centered at 192 THz and $1.56 \mu\text{m}$, respectively. Every figure has been normalized for simplification.

• Fiber Propagation

As mentioned in Chapter 2, the optical pulse suffers from dispersion and non-linear effects while propagating through the optical fiber. In Fig. 2.4(c) and Fig. 2.5, a simulation of the evolution of an optical pulse within an optical fiber with a total distance of 5 km under the effect of dispersion and SPM respectively, were performed independently. Nevertheless, this is not the case in real experiments, where both the dispersion and SPM are present within the optical fiber all at once. In this respect, the propagation of the optical pulse inside the optical fiber can be simulated by employing the split-step Fourier method, which takes the form:

$$\frac{\partial A}{\partial z} = \left(\hat{D} + \hat{N} \right) A, \quad (4.18)$$

being z the propagation direction, A the amplitude of the electric field, and \hat{D} and \hat{N} are the differential dispersion and nonlinear operators,

$$\hat{D} = -\frac{i\beta_2}{2} \frac{\partial^2}{\partial T^2} + \frac{\beta_3}{6} \frac{\partial^3}{\partial T^3} - \frac{(\alpha + g)}{2}, \quad (4.19a)$$

$$\hat{N} = i\gamma \left(|A|^2 A + i s T_0 \frac{\partial}{\partial T} (|A|^2 A) - \tau_R T_0 A \frac{\partial |A|^2}{\partial T} \right). \quad (4.19b)$$

In the split-step algorithm, an approximate solution can be obtained when applying the dispersion and nonlinear effects independently when the optical pulse propagates over a small length h as,

$$A(z+h, T) \approx e^{(\frac{h}{2}\hat{D})} e^{(\int_z^{z+h} \hat{N}(z')dz')} e^{(\frac{h}{2}\hat{D})} A(z, T) . \quad (4.20)$$

This equation is also known as the symmetrized split-step Fourier method. In this case, the optical fiber is divided into individual segments with the same size and equally spaced h , where the pulse is first propagated through a dispersive fiber with length $h/2$, whose effect is described in the frequency domain. Afterwards, the inverse fast Fourier transform (IFFT) is applied to change back to the temporal domain, where the optical pulse propagates under the SPM nonlinear effect over a distance h . Finally, the electric field is represented again in the frequency domain by the FFT, where the pulse propagates through the remaining $h/2$ dispersive fiber. The split-step Fourier method has become the key element for the description of pulse propagation in optical fibers due to its fast execution and accuracy.

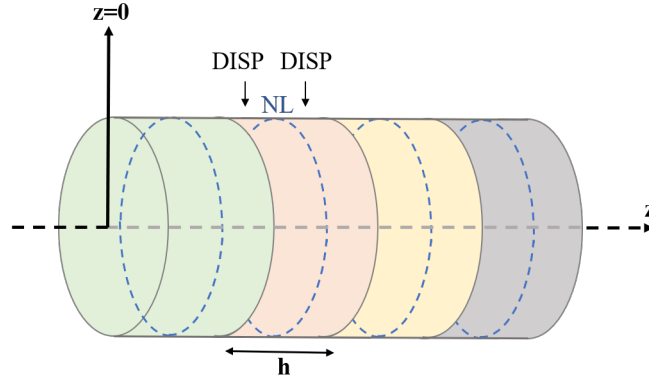


Figure 4.15: Diagram of the symmetrized split-step Fourier method

In our case, it has been simulated the propagation of an ultrafast pulse through the optical fibers employed in our laser configuration, i.e. SMF and EDF. As shown in Fig. 4.16(a)-(b), the 1550 nm optical pulse suffers from different effects along its propagation due to the variation of the dispersion and nonlinear coefficients for each fiber.

- The propagation through the SMF is governed by the dispersion of the optical pulse, as shown in Fig. 4.16(a). In this case, an unchirped optical pulse with 270 fs of temporal duration at FWHM and a peak power of 2.5 kW at the input of the optical fiber has been simulated. The pulse evolution is studied along a fiber length of 10 m, where the pulse demonstrates a breathing behavior. Due to the dispersion and SPM coefficients, the pulse is stretched in time, reaching a quasi-stable soliton operation mode. At the output, the optical pulse is characterized by a 4.26 kW peak power and a pulse duration of 106.8 fs.
- On the other hand, in order to simulate the amplification process along the EDF fiber, a gain factor g has been incorporated into the split-step Fourier code for each step with a value of $1 \cdot 10^3 \text{ km}^{-1}$ and $P_{sat} = 10^5 \text{ W}$. Consequently, a 270 fs optical pulse with a 2.5 kW of peak power has been programmed to travel along 16 m of normal dispersion EDF. The soliton-like pulse evolves into a gain-guided pulse, whose output profile

can be approximated to a Gaussian shape. For this simulation, a 26.5 kW optical pulse with a pulsewidth of 121.2 fs has been measured at the output of the optical fiber.

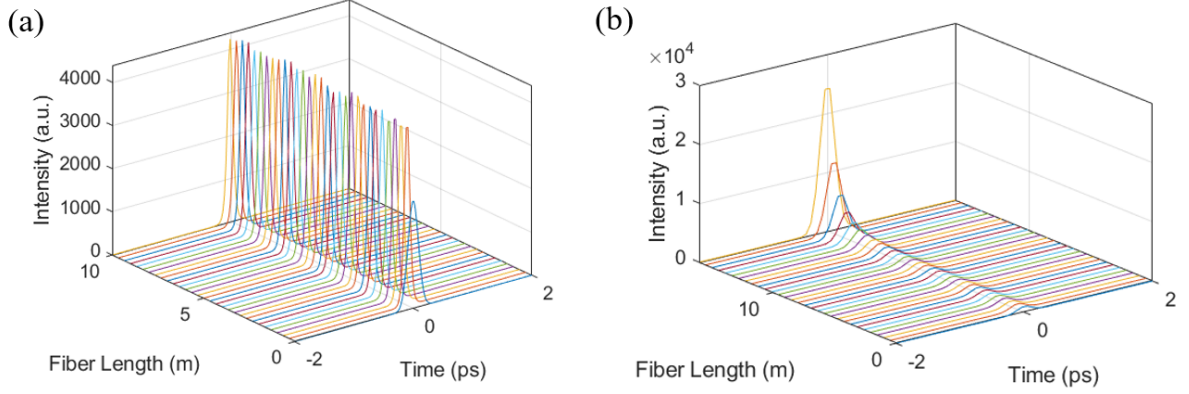


Figure 4.16: Simulation of pulse propagation through the different fibers used in the proposed laser set-up (a) SMF and (b) EDF.

• Ring Fiber Resonator Cavity

Once we have studied how the dispersion and nonlinear effects affect an ultrafast laser pulse while propagating through an optical fiber, a complete ring fiber laser is going to be simulated. In order to reproduce the experimental set-up, the simulation is divided in a EDF+SMF+SESAM+SMF fiber configuration. For simplicity, an initial Gaussian pulse has been assumed to circulate inside the resonator fiber laser cavity.

The fiber configuration is as follows: firstly, a Gaussian optical pulse of 270 fs centered at 1560 nm and with a peak power of 2.5 kW propagates through 16 m of EDF. To simulate the optical gain, it has been applied Eq. (4.10) with a small signal gain coefficient of $g_0 = 1 \cdot 10^3 \text{ km}^{-1}$ and a saturation power of $P_{sat} = 10^5 \text{ W}$. As explained in Eq. (4.19a), the optical gain has been incorporated along the fiber loss coefficient α during the dispersion split-step segment. To reproduce the optical fiber coupler, the pulse is separated into two arms, where 30% of the pulse corresponds to the cavity laser output, whereas 70% is re-circulated inside the resonator. At the output, the optical pulse preserves its Gaussian shape with a pulsewidth of 120 fs and a peak power of $\sim 80 \text{ kW}$ in the case of the 70% port, and 30 kW for the 30% case. The optical pulse enclosed within the laser cavity (70%) is propagated through 12 m of SMF, recovering its initial temporal width due to the dispersion coefficient. Afterwards, the SA absorption effect has been simulated. Despite the reflection configuration of the experimental set-up, the saturable absorption effect has been simulated in transmission for simplification purposes. A normalized linear transmission $T_{lin} = 0.27$ and saturable transmission $T_{ns} = 0.45$ coefficients have been applied along with a modulation depth of 0.18 and a saturation power of $P_{sat}(SA) = 0.3 \text{ W}$. The electric field of the optical pulse when transmitted through the saturable absorber is,

$$E_{SA} = \sqrt{T_{ns} \left(T_{lin} + MD \frac{P_{SMF}}{P_{SMF} + P_{sat}(SA)} \right)} E_{SMF} \quad (4.21)$$

where E_{SMF} and P_{SMF} correspond to the electric field and optical power of the pulse after the propagation through the previous SMF fiber.

The optical power of the pulse is reduced due to the high absorption coefficient of the SA, introducing a fiber loss of 27 dB (including coupling losses). Thus, the 2.5 kW optical pulse propagates through 10 m of SMF, without experiencing any nonlinear effect due to the low optical power, reaching again the EDF fiber. The evolution of the optical pulse in the temporal domain while travelling through each segment of fiber has been plotted in Fig. 4.17.

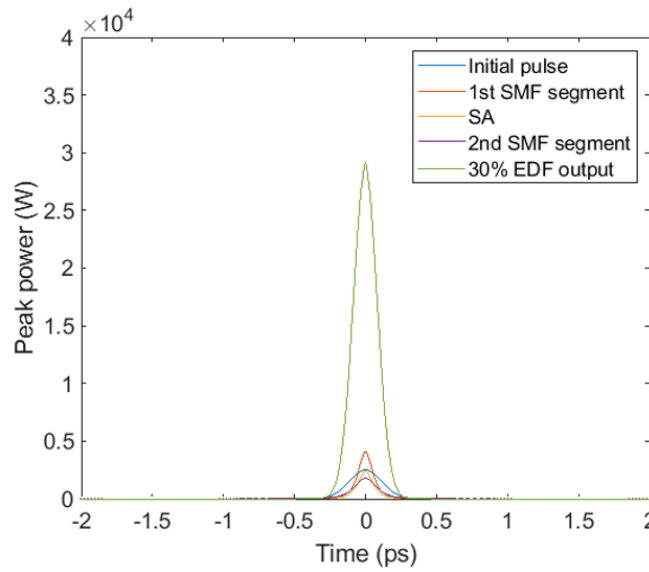


Figure 4.17: Evolution of a 270 fs Gaussian pulse with a peak power of 2.5 kW in a ring fiber laser cavity composed by 16 m of EDF, 12 m of SMF, a passive saturable absorber and a second section of 10 m of SMF.

Nevertheless, it must be noticed that the coupling between different fibers (EDF and SMF principally) is not perfect, hence an optical loss has to be taken into account. A transmission coefficient ratio (fraction of unity) of 0.7 (0.3 of attenuation) between each fiber connection has been incorporated in the MATLAB code. Furthermore, since the SA is located in a free-air configuration, an additional optical loss of 0.3 is inserted before and after the saturable absorption effect.

After the first propagation, multiple roundtrips can be done to study the stability of the simulated solution in terms of peak power and optical pulsewidth. In this sense, to reproduce the cavity roundtrip, a *for-loop* is added to the resonator MATLAB code. For each roundtrip, the optical pulse propagates through the EDF+SMF+SESAM+SMF fiber configuration. The evolution of the optical pulse at the output of the 30% coupler port is depicted in Fig. 4.18(a) for 10 roundtrips. On the other hand, the 70% is sent back to the laser cavity, where the peak power of the output pulse is measured, represented in Fig. 4.18(b) along with its temporal width Fig. 4.18(c).

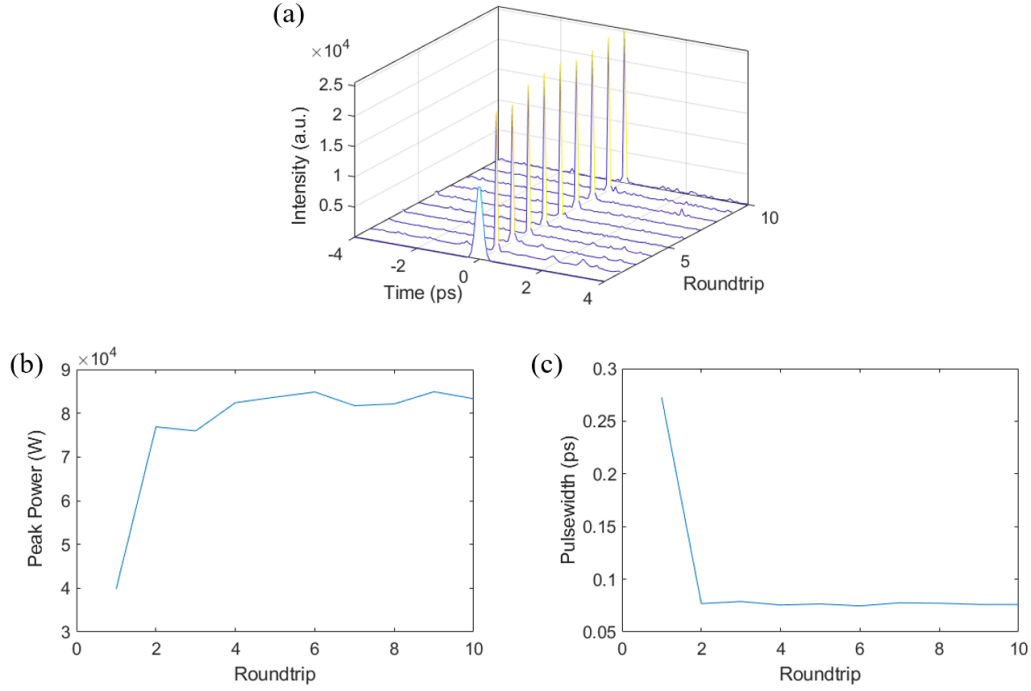


Figure 4.18: Stability of the simulated fiber ring laser cavity: (a) Output pulse (30% coupler port) stability simulation for 10 roundtrips of the laser cavity, (b) Simulation of the stability of the optical pulse inside the laser cavity (70 % coupler port) for 10 roundtrips, (c) Peak power balance in 10 roundtrips for the 70% laser pulse (cavity pulse), and (d) Output laser pulsewidth (30% port) balance in 10 roundtrips.

4.5 Conclusions

In conclusion, an introduction to the fiber laser theory and mode-locked lasers has been presented in this chapter. Furthermore, a complete explanation of the saturable absorber properties applied in passively mode-locked fiber lasers has been discussed. Among semiconductor saturable absorbers, InN materials have demonstrated huge advantages due to their polarization independence, related to their wurtzite structure, the thermal and chemical stability, high-quality crystal lattice when constructed by PAMBE fabrication processes, and its direct bandgap structure, which makes InN a good candidate for applications in the C-band range (emission wavelength centered in $1.5 \mu\text{m}$). Moreover, results on the optical characteristics of an InN sample have been obtained. In this case, a bulk wurtzite $1 \mu\text{m}$ InN layer deposited on a $4 \mu\text{m}$ GaN-on-sapphire layer with a 0.8 eV bandgap has been characterized, demonstrating a huge nonlinear behavior ($\alpha_2 = -3500 \text{ cm/GW}$ and 17% of modulation depth).

This InN semiconductor material has been used as a SESAM in an experimental 38 m ring fiber laser cavity, enabling the self-starting operation mode-locking process and emitting an ultrafast laser pulse centered at 1564 nm with 5.6 MHz repetition rate. The temporal profile can be approximated to a Gaussian shape, with a pulse duration of 268.7 fs , while in the frequency domain a 19.2 nm bandwidth is obtained

(TBP=0.445). The maximum optical power achievable by this resonator cavity is 28 mW of average power, equivalent to a peak power of 24 kW and an energy of 4.5 nJ.

Finally, a simulation of the ring fiber laser cavity has been performed in order to reproduce the experimental values and to evaluate possible improvements. In this sense, a Gaussian 270 fs optical pulse with a peak power of 30 kW centered at 1560 nm is constructed by a MATLAB home-made software. The propagation of the optical pulse within each segment of the ring fiber laser cavity EDF+SMF+SESAM+SMF has been performed by a split-step algorithm, where the peak power and pulsewidth are analyzed at the output of the fiber resonator. Furthermore, the optical pulse's stability for 10 roundtrips has been studied. A good approximation of the experimental values has been obtained, as well as the stability of the optical pulse in terms of peak power and pulsewidth. The simulated optical peak power at the 30% port coincides with the experimental peak power measured at the output of the fiber laser. As mentioned before, a 28 mW average power (24 kW of peak power) has been obtained. By taking into account the optical losses experienced by the optical pulse after propagating through the fiber laser cavity and the attenuation introduced between the fiber end facets (0.3 ratio), the simulated peak power inside the laser cavity corresponds to 52.5 kW, close to the real value (56 kW according to estimations).

Nevertheless, ultrashort pulses generated by these fiber lasers are restricted to a few hundred of kW of peak power and tens of fs as temporal pulse duration, limiting its use in industrial applications. Therefore, as demonstrated by these results, the optical pulse can be enhanced in terms of peak power and temporal pulsewidth by reducing the optical losses within the laser cavity introduced by both the saturable absorber and the laser configuration system. Keeping this idea in mind, in this work we proposed two main improvements for this ring fiber laser cavity: (i) the enhancement of the InN samples by an increase of the crystal quality due to the reduction of the Burstein-Moss effect (carrier concentration), and (ii) the substitution of the SESAM in a free-air configuration by an all-fiber ring resonator cavity, eliminating the insertion losses generated due to the reflections introduced by the optical lenses and its back reflections. These improvements will be explained in the next chapter.

Chapter 5

Optimization of ultrafast InN based fiber laser

Contents

5.1	Improvement of InN semiconductors	77
5.1.1	Introduction of a buffer layer	79
5.1.2	Deposition control	87
5.2	Improvement of the laser system	97
5.2.1	All-fiber configuration	98
5.2.2	High-power ultrafast all-fiber laser	105
5.3	Conclusions	110

In optical radiation sensing, the development of reliable ultrafast fiber laser technology based on passively saturable absorbers presents a very challenging task. In addition, achieving ultrashort emission is even more demanding since, on top of the lack of saturable absorbers with ideal electrical and optical properties, it should be added the need to address high-power reliable laser sources which can be employed in a wide variety of applications. Despite the existence of a wide variety of III-group semiconductor materials as saturable absorbers with high nonlinear properties, other parameters such as temperature resistance, chemical stability, or electrical resistance should be accomplished for the generation of highly-stable high-power ultrafast mode-locked fiber lasers.

With the growing interest in developing semiconductor materials with enhanced crystal structures and optimized fabrication techniques, the monitoring of material deposition is now considered to be fundamental in the pursuit of that goal. The introduction of highly-controlled fabrication mechanisms, along with a careful selection of the structure of the material during the deposition process, has enabled the development of high-quality semiconductor saturable absorbers with the appropriate characteristics (temperature, chemical and electrical resistance, or nonlinear behavior, among others) and thus the improvement of laser sources in relation to the pulsewidth and optical power.

In this chapter, we propose a method to enhance the optical characteristics of the InN-based semiconductor materials employed in this thesis as saturable absorbers in an Er-doped mode-locked fiber laser in terms of their material content structure and better control of their deposition parameters. The core idea of the system is the use of a buffer layer deposited between the InN layer and the GaN-on-sapphire template. The closer lattice constant of this buffer layer, in comparison to the sapphire substrate, implies the fabrication of a higher quality crystal structure due to the reduction of defects on the material surface, as it will be explained in Section 5.1.1. On the other hand, higher control of the fabrication process introduced in Section 5.1.2 translates into a lessening of the carrier concentration, which leads to a higher nonlinear behavior in the saturable absorber material. Then, we extend the demonstration of the improvement of the optical properties of the semiconductor material by testing its characteristics as a saturable absorber in our ring fiber laser resonator cavity in relation to the output peak power and temporal pulsewidth.

Nevertheless, despite the design of the saturable absorber structure, the introduction of this material within the laser cavity is also a challenge for the development of more reliable and efficient ultrafast laser sources. Particularly, saturable absorbers located in open-air configurations have demonstrated high losses, which can be detrimental to the formation of high-power ultrashort pulses. The ongoing race to mitigate these effects has led to all-fiber laser configurations, where several methods have been proposed and attempted. Therefore, in section 5.2 we present the design, proof-of-concept, of the first passive mode-locked all-fiber laser system based on an InN as SESAM, capable of generating sub-100 fs, 70 kW pulses centered in the near-infrared region (1560 nm). We first demonstrate the concept by analyzing the losses introduced by the all-fiber device and comparing them to those obtained by the free-air configuration, described in Chapter 4. Then we extend the demonstration with the incorporation of the enhanced InN semiconductor samples mentioned before, showing the high potential of the fiber laser for high-power ap-

plications. Finally, we demonstrate that this concept can be further explored to achieve ultra-high-power levels (in the order of MW) by the development of long all-fiber laser cavities in section 5.3.

5.1 Improvement of InN semiconductors

The fabrication of high-quality semiconductor materials is not an easy task. Among all III-nitrides, growth technology for InN has been the most challenging due to the lack of lattice-matching substrates and the thermal decomposition of InN of about 470 °C. Its optical properties are adversely affected by these effects, resulting in what are called material defects. As a general rule, a defect is any distortion in an otherwise perfect crystal. During the fabrication process, all crystals present imperfections in some way or another. Defects can be classified depending on their structure and symmetry, which can be categorized into two main groups, point defects, whose imperfection occurs in a specific location within the crystal lattice, or line/area defect, which affects an extended lattice site. Point defects can in turn be classified into intrinsic and extrinsic distortions:

- Intrinsic defects also known as native defects, refer to the presence or absence of certain atoms in the perfect crystal structure. In this sense, these distortions can be summarized in lattice vacancy, which consists of a missing atom in the crystal structure, and the interstitial defect, where an atom is positioned between two lattice sites [157].
- On the other hand, extrinsic defects are related to the introduction of foreign atoms in the crystal, referred to as impurities. For a compound semiconductor, such as in GaN, the sites of the atoms can be swapped, that is the atom of Ga can occupy the site of a N atom or backwards. This effect would change the properties of the material, as it will be explained later.

Nevertheless, point defects can also be agglomerated into clusters, generating extended defects. The most important line defects are dislocations, which consist of the misalignment of a series of atoms from their perfect lattice sites, generally related to thermal and mechanical stress. A particular example of lattice dislocations is grain boundaries, in which two contiguous crystalline areas or grains with different orientations are not well-matched up. Grain boundary defects are of particular importance at the interfaces of different materials, such as between the thin film semiconductor sample and its substrate (with different lattice constants), giving rise to lattice strains. These effects are normally produced during the growth process and are the preferred sites for corrosion and precipitation generation. Nevertheless, these dislocations can be relaxed by expanding the film laterally, creating what is called misfit dislocations. If the dislocation is misplaced on the surface, then it is known as threading dislocation, very common in InN bulk thin films grown on sapphire substrates.

In this work, we will focus on dopants, since they are the predominant defect in bulk InN semiconductor thin films. The semiconductor is said to be intrinsic or undoped (not to be misled by intrinsic or native defects), when its structure

does not present dopant species. On the contrary, a semiconductor is extrinsic or doped when dopant atoms are included. Atomic dopants change the free electron and hole concentration of a semiconductor, either by acting as donors or acceptors. The excess of valence electrons in donor atoms provides an increase in the free electron concentration (charge carrier density represented by the parameter n_0) of the intrinsic semiconductor, leading to a n-type semiconductor material. Whereas, a p-type semiconductor is generated due to the absorption of electrons by the acceptor atom from the intrinsic semiconductor valence band, producing an increase of the free hole carrier concentration p_0 . Thus, the energy position of the Fermi level of an extrinsic semiconductor can be varied depending on the excess of electron or hole concentration. In the case of n-doped semiconductors, the Fermi level is closer to the conduction band, while in p-type materials, the Fermi level is below the intrinsic semiconductor level, getting closer to the valence band. The doping concentration may vary between 10^{13} cm^{-3} to 10^{18} cm^{-3} in most semiconductors depending on the growth parameters such as temperature, dopant species, and growth rate, among others, during the fabrication procedure. Therefore, these parameters can be tailored to generate the desired properties of the semiconductor and thus the perfect device for any specific application.

However, if the concentration of dopants is high enough, generally with a carrier concentration above 10^{18} cm^{-3} , the doped semiconductor acts more like a conductor material, generating what is called a degenerate semiconductor. Thus, when the concentration of electrons is higher than the conduction band edge density of states, then the Fermi level is pushed inside the conduction band and thus changing the energy band structure of the semiconductor material. This effect, known as Burstein-Moss, generates an apparent shift in the energy bandgap, which can be represented with the equation $E_g + \Delta E$, where E_g is the intrinsic bandgap energy and ΔE corresponds to the Burstein-Moss shift. This implies an increase in the apparent bandgap energy of the semiconductor, which can be measured by transmission measurements (see Chapter 4). An example of the Burstein-Moss effect occurs in InN semiconductor materials due to the addition of oxygen and hydrogen dopants within the interlayers or nitrogen vacancies generated during the fabrication process [158]. In this sense, a bandgap energy between 0.7 eV to 1.9 eV has been measured, corresponding to a carrier concentration that goes from 10^{17} cm^{-3} for high-quality InN crystals grown by PAMBE techniques to up to 10^{21} cm^{-3} , more common in InN films grown by sputtering deposition. Therefore, as the carrier concentration increases inside the semiconductor material, a stronger Burstein-Moss shift is produced.

It has become increasingly apparent that understanding defects at a fundamental level is essential for the development of efficient, high-quality, and reliable optoelectronic devices. An example of this is to improve the efficiency of light-emitting diodes and solar cells, particularly in those based on novel materials, where III-nitrides continue to be a target for a great deal of researchers. A deeper understanding of point and line defects at an atomic level has been accomplished by combining advances in thin-film growth, microscopy, spectroscopy, and computational modeling. This significant increase in knowledge is enabling engineers to develop new functionalities for semiconductors, leading to higher crystal qualities, and better electrical and optical properties such as chemical stability, temperature resistance, and electrical

carrier mobility. In the next sections, a full study of the improvement of the material properties will be carried out in order to obtain high-quality InN semiconductors, as well as the effect of these improvements on laser performance when applied as saturable absorbers.

5.1.1 Introduction of a buffer layer

In the past decades, nitride semiconductors of group III (GaN, AlN and InN) have attracted considerable attention, as they may be considered among the most important high-tech materials for electronic and optoelectronic devices due to their use in a wide variety of applications such as lasers, sensors, solar cells or terahertz emitters. Among them, InN has demonstrated outstanding electrical properties, including high electron mobility ($12 \cdot 10^3 \text{ cm}^2/\text{Vs}$), large saturation velocities (10^8 cm/s), and small effective mass, essential characteristics in high-speed electronic devices. Besides, InN semiconductor materials possess a low growth/synthesis temperature, which along with its narrow bandgap energy of 0.7 eV is compatible with the development of near-infrared light sources. However, in comparison to other III-group semiconductors (such as GaN), the doping effect is an essential factor in InN, where these parameters can be limited by high residual electron concentrations within the non-intentionally doped material, as well as the carrier accumulation in the layer surface.

The lack of suitable substrates fundamentally limits the ability to produce intrinsic InN epilayers. Common substrates, including Si, GaN, SiC, and sapphire, have a very large lattice constant mismatch compared to InN, which ranges from 7, 11, 14, and 27%, respectively [159]. Large lattice mismatches result in large amounts of defects. These defects act as donors, resulting in high background electron concentrations, which, in turn, reduces the carrier mobility of the material. Furthermore, several factors affect the carrier mobility of a semiconductor, including temperature, electric field, doping concentration, and even the material quality of the semiconductor. However, major progress has been made in addressing these challenges in recent years. By using a buffer layer during nucleation, the strain is reduced, which improves carrier mobility.

In our case, InN epitaxial layers grown on sapphire substrates demonstrate high quality when they are grown by MBE at a relatively low cost. Nevertheless, due to the large lattice mismatch between InN and sapphire materials, an intermediate buffer layer should be introduced in order to reduce the density of structural defects and thus improve the film quality. In this sense, by including an AlN or GaN buffer layer to the substrate surface it has been demonstrated the improvement of the electrical and structural properties.

In order to demonstrate the improvement of the electrical and optical properties of the InN semiconductor, an InN-based buffer layer is introduced between the InN layer and the GaN-on-sapphire substrate during the fabrication process (sample S0'). A second InN semiconductor without the buffer layer is also presented (sample S0) for comparison purposes. The fabrication of both samples has been performed under similar conditions. The semiconductor material consists of an InN thin film with a thickness of $1\text{-}\mu\text{m}$ deposited on a $4\text{-}\mu\text{m}$ GaN-on-sapphire layer by the PAMBE technique at a 450°C temperature and at a nitrogen growth rate of 280 nm/h . In

relation to sample S0', the InN buffer layer consists of a heterostructure constituted by 11 periods of InN/In_{0.7}GaN_{0.3} with a width of 4.5 nm and 7 nm respectively, as shown in Fig. 5.1(a), obtained by the dark-field transmission electron microscopy (TEM) technique. A figure of the surface morphology of each sample by atomic force microscopy (AFM) in a region of 1 μm x 2 μm is represented in Fig. 5.1 (b) and (c). In the case of sample S0, that is, without the buffer layer, the semiconductor presents visible pits on its surface which constitute the surface terminations of extended defects with a pyramid inverted structure mostly created by threading dislocations and with a density of $2 \cdot 10^8 \text{ cm}^{-2}$. Whereas for the InN sample with the buffer layer (sample S0'), a smooth surface with atomic terraces is observed, with a root-mean-square roughness which has been reduced from 2 nm in the case of S0 to 0.5 nm for sample S0'. These results demonstrate a reduction of the defect density and thus an improvement of the structural quality.

After the characterization of the morphology of the samples, a complete study of the optical properties of the semiconductors has been carried out.

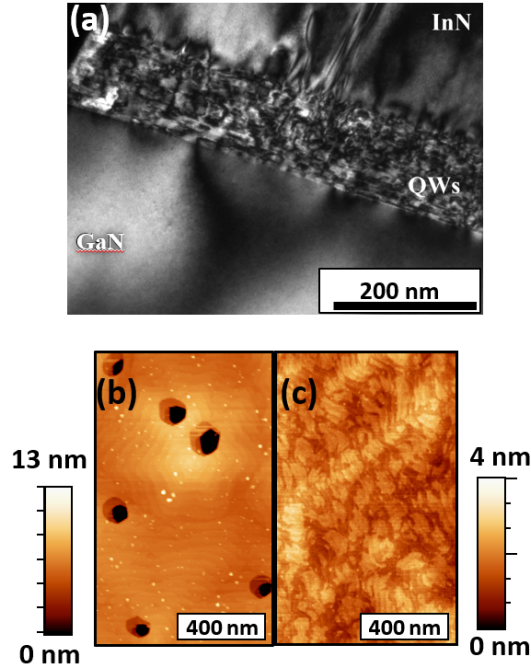


Figure 5.1: Structural morphology of InN layers, (a) TEM image of the InN layer (bright area) deposited on an InN/InGaN heterostructure (dark area), and AFM figures of surface structure for samples (b) S0 without GaN buffer layer, and (c) S0' with the GaN-on-sapphire buffer layer [160].

• Optical Characterization

– Linear transmission:

As explained in Chapter 4, the optical transmittance spectrum as a function of the incident wavelength $T(\lambda)$ of the InN samples has been measured by an optical spectrum analyzer (OSA) using a white lamp as the radiation source as shown in the inset of Fig. 5.2. From this figure, a redshift of the linear transmission of the InN sample with the buffer

layer (sample S0') compared to the semiconductor without the InN/In-GaN buffer layer (S0) is observed. From this measurement, the linear absorption coefficient has been calculated by employing the equation $\alpha = -\ln[T(\lambda)]/l$ (neglecting the reflection losses), where l is the layer thickness ($1 \mu\text{m}$ in this case), and $T(\lambda)$ the linear transmittance at $1.55 \mu\text{m}$, which corresponds to 23% for sample S0 and 9% for S0', respectively. Thus, a higher linear absorption coefficient at $1.55 \mu\text{m}$ operation wavelength is obtained, where sample S0 demonstrates $\alpha_0 = 1.4 \cdot 10^4 \text{cm}^{-1}$, whereas the absorption of S0' is $\alpha_0 = 2 \cdot 10^4 \text{cm}^{-1}$.

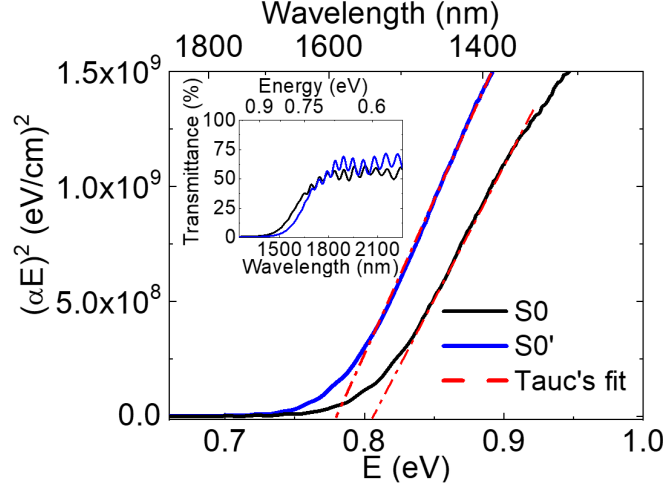


Figure 5.2: Representation of the bandgap energy measurement by the Tauc's fit calculation of the InN sample without the buffer layer (S0) and with the GaN template (S0'). The linear transmittance of the InN samples as a function of the incident wavelength is represented at the inset, where the black thick line represents sample S0 whereas the blue line constitutes sample S0' [160].

Furthermore, a Tauc's plot has been performed where the linear absorption for each InN sample is represented as a function of the incident energy (E). The value of the exponent of the $(\alpha E)^2$ term is related to the nature of the electronic transition of the material, which in this case denotes the direct bandgap energy structure of InN materials. The optical bandgap or the absorption edge energy can be determined by extrapolating the linear fit of the squared absorption curves towards the energy baseline, denoted by dashed red lines in Fig. 5.2. In this sense, a bandgap value of $E_g \sim 0.8 \text{eV}$ and $\sim 0.77 \text{eV}$ has been estimated for samples S0 and S0' respectively. The relation between the energy bandgap and the carrier concentration by the curve obtained by J. Wu *et al.* in [143], gives an estimation of 10^{19}cm^{-3} for sample S0, and $4 \cdot 10^{18} \text{cm}^{-3}$ for sample S0'. This decrease in the carrier concentration of the InN material with the buffer layer is explained due to the reduction of the defect density within the semiconductor.

– Nonlinear transmission:

The nonlinear transmission measurements were performed by the Z-scan technique, as explained in Chapter 4. In this sense, a 250 fs laser source with a repetition rate of 5 MHz defined by a maximum peak power of 40

kW has been employed in order to stimulate the samples and to study their nonlinear behavior. The InN samples are located in a free-air translation stage, remotely controlled by a Labview program. A 3-cm optical lens has been used to increase the incident intensity on the sample surface. Furthermore, a collimator lens collects the output signal after the transmission through the semiconductor sample and measured by a Ge-photodetector (Thorlabs, SM05PD6A).

The nonlinear behavior of the InN samples has been studied in two steps (i) by measuring the nonlinear transmission response of the material while varying the z-position of the sample with respect to the focal point of the optical lens (Z-scan technique) as represented in Fig. 5.3. This procedure allows us to obtain an estimation of the nonlinear absorption coefficient α_2 for each sample following the expression described in Eq. (4.15). In the case of sample S0, the nonlinear absorption coefficient is $\alpha_2 = -3.5 \cdot 10^3$ cm/GW, while S0' demonstrates an α_2 coefficient of $\alpha_2 = -13.5 \cdot 10^3$ cm/GW, extracted from the measurements of nonlinear transmission of Fig. 5.4 (a).

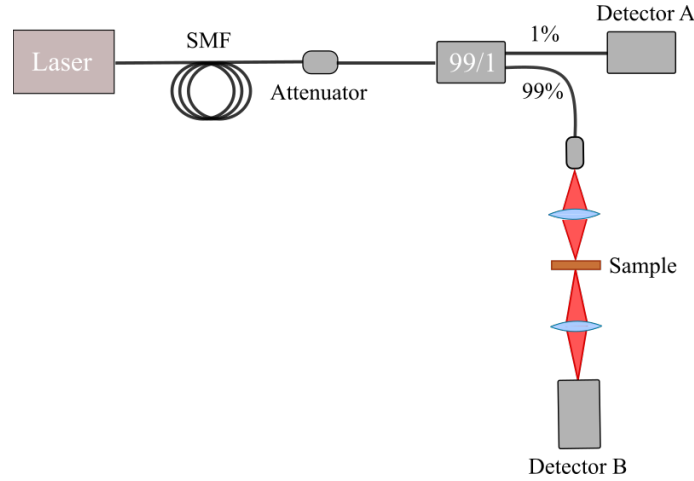


Figure 5.3: Schematic representation of the experimental Z-scan technique: the 1% of the output fiber laser pulse is characterized by photodetector A, whereas the 99% of the output power is sent to a free-air focusing set-up in order to characterize the transmission of the InN semiconductors S0 and S0' [153].

(ii) Next, the optical intensity of the incident pulse impinging the material sample at the focus is varied from 0 to the maximum optical power of 40 kW provided by the laser source in order to obtain the saturable absorber main characteristics, i.e., saturable and non-saturable transmittance (T_{lin} and T_{ns} respectively), the modulation depth (MD), defined as $MD = T_{ns} - T_{lin}$ and the saturation fluence (F_{sat}). The transmission of the InN samples S0 and S0' as a function of the optical fluence is represented in Fig. 5.4 (b). The SA parameters are estimated following the equation defined in Eq. (4.16). In this sense, the transmission results of the sample without the buffer layer (S0) are the ones above described in Chapter 4, where a linear transmission of 28% and a non-saturable transmittance of 45% is obtained compared to the 13% and 40% of the sample with the InN/InGaN MQW buffer (S0'). Thus, the MD is estimated in

17% for S0 and 27% for S0'. Accordingly, the change of the modulation depth parameter can be explained by the drastic reduction of the linear transmission in the sample with the buffer layer, which translates into an increase in material efficiency. In relation to the saturation fluence, a value of $900 \mu\text{J}/\text{cm}^2$ is obtained for sample S0, whereas S0' demonstrated a slightly higher saturation fluence of $1015 \mu\text{J}/\text{cm}^2$ as it can be appreciated in Fig. 5.4 (b). These properties make sample S0' an ideal candidate for implementation as saturable absorbers in ultrafast laser sources.

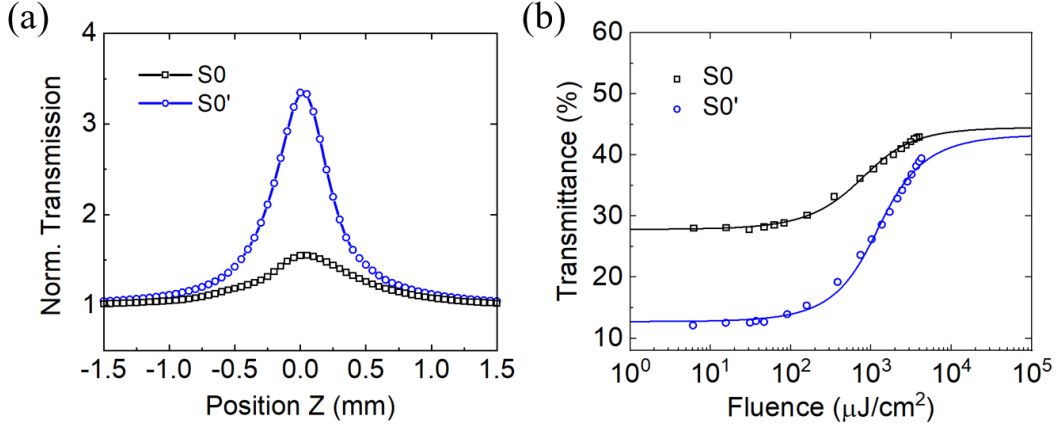


Figure 5.4: Nonlinear transmittance of the InN semiconductor without the buffer layer S0 represented with black squares, and the InN sample S0' in blue circles in relation to the focal distance by the Z-scan technique (a), and as a function of the incident fluence when centered at the focal point (b). The nonlinear transmission fit curve has also been plotted as a solid line for both samples [160].

• Laser performance

In this way, samples S0 and S0' were placed within a fiber ring laser cavity to test their performance as a saturable absorber. The resonator cavity components are the same as those described in Chapter 4. The ring laser consists of 40 m of optical fiber formed by a commercial EDFA system (Accelink, TV Series) which is employed as the amplification device with a maximum gain of 24 dBm. Furthermore, the backward optical power of the light inside the resonator is controlled by an isolator device after its transmission through the saturable absorber, placed in a free space region. The rest of the resonator cavity is based on SMF, constituted by a fiber optical coupler of 70/30, where 70 % of the radiation is recirculated, whereas the 30 % is launched out of the ring resonator as the ultrafast laser source. As described in previous chapters, the resonator (indicated in Fig. 5.5 with blue dashed lines) consists of a dispersion-managed cavity with a net dispersion coefficient of -0.26 ps^2 (corresponding to a SMF dispersion of -0.52 ps^2 for a 25 m-length, and 0.26 ps^2 for the 16 m of EDF), thus operating in the anomalous dispersion regime. In relation to the SA, the intensity of incident light is increased onto the surface of the material by the use of two 3-cm focal achromatic lenses. The emitted light is collected with a collimator and launched with a microscope objective (see Fig. 5.5).

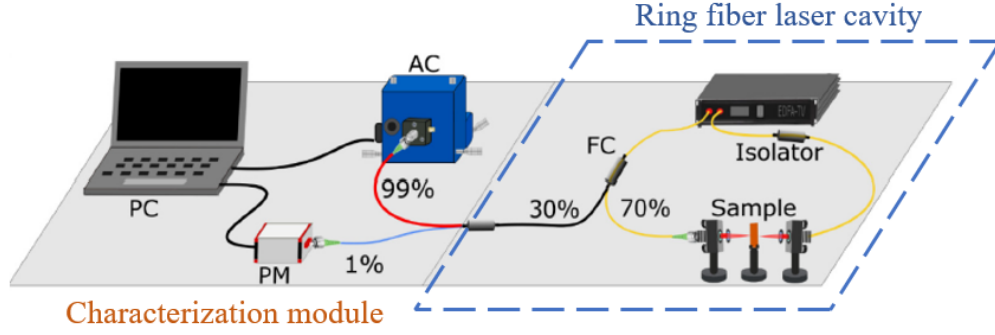


Figure 5.5: Experimental laser set-up for the characterization of the InN semiconductor with the GaN-on-sapphire substrate: a ring fiber resonator of 40 m constituted by SMF and an EDFA system generates an ultrafast pulse measured at the 30% output port and characterized by an AC, OSA and power-meter devices [160].

An additional optical fiber coupler with a ratio of 99/1 has been incorporated at the 30% laser output to monitor not only the main properties of the resonator cavity, such as repetition rate and average power, but also to characterize the ultrafast laser pulse in terms of temporal duration and its optical spectrum as shown in Fig. 5.5. In this sense, an electrical spectrum analyzer (Agilent Technologies, model N9010A) has been connected to the 1% port, measuring a 5.25 MHz repetition rate. So, the repetition rate of the experimental laser set-up coincides with the value predicted by the cavity length measurement. It can also be confirmed the absence of higher-order harmonic generation, as shown in Fig. 5.6. Furthermore, a signal-to-noise ratio (SNR) of 45 dB has been observed during the ESA measurement due to the maximum dynamic range available of the balanced detector (PDB410CAC, Thorlabs). The laser demonstrates high-quality and good stability.

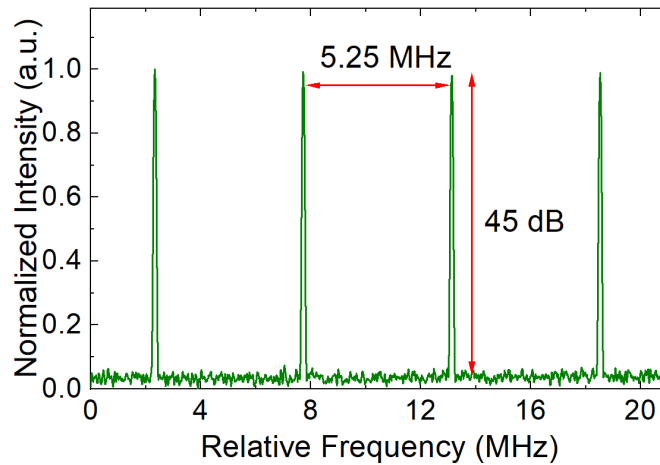


Figure 5.6: Electrical spectrum of the output laser with the InN layer grown on a GaN buffer template as saturable absorber, displaying a 5.25 MHz repetition rate with 45 dB of SNR [160].

Additionally, the optical spectrum and temporal width of the output laser have been studied by a Yokogawa AQ-6315B and an autocorrelator APE Mini

Accelink (AC in Fig. 5.5), respectively. The laser properties are therefore analyzed in terms of the power inside the resonator, i.e., the variation of the energy applied to the SA by an InGaAs-based power meter (Thorlabs, PM100USB), represented in Fig. 5.5 as PM. In order to compare these results, both samples S0 and S0' have been investigated.

- In the case of the InN sample with the buffer layer of GaN-on-sapphire substrate (S0'), a mode-locking operation mode has been accomplished for the laser set-up described in Fig. 5.5. A maximum average power of 30.6 mW is obtained at maximum pump power of the EDFA system. With respect to the optical spectrum and pulse duration, a spectral width of 21.8 nm and a pulsewidth of 220 fs is obtained from the OSA and AC experimental traces, as represented in Fig. 5.7(a) and (b). At maximum average power, the optical pulse presents a peak power of 26.5 kW, corresponding to an optical energy of 5.8 nJ. Moreover, the calculated TBP value shown in Fig. 5.7(c), is 0.407 at maximum power, which implies that the optical pulse is somewhat chirped.

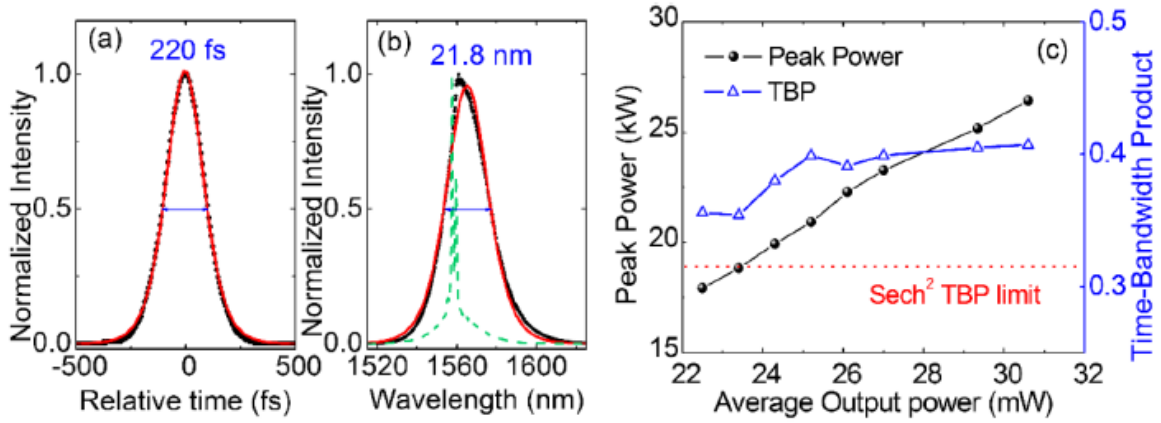


Figure 5.7: Output laser pulse characterization of the InN/InGaN SA at a maximum $P_{av} = 30.6$ mW using a 70/30 OC in the laser set-up by the measurement of the (a) AC trace showing a temporal pulse duration of 220 fs, and (b) the spectrum obtaining a value of 21.8 nm. The green dashed line represents the optical spectrum of sample S0 demonstrating its incapacity to reach the mode-locking operation using the same laser set-up. The red solid line in both figures symbolizes the sech² fit of the pulse profile. An analysis of the variation of the output peak power and TBP value has been represented in (c) in terms of the average power inside the resonator [160].

- On the other hand, the saturable absorber without the buffer layer (S0) does not demonstrate mode-locking operation when performed with the laser set-up of Fig. 5.5. The InN SA shown in Fig. 5.7(b) only reached the transition stage where both mode-locking and CW are present. The mode-locking regime was only possible to obtain if the 70/30 optical fiber coupler of the laser set-up was substituted by a 90/10 fiber coupler. At the maximum average power of 10.3 mW, the SA demonstrates a spectral width of 17.1 nm and a temporal pulsewidth of 250 fs [145]. Therefore,

the TBP value is 0.363, demonstrating a slightly chirped output pulse compared to the transform-limited situation (0.315). These values imply that the maximum peak power and optical energy available for this type of SA and laser configuration, correspond to 7.95 kW and 2 nJ respectively.

It must be noted that a maximum average power of 30.6 mW at the output of the laser system implies an optical power inside the cavity above 70 mW, corresponding to a maximum fluence of 9 mJ/cm² onto the InN thin film. Nevertheless, the SA has not exhibited any optical damage, demonstrating that the InN semiconductor material would be appropriate for high-power applications, usually employed in electrical devices operating at 1.55 μ m. A complete description of the optical parameters for each sample has been collected in Table 5.1.

Sample	α_2 (cm/GW)	F_{sat} (μ J/cm ²)	P_{peak} (kW)	τ (fs)
S0 (90/10)	$-3.5 \cdot 10^3$	900	7.95	250
S0' (70/30)	$-13.5 \cdot 10^3$	1015	26.5	220

Table 5.1: Experimental values of the optical properties of the InN semiconductor samples S0 and S0' when applied as saturable absorbers in a transmission fiber laser configuration system. The 90/10 and 70/30 refer to the fiber coupler used to obtain the mode-locking operation for each sample.

• Discussion of experimental results

In this study, due to the introduction of a change in the material structure, in this case, an implementation of an intermediate layer connected to the InN material and the GaN substrate, it has been achieved a lessening of the residual doping and thus, the associated Burstein-Moss effect. The reduction of the defect density by the decrease of dopant inside the crystal lattice, has enabled the generation of a high-quality InN sample with a superior morphology and surface quality during the fabrication process. As a consequence of this fact, the optical properties of the saturable absorber have been largely improved with respect to the latest results [142], such as a higher nonlinear absorption parameter and higher nonlinear response (increase in the modulation depth).

Furthermore, this new structure has enabled the improvement of an ultrafast fiber laser source. Not only the temporal duration of the output optical pulse has been reduced, but also it has allowed getting more energetic pulses due to the higher nonlinear transmission change of the sample, as explained by H. A. Haus [102]. Also, a higher absorption coefficient in the linear regime has been measured, leading to higher optical peak powers. In sample S0' the peak power and pulse energy is three times greater than the ones obtained in sample S0. An explanation for this can be found in the fact that the residual doping effect of the InN/GaN layers decreases during its growth process.

The incapacity of sample S0 to generate mode-locking operation with this laser set-up can be explained due to its lower linear absorption coefficient compared to sample S0'. On the contrary, sample S0' has a larger absorption parameter which compels the saturable absorber to operate in the nonlinear regime under

the effect of high peak powers inside the laser resonator cavity while hindering the propagation of the CW mode, thus starting the mode-locking operation regime. These results make sample S0' a better candidate for ultrafast laser generation in the C-band window.

In comparison to other semiconductor materials, such as InGaAs or graphene which show ultra-broadband absorption properties, InN samples demonstrate broader bandwidth operation and higher modulation depth. In recent years, 2D-materials have been developed, including carbon nanotubes with high non-saturable losses and controllable bandwidth depending on the size of the nanotube, topological insulators, with a broadband saturable absorption coefficient except for its lower modulation depth, black phosphorus whose bandgap can be modulated but limited in terms of modulation depth and polarization effects, and transition metal dichalcogenides which are restricted to the 1-2 eV bandgap energy operation. However, these materials also have a low damage threshold level, commonly under the value of 2 mJ/cm^2 , limiting the maximum power emitted by the laser system based on these semiconductors and giving InN samples a great advantage when applied in high energy industrial applications. Additionally, fiber lasers using a saturable absorber based on InN do not require any polarization-controlling element within the resonator cavity, due to the polarization independence property of the semiconductor samples. As compared with fiber lasers which use nonlinear polarization rotators, or other semiconductor-based saturable absorbers, this feature makes InN clearly superior.

In conclusion, we demonstrate an improvement in the saturable absorber's properties of the semiconductor samples due to the InN saturable absorber's performance variation in terms of its residual doping concentration. This reduction has not only permitted obtaining a larger nonlinear transmission change at $1.55 \mu\text{m}$ and a higher modulation depth of 30%, but also has demonstrated ultrashort laser behavior when inserted in a fiber laser resonator cavity for mode-locked operation. In this sense, the peak power and pulse energy grew by a 3-fold improvement compared to previous results, with an ultrafast pulse of 220 fs with a 26.5 kW of peak power and a high energy of 5.8 nJ.

Nevertheless, as it was mentioned before, in this thesis we have also improved the laser performance of these samples by better controlling the carrier concentration during the deposition process, as it will be explained in the following section.

5.1.2 Deposition control

Among the materials employed as saturable absorbers, semiconductor elements demonstrate a small saturation intensity as well as a moderate modulation depth, which makes them an appropriate SA for commercial optical lasers. Nevertheless, these materials also have a narrow working bandwidth and a low damage threshold level, limiting their use for some industrial applications. Furthermore, structural defects such as vacancies, grain boundaries, and impurities are commonly present in semiconductor SAs, deteriorating their crystal quality. As a result, improving crystal quality can be an advantageous step toward enhancing the optical properties of

the crystal, such as the absorption band, modulation depth, or saturation intensity. Since the crystal structure of the saturable absorber is critical to the implementation of high-power ultrafast pulsed lasers, the main material defects created during the deposition process should be addressed by new fabrication processes.

Indium nitride (InN) has shown outstanding advantages over other semiconductor SAs because of the bandgap energy range (0.65–0.9 eV) and the ability to extend emission wavelengths from the infrared to the ultraviolet region when alloyed with AlN or GaN. Nevertheless, these materials can be easily n-doped during the fabrication process due to the presence of common impurities such as oxygen or hydrogen atoms. The background electron concentration can be reduced from 10^{20} cm^{-3} (usual value of highly doped InN semiconductors) to 10^{17} cm^{-3} for planar structures (or 10^{13} cm^{-3} in the case of nanowires) by the improvement of the epitaxial growth process by the PAMBE mechanism. Consequently, at room temperature, the absorption edge energy falls to 0.7 eV, where the operation wavelength is extended into the infrared region.

Therefore, we report an enhancement of the crystal quality of the InN layers which implies a reduction of the free carrier concentration during the fabrication process. Better control of the material deposition method leads to an improvement of the saturable absorber's properties of the InN material, such as a higher nonlinear optical response and a higher absorption behavior. Afterward, we study the effect of this improvement on the performance of the InN semiconductor as a saturable absorber. This section reflects the results of the work published in [153].

Firstly, we will characterize the material structure of the InN semiconductors employed in this section. The fabrication of the InN epitaxial layers was performed by the PAMBE technique and deposited on a GaN-on-sapphire substrate. Compared to previous fabrication parameters, a 450°C growth temperature and a 290 nm/h nitrogen growth rate have been fixed for this case. To prevent the accumulation of In droplets on the surface of the sample, the indium flux was interrupted every 10 minutes during the growth deposition, thereby consuming any excess of In. There are two samples in our study, each of which has a different thickness of InN: sample S1 and sample S2, with respective InN thicknesses of 360 nm and 780 nm. The substrate template has a common structure in both samples, made up of GaN-on-sapphire with a thickness of 4 μm /350 μm . Any buffer layer has been incorporated during the fabrication process, as opposed to former studies. Therefore, in order to evaluate the variation of the saturable absorber's properties of the newly InN samples, the aforesaid 1 μm -thick InN samples S0 and S0' have been incorporated here for evaluation. The growth rate of the reference samples is set to 280 nm/h with In growth interruptions every 5 minutes under nitrogen deposition, demonstrating a higher residual doping concentration as it will be explained later on. Therefore, a reduction of the defect density is expected, leading to an enhancement of the structural quality and crystal morphology (smooth surface with fewer threading dislocations).

Once the morphology of the samples is characterized, the optical properties of the newly semiconductors are investigated. We will follow the same structure as in the previous section: the semiconductor transmission behavior is first studied in both the linear and nonlinear regimes. Afterwards, the evaluation of the InN

samples as saturable absorbers in a mode-locked ring fiber laser cavity is studied. These results are discussed in a final section and compared to the prior InN-based S0 and S0' structures.

- Optical Characterization

- Linear transmission results

The linear transmission of the samples under study is analyzed by a white lamp emitting in a spectral bandwidth from 500 nm to 2500 nm as represented at the inset of Fig. 5.8. At 1560 nm (operation wavelength of the optical fiber laser), the linear transmission has been measured to be of 16% for sample S1 and 3% for sample S2, compared to the 23% and 9% of reference samples S0 and S0'. In this case, sample S2 demonstrates a redshift of the bandgap energy, which can be explained by the variation of its fabrication parameters. Nevertheless, sample S1, although showing the same tendency as sample S2 for wavelengths greater than 1750 nm, a slow transmission growth behavior can be observed for incident wavelengths ranging from 500 nm to 1500 nm, in contrast with previous semiconductors S0 and S0' which have an abrupt increase of transmission in the 1500 nm wavelength region. This difference may be explained due to the thinner InN layer of sample S1.

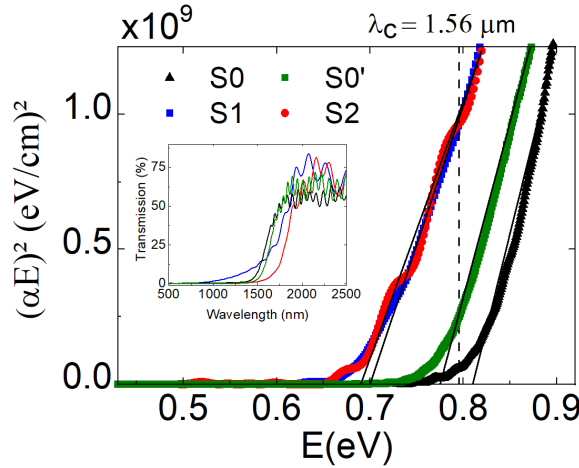


Figure 5.8: Bandgap energy calculation by the Tauc's plot in direct electronic transitions for the reference samples S0 and S0', represented with a black line and green line, respectively, compared to S1 (blue line), and S2 (red line). the operation wavelength of the laser is indicated by a vertical dashed line. The transmission of each sample as a function of the incident wavelength is shown at the inset [153].

The linear absorption coefficient of the samples can be calculated by taking into account the transmission measurements at 1560 nm and its InN layer thickness as explained in Chapter 4. For the case of the newly samples, the linear absorption has been estimated in $\alpha_0 = 4 \cdot 10^4 \text{ cm}^{-1}$ either for S1 and S2, compared to the $\alpha_0 = 1.4 \cdot 10^4 \text{ cm}^{-1}$ and $\alpha_0 = 2 \cdot 10^4 \text{ cm}^{-1}$ for S0 and S0' respectively. This change in the saturable absorption can be explained by the redshift of the bandgap which has been enhanced by a better control of the fabrication conditions.

The linear absorption of the material samples has been represented in relation to the energy of the incident light in Fig. 5.8. The bandgap energy estimation is performed by the Tauc's plot, i.e., extrapolation of the linear part of the absorption curves by the energy baseline, represented with a black line in Fig. 5.8. The bandgap energies are calculated as 0.69 eV and 0.67 eV for samples S1 and S2, in comparison to the 0.8 eV of sample S0 and 0.77 eV for the case of S0'. S1 and S2 show a lower bandgap energy, indicating reduced Burstein–Moss effects. Moreover, the growth conditions related to N deposition intervals were better controlled, leading to a reduction of the free carrier concentration, estimated from the energy bandgap calculated in [143]. A carrier concentration of $<10^{18} \text{ cm}^{-3}$ has been estimated for samples S1 and S2 in comparison with the $4\text{--}5 \times 10^{18} \text{ cm}^{-3}$ for sample S0' and over 10^{19} cm^{-3} for S0. This decrease of the carrier concentration also implies the improvement of the crystal quality.

– Nonlinear transmission results

(i) In order to measure the nonlinear transmission of the InN samples, the open-aperture Z-scan technique is used. A 40 kW ultrafast mode-locked fiber laser with a temporal width of 250 fs operating at 1560 nm excites the semiconductors which are located in a free-air translation stage as shown in Fig. 5.3. The incident light is focused on the semiconductor surface by a 3-cm optical lens, demonstrating a maximum energy fluence of 7 mJ/cm^2 obtained from a beam waist of $8.5 \mu\text{m}$ and a Rayleigh distance of $223.2 \mu\text{m}$, characterized by the knife-edge technique as explained in Chapter 4. To control possible fiber laser oscillations, the reference optical output power of the fiber laser is measured by a powermeter (Detector A, Thorlabs PM100USB) while the transmitted light is measured by a Ge photodetector (Detector B, Thorlabs SM05PD6A).

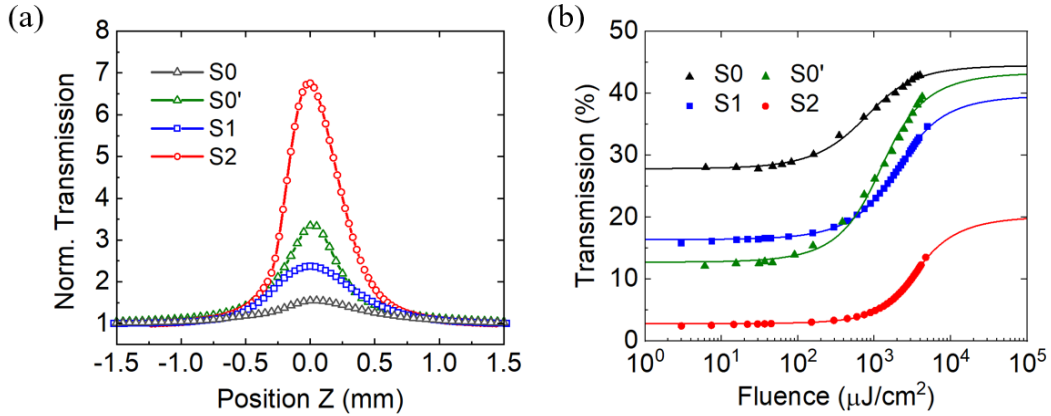


Figure 5.9: Nonlinear transmission measurement of the InN semiconductor reference samples S0 and S0', (represented in black dots and green dots respectively), S1 (blue dots) and S2 (red dots), (a) in terms of the focal distance at maximum fluence, and (b) by varying the incident pulse fluence at 1560 nm [153].

The nonlinear transmission of each InN as a function of the sample position z is shown in Fig. 5.9(a). For the case of maximum incident power (40 kW implies a fluence of 7 mJ/cm^2 in the material surface), the maximum nonlinear change ΔT , calculated as the ratio between the nonlinear

and linear transmission of the material sample, $(T_{ns}/T_{lin}) \cdot 100(\%)$, has been measured in 241% for sample S1 and 715% for S2, which implies a 5-fold improvement with respect to previous results for S0 respectively as depicted in Fig. 5.9(a). The reduced transmission change of sample S1 compared to previous reference samples, can be explained by the smaller InN layer thickness and the higher linear transmission coefficient measured at 1560 nm.

(ii) Furthermore, an estimation of the intensity-dependent nonlinear absorption coefficient α_2 for each sample at the maximum light intensity regime (focal position of the semiconductor sample in the Z-scan configuration) can be performed by fitting these curves to the equation described in Eq. (4.15). The nonlinear saturable absorption coefficients for samples S0, S0', S1 and S2, obtained by this procedure are $\alpha_2 = -3.5 \cdot 10^3$, $\alpha_2 = -13.5 \cdot 10^3$, $\alpha_2 = -3 \cdot 10^4$ and $\alpha_2 = -2.7 \cdot 10^4$ cm/GW respectively. A higher nonlinear absorption response was obtained for samples S1 and S2 compared to reference samples S0 and S0'. This implies a relation between the nonlinear absorption (α_2) and the difference between the excitation wavelength and the bandgap energy.

(iii) Once the nonlinear transmission as a function of the z position is characterized, we will focus on the variation of the maximum nonlinear transmission value (at focal point) with the fluence of the impinging optical pulse, plotted in Fig. 5.9(b). These nonlinear transmission coefficients are listed in Table 5.2.

Sample	F_{sat} ($\mu\text{J}/\text{cm}^2$)	T_{lin} (%)	T_{ns} (%)	ΔT (%)
S0	357.2	27.8	44.5	160
S0'	383.8	12.7	43.3	340
S1	756.6	16.4	39.6	241
S2	831.5	2.81	20.1	715

Table 5.2: Comparison of the nonlinear optical parameters of the different InN semiconductor samples obtained from the experimental fitting of the intensity-dependent nonlinear transmission measurements.

In the case of maximum incident fluence, the linear transmission coefficient is estimated in 16.4% for S1 and 2.8% for sample S2 compared to the 27.8% and 12.7% of samples S0 and S0' respectively. Whereas the non-saturable transmittance has been measured to be of 39.6% and 20.1% for samples S1 and S2 respectively, in comparison to the 44.5% and 43.3% of samples S0 and S0'. These results imply that the modulation depth, is set to 23% for S1 and 17% for S2, while S0 and S0' have modulation depths of 17% and 30% respectively. In relation to the optical fluence, samples S1 and S2 demonstrate to have a higher saturation fluence.

- **Laser performance**

To test their performance as saturable absorbers, samples S0', S1 and S2 were placed within a fiber ring laser cavity in reflection configuration. The optical resonator proposed here consists of a mode-locked fiber laser, which

is composed by 16 m of erbium-doped fiber inside an EDFA amplifier with a maximum gain of 24 dBm and a GVD of $0.016 \text{ ps}^2/\text{m}$. The rest of the fiber laser cavity is based on 22 m of SMF, with a GVD coefficient of $-0.021 \text{ ps}^2/\text{m}$, and constituted by a VOA attenuator, an isolator (ISO), and a 70/30 optical fiber coupler, where 70% of the optical power is integrated again inside the laser cavity. An additional fiber circulator device is incorporated into the laser cavity, since the saturable absorber is located in a free-space region in reflection configuration. To do this, a thick aluminum layer has been deposited on the InN thin film by using the radio-frequency sputtering technique, in order to create the SESAM device. In this study, an ATC ORION-3-HV sputtering chamber was used, placed in Grupo de Ingeniería Fotónica (GRIFO) facilities at the University of Alcalá in Spain. These Al-mirrors are approximately 300 nm thick, with a deposition rate of 240-250 nm/h, and were grown at room temperature with a flux of Ar of 2 sccm. The power applied to the Al target during deposition was 75 W, and the chamber pressure during growth was maintained at 5 mTorr [132, 133]. A 3-cm optical lens is inserted in front of the saturable absorber either to focus the maximum light of the fiber laser into the InN sample surface and to collect its back-reflection and sent it back to the optical fiber resonator cavity. The complete description of this laser set-up can be found in Fig. 5.10. The SESAM samples are placed so that the [0001] crystal lattice direction of the InN layer is parallel to the propagation direction z . By doing this, no polarization effects have been observed inside the resonator cavity, due to the polarization independence of wurtzite structures, such as the case of the InN samples, when illuminated along its z -axis. The net dispersion coefficient of the laser cavity corresponds to -0.21 ps^2 , where the dispersion of the EDF and SMF optical fibers predominate over the dispersion generated by the saturable absorber (less than 0.0001 ps^2), due to the low layer thickness of the InN samples. As a consequence, the laser cavity is said to operate in the anomalous dispersion regime.

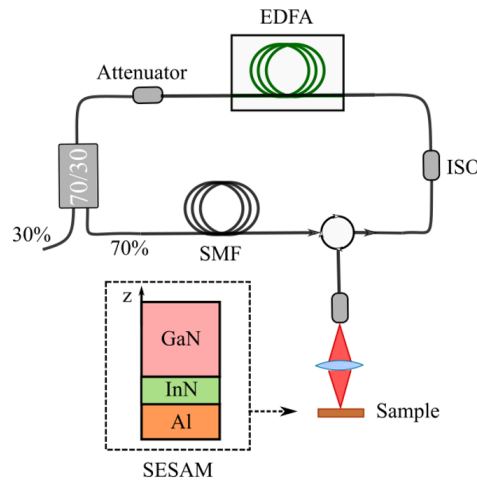


Figure 5.10: Ultrafast mode-locked fiber laser set-up using InN bulk as saturable absorber in a reflection configuration. The laser cavity is composed by an EDFA amplifier, an isolator (ISO) and a VOA attenuator, and a 70/30 fiber coupler based on standard SMF. The SESAM is placed in the z -axis propagation direction within the laser cavity and whose structure is represented at the inset [153].

The laser performance generated by the mode-locked fiber resonator cavity based on the InN SESAM as saturable absorber is characterized by the 30% port of the optical fiber coupler. In this sense, highly-stable stretched Gaussian pulses have been measured at the output of the mode-locked fiber laser system, as expected in dispersion-managed cavities. The repetition rate of this train of pulses is measured by an oscilloscope (Keysight Technologies MSO9404A), with a 4GHz bandwidth and a sample rate of 40 GSa/s, and an optical 20 GHz-photodetector (PDB410CAC, Thorlabs). It must be noted that due to the power limitation of the fiber photodetector (optical damage for average powers over 20 mW), an additional 99/1 fiber coupler has been inserted at the end of the 30% port. In this case, a repetition rate of 5.6 MHz was measured, corresponding to 178.5 ns between consecutive pulses. Therefore, the laser cavity operates in the fundamental mode, since the repetition rate value coincides with the experimental 38 m length of the laser cavity. Further information about the repetition rate can be obtained by the 32 GHz RF ESA (Agilent N9010A) in terms of the SNR, with a value of >45 dB. In the RF-spectrum, the output signal shows no side peaks between consecutive pulses, demonstrating the mode-locking stability of the laser cavity.

Besides, the autocorrelation trace and the optical spectrum have been characterized for each InN semiconductor sample in terms of the output power of the laser cavity. In this case, the variation of the optical power of the fiber resonator is modulated by the VOA device inside the cavity. While the gain level of the EDFA system remains unchanged, the optical losses introduced by the VOA, change the output laser power from 10 mW to the maximum power achievable by this set-up of 31.6 mW. For comparison purposes, samples S0', S1 and S2 are studied in relation to their spectrum and autocorrelation traces as depicted in Fig. 5.11(a) and (b).

- Firstly, we analyze the autocorrelation and spectrum of the reference sample S0. The mode-locked fiber laser has an average power of 31.2 mW (72.8 mW inside the resonator cavity), corresponding to a maximum output peak power of 22.3 kW and pulse energy of 5.2 nJ. In relation to the pulse duration and optical spectrum, sample S0' demonstrates a FWHM of 166.2 fs in the temporal domain, whereas a 3 dB bandwidth of 22.6 nm is measured in the frequency domain, with a central wavelength of 1560 nm. These results have been obtained by applying a Gaussian fit to the experimental values and represented as a solid line in Fig. 5.11(a). The relation between the autocorrelation (τ_{AC}) and the output pulse (τ_{pulse}) has also been included in the autocorrelation figures for each sample. The corresponding TBP value has been calculated at 0.453, very close to the transform-limited condition for Gaussian pulses (0.445).
- By using sample S1, an intracavity average power of 35 mW was needed to accomplish the mode-locking operation. For the maximum intracavity pump power of 73.7 mW achievable by the resonator cavity, that is, with minimum attenuation of the VOA device, the output power of the fiber laser is 31.6 mW, corresponding to a peak power of 25.5 kW and a pulse energy of 5.6 nJ. The pulse duration of the output pulse is therefore calculated as the FWHM of the fitted autocorrelation curve to a Gaus-

sian pulse profile. In this case, a pulse duration of 156.3 fs is obtained taking into account the Gaussian transformation parameter from the AC pulsewidth of $\tau_{AC} = 221$ fs, as explained in Chapter 4 [156]. On the other hand, a 3 dB bandwidth of 26.4 nm has been measured in the optical spectrum of sample S1 and at a central wavelength of 1564 nm. Therefore, the TBP value, measured as the product of the FWHM in the temporal and frequency domain, corresponds to 0.49. In other words, the optical pulses are slightly chirped, far from the transform-limited condition. The optical spectrum of the fiber laser does not exhibit Kelly sidebands, which indicates that intracavity nonlinearity and dispersion are weak.

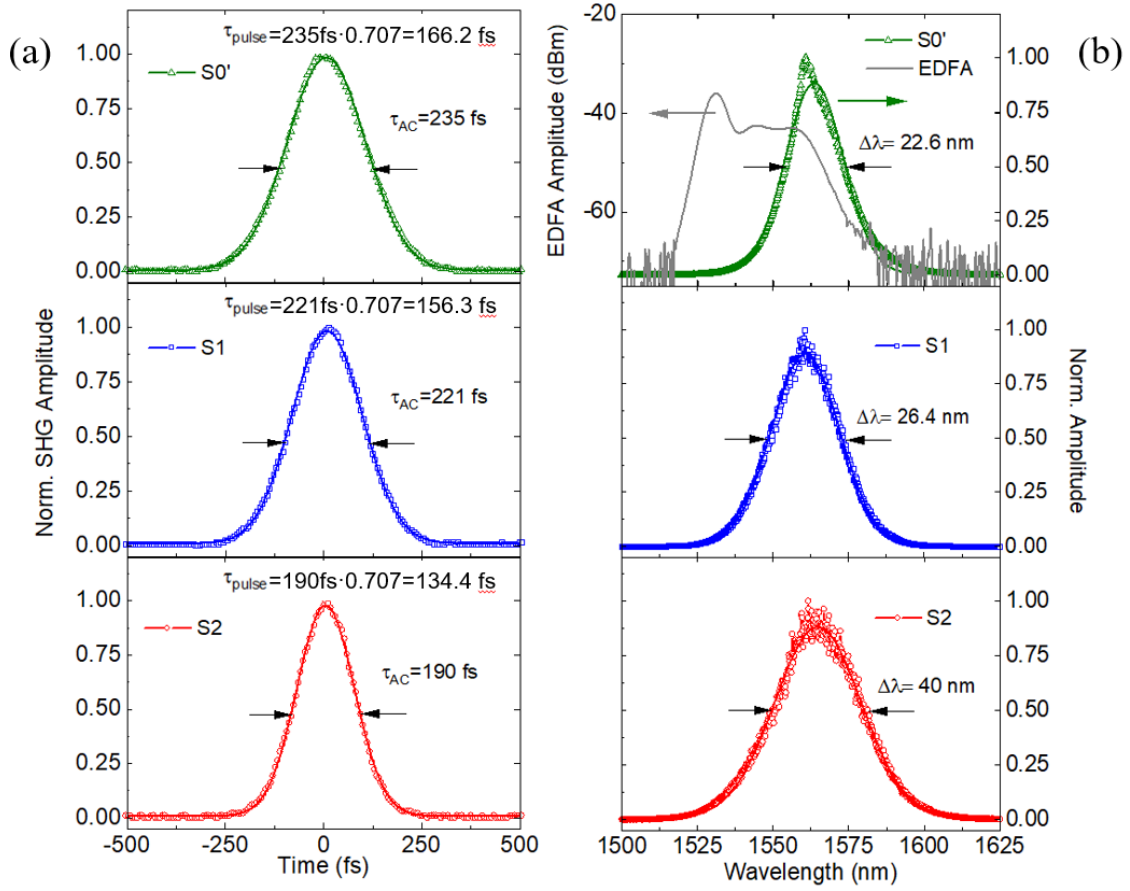


Figure 5.11: Optical laser characterization of the mode-locked fiber resonator cavity by using samples S0 (green dots), S1 (blue dots) and S2 (red dots) in terms of the (a) autocorrelation trace and (b) the optical spectrum, fitted to a Gaussian profile and represented with a solid line for each case [153]. The figure of the ASE of the EDFA has been included in the spectrum (gray solid line) for comparison purposes.

- In the case of sample S2, highly-stable mode-locking operation was obtained for a minimum value of 38.5 mW for the intracavity pump power. By reducing the optical losses introduced by the VOA device to the minimum, a maximum output intracavity pump power of 70 mW is measured. In this way, we measured a maximum output average power of 30 mW, which implies a 28.2 kW of peak power and 5.4 nJ of pulse energy. In terms of the pulse duration, it has been calculated that the pulse duration of the autocorrelation function fitted to a Gaussian pulse profile is 134.4

fs ($\tau_{pulse} = \tau_{AC} \times 0.707 = 134.4$ fs and the corresponding autocorrelation duration $\tau_{AC} = 190$ fs), while the optical bandwidth at 3 dB decay is 40 nm, with an optical wavelength centered at 1569 nm. Moreover, the TBP value is of 0.62, denoting a more chirped pulse than for the case of S1 at the output of the mode-locked laser cavity.

- Discussion of experimental results

In conclusion, due to the introduction of a change in the growth process, higher quality conditions have been achieved, leading to a reduction of the residual doping and thus, the associated Burstein-Moss effect. As mentioned in the material characterization section, the key to controlling the growth conditions is to have consistent time intervals for the N depositions during the fabrication process. As a consequence of this fact, the optical properties of the saturable absorber have been largely improved with respect to the latest results, thus comparing samples S1 and S2 with samples from previous works S0 and S0'.

With regards to the nonlinear behavior, due to the decreasing carrier concentration of the sample, and therefore, the reduction of the Burstein-Moss effect, a redshift in the bandgap energy, i.e., a displacement of the operating wavelength is produced. Furthermore, a higher nonlinear absorption coefficient has been measured because of the improved growth conditions, which have enabled a higher nonlinear response of the semiconductor saturable absorbers at high incident optical powers. Therefore, this increase in the nonlinear behavior of the sample may induce high-order nonlinearities that generate a displacement in wavelength and pulse chirping. As it is shown in Fig. 5.9(b), these materials tolerate high incident fluence, since any sign of optical damage has been observed at the maximum intracavity fluence of 10.5 mJ/cm^2 , which corresponds to 31.6 mW of average power at the laser output and a 73.7 mW within the resonator cavity. Due to the peak power limitation of the laser cavity, we were unable to measure the damage threshold in our experimental set-up. A recent study by our group has shown that this type of passive mode-locked laser can achieve the highest value of incident energy fluence (1 TW/cm^2) without damaging the bulk InN saturable absorber [161]. In contrast, the absorption saturation of samples S1 and S2 requires a higher optical fluence, expanding the operating energy range and demonstrating the feasibility of InN semiconductors in high-power industrial applications in the C-band operation, such as surface micromachining or biophotonic imaging, among others.

Furthermore, these new materials have enabled the improvement of an ultrafast fiber laser source. Not only the temporal duration of the output optical pulse has been reduced, 134.4 fs compared to the 166.2 fs obtained for reference sample S0, but also it has allowed getting broader spectra, ranging from 22.6 nm for S0, to up to 40 nm for sample S2. Moreover, as shown in Fig. 5.11(b), for sample S1 (1564 nm) as well as for S2 (1569 nm), it is observed a redshift of the central wavelength compared to the reference sample S0 (1560 nm). This effect can be explained by both the influence of the bandgap redshift and the EDFA gain spectrum signal, whose figure has been included in the spectrum of sample S0 in Fig. 5.11(b), as a result of better control of the fabrication conditions. The correlation between the pulse duration and optical bandwidth

between samples S1 and S2 can be associated with the variation of the effective length (for S1 is 190 nm, whereas for S2 this value increases to 239 nm).

In addition, more energetic pulses have been measured due to the higher transmission change of the sample, in conjunction with a smaller absorption coefficient in the linear regime, leading to higher optical peak powers (28.2 kW and 5.4 nJ in comparison to the 22.3 kW and 5.2 nJ in S0'). Therefore, higher-order nonlinear effects are also likely to be induced by the enhanced nonlinear response, causing chirped pulses, and thus the spectral shift towards longer wavelengths generated in samples S1 and S2 as demonstrated in Fig. 5.11.

Over the last few decades, new types of saturable absorbers have been investigated with enhanced properties such as ease of fabrication, compactness and high efficiency in pulse laser generation. Among them, two-dimensional (2D) materials have attracted much attention in multiple applications, including nonlinear optics, optoelectronics and biomedicine, due to their morphological structure (composed of a few layers of atoms disposed in a single direction) and optical properties. These 2D materials can be categorized as graphene, topological insulators (TIs), transition metal dichalcogenides (TMDs), and black phosphorus, commonly used for ultrafast laser generation. Furthermore, MXene, bismuthene or antimonene have recently been studied for laser operation because of their broad bandwidths and ultrafast recoveries. Accordingly, the characteristics of the modified InN based SAs of this work have been compared to some 2D materials employed in this type of mode-locked laser Er-doped configurations, as shown in Table 5.3.

As compared to black phosphorus [120], bismuthene [162], or graphene [163], this work yielded the shortest pulsewidth in a dispersion-managed resonator. However, the modulation depth of TIs, BPs and bismuthene saturable absorbers is still lower than those reported for other 2D materials. Furthermore, InN-based saturable absorbers demonstrate a high modulation depth and similar saturation intensities in the high-power operation range compared to graphene or MXene among others. In addition, the peak power at the output of the laser cavity obtained by the InN material was more than nine times greater than that of 2D materials, with a value of 28.2 kW and 5.4 nJ. In comparison to previous work [160], the nonlinear absorption has increased by two times, while the temporal width of the modified SA lowered to the shortest pulse duration achievable by our laser set-up. Consequently, these materials have proven to be more efficient than any other saturable absorber for ultrashort generation in the high-power regime.

Among other semiconductor materials, InN-based SESAMs have shown superior properties including fabrication ease, crystal quality, robustness, as well as a higher peak power. This study indicates that InN may be considered as the appropriate choice for the development of SAs in the telecommunications spectrum.

However, further study is required in order to determine the best InN semiconductor structure along with the appropriate fabrication parameters which may lead to the ideal mode-locked ultrafast laser operation regime.

SA	λ (nm)	$\Delta\lambda$ (nm)	τ_{pulse} (fs)	MD (%)	I_{sat} (MW/cm ²)	P_p (kW)	Ref.
Graphene	1545	48	88	11	2×10^3	0.57	[163]
TI-Bi ₂ Se ₃	1557.5	4.3	660	3.9	12	0.22	[118]
TMD-WSe ₂	1557.4	25.8	163.5	21.9	15.4	1.79	[164]
TMD-MoS ₂	1560	24.4	154	19.12	1.361	1.12	[165]
BP	1555	40	102	10	15	0.49	[120]
MXene	1555	22.2	159	24	39.1×10^3	2.6	[166]
Bismuthene	1561	14.4	193	5.6	48.2	3.28	[162]
InN	1562	22.6	166.2	30.6	1.6×10^3	22.3	[160]
InN	1569	40	134.4	17.3	4.4×10^3	28.2	[153]

Table 5.3: Comparison of the optical parameters for the laser performance employing the 2D materials as SA with the ones obtained for the InN semiconductor SESAM samples. The I_{sat} parameter represents the saturation intensity, while P_p is the peak power of the optical pulse [153].

5.2 Improvement of the laser system

In the last sections, we talked about the limitations of the semiconductor saturable absorbers characteristics, such as high modulation depth, fast recovery times and strong nonlinear behavior, during its fabrication process, including robustness, crystal quality and residual doping. These properties are essential for the development of efficient and stable ultrafast lasers, required in the vast majority of industrial applications. Nevertheless, saturable absorbers have also demonstrated low-power tolerance, with damage threshold levels in the range of 2 mJ/cm² of incident fluence. This property is of particular importance in many industrial fields, such as telecommunications, medicine, or military applications. Therefore, the fabrication of promising saturable absorbers with superior characteristics is still a longstanding goal.

Even though InN semiconductor saturable absorbers are presumed to have a high damage threshold level (we couldn't characterize this property due to the limitation of the maximum power achievable by the amplifier laser source), multiple noise components are incorporated in the output laser signal. As a result of using free space optics for the SESAM configuration, the resonator cavity system showed significant insertion losses, estimated at 8.5 dB, and a consequent laser performance degradation. In this sense, we firstly propose the use of InN thin films as SESAMs in an all-fiber laser device by introducing a graded-index lens (GRIN) as the coupling device between the SA and the optical fiber laser system. This configuration enables the reduction of the insertion losses not only introduced by the SA but also eliminates external noise sources related to the free space performance of previous set-ups. Therefore, by keeping the pulse duration and average power of the intracavity laser pulse constant, while lowering the repetition rate (f_{rep}), i.e., a longer ring fiber resonator cavity implies a longer distance between consecutive pulses (t_{rep}) in the output laser train, the peak power can be enhanced.

In the next sections, we will discuss the results obtained for the proposed solutions. Firstly, an introduction to better laser performance through the reduction of laser cavity insertion losses is presented. Afterwards, a stable high-power ultrafast laser source is generated by employing the later low-loss laser cavity. These results have also been published in [167].

5.2.1 All-fiber configuration

New fabrication techniques for all-fiber systems have been developed in recent years due to the demand for robust, high-power ultrashort fiber lasers. These methods involve depositing the SA onto the optical fiber, for instance by gluing the SA with a composite material (polyvinyl alcohol or polymethyl methacrylate) between two fiber ends and linking them with a fiber connector. This method, known as butt-coupling, is usually employed in commercial systems due to its simplicity, but is however limited in terms of optical power because of the low damage threshold of the corresponding coupling device. In order to counteract these limitations, new coupling devices based on the evanescent-wave theory were carried out. In this case, the saturable absorber is located on the sidewalls of the optical fiber, such as in side-polished fibers, tapered fibers, and in cladding-etched fibers [168–170]. The main property of these types of fibers is that the core-cladding structure is modified so that part of the optical waveform propagating through the optical fiber interacts with the SA. Even so, this type of fibers generates nonlinear polarization rotation effects within the resonator, thereby decreasing the output energy achievable by the laser system.

In this section, which presents the results published in [167], we propose to use an InN SESAM, paired with a GRIN lens in an all-fiber alignment-free laser device to reduce the insertion losses of SA. By eliminating the optical path in air, the resultant solid assembly minimizes the reflection losses generated at the interfaces and reduces the aberrations caused by the optical elements, ultimately leading to an increase in ultrafast laser performance. A full explanation of the laser configuration, as well as the coupling device assembly, will be explained in the following section. Next, the experimental results of the laser performance after the introduction of the GRIN-to-SA in the all-fiber resonator cavity are discussed.

- **Laser set-up**

As it was mentioned before, a GRIN-rod lens was introduced between the SESAM and the optical fiber end, in order to decrease the insertion losses generated by the free-space configuration of previous laser set-ups. An off-the-shelf lens (GRIN2315, Thorlabs) GRIN lens have been used, with 0.245 mm of focal distance, due to the sapphire and InN width of the sample under study (0.3 mm with a refractive index of 1.7), and with a standard 100 nm spectral response around the wavelength of the laser (in this case 1550 nm). With a reflectance of 10% from 380 to 2000 nm and total polarization preservation, the GRIN lens is suitable for industrial applications. The semiconductor saturable absorber consists of an InN epitaxial layer deposited by the PAMBE technique on a commercial GaN-on-sapphire substrate with 450°C and 290

nm/h as the growth temperature and growth rate parameters respectively. In this study, three different InN samples with thicknesses of 1 μm (reference sample S0), 360 nm (sample S1), and 780 nm (sample S2) have been analyzed for the purpose of comparing the laser characteristics of the improved coupling device in the all-fiber set-up. The SESAM device, based on a 300 nm-thick aluminum layer deposited on the InN film by RF-sputtering at room temperature, showed singular nonlinear characteristics within the telecommunication region, as demonstrated in latter studies. Both the InN-based device and the fiber facet are directly glued to the GRIN lens faces by a UV-curing optical transparent cement (NOA68, Thorlabs). The complete coupling device design and its components can be seen in Fig. 5.12.

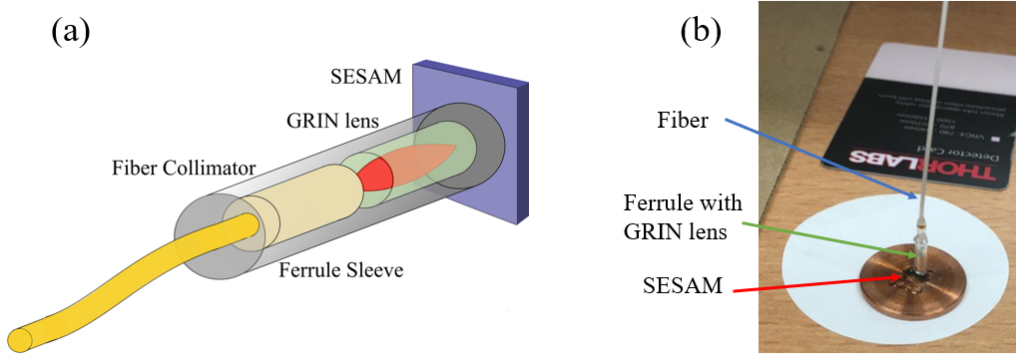


Figure 5.12: (a) Schematic structure of the GRIN-to-SESAM coupling device employed in the all-fiber laser set-up [167]. (b) Photograph of the experimental all-fiber GRIN-to-SESAM coupling device.

When compared to the aforementioned methods, the GRIN lens coupled with the InN SESAM showed a low insertion loss, a high damage threshold, and polarization insensitivity. (i) The introduction of the GRIN lens increases the robustness of the fiber laser system, since any alignment would be necessary to achieve the mode-locking operation. (ii) Furthermore, the efficiency of the fiber laser is enhanced due to the decrease of the internal and external loss sources, such as the reflections of the optical lenses in the free-air configuration and the ones introduced by the SA. (iii) The high-damage threshold level of the InN semiconductors described in this work, allows their implementation inside an all-fiber laser cavity, which will enable them to obtain higher optical output powers than those reported in previous studies [153,160]. In this sense, all-fiber laser assemblies based on InN may be used in industrial settings in the telecommunication region owing to these results.

On the other hand, the fiber laser set-up comprises a ring-fiber laser cavity with the InN SESAM coupling device in reflective mode. The fiber cavity is based on 16 m of EDF (net dispersion coefficient of 0.256 ps^2 at 1550 nm) as part of an EDFA amplification system (24 dBm of maximum gain), and 25 m of SMF (corresponding to -0.462 ps^2), guaranteeing the stability and resistance to vibrations as well as with other perturbations. Additional optical fiber elements such as an isolator (ISO), a circulator (connected to the fiber coupling GRIN-to-SESAM device) and an optical coupler of 70/30 based on

conventional SMF are also included within the resonator cavity, as represented in Fig. 5.13. The total dispersion of the laser cavity has a value of -0.21 ps^2 , thus operating in the anomalous dispersion regime, albeit with dispersion-managed behavior.

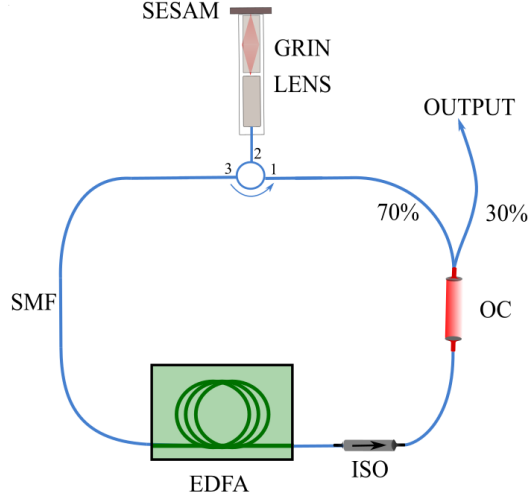


Figure 5.13: Schematic chart of the all-fiber Er-doped laser set-up in reflection configuration using the coupling with GRIN lens [167].

Under normal-incidence illumination, the polarization independent wurtzite structure of the saturable absorber rendered the polarization controller unnecessary. Consequently, polarization preservation ensured that any losses were introduced by the GRIN lens. It must be noted that in order to preserve the maximum energy inside the laser cavity provided by the EDFA amplification device, all the fiber connections have been fused, minimizing the internal losses. Nevertheless, a higher probability of burning the optical fibers of the resonator is observed according to the reduction of losses and the increase of the optical power propagating through the all-fiber laser cavity using the GRIN lens.

- **Laser characterization**

Optical characterization of the laser output has also been carried out by using a RF-spectrum analyzer (Agilent N9010A) with an optical bandwidth of 32 GHz, and a 4 GHz oscilloscope (Keysight Technologies MSO9404A). As shown in Fig. 5.14(a), the resonator cavity has a time interval of 200 ns, according to the ring fiber laser cavity's optical round trip (41 m), thus operating in the fundamental mode (higher harmonic generation has not been observed for this configuration). Moreover, a broadband RF-spectrum of the pulse train has also been measured with 180 Hz of resolution bandwidth and 1001 data points, demonstrating a stable repetition rate of 5 MHz in the fiber cavity (Fig. 5.14(b)). In this case, the 14th harmonic of the electrical spectrum was measured with a SNR of 42 dB with a 20 Hz resolution bandwidth and a step of 10 kHz, and a 1% of the laser pulse for the purpose of preventing any optical damage to the detector. As it can be extracted from Fig. 5.14(b), the background level with and without signal on the detector coincides. Besides, most of the energy of the output signal of the laser pulse train is located within the optical pulse (the integral area underlying the optical spectrum), since no

pedestal is observed in the experimental RF-spectrum, hence confirming that the SNR is at least 42 dB. Furthermore, measurement of 1 GHz-span of the pulse train RF-spectrum (inset of Fig. 5.14(b)) has been added in order to demonstrate the absence of parasitic disturbances, proving the quality of the mode-locking stability.

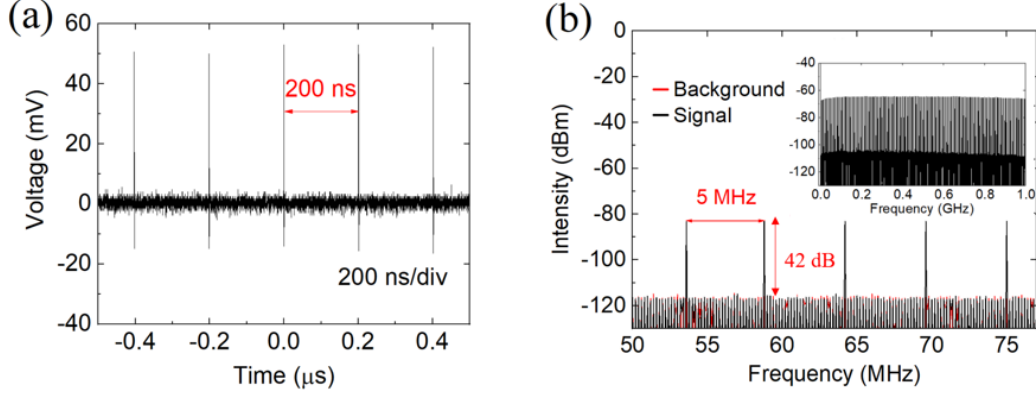


Figure 5.14: Optical characterization of the output laser pulse in terms of (a) repetition rate of the mode-locked pulse train measured by an oscilloscope, and (b) measurement of the SNR by the ESA device [167].

In relation to the laser steadiness, continuous monitoring of the average power at the output of the laser cavity over time was conducted to demonstrate the stability of the all-fiber assembly, as shown in Fig. 5.15. A total of 60 hours of monitoring were devoted to the stability measurement of the output laser pulse with a time interval of 1 min. According to Fig. 5.15, an average power of 30 mW was measured, with a slight increase in optical power of 0.042 mW. A picture of the optical spectrum of the pulse at the beginning and at the end of the monitoring measurement is included in the inset. From these results, we can conclude that the stability of the fiber laser cavity system, as well as the SA device, are suitable for long-time use without any optical damage, an indispensable characteristic in high-power industrial applications.

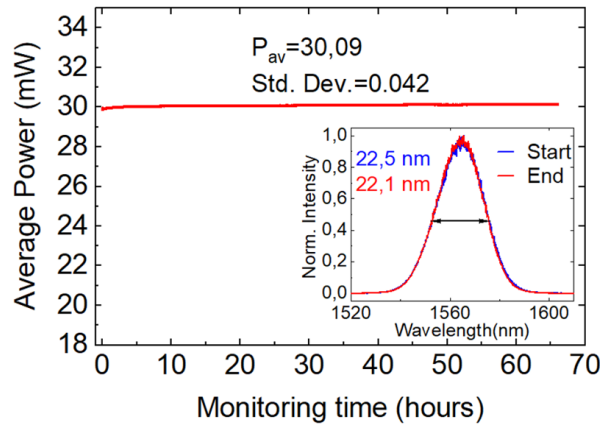


Figure 5.15: Analysis of the stability of the output pulse in the fiber laser cavity in terms of its average power as a function of time [167].

In addition, an analysis of the temporal evolution of the optical pulse at the output of the 30% optical coupler port of the ring fiber resonator cavity was performed by an optical 1.5 GHz-photodetector (Thorlabs FPD310-FC-NIR), an optical spectrum analyzer (Yokogawa AQ-6215B), and a commercial autocorrelator (APE Mini PulseCheck). Consequently, an analysis of the pulsewidth and optical output power of each of the InN semiconductor materials is performed. These samples, named as S0, S1 and S2, are incorporated in this laser configuration in reflection configuration for comparison purposes. The mode-locking operation of the all-fiber laser system was characterized in all cases when the resonator cavity was pumped by the maximum gain achievable by the EDFA system.

- The autocorrelation and optical spectrum of the reference sample S0 are firstly analyzed, represented in Fig. 5.16(a) and (b) with green dots. In this case, a temporal pulse duration of 226 fs is measured in the autocorrelation trace after applying a Gaussian fitting function (black line), leading to a pulsewidth of 160 fs, as represented in Fig. 5.16(a). Whereas for the optical spectrum, a FWHM of 20.4 nm at 3 dB decay is observed in the frequency domain, with the pulse centered at the wavelength of 1564 nm. Thus, the TBP for sample S0 is estimated at 0.445, which coincides with the theoretical value of the transform-limited condition for Gaussian pulses (0.44). In relation to the optical power, for the maximum intracavity pump power of the all-fiber system, an average power of 40 mW was measured, which in conjunction with the pulse duration corresponds to a peak power of 50 kW and a pulse energy of 8 nJ.
- Whereas in the case of the introduction of the enhanced InN semiconductor S1 (see Section 5.1.2), the pulse duration in the temporal domain has been reduced to 94 fs in the output pulse (corresponding to a pulsewidth of 134 fs in the autocorrelation trace) obtained by a Gaussian fit. On the other hand, the optical bandwidth of the output pulse increased to 39.4 nm measured at FWHM in the optical spectrum with a central wavelength of 1570 nm. In this case, the TBP value was measured at 0.46, thus denoting that the optical pulse is slightly chirped compared to the transform-limited situation. Moreover, the average power of the output laser pulse is 35 mW, which implies a peak power and a pulse energy of 74.4 kW and 7 nJ respectively. The reduction of the average power can be explained by the increase in linear absorption introduced by these semiconductors (S1 and S2) compared to the reference sample S0.
- Finally, by inserting sample S2 into the all-fiber laser system, the pulse duration of the autocorrelation trace measured at the output of the resonator cavity was 131 fs (Gaussian fit), whereas the optical pulsewidth in the temporal domain was 92 fs, the minimum pulsewidth obtained with this semiconductor so far. The 3 dB bandwidth of the optical spectrum has been calculated at 42 nm, which corresponds to the maximum bandwidth achievable by the semiconductors described in this work. The central wavelength of the optical pulse performed by sample S2 is shifted to 1576 nm, as shown in Fig. 5.16(b). Therefore, a TBP value of 0.46 is obtained, demonstrating a higher chirped behavior compared to previous

samples S0 and S1. In terms of optical power, at the maximum pumping level, the average power of the resonator was 30 mW for the case of sample S2, while the peak power and pulse energy were 65.2 kW and 6 nJ, respectively.

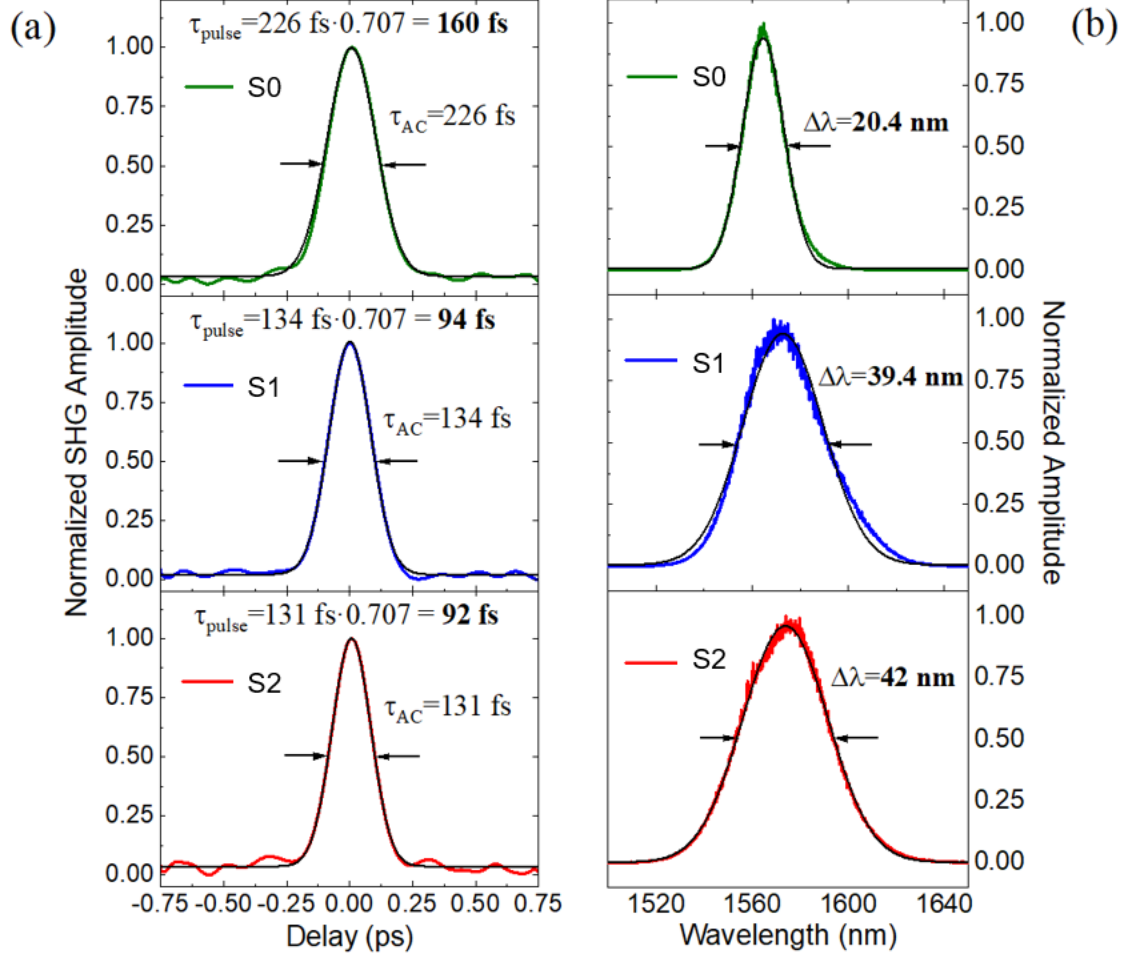


Figure 5.16: Fiber laser performance of the GRIN-to-SESAM InN devices of the sample S0 (green dots), sample S1 (blue dots) and sample S2 (red dots) represented as a function of the temporal duration measured from the autocorrelation function (a), and the optical bandwidth obtained from its corresponding spectrum (b) after applying a Gaussian fit (solid black line) [167].

- Discussion of experimental results

The presented results, published in [167], successfully demonstrated the enhancement of the laser execution by employing an elemental fiber coupling device based on a GRIN-rod lens in conjunction with an InN SESAM in a passively mode-locked all-fiber laser system operating in the telecom region. In addition to ensuring a compact, turnkey and alignment-free design, this coupling element also provides a highly stable optical femtosecond pulse train. In spite of the clearly stretched pulse patterns in the generated spectrum, the estimated overall dispersion is consistent with mode-locked soliton operation. An exact amplifier dispersion value cannot be determined experimentally due

to the lack of information provided by the company. Furthermore, the self-starting operation has been enhanced due to the all-fiber configuration, where the fiber ends are spliced in order to reduce possible back-reflections within the resonator, which may be detrimental to the optical power.

Until now, the laser performance of InN-based saturable absorbers, both in the transmission and reflection configuration, has been limited in terms of optical power and pulsewidth because of the fiber coupling and the insertion losses introduced by the semiconductor material. Nevertheless, the elimination of the defocusing behavior and the optical aberrations generated by free-space configurations, measured as an 8.5 dB loss in previous laser configurations (see Section 5.1), leads to the lessening of the insertion losses introduced within the laser cavity to a total value of 5 dB. As a consequence, the nonlinear transmission response of the saturable absorber increases since a higher intensity is circulating within the resonator. Due to the decrease of the linear losses within the laser cavity, an improvement of the optical fluence on the SA element is expected. If a larger power in the resonator is achieved, a higher absorption saturation is also obtained in the saturable absorber. Also, a decrease in the coupling losses to the SA may imply effectively a lower saturation fluence and therefore an increase in the stability of the optical laser in the resonator. Through this reduction of insertion losses by a factor of 3.5 dB, it is possible to generate 90-fs ultrafast pulses, which corresponds to a reduction of the 40% when compared to the air configuration (a temporal width of 220 fs was obtained for the transmission configuration, while a 134 fs was measured in reflective mode). The variation of the optical pulsewidth of the different samples is related to the improvement of the nonlinear absorption coefficient, calculated as $\alpha_2 = -3.5 \cdot 10^3$ for reference sample S0, $\alpha_2 = -3 \cdot 10^4$ in the case of S1, and $\alpha_2 = -2.7 \cdot 10^4$ cm/GW for sample S2, and thus to the decrease in the residual carrier concentration associated to the Burstein-Moss effect (see Section 5.1.1). By adding the GRIN coupling device, there is an enhanced pulse focus on the InN-based active layer, resulting in a larger induced nonlinear effect. As a result, the pulse's temporal width is shortened while its stability is preserved.

In addition, the optical spectrum bandwidth of the output pulse has increased by a 35 % in comparison to latter sections, with a FWHM of 40 nm. The absence of pulse deformation in the optical spectrum figure, usually associated with optical pulse breaking, reveals the quality of the output pulse as well as the stability of the mode-locking operation within the laser cavity. Due to the bandgap energy difference between reference sample S0 and the improved InN semiconductors S1 and S2, a redshift in wavelengths can be appreciated, ranging from 1564 nm to 1576 nm. Furthermore, the increase of the nonlinear behavior of the SA within the laser cavity may generate an increase in the pulse chirping.

Due to the enhanced laser performance, the intensity impinging on the saturable absorber increases, leading to higher nonlinear behavior, and thus a shorter pulse (time duration) with a higher optical peak power. The maximum power achievable for the all-fiber configuration has been measured in 40 mW and up to 7 nJ of pulse energy without the need for additional ampli-

fication. This translates into a threefold increase in peak power and energy due to the pulse compression, where 74 kW and 8 nJ have been obtained in this work, while only 28 kW and 5.4 nJ in pulse peak power and pulse energy respectively, were measured in the air configuration set-up. A comparison of these results is listed in Table 5.4.

Samples	τ_{AC} (fs)		$\Delta\lambda$ (nm)		P_{peak} (kW)	
	Air	GRIN	Air	GRIN	Air	GRIN
S0	190	160	19	20.4	24	50
S1	156.3	94	26.4	39.4	25.5	74.4
S2	134.4	92	40	42	28.2	65.2

Table 5.4: Autocorrelation temporal duration and spectral bandwidth measured by using samples S0, S1 and S2 for free-space configuration (Air) [153] compared to all-fiber laser system founded on a GRIN lens (GRIN) for a reflection configuration laser cavity as well as the corresponding peak powers [167].

An Er-doped fiber laser ring cavity with a pulse duration of 92 fs has been found to be among the shortest pulse durations that can be acquired by a saturable absorber without additional post-amplification. An interesting feature of these semiconductors is their high peak pulse energy emission as well as their ability to withstand high temperatures, since a higher damage threshold level has been measured than those reported for two-dimensional semiconductors. From these results, it appears that the InN SA coupling device is uniquely effective over other laser-related devices when it comes to generating ultra-short pulses and enhancing laser stability. However, the increase of the optical fluence (and hence the temperature) on the material surface would lead to an enhancement of the nonlinear transmission change of the SA and thus to a better laser performance in terms of pulse duration and optical power as seen along this chapter. To do this, a longer all-fiber resonator cavity has been proposed for high-power ultrafast mode-locking laser development.

5.2.2 High-power ultrafast all-fiber laser

Ultrafast high-power mode-locked fiber lasers can be applied in a tremendous number of applications, such as in laser micromachining, material processing, surgery or electronics among others. However, these lasers are restricted in terms of peak power and pulse energy with a maximum value of a few hundred of kW and tens of nJ respectively. Following the line proposed by Gallazzi et al. [171], the peak power of the output laser pulse can be increased by changing the repetition rate (f_{rep}) of the resonator cavity. The easiest way would be by incrementing the length of the SMF optical fiber in the ring fiber cavity that has been employed in this thesis. It must be noted that the dispersion-managed condition of the fiber laser cavity will no longer be supported because of the increase of the dispersion coefficient of the SMF optical fiber. Therefore, extended optical pulses with a temporal width of nanoseconds are expected in this type of configurations. Different optical fibers such as PCF, or UN3 can also be employed for the expansion of the pulse. Nevertheless, these fibers are not compatible with low-cost ring fiber laser fabrication, as well as

the instabilities associated with high-power propagation. Therefore, we will focus on using SMF optical fibers for simplicity.

In this framework, we here expose preliminary results of high-power ultrafast pulse generation, increasing the length of the SMF optical fiber to the laser set-up presented in Fig. 5.12, constituted by an all-fiber laser configuration with the InN based SESAM coupled to a GRIN-to-fiber optical device for loss reduction.

- Laser set-up

In this case, a VOA has been incorporated after the SESAM to control the power inside the resonator cavity. Furthermore, a SMF fiber span is connected between the VOA and the EDFA amplification device for the reduction of the repetition rate. The rest of the fiber components are the same as the ones used in the previous sections, based on standard SMF and EDF fiber with a total net distance of 50 m (5.2 MHz of repetition rate) for the original laser cavity. Four different lengths of SMF fiber have been tested as the additional fiber span: 200 m (total cavity length of 250 m), 500 m (550 m long cavity), 1 km (1.05 km total cavity length) and 4 km (4.05 km of total length), respectively. The laser set-up has been plotted in Fig. 5.17. As it was mentioned before, due to the addition of the SMF, the laser will no longer work as a dispersion-managed cavity, but in the anomalous dispersion regime with a dispersion coefficient greater than -0.6 ps^2 . As demonstrated in previous section 5.2.1, the minimum pulsewidth was measured for sample S2, with a value of 92 fs and a spectral width of 42 nm for the all-fiber laser configuration with the InN SESAM connected to the fiber end by a GRIN device. As a consequence, we will employ sample S2 as the InN semiconductor SESAM to be compared to the latest results.

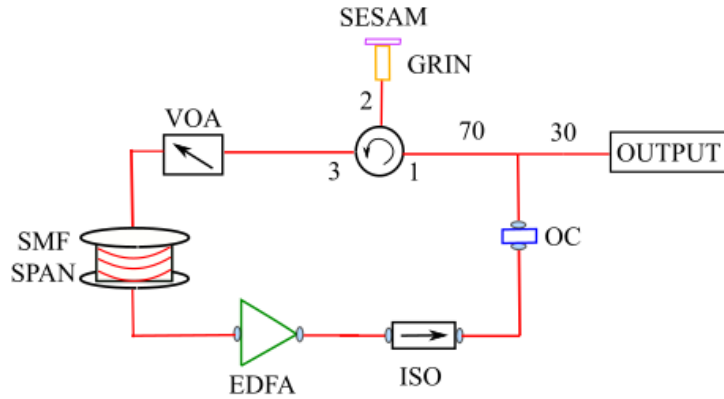


Figure 5.17: Set-up of the expanded GRIN-to-fiber laser by the addition of a SMF fiber span of 200 m, 500 m, 1km and 4 km respectively. A VOA device is inserted between the SESAM and fiber span to control higher-harmonic generation.

- Experimental results

The stability of the output laser pulse has been characterized at 1560 nm in terms of temporal pulsewidth, by the measurement of the autocorrelation traces by the autocorrelator, and the spectral width at FWHM by the OSA

device. In addition, it has been evaluated the output average power as well as the SNR of the output signal by the RF spectrum, and the repetition rate by the ESA. Higher harmonics have been observed during the experimental measurements, nevertheless, in this work, we will focus on the fundamental mode for comparison purposes. No damage threshold has been observed in the saturable absorber during these measurements. However, we did notice an increase in temperature in the GRIN-to-fiber coupling device, where the UV-curing optical adhesive started to melt for cavities longer than 500 m, and thus produced the misalignment of the coupling device. To avoid this, we inserted a mechanical device consisting of a thermal semiconductor cooling refrigerator located on the other side of the SESAM sample to redirect the excess temperature to the external environment (see Fig. 5.12(b)). All the following measurements have been performed with the cooling refrigerator allowing to measure output laser pulses for longer cavities (up to 4 km).

- Firstly, an additional fiber span of 200 m has been incorporated into the original fiber laser cavity, measuring an intracavity average power of 24 mW when pumped at maximum by the EDFA amplification system. The laser pulse is stabilized in the 2nd-order harmonic mode. Therefore, in order to accomplish the fundamental stage, the intracavity power must be reduced by the VOA fiber device. The fundamental mode is locked by the fiber laser system when the average power at the output of the laser cavity is reduced to 22 mW (corresponding to an intracavity power of 51.3 mW), leading to an optical pulse with a FWHM of 173 fs in the temporal domain. In relation to the spectral domain, the FWHM is measured at 20.7 nm centered at 1559.4 nm. Therefore, the TBP value corresponds to 0.442, which is very close to the transform-limited condition of Gaussian pulses. Taking into account these results and the repetition rate (800 kHz), the peak power and pulse energy are calculated as 159 kW and 27.5 nJ, respectively. It is worth noting that the maximum peak power and optical fluence impinging on the surface of the saturable absorber would be equivalent to 371 kW and 56 mJ/cm². However, any sign of damage is observed on the semiconductor material. A comparison of the autocorrelation and optical spectra for each case has been represented in Fig. 5.18 (a) and (b).
- Subsequently, we increased the length of the resonator cavity by adding 500 m of SMF as the fiber span. When locked to the fundamental mode, related to a repetition rate of 363 kHz, the output Gaussian pulse has a temporal duration of 176 fs and 21 nm in the spectrum with a central wavelength of 1558 nm, and a TBP value of 0.457, therefore, a higher dispersion contribution is generated when a longer SMF optical fiber is inserted, moving away from the transform-limited situation. The average power has been measured at 20.4 mW for the fundamental mode (and an intracavity power of 47.6 mW), which implies a peak power of 319.3 kW and a pulse energy of 56.2 nJ at the output of the fiber laser, whereas a peak power of 745 kW and an energy of 131 nJ (115.4 mJ/cm²) is obtained inside the resonator cavity.
- In the case of 1 km of fiber span, the fundamental mode is locked in the

resonator fiber laser cavity with a repetition rate of 191.8 kHz, and emitting trains of pulses with an average power of 16.5 mW. When adjusted to Gaussian shape, the pulsewidth of the optical pulse can be measured at 180 fs and 21 nm, centered at 1556.5 nm. These results imply a chirped pulse with a TBP value of 0.468 due to the increase of the SMF fiber inside the laser cavity, and thus to the increase of the dispersion effect. The peak power at the output of the laser cavity is measured in 478 kW, while the intracavity peak power is 1.1 MW. On the other hand, the energy of the laser pulse is calculated as 86 nJ, whereas within the resonator cavity, the energy per pulse is 200 nJ, which corresponds to an optical fluence of 176.9 mJ/cm².

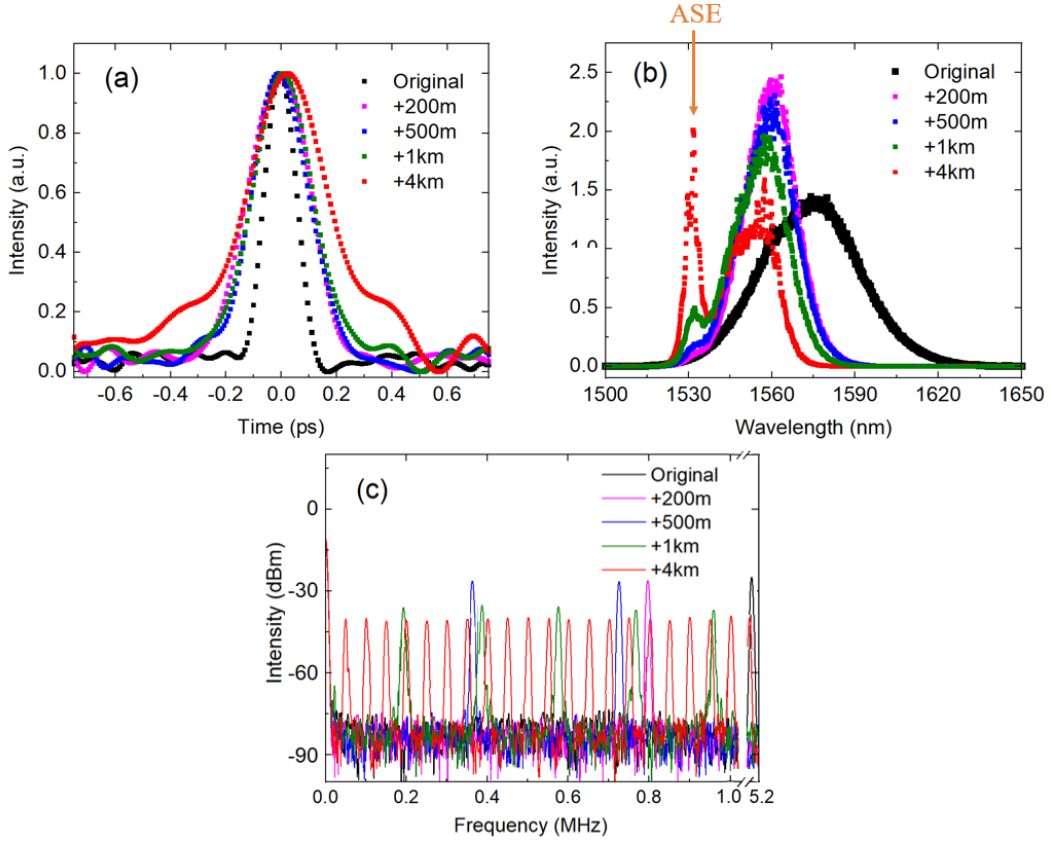


Figure 5.18: Characterization of the output laser pulse in terms of pulse duration and spectral width by representing the autocorrelation traces (a) and spectrum (b) for each fiber span added to the fiber laser cavity. The repetition rate measured by the RF spectrum is also represented in (c).

- Finally, if we insert a fiber span of 4 km in the laser cavity, a train of pulses of 13.5 mW of average power is emitted at a repetition rate of only 50 kHz. The temporal duration increases to 248 fs, while the FWHM of the spectrum is measured in 20.5 nm with a central wavelength of 1544.4 nm. A chirped pulse with a TBP value of 0.639 is generated as a consequence of the high dispersion coefficient of the SMF optical fiber within the laser cavity. At the output of the laser cavity, we measured a peak power of 1.08 MW and a pulse energy of 270 nJ. This entails an intracavity peak power of 2.52 MW and an energy of 630 nJ, leading to an optical fluence

of 55 mJ/cm². Still, no damage is observed in the saturable absorber. A comparison of the autocorrelation and optical spectra, as well as the peak power and TBP for each fiber span, is shown in Table 5.5.

Length	f_{rep} (kHz)	$\Delta\tau$ (fs)	$\Delta\lambda$ (nm)	TBP	P_{peak} (kW)
Original	5200	92	42	0.46	65.2
+200 m	800	173	20.7	0.442	159
+500 m	363	176	21	0.457	319.3
+1 km	192	180	21	0.468	478
+4 km	50	248	20.5	0.639	1080

Table 5.5: Comparison of the output laser characteristics for different fiber spans in the all-fiber laser cavity using the GRIN lens.

- Discussion of results

The presented results demonstrated the increase of the peak power by elongating the fiber length of the laser cavity, leading to a reduction of the repetition rate while maintaining the temporal duration within the femtosecond range.

As it can be observed from the experimental measurements, the temporal duration of the output laser pulse increases as it was expected and according to the simulations proposed in Chapter 4, due to the dispersion coefficient of the SMF optical fiber, which increments the value of the GVD coefficient of the laser cavity, thus the dispersion-managed condition is no longer fulfilled. In comparison to the original laser cavity, with a length of 50 m and a repetition rate of 5.2 MHz, where the minimum temporal duration was measured for the fundamental mode with a value of 92 fs (represented for comparison purposes in Fig. 5.18(a)), the pulsewidth increases to 170-180 fs, which is maintained from 200 m to 1 km, while this value reaches its maximum when a fiber span of 4 km is incorporated (248 fs). This suggests that between 1 km and 4 km, the dispersion coefficient is sufficiently high as to deteriorate the quasi-soliton behavior of the optical pulse propagation through the laser cavity. This leads to a high anomalous dispersion coefficient, which destroys the optical pulse (pulse-breaking). This effect can be seen in the autocorrelation trace of the optical pulse for the case of 4 km (Fig. 5.18(a)), where two side-lobes are present, related to the generation of a second pulse.

This effect can also be observed in the spectral domain. When comparing the fundamental mode spectrum of each laser pulse with different lengths of fiber spans, it can be observed that the pulse becomes narrower as the length of the cavity increases, compared to the original case, where a spectral width of 42 nm was measured. In this sense, the FWHM of the optical spectrum was reduced to ~ 20 nm due to the addition of the fiber spans, related to the dispersion coefficient of these fibers. However, it can also be seen that as we increase the length of the laser cavity, a higher contribution of the continuous component, related to the ASE of the optical fiber amplifier, is measured in the optical spectrum, noticeable for the 1 km and 4 km, as depicted in Fig. 5.18 (b) with a solid arrow. Furthermore, the central wavelength of the output pulse is shifted towards shorter wavelengths, due to the increase of the dispersion

effects within the SMF optical fiber as we increase its length, thus getting closer to the main peak of the ASE signal (1530 nm), as it can be observed in Fig. 5.18(b). These two effects on the spectral domain generate a higher chirp in the optical pulse, measuring a value of TBP of 0.442 for 200 m to 0.639 at 4 km, distancing from the transform-limited case as a consequence of the increment on the dispersion within the laser cavity. This is also related to the fact that an increase in the length of the SMF fiber within the laser cavity, along with the increase in the dispersion coefficient, also enhances the losses introduced in the resonator, thus increasing the background noise level.

It should be noticed that only the fundamental mode is measured for comparison purposes, denoting the stability of the fiber laser. In this case, the average power is reduced from 25 mW for the original laser cavity (50 m and 5.2 MHz), to 13.5 mW for the laser cavity with an additional fiber span of 4 km. This effect can also be noticed in Fig. 5.18(c), where the SNR of the output laser pulse is measured by an ESA system, while comparing the repetition rate for each addition of fiber span, measured with 20 Hz of resolution bandwidth and a span of 10 kHz. From this measurement, it is remarkable how the SNR decreases from 50 dB (for 200 m) to 30 dB (for 4 km) as the length of the fiber span increases, approaching the background noise level.

In relation to the peak power, it has been possible to increase the value from the original case, with a peak power of ~ 65 kW, reaching its maximum value of 1.08 MW for the 4 km-long cavity at the output of the ring fiber resonator cavity within an optical pulse of less than 250 fs of temporal duration.

5.3 Conclusions

In conclusion, the improvement of either the saturable absorber's properties of the InN semiconductors, as well as the high-power ultrafast laser performance has been successfully demonstrated along this chapter.

Introduction of buffer layer

In relation to the saturable absorber, we firstly enhanced the optical and electrical characteristics by the reduction of the carrier concentration. The insertion of a buffer layer based on an InN/InGaN heterostructure located within the InN thin film and the GaN-on-sapphire substrate, permits not only to reduce of the lattice mismatch between these two components, but also the residual doping concentration in the InN semiconductor. The reduction of the defect density, observable on the material surface, and thus the structural quality, entailed a decrease of the energy bandgap (redshifted), strongly associated with the material carrier concentration. The main impact of the new structure has been a vast increase in the modulation depth due to a higher nonlinear response, and as a consequence of the reduction of the residual doping in the sample. The InN material with the heterostructure buffer layer enhances its performance as saturable absorber in mode-locking fiber laser exhibiting a three times greater optical power when implemented in a fiber laser cavity and a reduction of the output pulsewidth (166 fs in the temporal domain and a spectral bandwidth of 22 nm) due to the enhanced nonlinear properties of the optical material.

Deposition control

Subsequently, the crystal quality of the SA was increased by a careful selection of the growth parameters during the material deposition process. By adjusting the time interval of the N layer exposure, essential in the PAMBE fabrication technique, the residual doping concentration can be better controlled and thus the Burstein-Moss effect. The SA characteristics of the InN based semiconductor are largely improved. A redshift of the bandgap energy has been generated, which can be explained by the lowering of the carrier concentration of the SA. In addition, the improvement of the growth conditions has generated a higher nonlinear response, due to the higher nonlinear absorption coefficient. With regard to the laser performance, these layers have demonstrated to develop shorter pulses with a time duration of 134 fs and broader bandwidths with a maximum value of 42 nm. In addition, this effect introduces a shift in the output pulse wavelength as well as a higher pulse chirp. As for the optical power, the effect of the higher nonlinear transmission change along with the smaller absorption parameter of the enhanced InN, has produced more energetic pulses, and nine times greater than those reported for the best 2D material performance.

GRIN-to-SESAM coupling device

The introduction of an all-fiber laser system operating in the C-band wavelength region has permitted to decrease in the intracavity insertion losses associated with the reflections and optical aberrations generated in free-space configurations. The all-fiber laser system is composed of an InN layer together with a GRIN lens in a simple and solid coupling device. The reduction of the linear losses has increased the optical power recirculating within the laser cavity, and thus the optical fluence traveling through the SA material. This effect has been translated into a higher nonlinear response ($T_{ns}/T_{lin} \cdot 100(\%) = 700\%$). In relation to the laser performance, the use of an all-fiber laser set-up generates an ultrafast train of pulses with a temporal pulsewidth as short as 90 fs, which corresponds among the shortest pulse durations viable for this type of semiconductors in mode-locked fiber laser systems. The use of this fiber coupling device for the saturable absorber in a passively mode-locked fiber laser in reflection configuration has enabled to obtain higher optical powers at the output of the resonator, with an improvement of 2 nJ with respect to free-space configurations.

High-power all-fiber mode-locked laser cavity

Finally, we employed these enhanced InN-based saturable absorbers inserted in an all-fiber laser cavity by a GRIN-to-fiber coupling device for the development of ultrafast pulse generation with high-power levels. In this case, the increase of the optical power has been conducted by the reduction of the repetition rate of the all-fiber laser system, by the increase of the fiber length of the laser cavity. For simplicity, we elongated the SMF portion of the laser cavity with different fiber spans from 200 m to 4 km. This permitted to reduce the repetition rate by 100 times, from 5.2 MHz from the original laser cavity to 50 kHz for the case of 4 km, while obtaining trains of Gaussian pulses with a temporal duration from 92 fs in its original set-up, to <250 fs, keeping the pulse in the femtosecond range. Whereas in the spectral domain, the FWHM of the optical pulse has been measured with a stable value of ~ 20 nm centered in the 1550 nm operation band for all the added fiber spans,

denoting the stability of the fiber laser system. The use of long fiber laser cavities with the InN SESAM coupling device has enabled to obtain pulses with optical peak powers ranging from hundreds of kW to 1 MW, without damaging the InN SESAM. Nevertheless, some noise contributions have been measured for cavities longer than 1.05 km, reducing the average power of the output laser pulse, while enhancing the CW components of the ASE signal, deteriorating the laser performance in the spectral domain due to the increment of the dispersion coefficient within the laser cavity.



Chapter 6

Sensing applications of ultrafast InN based fiber lasers

Contents

6.1	Gas sensing	114
6.1.1	Supercontinuum generation	115
6.1.2	Experimental set-up	117
6.1.3	Preliminary results	118
6.1.4	Discussion of results	120
6.2	Biomedical sensing	121
6.2.1	Pulse compression for high-power laser systems	122
6.2.2	Design of the “all-fiber” spectroscopy laser source	123
6.2.3	Numerical simulations	128
6.3	Conclusions	140

High-power optical fiber laser sources are essential in a wide variety of industrial applications, such as in the material field with laser micromachining or material processing, and in the telecommunications field with the development of long-haul transoceanic fiber cables. Nevertheless, the greatest impact has occurred in the environmental and medical field, such as in the monitoring of the evolution of global warming or the detection and prevention of diseases, reducing the time of diagnosis while providing highly accurate results [172, 173].

In general, diagnostic devices are based on the detection and characterization of specific molecules by reliable and stable light sources, capable of reaching high-power levels (higher incident powers imply a longer penetration depth and higher SNR) as well as a short pulse duration in order to obtain high spatial and temporal resolution in the imaging system. However, the penetration depth and the reduced size of the biomolecules under study are still a difficult task in most imaging devices. Thus, highly accurate and sensitive modern optical detection techniques must be developed so that biomolecules with low concentration can be mapped more easily in living samples.

In this chapter, we propose the use of our laser system for spectroscopic applications as a diagnostic device for the evaluation of biological samples. In this sense, we report a first estimation of the absorption measurement capability of the laser system of a gas sample in Section 6.1, leading to the results published in [171]. Afterwards, we propose a modified design of the fiber laser set-up for CARS imaging to enable direct real-time measurements of biological samples in Section 6.2. In this case, an assessment of the laser performance and the imaging capabilities of the complete system have been conducted by simulations, whose findings have been submitted for publication [174].

6.1 Gas sensing

In relation to the environmental field, global warming has become an important concern. Detection and quantification of gases such as carbon dioxide and methane using laser-based trace-gas sensors have attracted a great deal of attention because they introduce a low-cost, high-performance, and highly accurate technological approach that contributes to monitoring air pollution with a view to reducing global warming, while guaranteeing a secure and safe society. As gas quality requirements become more stringent, the use of gas detection systems has become increasingly important for safety and environmental monitoring. Laser-based trace-gas sensor technology is notable for its high sensitivity in comparison to other sensor technologies [175].

The principle of laser-based trace-gas sensor technology is based on the detection of the output energy of an optical source after the interaction with the gas molecules. By absorbing the power of the incident light at a specific wavelength, the gas molecule starts to vibrate. These vibrations can be seen in the spectrum of the output light as a dip in a specific wavelength, measuring what is called the absorption line of the gas molecule. By changing the optical wavelength of the incident pulse, different absorption lines of the gas molecule can be measured. Based on the wavelength position and depth of the dip, we can determine the type and

concentration of the gas under study. Many relevant gas absorption lines related to exhaust fumes fall within this region such as carbon monoxide, carbon dioxide, methane, hydrogen sulfide, and acetylene [176]. Therefore, the use of a broadband spectral laser source is essential for detecting multiple absorption lines at the same time.

As a result of the expansion of the telecommunications industry, fiber-optic components are readily available for the NIR, making it possible to establish fiber lasers as a primary source [177]. In this sense, mode-locked fiber lasers are the preferred approach due to their cost-effectiveness and compactness, where erbium-doped fiber lasers provide an advantage over other laser sources due to their tunability from 1520 to 1580 nm. Furthermore, passive fiber lasers based on saturable absorbers have noteworthy properties due to their thermal and chemical stability as well as their insensitivity to external perturbations. In this work, we presented an InN-based semiconductor material as the saturable absorber used in an Er-doped ring fiber laser cavity for mode-locking operation, obtaining highly stable ultrashort pulses, having a broad absorption capacity, and being capable of supporting high incident powers, demonstrating its thermal stability. These characteristics of the InN-based fiber laser system make it a preferred option for spectroscopic purposes.

In this section, we propose the first application of our laser set-up, centered on gas spectroscopy. To do this, supercontinuum generation has been incorporated at the output of the scheme in order to achieve a broad spectral bandwidth. We present a preliminary demonstration of this gas sensing application by the measurement of hydrogen cyanide ($H^{12}C^{14}N$) and carbon monoxide with a pressure of 5 Torr ($H^{12}C^{16}O$), and with 150 Torr ($H^{13}C^{16}O$) contained in a closed cell.

6.1.1 Supercontinuum generation

In order to measure a broad spectral region, a broad spectral bandwidth signal is demanded. The wider the spectral bandwidth of the incident pulse, the wider the absorption spectrum coverage for a single measurement. To do this, supercontinuum generation (SC) is the most common spectral broadening procedure performed in sensing application systems involving ultrashort pulses. In this section, we will briefly introduce the theory of supercontinuum generation and its use in optical fibers.

The concept of supercontinuum generation has continuously attracted scientific and technological attention since it was first discovered in the early years of nonlinear optics [178]. Supercontinuum light provides ultra-broadband radiation, due to the propagation of intense laser pulses through a nonlinear medium. The adaptability of its spectral bandwidth is one of the greatest advantages of SC sources. The use of their full bandwidth has been demonstrated to be invaluable in applications such as frequency comb metrology, high-capacity multi-wavelength encoding of information, the generation of short pulses of light, and optical sensing and imaging systems.

Multiple materials have been tested for supercontinuum generation, such as a bulk glass of borosilicate [179], nevertheless, the most useful light source is produced within an optical fiber, due to its small effective area (permitting the preservation of the spatial coherence properties of the incident light) and with a considerable

interaction length. The optical properties of the output supercontinuum signal can be controlled depending on the pulse duration, the central frequency and the optical power of the pumping laser source; a shorter incoming pulse will generate a broader frequency extent, while an increase in the incident power implies an enhancement of the broadening factor in the supercontinuum generation. In the case of propagating through an optical fiber, a longer propagation length will increase the SC process. Multiple nonlinear processes, related to the third order susceptibility, such as dispersion, SPM, FWM or SRS, can explain the generation of supercontinuum laser sources in optical fibers [180]. As shown in Chapter 2, the sign of the second-order dispersion coefficient is fundamental to determining the broadening mechanism of the optical pulse while propagating through an optical fiber.

- For $\beta_2 > 0$ (normal dispersion regime) SPM is the dominant effect. In the case of femtosecond pulses, SPM and FWM generate the spectral broadening of the initial unchirped pulse, thus introducing a certain chirp in the output signal. Nevertheless, an additional effect based on SRS is also present.
- On the other hand, in the anomalous dispersion regime ($\beta_2 < 0$), two different scenarios can be produced, the soliton fission regime and the modulation instability regime.
 - For ultrashort pulses with time durations in the femtosecond range, the incident pulse propagates along the optical fiber as a higher-order soliton. This pulse is initially broadened and compressed due to the breathing behavior as a consequence of the dispersion and nonlinear coefficients of the optical fiber. Nevertheless, the presence of higher-order dispersion coefficients and SRS effects leads to the break-up of fundamental solitons (soliton fission), and the pulse broadening towards longer wavelengths due to SRS. This process is known as Raman soliton self-frequency shift. The effects of higher-order dispersion result in the resonant transfer of energy to shorter wavelengths for each newly formed soliton, and the effects of inelastic light scattering within the bandwidth of each soliton lead to an increasing frequency shift. An example of this regime has been accomplished by Ranka et al. [181], where a 100 fs optical pulse in the nanojoule energy region centered at 770 nm, was sent into 75 cm of a photonic crystal fiber (PCF), generating a SC signal spanning from 400 nm to 1500 nm.
 - In contrast to soliton fission, the breakup of picosecond or longer duration pulses in the pumping laser source is generated due to modulation instability (MI) and FWM processes. This phenomenon causes frequency sidebands in the spectrum (Stokes and anti-Stokes), evolving into fundamental optical solitons [182], which subsequently suffer Raman self-frequency shift. An example of a SC generation simulation generated by modulation stability with a temporal duration of 360 fs and a spectral broadening of more than 200 nm has been developed, as shown in Fig. 6.1, by propagating a 250 fs-Gaussian pulse with a peak power of 5 kW through 10 m of SMF based on the code of [183]. The temporal shift of the optical pulse is due to the definition of the temporal window in the simulation code.

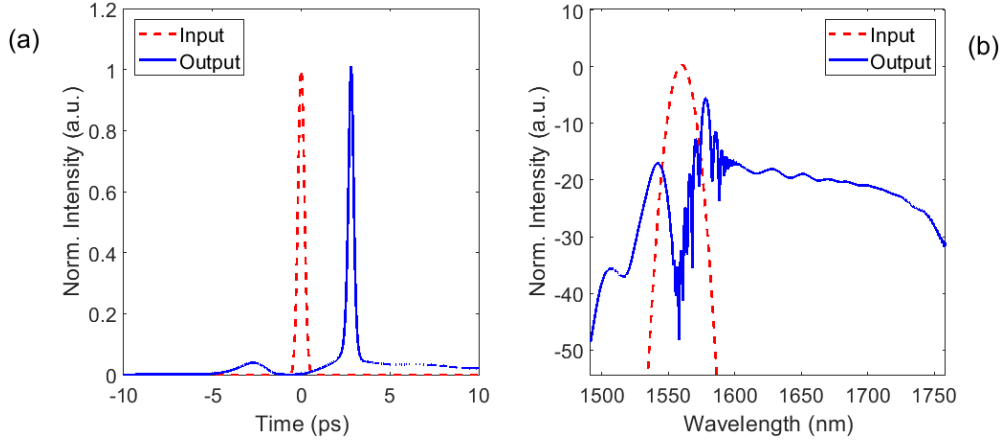


Figure 6.1: Simulation of SC generation of an initial Gaussian pulse with a temporal width of 250 fs and a peak power of 5 kW (red dashed line) propagating through 10 m of SMF. A temporal duration of 360 fs and a spectral broadening of more than 200 nm has been obtained at the output.

6.1.2 Experimental set-up

The laser source has been assembled at instituto de Óptica Daza de Valdés (IO-CSIC) research group, with a similar scheme to the previously-described mode-locking fiber laser used in this thesis. The resonator consists of a ring fiber laser cavity based on SMF, with an EDFA system as the gain medium device and an InN semiconductor material as the saturable absorber. Nonetheless, the SA has been placed in an open-air configuration to simplify the laser set-up [161]. Nevertheless, in order to achieve the appropriate conditions for soliton formation inside the resonator cavity and the temporal and spectral properties demanded for spectroscopic purposes, a reel of 1 km of SMF fiber has been inserted between the SESAM device and the amplification medium [171]. The suitable properties of the initial pulse for SC generation were set so that an ultrafast Gaussian pulse of ~ 240 fs and 25 nm in the spectral domain with a central wavelength of 1560 nm was achieved in the laser cavity with a total distance of 1.05 km (and thus 196 kHz of repetition rate) operating in the anomalous dispersion regime. In order to obtain the maximum output power, a VOA device was also inserted within the laser cavity, capable of controlling the transition between the fundamental mode (maximum energy per pulse in the oscillator) and higher harmonics (see Chapter 5). Therefore, an ultrashort laser pulse with an average power of 30.5 mW was measured at the output of the laser cavity, corresponding to a peak power of 650 kW and a maximum energy of 155 nJ.

Subsequently, another SMF fiber is placed at the output of the laser for SC generation. This fiber is a 2.3 km reel of standard SMF. An analysis of the pulse compression, as well as the maximum power at the output of the broadening fiber, was characterized by an autocorrelator (APE Mini PulseCheck), an OSA device (Yokogawa AQ-6215B) and a power-meter (PM100USB, Thorlabs) respectively after traveling through the 2.3 km-SMF. The optical pulse has been compressed to ~ 100 fs, whose profile has been modified to a Lorentzian shape with a pedestal observable in the autocorrelation function, which can be explained due to the nonlinear

compression of the output soliton pulse of the laser cavity, as shown in Fig. 6.2(a). In the frequency domain, a spectral broadening of more than 200 nm was achieved, expanding the spectral coverage to the red side of the spectral region (see Fig. 6.2(b)). The optical power of the SC pulse was measured in 12.5 mW.

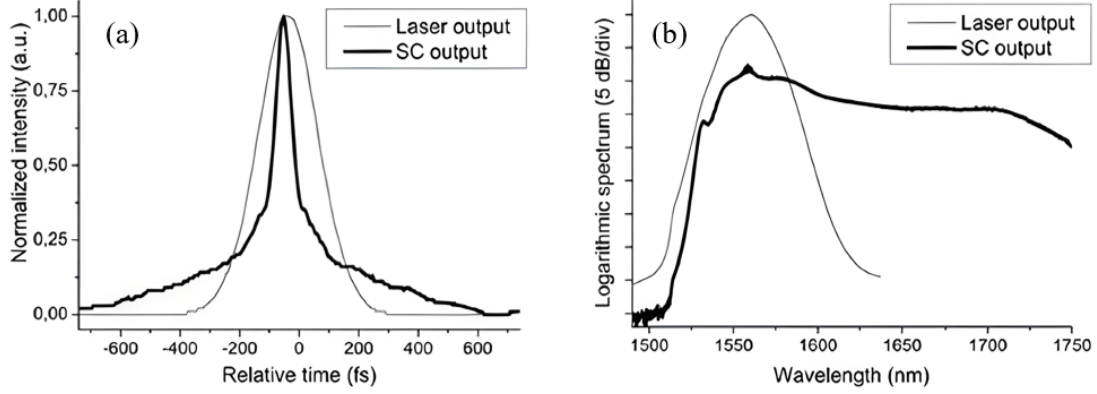


Figure 6.2: Supercontinuum generation characterization at the output of 2.3 km of SMF in terms of (a) autocorrelation function and (b) optical spectrum, represented by a solid black line, when pumped with an ultrafast 240 fs-laser source and a peak power of 650 kW, plotted with a solid grey line [171].

Now that we have demonstrated that a SC generation can be achieved by this laser set-up, a spectroscopic gas station has been developed, capable of analyzing different samples in the NIR spectral region.

6.1.3 Preliminary results

The detection set-up consists of inserting the gas sample between the laser source and the optical photodetector. In its easiest form, the gas sample is located in-line with the laser source in a free-air open-path configuration, characteristic of gas remote sensing applications. The gas is distributed over a certain distance (L) known as optical path. Nevertheless, the intensity attenuation and external contributions of the open-air scheme limit its use to several meters. This laser set-up can be reduced by inserting mirrors located at the sides of a gas cell. The incident light enters the gas cell, where it is reflected multiple times, thus increasing the effective optical path length, named as multipath cell, to hundreds of meters. Compared to the single long-path cell, this method enables an increase in sensitivity, while retaining a simple optical design.

Therefore, in order to obtain the maximum sensitivity in the spectroscopic device and the easiest configuration in a lab environment, a multipath gas cell has been incorporated at the end of the SC generation stage generated by the SMF. The first scheme, although indispensable for remote sensing, has not been used due to lab space limitations. In this sense, the gas cell consists of a ~ 19 cm-long glass tube with two aluminum mirrors, creating 5 internal reflections, corresponding to an effective total length of 80 cm. The gas cell contains a mixture of $H^{12}C^{14}N$ with a pressure of 5 Torr, and two different samples of carbon monoxide, ($^{12}C^{16}O$ and $^{13}C^{16}O$), with a pressure of 150 Torr. These gases have their absorption lines in the

wavelength region between 1500 nm and 1650 nm, therefore the developed SC laser source is suitable for this task. For the purpose of reducing the insertion losses and optical attenuation introduced by the open-path free-air configuration, the gas cell has been configured with fiber optic connectors at the entrance and the output of the gas cell. A 99/1 fiber coupler has been added between the output of the SC generation SMF and the gas cell in order to avoid optical damage due to the high peak power levels achieved by this laser set-up.

The absorption spectrum is measured at the output of the gas cell in transmission configuration and analyzed by an OSA device (Yokogawa AQ-6215B) with a spectral bandwidth ranging from 1500 nm to 1750 nm with an integration time of 2s and a spectral power density much higher than those obtained from LED devices (12.5 mW of average power in 200 nm spectral bandwidth leading to 2.5 nWm compared to 2mW in 120 nm of an IR 1550 nm thorlabs LED with a power spectral density of 0.24 nWm). It must be noted that the spectral function is measured up to 1750 nm due to the limited range of the OSA device. Therefore, the spectral broadening of the output pulse is presumed to be wider. Nevertheless, since we are interested in measuring the HCN and CO gas molecules, we will focus on the spectral range between 1500 and 1650 nm. The optical spectrum measured at the output of the resonator cavity, after the interaction between the gas molecules and the SC pulse, is depicted in Fig. 6.3.

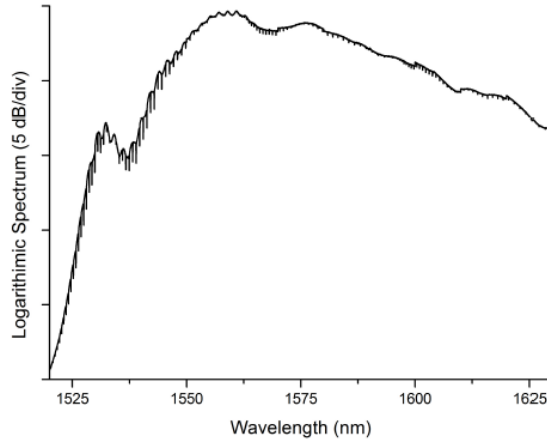


Figure 6.3: Optical spectrum of the SC pulse after the interaction with the $H^{12}C^{14}N$, $^{12}C^{16}O$ and $^{13}C^{16}O$, gas molecules. The absorption lines of the corresponding gas molecule can be observed superimposed on the output pulse measured at the end of the gas cell [171]. The integration of the OSA device is set to 2s.

Since we are measuring in the NIR region, the energetic transitions that are going to be characterized are the vibro-rotational transitions. The vibrational transitions are generated due to the absorption of the energy of the incident pulse and the excitation of the molecule to an upper state ($\Delta\nu = 1$). Nevertheless, this vibrational transition is also composed of rotational transitions divided into branches (R, Q and P), denoted as $\Delta J = 1, 0$ or -1 respectively, which depend on the spin of the molecule under study. In this case, both the R and P branches are observable for each of the gas samples, in contrast to branch Q, less common in gas molecules. Firstly, the absorption lines of the $H^{12}C^{14}N$ compound can be characterized between 1520 nm

and 1555 nm, as shown in Fig. 6.4(a). In the case of carbon monoxide, the R and P branches are measured from 1560 nm to 1595 nm for $^{12}\text{C}^{16}\text{O}$, plotted in Fig. 6.4(b), while for $^{13}\text{C}^{16}\text{O}$, these lines are observable in the 1595 nm to 1630 nm spectral region, as represented in Fig. 6.4(c). These results show a great similarity with the absorption spectra of each of the gas molecules compared to previous calibrations from published literature [184, 185].

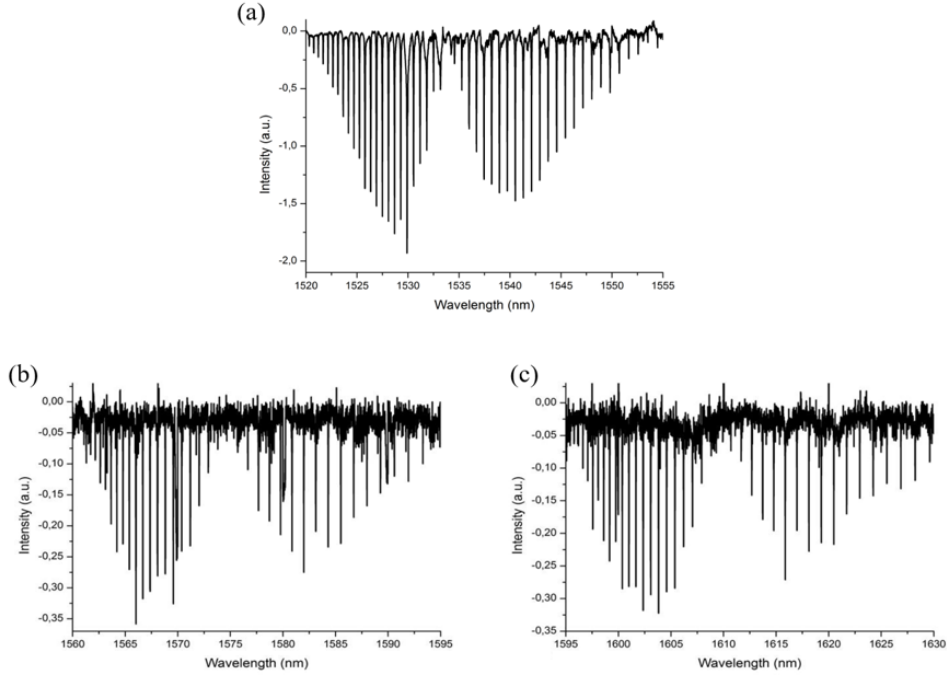


Figure 6.4: Optical spectrum after baseline subtraction of the absorption lines of (a) $\text{H}^{12}\text{C}^{14}\text{N}$, (b) $^{12}\text{C}^{16}\text{O}$, and (c) $^{13}\text{C}^{16}\text{O}$ measured by the in-house SC pulse [171].

6.1.4 Discussion of results

In our work [171], it has been demonstrated the applicability of an ultrashort mode-locked fiber laser with an InN semiconductor as SESAM, for SC generation in the NIR region. These measurements have been conducted in the IO-CSIC facilities, with a similar laser source as the one described in previous chapters. Nevertheless, for simplification purposes, it has been used in the laser set-up with the SA in open-air configuration, since a higher control of the higher harmonic generation is obtained. The properties of the saturable absorber, such as high modulation depth, high nonlinear behavior and a high damage threshold level, has permitted to develop ultrafast Gaussian pulses with a temporal duration as short as 240 fs and a broad initial bandwidth of 25 nm, propagating through a ring fiber resonator cavity based on low-cost SMF with a total length of 1.05 km. The dispersion and nonlinear coefficients of the off-the-shelf components of the laser cavity, enable the propagation of dispersion-managed solitons. Furthermore, a highly stable pulse has been obtained with a repetition rate of 196 kHz, with an average power of 30.5 mW, which corresponds to a peak power of 650 kW and an energy per pulse of 155 nJ. At the output, an ultra-stable SC pulse with an average power of 12.5 mW,

and a maximum measured spectral broadening of >200 nm has been obtained when propagated through 2.3 km of SMF.

The properties of the fiber laser cavity based on an InN SESAM along with the SC generation achieved in SMF propagation, have permitted to develop a simple and low-cost spectroscopic device. The SC generation signal has been utilized as the incident pulse for gas absorption in a sensing device. The incorporation of a gas cell with fiber connectors at the entrance permits the reduction of the insertion losses and external distortions, characteristic of open-air gas detection configurations. The all-fiber connection leads to a lessening of the attenuation losses generated in the links, thus a higher power is introduced within the gas cell. As a consequence, the absorption is measured with higher sensitivities. Preliminary results have been obtained with this sensing set-up, studying and analyzing the absorption lines of a mixture of gases, composed of molecules of HCN and CO at different pressures. The experimental measurements have demonstrated that the SC spectral bandwidth is wide enough to measure the absorption lines of each compound, and even capable of identifying the corresponding vibro-rotational energy transitions.

6.2 Biomedical sensing

The analysis and identification of the different components of a biomolecule become of great importance in the medical field, specifically in the detection and prevention of diseases. The light beams employed in spectroscopic imaging techniques should accomplish certain principles, including enough energy to excite the sample, while reaching a sufficient penetration depth without performing any molecular damage to the sample, as well as a certain recording speed should be accomplished in order to measure the *in vivo* biological processes of the living cell.

In recent years, the number of optical detection systems designed for biological imaging has grown as laser technology has become less expensive, more compact, and more reliable [186]. Despite their robustness and high sensitivity, the vast majority of these systems demonstrate a relatively narrow spectral coverage. Moreover, detection over a large spectrum often requires a long time due to the complexity of the acquisition device. Due to this, a single system can only detect a limited number of molecules. New approaches, such as the use of broadband optical pulses that record large spectral bandwidths at one time, have been investigated to address this problem [187], expanding their spectrum region from the ultraviolet to the far infrared range, via nonlinear conversion due to the high peak intensities of their ultrafast pulses.

In the last decades, new high-speed vibrational imaging techniques have emerged, with improved characteristics in terms of resolution, sensitivity and penetration depth. In relation to this, coherent anti-Stokes Raman scattering (CARS) spectroscopy stands out due to its ultra high-speed acquisition rate as low as 3.5 ms per pixel capable of real-time imaging of small molecules with micromolar concentration.

In this work, we propose the use of an ultrafast fiber laser system as the excitation source in a spectroscopic device for biological imaging as the one used in previous chapters. To do this, the laser pulse shall be temporally compressed (spec-

trally expanded) in order to achieve the broadest possible pulse in the frequency domain, which will be used to cover the maximum molecular spectral range in one measurement. Therefore, in the next section, we will explain the main techniques for pulse compression in the femtosecond range. Subsequently, we describe the laser set-up used in this work to accomplish the required characteristics for biological spectroscopy, which have also been validated by numerical simulations carried out with a MATLAB software.

6.2.1 Pulse compression for high-power laser systems

Nonlinear pulse compression can be achieved in optical fibers by the correct selection of the dispersion and nonlinear optical properties of the fiber to obtain the minimum temporal duration at the output after propagation of an initial chirped or unchirped pulse. Nonlinear pulse compression in fiber optics can be grouped into two main categories, depending on the configuration and optical elements employed, based on the use of soliton-effect compressors or with grating-fibers.

- In relation to soliton-effect compressors, the input pulse propagates through an optical fiber in the anomalous dispersion regime, where the nonlinear effect of SPM increases the optical bandwidth, creating a chirped pulse at the output with a larger temporal duration as the one measured at the entrance. Subsequently, the chirp parameter is counteracted by the dispersion coefficient of the optical fiber, and thus the pulse duration is strongly reduced [188]. The length of the optical fiber is suitably chosen for the required characteristics at the output. The maximum pulse compression will depend on the initial peak power (and thus on the soliton order N). However, the compressed pulse has a lower pulse quality since only a fraction of the input energy is conserved, leaving the remainder as a broad pedestal. A solution can be achieved by using the dispersion management method, so that the average GVD is relatively small, but the value of β_3 is high. An example of this pulse compression method has been observed in the temporal evolution of the optical pulse while travelling through the ring fiber laser cavity used in this work, as described in Chapter 4.
- By contrast, in grating-fiber compressors, the input pulse is initially broadened in the spectral domain by propagating it in a normal dispersion fiber, leading to a positively chirped output pulse. Then, the optical pulse is sent through a grating pair (prism pair, a chirped mirror or diffraction grating, among others), compressing it temporally due to the anomalous GVD coefficient (each frequency suffers a different phase-shift, i.e., the trailing edge catches up the leading edge of the pulse).

Depending on the desired compression, the dispersion coefficient GDD introduced by the grating pair can be controlled by the length between the two elements as,

$$GDD = -\frac{m^2 \lambda^3 L}{2\pi c^2 \Lambda^2} \left[1 - \left(-m \frac{\lambda}{\Lambda} - \sin \theta_i \right)^2 \right]^{-3/2}. \quad (6.1)$$

Therefore, the amount of dispersion introduced by the grating pair depends on its characteristics, including the grating pair distance L , the number of lines per length in the grating pair (period Λ) and the diffraction order $m = 0, \pm 1, \pm 2, \dots$, which depends on the type of configuration (positive values for transmission configuration and negative for reflection), and the number of passes (1 for single pass, 2 for double pass, etc.). Furthermore, we can observe from this equation how the dispersion depends on the incident wavelength as well as the angle of incidence (θ_i) of the optical pulse. In general, the manufacturer specifies the appropriate angle of incidence in order to obtain the maximum transmission/reflection through the grating pair, commonly around 30° . The grating separation required to compress the incident pulse will depend on the amount of positive chirp to compensate. In this sense, for femtosecond pulses, $L_g \sim 10$ cm or less, whereas for longer pulses, the distance becomes impractically large (>10 m).

Nevertheless, the grating pair compressor system presents some disadvantages, such as spatial dispersion and diffraction losses [189]. The cross-section of the incident beam diverges when passing through the grating pair, varying from a Gaussian shape to a more elliptical form. This deformation becomes important as the separation between the gratings increases. Nonetheless, this effect can be minimized by sending back the optical beam through the grating pair, that is, a double-pass configuration. In this double-pass configuration, the beam is recollimated into its original cross-section form, while doubling the GDD coefficient, which reduces the grating separation by a factor of 2.

The design of the all-fiber spectroscopy laser source is explained in the next section. In this work, we have employed both the soliton and the grating pair scheme for pulse compression in order to achieve the required characteristics in the optical pulse for spectroscopic devices.

6.2.2 Design of the “all-fiber” spectroscopy laser source

The objective of this section is to create a laser system capable of analyzing different biological samples at different optical wavelengths with enough resolution, while reaching the maximum penetration depth achievable without loss of energy due to scattering or other external disturbances. To do so, a spectroscopic device based on CARS spectroscopy has been designed for the real-time identification of molecules by studying their chemical bonds (vibrational frequencies).

Raman’s spectra can be divided into two areas based on the wavenumber of the vibrational transitions involved: the low wavenumber region or fingerprint, which varies from 800 to 1800 cm^{-1} ($5\text{ }\mu\text{m}$ - $15\text{ }\mu\text{m}$), and the high wavenumber or lipid region, which varies from 2800 to 3800 cm^{-1} ($2.5\text{ }\mu\text{m}$ - $3.5\text{ }\mu\text{m}$). Together, the fingerprint and lipid regions provide a more accurate biochemical analysis of the sample composition.

In terms of detection, the Raman scattered light is typically collected by a spectrograph. Nevertheless, higher resolution detection systems based on interferometers for Fourier Transform (FT) detection can also be incorporated. Multiple schemes

have been proposed for measuring both the fingerprint and the lipid region at the same time. In its simplest form, an InGaAs detector, which operates in the spectral region from $0.9\ \mu\text{m}$ to $1.7\ \mu\text{m}$, can be applied for measuring the fingerprint region. Preliminary results of the analysis of biological samples such as polystyrene and polyethylene microspheres by a CARS spectroscopic device have been obtained [190]. Nevertheless, only a small portion of the lipid region can be registered with this photodetector with low resolution.

An alternative relies on using two separate laser sources with different wavelengths, centered in the fingerprint and lipid regions, respectively. This type of laser set-ups allows for obtaining greater resolutions due to temporal synchronization in the sample plane (nonlinear Raman spectroscopy). Each of the wavelengths is transmitted through the sample under study, whose backscattered light is collected by a charge-coupled device (CCD). An example of this scheme is employed by our collaborators in the UltraFast Laser (UFL) group in James C. Wyant of Optical Sciences from the University of Arizona (Tucson, United States of America), which consists of an all-fiber laser system emitting pulses at $1550\ \text{nm}$, and generating the two wavelengths by nonlinear processes. The development and study of the biological samples by the spectroscopic device, as well as the construction of the laser set-up, have been performed in the University of Arizona facilities.

- Laser cavity:

In order to generate the ultrafast pulse, a ring fiber resonator cavity based on mode-locked generation is employed. The laser cavity consists of $15\ \text{m}$ of SMF, where a single-mode telecom-grade $980\ \text{nm}$ diode pump laser signal is inserted within the resonator by $1\ \text{m}$ of $980/1550\ \text{nm}$ WDM fiber coupler device (Corning). The signal is amplified by an Er-doped fiber (Liekki) with a length of $2\ \text{m}$, where a fiber optical isolator is added to ensure unidirectional operation within the laser cavity. The mode-locking operation is achieved by the SA, based on a SWCNT-polymer composite (single-wall carbon-nanotubes), embedded in the optical fiber in a tapered-fiber form. This type of SA has been characterized in previous works by the UFL group [191,192]. The mode-locking operation is optimized by a polarization fiber controller, since in this case the SA is polarization dependent. The mode-locking operation is initialized when the pump power is above $90\ \text{mW}$, where the slow SA begins the self-starting operation mode. The net dispersion coefficient of the ring fiber resonator cavity is $-0.1\ \text{ps}^2$, thus the laser works in the anomalous dispersion regime. The laser cavity set-up is plotted in Fig. 6.5 delimited by red dashed lines.

At the maximum pump power of $260\ \text{mW}$, the resonator cavity output power, measured by a universal fiber optic detector (818-IS-1, Newport), is $4\ \text{mW}$ in the form of a train of Gaussian pulses separated by a repetition rate of $14\ \text{MHz}$ and a SNR of $70\ \text{dB}$. The output pulse duration was measured in $\sim 1\ \text{ps}$ measured by an autocorrelator (FR-103XL, Femtochrome Research Inc.) and visualized by an oscilloscope (TDS1002, Tektronix), corresponding to a peak power of $40\ \text{W}$ and an energy per pulse of $40\ \text{pJ}$. In the spectral domain, the output pulse, measured by an OSA (MS9710B, Anritsu), is centered at $1561\ \text{nm}$ with a maximum bandwidth of $4\ \text{nm}$. It must be noted that in this

case, no Kelly sidebands are observable in the fundamental harmonic optical spectrum, due to the dispersion management in the laser cavity.

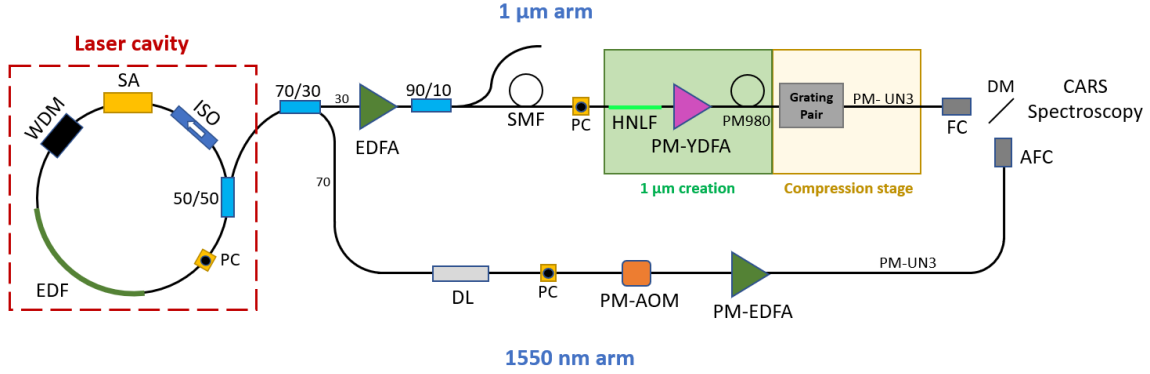


Figure 6.5: Representation of the all-fiber laser scheme for its application as the main laser source in the spectroscopic device based on the CARS technique. Two different branches have been defined for this purpose, named as 1 μm arm and the 1550 nm arm, where multiple types of fibers, such as SMF, HNLFF, PM980 and UN3, are employed to acquire the required pulse's characteristics for high-quality spectroscopic images.

- Dual-comb formation:

As explained in Chapter 3, the spectroscopic device is based on nonlinear Raman effects, in which two narrowband pulses (pump and Stokes beams) are used. Therefore, we need to create two separate pulses at different wavelengths. In this work, we propose to use the above-described laser source, to generate the two wavelengths through two different laser arms, as depicted in Fig. 6.5, named as the 1 μm arm and the 1550 nm arm. The output laser signal is divided by a 70/30 fiber coupler, where the 30% of the output laser cavity power corresponds to the 1 μm arm, whereas the remaining 70 % of optical power is sent to the 1550 nm arm.

- In the case of the upper arm, which will correspond to the excitation source centered at 1 μm , the output 1550 nm laser cavity signal is amplified by a 7 m-long EDFA (Coractive EDF-L900), with a maximum gain of 18 dB, expanding the output pulse laser to 38 nm of spectral bandwidth and 500 fs in the temporal domain, with a maximum average power of 100 mW. Then, the pulse is split into two arms by a 90/10 fiber coupler for monitoring purposes. The 90 mW power pulse is spliced to 1.5 m of SMF for soliton compression of the up-chirped pulse. At this point, we will use the above-described SC generation method to create the 1 μm seed pulse. To achieve this, we insert a HNLFF (OFS) at the output of the SMF with a total length of 5 cm and a dispersion coefficient of $6.3 \cdot 10^{-27} \text{ s}^2/\text{m}$ and $\beta_3 = 5.7 \cdot 10^{-42} \text{ s}^3/\text{m}$ as the TOD value, whereas in the case of nonlinear properties, the SPM coefficient is $\gamma = 23 \cdot 10^{-3} \text{ W}^{-1}/\text{m}^{-1}$. Nevertheless, a $\sim 20\%$ total loss is generated between the SMF and HNLFF due to the optical fiber splice (due to the difference in the fiber diameter). The 1 μm output pulse generated in the broadening fiber due to

SC generation is amplified by a lab-built Ytterbium-doped fiber amplifier (YDFA, Yb1200-12/125DC-PM, Liekki), controlled by a laser diode driver (Model 5700-30, Newport) and a Modular Temperature Controller (Model 8000, Newport) with a maximum power supply of 17 A (DLM8-75, Sorensen), obtaining a maximum average power of 100 mW for the 1 μm pulse. Polarization fiber controllers and polarization-maintaining optical fibers (PM) have been added to the laser set-up in order to optimize the maximum optical power generated in the 1 μm arm, as well as to maintain the stability of the mode-locking train of pulses. At the output of the amplification stage, a PM980 (PANDA PM-980, Corning) optical fiber is included in order to compensate the optical chirp generated by the HNLF and the YDFA.

Nevertheless, as it was mentioned in Section 6.2.1, it is essential to obtain an optical pulse with a broad spectral bandwidth as to measure the maximum absorption peaks of the sample under study in a single measurement. In this sense, we propose the incorporation of a pulse compression scheme based on a grating pair (Edmund Optics), located at the output of the 1 μm arm, as denoted in Fig. 6.5.

Pulse compression scheme:

A representation of the laser pulse compression scheme is given in Fig. 6.6. At the output of the PM980, the fiber laser pulse is transmitted in free-space through an optical isolator (F1-1060-3SC, Isolite) in order to protect the resonator cavity from backward laser signal. Then, the optical pulse is dechirped by a reflective grating pair, denoted as G_1 and G_2 . In order to compensate for the beam deformation effects of the grating pair, a double-pass configuration has been applied by introducing a highly-reflective Ag mirror (M_2). The output pulse is then reflected by a dichroic mirror (M_1), and introduced back again in an optical fiber for spectral broadening purposes. It is possible to separate the path of the compressed pulse from that of the input pulse by slightly tilting the reflecting mirror M_2 so that the mirror M_1 is out of the incident pulse path, and thus avoid additional optical power losses in the pulse compression stage. The addition of half-wave plates (P_1 and P_2), is included in the compression scheme in order to control the polarization state of the 1 μm pulse.

Once the 1 μm pulse is compressed temporally to its minimum value, in this case 80 fs, the optical pulse is sent through a broadening UN3 fiber (SCF-UN-3/125-25-PM, CorActive), which broadens the pulse spectrally up to 250 nm, while having a temporal width of 8 ps.

- On the other hand, the other branch of the laser set-up, described as the 1550 nm arm, is composed by an EDFA, similar to the one employed in the 1 μm arm, which amplifies the 1550 nm output laser cavity pulse up to 70 mW of average power. Furthermore, a delay-line (DL, F-VDL-1-3-FA-P, Newport) and a fiber coupled acousto-optic modulator (AOM, TEM-200-25-20-2FP, Brimrose) have been incorporated into the 1550 nm arm, since both devices are indispensable to perform the CARS measurement. In addition to this, a UN3 broadening fiber is included at the end of the

amplifying EDFA device in order to obtain the appropriate characteristics required to achieve the maximum resolution in the spectroscopic device, as it will be explained below.

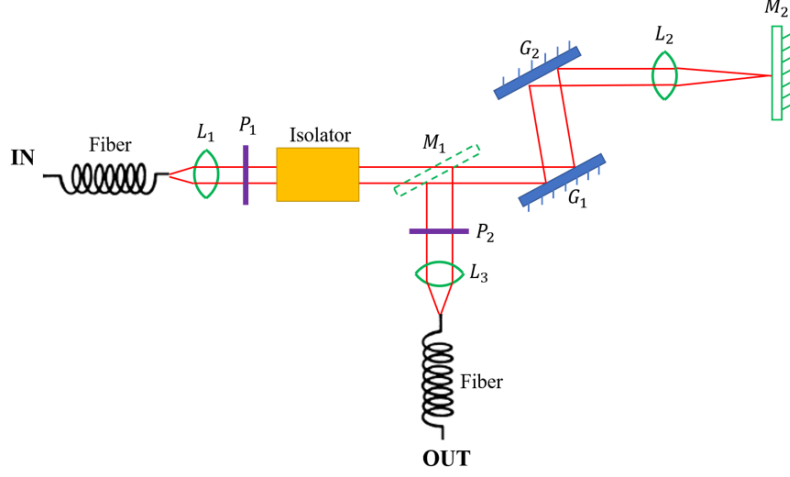


Figure 6.6: Pulse compression scheme of the 1 μm arm based on a grating pair configuration in reflection mode.

- Imaging components:

The imaging configuration is represented in Fig. 6.7, where the CARS signal is analyzed by the use of dichroic mirrors (DM, PBS513) in kinematic fluorescence filter cubes (DFM1, Thorlabs), which separates spatially both the pump and Stokes pulses, and microscope objectives to focus on the sample, whereas the anti-Stokes pulse centered in the visible range is measured by photomultiplier modules (PMT, H10720-20, Hamamatsu). The experimental data is amplified and analyzed by a lock-in device (Zurich Instruments) and recorded by a digitizer, both controlled by a LabVIEW® software program.

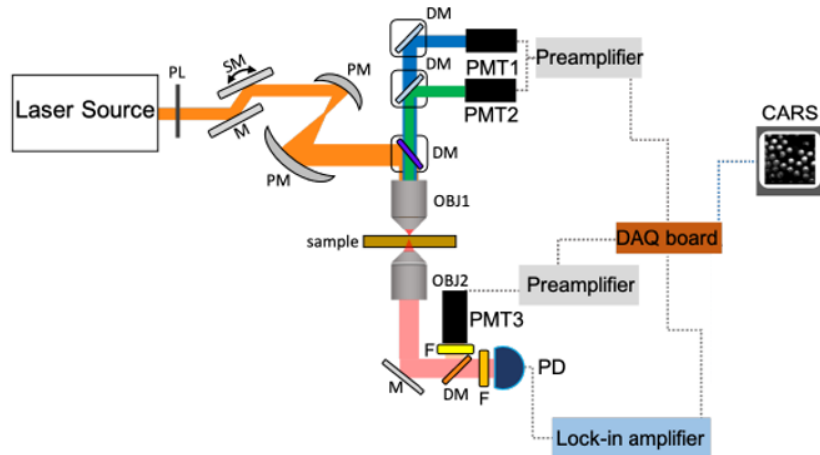


Figure 6.7: Schematic of the spectroscopic imaging system for the study of the biological samples [193].

In order to demonstrate that this above-described system is capable of obtaining a better resolution and spectral coverage than those obtained in previous results [190, 193], we developed a complete simulation code. The purpose of the present section is to develop a quantitative interpretation tool for the time-resolved coherent Raman scattering experiments by analyzing the relationship between pump and Stokes beam pulse bandwidths with respect to spectral resolution and spectral coverage with a complete simulation code done in MATLAB®, as well as to provide an insight on how the laser set-up can be improved. Finally, we employed this code for our particular laser system based on an InN semiconductor as SESAM, by using the optical pulses obtained in Chapter 5.

6.2.3 Numerical simulations

Coherent anti-Stokes Raman scattering (CARS) is the most recognized method in molecular spectroscopy due to its inherent characteristics such as high sensitivity and three-dimensional imaging capabilities.

CARS was firstly introduced in 2004 by Hellerer et al. [194]. It consists of the enhancement of the anti-Stokes (AS) signal when the difference between the pump and Stokes frequencies coincides with a Raman resonance of the sample under study. In order to obtain higher energy while retaining the desired spectral resolution, (defined as the ability to distinguish two close lying resonances), along with a high-speed acquisition, a linear chirp on the optical pulses is introduced. To do this, a dispersive medium, such as prisms, spatial modulators, or dispersion gratings, among others, is incorporated into the laser set-up, adapting the temporal and spectral pulsewidths of both pump and Stokes pulses. When the chirp of the pump and the Stokes pulses coincides, the laser is said to be in the chirp-matching condition, enhancing the resolution. This technique is known as spectral-focusing (SF). A schematic representation of a SF-CARS spectroscopy fiber laser is represented in Fig. 6.8. Initially, each pulse (pump at the top and Stokes at the bottom) is unchirped. After the propagation through a nonlinear medium, these chirps are modified in such a way as to coincide temporally and spatially in the focal plane of the sample under study (cross-correlation of the two pulses).

Parameters of SF-CARS spectroscopy:

- Previously, we discussed that the difference between the frequency components of the pump and Stokes electric fields, denoted as a single narrowed instantaneous frequency difference (IFD), is tuned around a single Raman coherence frequency ω_R . As the chirp rates for the Stokes pulses and pump pulses become closer, the bandwidth of the beating signal (cross-correlation) of these pulses becomes narrower. So, by achieving the chirp-matching condition, a constant IFD value is ensured across the whole pulsewidth, optimizing the CARS spectral resolution. Each of the Raman frequencies of the molecule under study can be analyzed by changing the temporal overlap between the pump and Stokes pulses, thus varying the IFD value with time, represented hereafter as Ω , as denoted in Fig. 6.8.

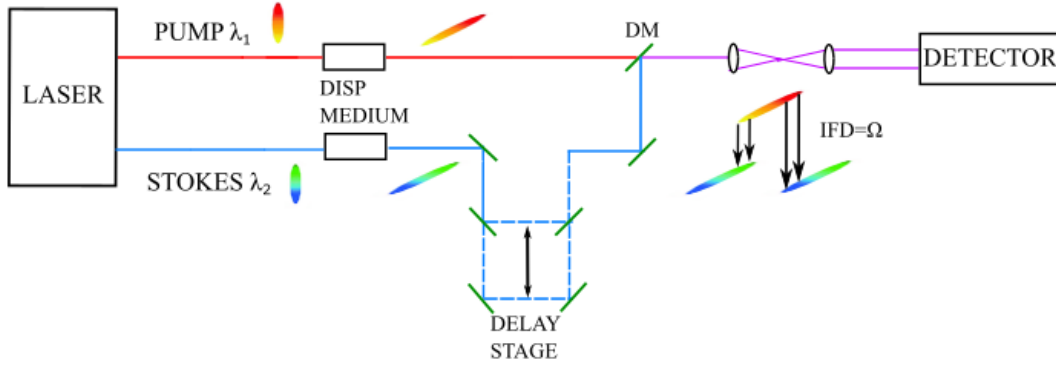


Figure 6.8: SF-CARS spectroscopy fiber laser scheme, showing the chirp-matching evolution.

- The spectral resolution of SF-CARS can be described as the bandwidth of this temporal interaction, which depends on the bandwidth of each chirped pump and Stokes pulses, as well as by the similarity of the chirps. The spectral resolution is maximum when the chirp of the pump and Stokes pulses are made to coincide. In the case of Gaussian pulses, an approximate equation of the spectral resolution ($\Delta\nu$ represented in cm^{-1} units) can be obtained in the chirp-matching case as described in [195], and simplified so that it only depends on the width of the pump (τ_p) and Stokes (τ_s) pulses as,

$$\Delta\nu = \frac{2 \ln 2}{\pi c} \sqrt{2 (\tau_p^{-2} + \tau_s^{-2})} , \quad (6.2)$$

Fig. 6.9(a) shows an example of the maximum spectral resolution of the cross-correlation of the two Gaussian pulses with $\tau_p=8$ ps and $\tau_s=4$ ps. Three different time delays are shown in the indent of Fig. 6.9(a) for the overlapping of the pump pulse (blue line) and Stokes pulse (orange dashed line).

- The anti-Stokes signal is characterized by $\omega_p + (\omega_p - \omega_s)$. Therefore, the spectral range ($\Delta\omega_{AS}$), i.e., the range of vibrational frequencies that can be assessed by the CARS system, can be obtained from the AS intensity signal width over time. This intensity can be approximated to $I_{AS}(t) \propto I_p^2(t) \cdot I_s(t)$, when scanning at different time delays.

In order to evaluate all these parameters, we represent both the pulse duration and spectral width of the pump and Stokes pulses in a spectrogram, as depicted in Fig. 6.9 (b), which provides a better understanding of the influence of pulse widths, interactions, and chirp on the spectral resolution of the CARS system. The spectrogram consists of a time-frequency map representation of the instantaneous frequencies of the optical pulses as a function of time, where the chirp is obtained as the slope of the signal trace. In this sense, the optical pulse is said to be up-chirped if the instantaneous frequency increases with time. The chirp-matching condition is therefore easily checked in this figure by comparing the pump and Stokes chirp slopes. Furthermore, the TBP value can be easily obtained from this figure, measured as the area of each of the ellipses (product of the temporal and frequency widths).

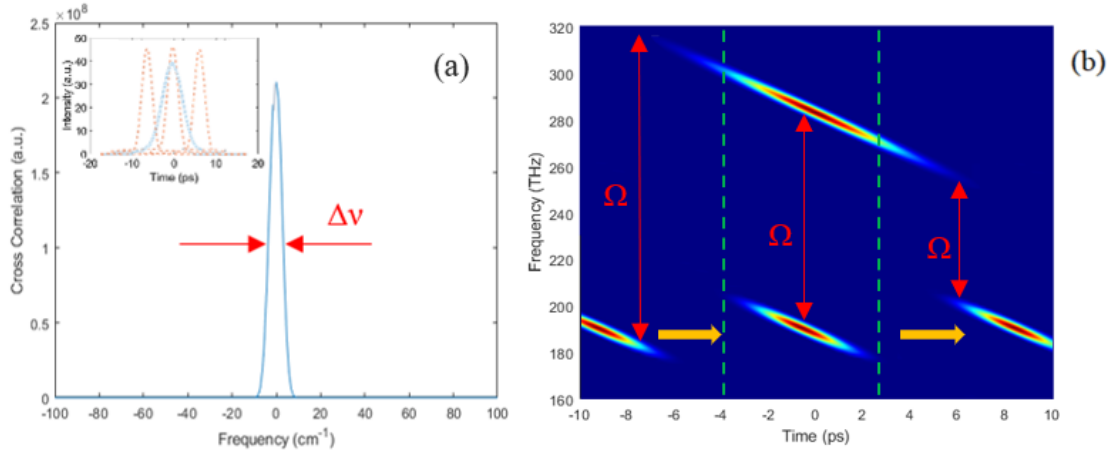


Figure 6.9: (a) Estimation of the spectral resolution of the anti-Stokes signal resulting from the cross-correlation between two Gaussian pulses at maximum interplay ($t=0$). The inset shows the evolution of the Gaussian pump (blue line) with 8 ps of pulse duration and Stokes (orange dashed line) pulse with a pulsewidth of 4 ps overlapping for three different time delays (pre-interaction, maximum interaction, and post-interaction). (b) IFD and spectral coverage calculation by the representation of Gaussian ultrashort pump and Stokes pulses with linear chirp in a time-frequency configuration, where the region under study is represented by a green dashed line at each time delay [174].

The IFD value, expressed as Ω in Fig. 6.9(b), is calculated at each time delay as the pump-Stokes frequency difference, which remains constant throughout the pulse duration of the interaction, but increases as one of the pulses is delayed in time. Two different regimes can be differentiated depending on the sign of the delay. The introduced delay is considered positive when the pump beam arrives before the Stokes beam, leading to a smaller IFD as the delay increases. Whereas, if the delay is negative, the IFD becomes larger as a function of delay time. An example of a positive delay is represented in Fig. 6.9(b). The easiest way to measure the spectral coverage of the CARS signal is by obtaining the maximum and minimum frequency differences over time, which mainly depends on the bandwidth of the pump and Stokes beams. It must be noted that since only a few frequencies of the pump and Stokes overlap in time, the excitation is restricted to the region around the Raman resonance frequency at each time delay, defined by what is called amplitude shaping, plotted in Fig. 6.9(b) with green-dashed lines. The out-of-resonance frequencies become part of the background noise. In order to reduce and eliminate the background noise, multiple techniques have been developed in recent years such as polarization-sensitive detection, Epi-CARS spectroscopy, or frequency modulation CARS [196, 197].

In the case of higher-order nonlinear contributions, the chirp is no longer linear, leading to a non-constant IFD value that changes over the pulse duration. This implies a reduction of the CARS signal intensity (thus deteriorating the spectral coverage) and a decreased spectral resolution of the spectroscopic device. A similar result can also be attained when the pulses are not chirp-matched, in which different slopes generate different IFD values in time and less output intensity.

Raman spectrogram:

The relation between the bandwidth of the pump and Stokes pulses and the spectral resolution is nontrivial. A small change in the chirp parameters as a result of spurious dispersion can deteriorate the spectral resolution.

This study attempts to find the optimal operating point of widely used commercially available fiber lasers by varying their pulse widths, energy, and chirp parameters. To do this, we developed a set of equations for the description of the AS signal obtained from the interaction of two pulses at frequencies centered at ω_p for the pump and ω_s for the Stokes beam, as well as linear and nonlinear effects such as GVD, TOD or SPM, among others, by the generalized nonlinear Schrödinger equation (GNLSE). For an adequate description of the CARS signal, the Matlab code implemented in the model has been performed in the time domain with 2^{15} nodes in the computational grid with a temporal step of 15 fs. Moreover, Fourier transforms and matrix calculations have been included in the simulation to speed up the CARS field calculation. The code analyzes the resolution and coverage of CARS systems and gives the user a clear idea of their limitations. The simulation procedure can be listed in the following steps:

- i A time-frequency representation of the pump and Stokes beams (spectrogram) is used to check the condition of chirp-matching, and also to account for possible nonlinear effects of GVD and TOD on the pulse shape that could adversely affect coverage and resolution.
- ii Subsequently, we calculate the IFD value at each time delay between the pump and Stokes pulses. Additionally, the intensities of the AS and Raman signals are calculated during the pulse overlap, obtaining what is called the CARS spectrum and Raman spectrogram, which will be defined in the next section.
- iii Finally, the spectral coverage and spectral resolution are obtained at each time delay.

In the spectrogram, we firstly represent the simulated optical pulse in the temporal ($I(t)$) and frequency domain ($I(\nu)$), whose size is determined by the number of points (n) introduced in the simulation code. Therefore, the spectrogram is created as a $I(\nu, t)$ intensity matrix for each pulse. When a certain delay is introduced in the Stokes beam, the AS signal would therefore be measured as the difference in frequency between the pump and Stokes matrices. In order to accelerate the simulation, a single frequency value of the pump beam ν_i is selected instead of the whole matrix, calculating the output AS beam as the difference of the intensity vectors between the pump $I(\nu_i)$ with respect to all frequency vectors of the Stokes beam $I(\nu_{i,j})$, which will be equivalent to introducing a delay in that frequency vector of the Stokes beam.

The IFD value would be calculated in the same way by the difference of the Ω_i and Ω_j values of the pump and Stokes beams at each time delay, respectively. A scheme with the corresponding steps for the intensity calculation is shown in Fig. 6.10(a).

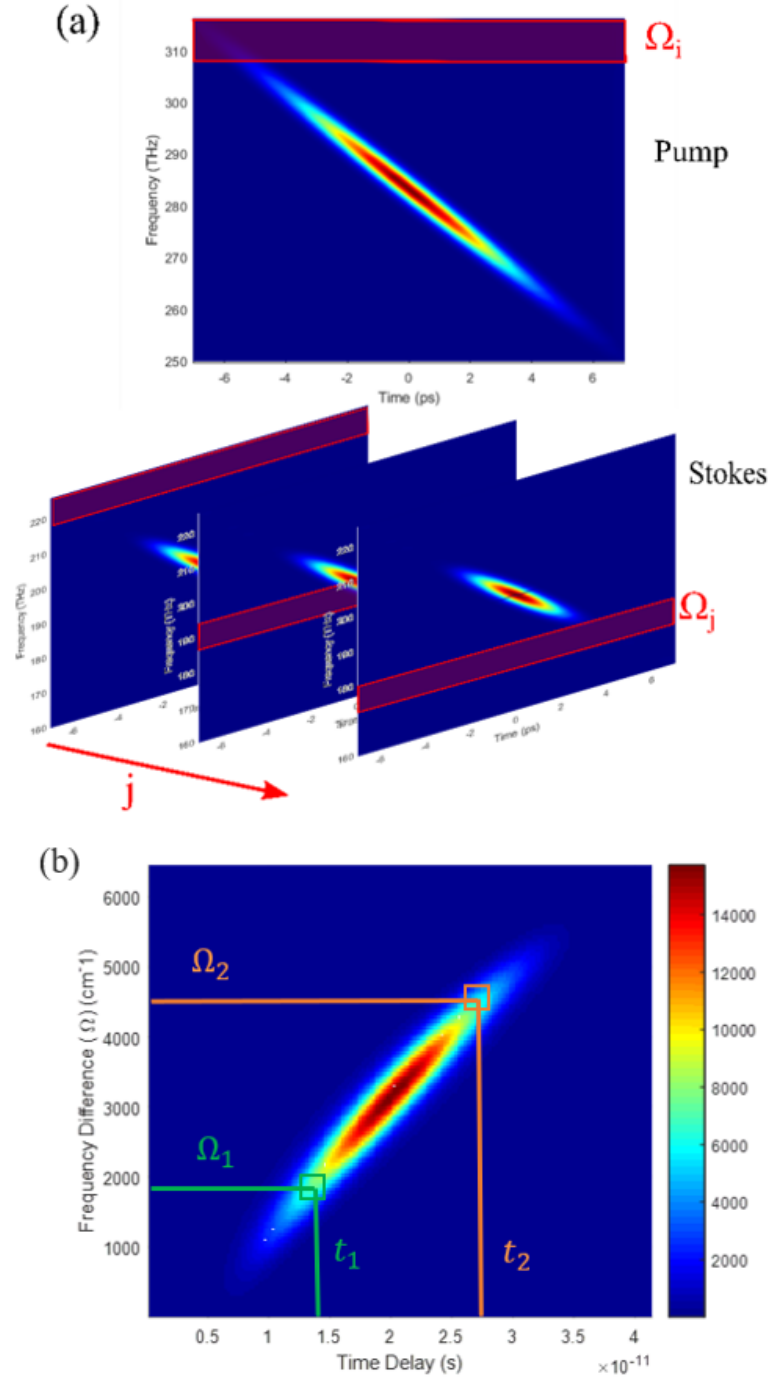


Figure 6.10: Diagram with the steps required to run the MATLAB CARS simulation code (a) Calculation of the IFD between the pump (up) and Stokes (down) pulse at each time delay. (b) the Raman spectrogram is developed by analyzing the anti-Stokes signal intensity in terms of time delay and the IFD. A colorbar function is used to differentiate between clusters at different IFD frequencies. The spectral coverage limits are indicated by a green and orange line, respectively [174].

In order to analyze and plot all these values, we collect AS signal intensities with similar IFD values, measuring the average intensity and representing it as a function of the IFD value and the corresponding time delay, generating what we call

the Raman spectrogram. An example of this schematic representation is shown in Fig. 6.10(b). From this representation, the spectral coverage and spectral resolution can be easily calculated. The spectral coverage is derived as the minimum (Ω_1) and maximum (Ω_2) limits, where the maximum value of the intensity in the Raman spectrogram decays to its half value (FWHM of the AS signal), as represented in Fig. 6.10(b) with an orange and green line respectively. This figure may also give us information on the time delay region of interest, where the two pulses fully overlap. The spectral resolution, on the other hand, can be measured as the FWHM of the cross-correlation function of the AS beam at each time delay, generating a resolution vector that varies during the pump and Stokes pulse overlap (region of coincidence). Therefore, the spectral resolution will be defined over the same region limits as the one described for the spectral coverage.

6.2.3.1 CARS simulation of the laser set-up

We first validated this Matlab code by simulating the optical pulses of the fiber laser set-up of Fig. 6.5 (using the GNLSE). In this case, the 1560 nm incident beam is elongated by SC generation, where the pump beam is now centered at 1040 nm. The pump beam duration is 13.4 ps (in the AC trace), with a spectral bandwidth of ~ 288 nm, whereas the Stokes beam has a pulse width of 1 ps, and a bandwidth of 47 nm in the spectral domain. These results give a chirp parameter of $C = 5.9$ and $C = 5.8$ respectively, therefore the chirp-matching condition is still fulfilled, essential for SF-CARS. The spectrograms of each of the pulses are represented in Fig. 6.11(a), where the slope of the pump beam (up) is parallel to the slope of the Stokes beam (down), that is, they have the same chirp value. At this point, two different scenarios can be presented.

- 1) In the first case, we will consider the 1040 nm beam as the pump pulse, whereas the one centered at 1560 nm is the Stokes beam. The two pulses are made to interact temporally and spatially on the sample surface under study, where a CARS signal is generated and measured by the photodetector. In relation to the Raman spectrogram obtained from these simulated results, the region that can be accessed with this new configuration is from 1905 cm^{-1} to 3650 cm^{-1} , as shown in Fig. 6.11(b), thus extending the lipid region absorption spectra to lower wavenumbers (and therefore approximating the fingerprint region) in comparison to previous results, which were only centered in the lipid region. In relation to the resolution, a Gaussian cross-correlation signal with a FWHM of 25 cm^{-1} has been measured, centered in the 3000 cm^{-1} wavenumber region, demonstrating a constant behavior along the region of interest (see Fig. 6.11(c)). However, due to the use of pulses with higher intensities (and therefore higher contributions of nonlinear components), a small percentage of nonlinear chirp to the pump beam in the form of a tail at higher frequencies is introduced, as shown in the Fig. 6.11(a). This nonlinear contribution may be related to the dispersion compensation in the pulse compression stage generated by the grating pair. If the optical pulse is not fully dechirped during pulse compression, an additional contribution of dispersion appears in the spectral bandwidth leading to some distortions in the optical pulse. Therefore, a balance between high intensity pulses, and the nonlinear effects generated during the pulse compression must be taken into account.

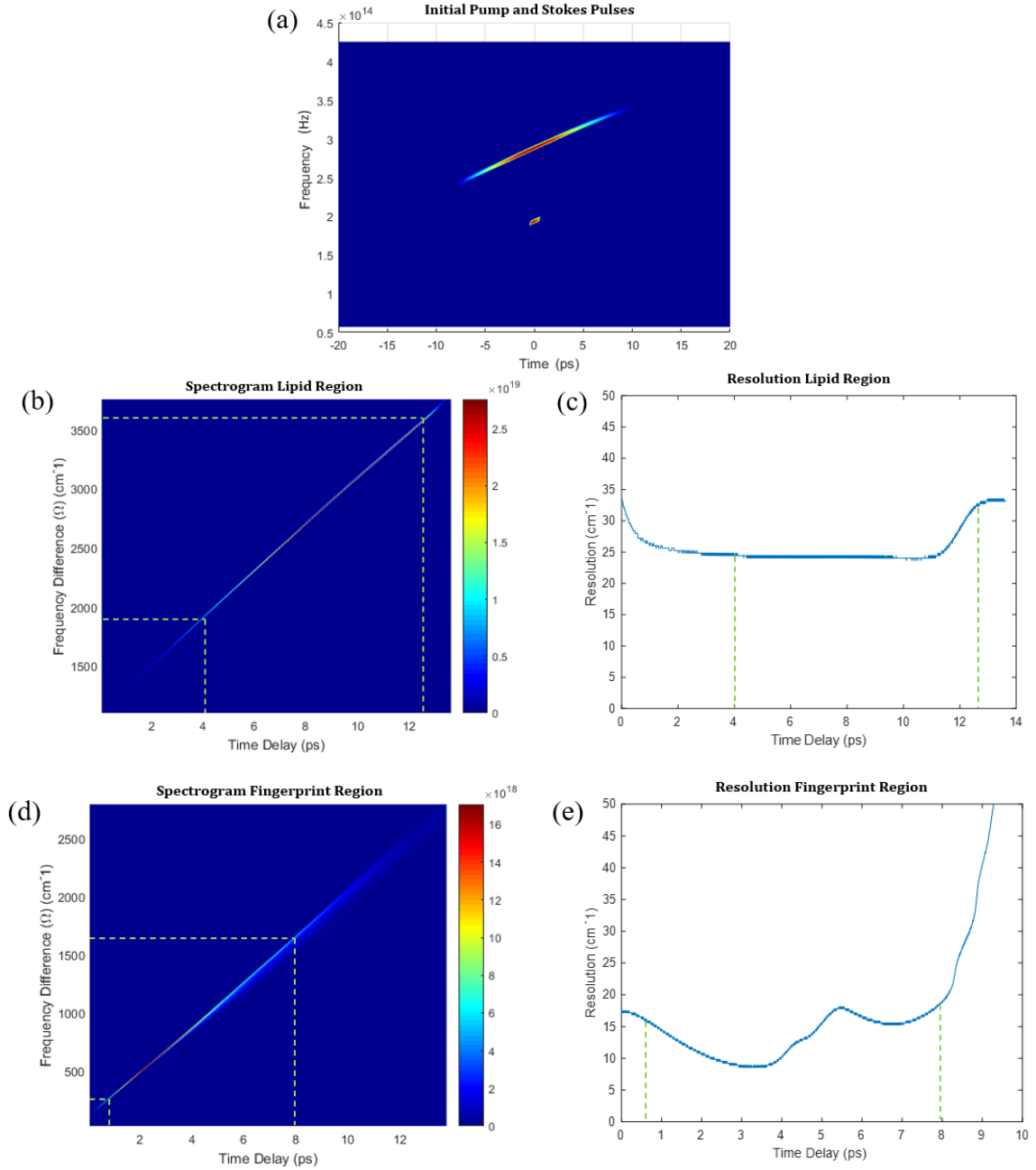


Figure 6.11: CARS simulated results of the laser set-up, (a) Pump (up) and Stokes (down) beams centered at 1040 nm and 1560 nm respectively, with a parallel slope and a chirp value of $C=5.8$. (b) Raman spectrogram of the pump-Stokes pulse interaction centered in the lipid region and with a spectral coverage ranging from 1900 cm^{-1} to 3650 cm^{-1} , and (c) Spectral resolution calculation from the cross-correlation function with a mean value of 25 cm^{-1} . (d) whereas in the case of the pump and virtual Stokes pulses (where the pump beam has been divided into two parts and made to interact with each other), a Raman spectrogram centered in the fingerprint region is obtained with a spectral coverage from 230 cm^{-1} to 1650 cm^{-1} , and (e) the corresponding simulated spectral coverage with a minimum value of 7 cm^{-1} .

- 2) On the other hand, in order to expand the spectral coverage of the spectroscopic fiber laser device, a novel approach for the measurement of the fingerprint region may be introduced. In this case, only the pump beam (centered at 1040 nm) is employed. An open-space dichroic mirror centered at 1 μm , separates the pump beam into two subsequent pulses, i.e., the Stokes pulse (lower-frequency part of the initial pump beam) interacts with the pump beam (higher-frequency part of the initial pump beam). The corresponding Raman spectrogram is depicted in Fig. 6.11(d), where a spectral coverage spanning from 230 cm^{-1} to 1645 cm^{-1} is obtained in the time-delay region of interest of 0.7 ps to 8 ps. These new pulses are made to interact, generating a Gaussian CARS signal centered at 550 cm^{-1} . The spectral resolution has a minimum value of 7 cm^{-1} along this region, shown in Fig. 6.11(e). The asymmetric spectral resolution function can be explained from the spectrogram of the pump pulse. Any gap between the pulses is observable in the spectrogram, generating an overlap of the red components of the Stokes beam with the blue ones of the pump pulse. Thus the first values of the IFD are close to zero, whereas the rest of them increase as the time delay rises while tightening the spectral resolution function.

The improvement of the spectral resolution, in this case, can be explained since we are using the same beam both as the pump and Stokes pulses, thus the chirp-matching condition is fully accomplished, whereas when both arms of the laser set-up are employed, a small difference in the chirp value leads to small mismatches on the CARS signal and hence a lessening of the spectral resolution.

These results are comparable to similar configurations described in the literature [198], and open the path to the development of all-fiber laser CARS systems operating both in the fingerprint and lipid region (C-H vibrational resonances). In order to measure experimental biological samples with this configuration, further improvements should be made in terms of dispersion compensation and pulse compression of the pump beam.

6.2.3.2 CARS simulation with the InN-based fiber laser set-up

In the following section, we simulate the CARS signal generated by the ultrashort laser pulses of Chapter 5.2. To demonstrate the applicability of this spectroscopic device, we have verified its potential to analyze some biological samples.

In comparison to previous cases, the simulation has been carried out from the experimental results generated by the all-fiber laser resonator cavity based on the use of InN as SESAM. The ultrafast output laser pulse, with a temporal duration of 92 fs and a spectral bandwidth of 42 nm, represented in Fig. 5.15, has been employed as the initial propagation pulse in this simulation code. This pulse will propagate through different types of fibers in order to obtain the corresponding pump (1 μm) and Stokes (1550 nm) pulses necessary for CARS spectroscopy. It must be noted that in this case, due to the change in the temporal duration and repetition rate, a higher peak power and energy per pulse are obtained. The laser set-up employed for the generation of the pump and Stokes pulses has been represented in Fig. 6.12.

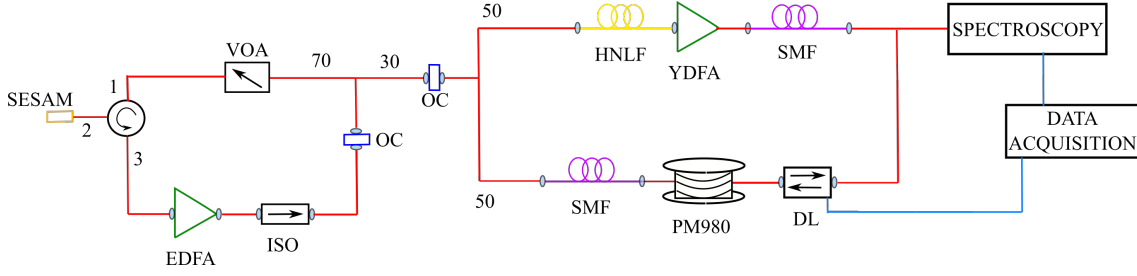


Figure 6.12: Experimental laser set-up of the CARS spectroscopic device based on the use of the InN SESAM all-fiber laser cavity for the generation of the pump and Stokes pulses.

- **1 μm arm:** As abovementioned, the expansion of the 1550 nm output laser pulse towards lower wavelengths can be generated by the use of a HNLF with the same dispersion and nonlinear properties as in Section 6.2.2, with a total length of 4.5 cm. Subsequently, a filter and an amplifier YDFA have been employed to construct the pump beam centered at 1 μm . Additionally, a 1.8 m SMF is inserted with a dispersion coefficient of $\beta_2=2.26 \cdot 10^{-26} \text{ s}^2/\text{m}$ and $\beta_3=31.9 \cdot 10^{-42} \text{ s}^3/\text{m}$ as the TOD parameter, whereas the SPM coefficient is set to $\gamma=4.2 \cdot 10^{-3} \text{ W}^{-1}\text{m}^{-1}$. At the output, a temporal duration of 6.7 ps and a spectral bandwidth of 42 nm centered at 1020 nm can be obtained from the FWHM Gaussian approximation of the AC and spectrum figures represented in Fig. 6.13(a) and (b), respectively. It must be noted that the introduction of broadening fibers such as SMF leads to the insertion of a certain value of chirp in the pump beam, which can be approximated to $C = 1.9$. This fact can also be demonstrated by the appearance of a certain slope when the pump beam is represented in the down part of the time/frequency figure of the spectrogram (see Fig. 6.13(c)). In terms of the output power, the pump pulse is 25 mW, which corresponds to a peak power and pulse energy of 0.7 kW and 4 nJ.
- **1550 nm arm:** In contrast, for the 1550 nm optical pulse generation, a SMF fiber with a total length of 2.3 m and with a dispersion and SPM coefficient of $\beta_2=-2.21 \cdot 10^{-26} \text{ s}^2/\text{m}$ and $\gamma=1.09 \cdot 10^{-3} \text{ W}^{-1}\text{m}^{-1}$ respectively, has been employed as the broadening fiber, following the same principle as the one described in Section 6.1. In addition, in order to obtain the same chirp parameter as the one defined for the pump pulse, a second broadening fiber has been incorporated into the Stokes arm, consisting of 1 m of PM980 fiber, with a GVD of $2.6 \cdot 10^{-26} \text{ s}^2/\text{m}$ and TOD of $39.2 \cdot 10^{-42} \text{ s}^3/\text{m}$, while the SPM value is of $\gamma=5.04 \cdot 10^{-3} \text{ W}^{-1}\text{m}^{-1}$. In this sense, a temporal duration of 12 ps and 188 nm of spectral width centered at 1568 nm have been measured for the Stokes beam as depicted in Fig. 6.13(a) and (b). In order to fulfill the chirp-matching condition, the C parameter was set to 1.9 as well, as shown in the upper part of the spectrogram of Fig. 6.13(c). The average power set for the Stokes beam is of 20 mW, which implies a peak power of 0.3 kW and 3.3 nJ as pulse energy.

Once the chirp-matching condition has been fulfilled, the pump and Stokes beams are made to interact spatially and temporally so a CARS signal can be generated. As explained in the previous section, two different regimes can be measured depending on the use of a single beam, in this case the pump beam, corresponding to the

fingerprint region, or the employment of the two laser pulses, pump and Stokes beams, leading to a CARS signal centered in the lipid region.

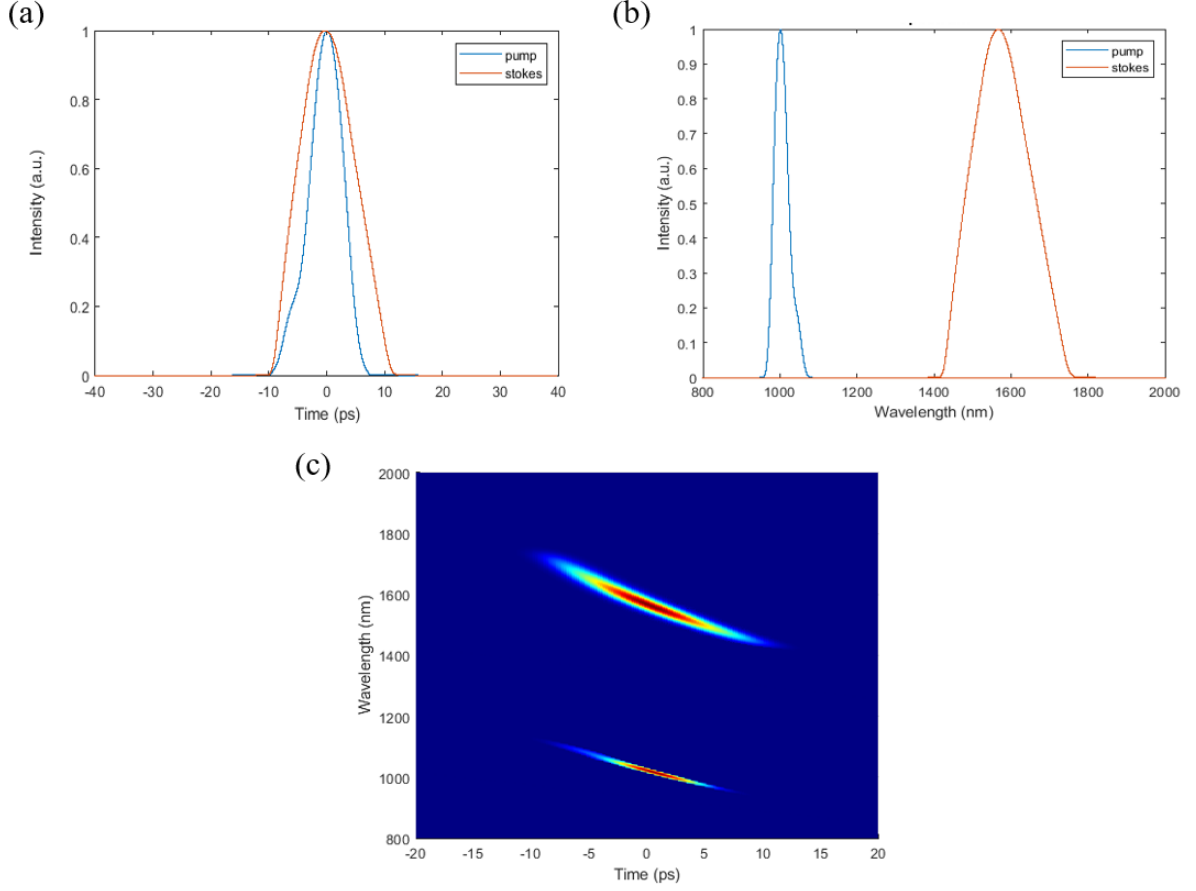


Figure 6.13: Pump and Stokes pulses simulation after the propagation through compressive and broadening fibers based on the experimental results obtained from Chapter 5.2 in the temporal domain (a) and in the frequency domain (b). The chirp-matching condition is evaluated by the representation of the 3D spectrogram figure (c) of the pump (down) and Stokes (up) pulses.

- 1) In the case of the fingerprint region, the lipid region is measured by using both the pump and Stokes pulses, represented in Fig. 6.14(b). In this case, the full pump beam has been used to interact with the Stokes beam, leading to a CARS signal centered at 3000 cm^{-1} . The spectral coverage is measured from 1450 cm^{-1} to 4350 cm^{-1} with a main value of spectral coverage of 25 cm^{-1} as depicted in Fig. 6.14(b). The resolution decreases to 3 cm^{-1} in the region of interest (10 to 27 ps of temporal delay). Furthermore, the reduction of the lower limit of the spectral coverage to 1400 cm^{-1} , in conjunction with the one obtained with the pump beam in the fingerprint region, implies that this system can cover from 180 to 4350 cm^{-1} without any gap in a single measurement and with enough resolution as to distinguish between consecutive absorption lines.

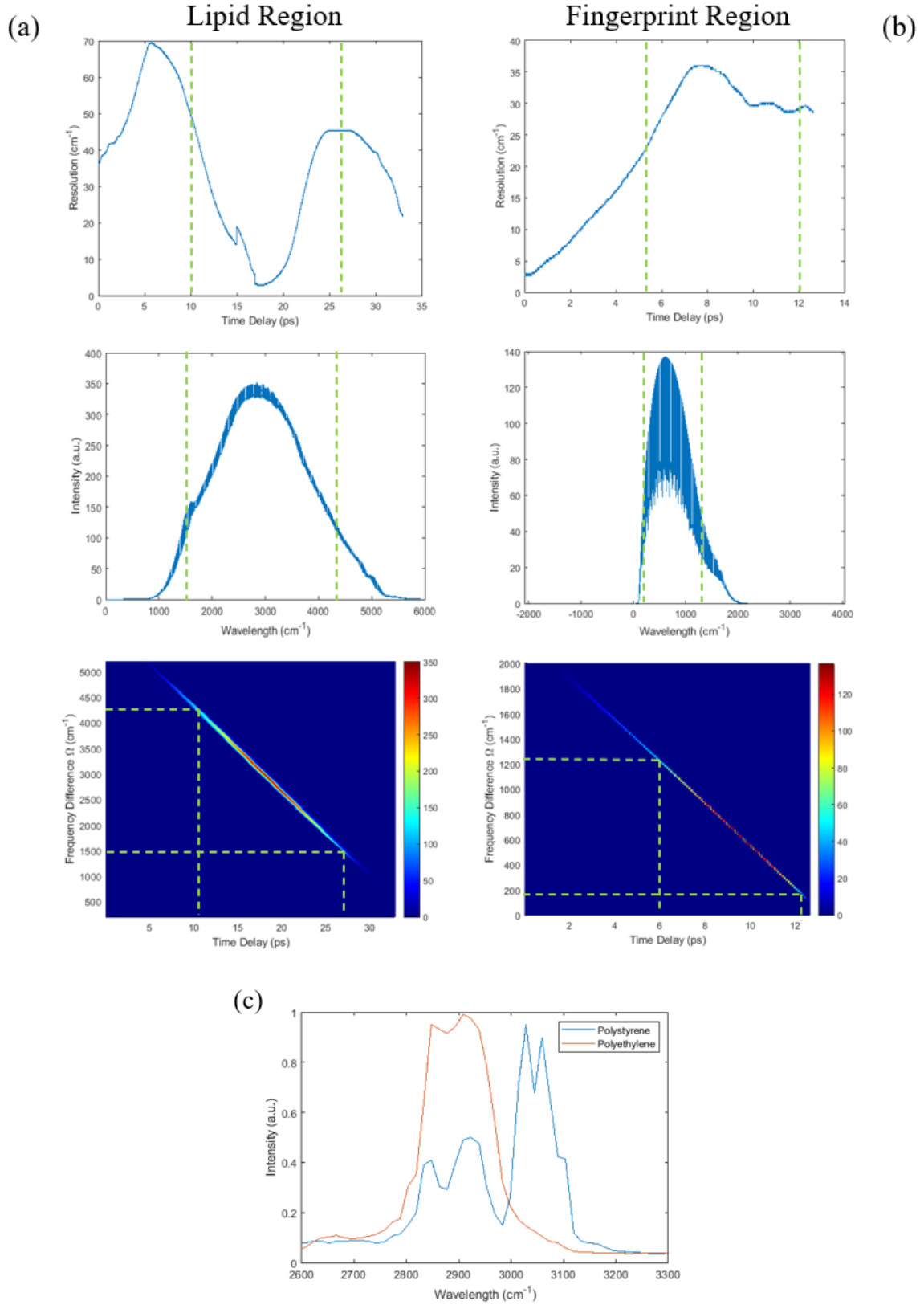


Figure 6.14: Simulation of CARS spectroscopy based on the experimental output laser pulses of Section 5.2 covering both the fingerprint (a) and lipid (b) regions, where the resolution (upper row), CARS signal (2nd row) and Raman spectrogram (lower row) are depicted for each spectral region, with the spectral bandwidth denoted with green dashed lines. The measurement of the absorption spectrum of polystyrene and polyethylene has also been simulated in (c).

- 2) On the other hand, the pump beam is separated by a dichroic mirror centered at 1020 nm, generating two subsequent pump pulses. These two pulses are made to interact, generating a Raman response centered at 800 cm^{-1} with a spectral resolution as low as 3 cm^{-1} . The spectral coverage, denoted with green dashed lines in Fig. 6.14(a), covers from 180 cm^{-1} to 1330 cm^{-1} , thus expanding the region to lower wavenumbers in comparison to previous results. The spectral coverage can also be corroborated by the representation of the Raman spectrogram. The increment of the spectral resolution in the region of interaction (5-12 ps of temporal delay) may be explained due to the non-linear tail of the 1550 nm beam observable in the Stokes spectrogram (see Fig. 6.13(c)). To demonstrate the viability of this configuration, a Raman spectrum of polystyrene and polyethylene has been synthetically developed, plotted in Fig. 6.14(c).

6.2.3.3 Discussion of results

In conclusion, we have been able to simulate the complete spectroscopic system consisting of a dual-comb fiber laser source based on a carbon-nanotube saturable absorber in a ring fiber laser cavity. A pump beam with 13.4 ps and 80 THz (288 nm) for the pulse duration and spectral width has been measured, whereas 1 ps and 5.8 THz (46 nm) is achieved for the Stokes beam, leading to a spectral coverage from 1900 cm^{-1} to 3650 cm^{-1} , thus expanding the absorption spectrum towards the fingerprint region of biomolecules with a resolution of 25 cm^{-1} in average. Furthermore, a new technique for the expansion of the region under study has been proposed based on the use of a dichroic mirror in the spectroscopic set-up for splitting the pump beam by its half into two subsequent pulses which interact between them, spanning the spectral coverage from 230 cm^{-1} to 1645 cm^{-1} . Thus, most of the fingerprint and lipid region of the biological spectra can be measured with high accuracy by using this type of laser set-up. Nevertheless, the complexity and cost of the spectroscopic scheme with the fibers used, have encouraged us to find of other alternatives, preserving the resolution and spectral coverage properties.

As a consequence, in this work we propose the introduction of the InN based all-fiber mode-locking laser system, and thus the employment of an ultrafast pulse with a time duration of less than 100 fs in the temporal domain, and a spectral bandwidth of more than 40 nm as the excitation source. The simulations of the 6.7 ps and 12.8 THz (42 nm) pump beam and the 12 ps and 23 THz (188 nm) Stokes beam demonstrated a resolution as low as 3 cm^{-1} and 2 cm^{-1} for the fingerprint and lipid region with a spectral coverage ranging from 180 cm^{-1} to 4350 cm^{-1} . These increments, in comparison to the previous results, denote the improvements achieved by this system in terms of dispersion and nonlinear contributions, due to the reduction of broadening and compression pulse stages (free-space grating pair), and also the elimination of polarization controllers due to the polarization independence of the InN SESAM. Moreover, a reduction of optical losses is achieved since the laser system is based on an all-fiber laser scheme, eliminating all the reflections introduced by the optical lenses in the free space configuration. These results demonstrate that this type of all-fiber laser configuration has promising potential as a laser source for Raman spectroscopy devices for sensing applications. This work paves the way for

experimental validation in a future line of research.

6.3 Conclusions

In this chapter, a first demonstration of a gas-trace spectroscopic device based on an all-fiber laser source centered in the C-band with an InN semiconductor as SESAM is presented. This technology provides reliable and highly accurate sensing measurements by means of pulse compression and supercontinuum generation generated by off-the-shelf and low-cost fiber components such as SMF and HNLF among others. The development of supercontinuum pulses allows extracting the absorption lines of gas compounds such as HCN or CO through a simple gas cell located in an all-fiber resonator system, reducing the attenuation losses generated in open-space configurations. In terms of spectral resolution and spectral range, this proof of concept demonstration has shown a spectral resolution of 20 pm (OSA resolution) over a bandwidth that covers from 1520 nm to 1630 nm.

Additionally, a new Raman spectroscopic device has been proposed based on the SF-CARS technique able to measure both the fingerprint and lipid region of biomolecules thanks to a dual-band disposition of the all-fiber laser source. The use of supercontinuum generation and compression stages, can enable spectral resolutions of less than 25 cm^{-1} while covering spectral regions ranging from 180 cm^{-1} to 4350 cm^{-1} when applying a laser source with InN semiconductors as SESAM. The robustness and sensitivity of the proposed spectroscopic device has been found suitable for the characterization of different compounds in a single measurement. In addition, since the majority of current spectroscopic devices are developed using open-air configurations, the use of all-fiber laser systems opens a new path of spectroscopy by exploiting ultrafast pulse propagation in optical fibers. Nevertheless, further research is needed to understand the CARS signal intensity dependency on the pump and Stokes pulses, in order to potentially improve the measurement capability of future spectroscopic devices. In addition, the variation of the spectral resolution over the time delay (as a consequence of the variations of the pump and Stokes pulses in both the temporal and spectral domain) may contribute to discontinuities in the absorption measurement, which shall be evaluated for potential performance effects.

Chapter 7

Conclusions

Contents

7.1	Conclusions and main contributions	142
7.2	Future perspectives	144
7.3	Author’s publications	146

This last chapter summarizes the results derived from this work, providing some general conclusions related to the topic of this thesis. In this chapter, we also provide future perspectives on possible research directions for this thesis, as well as some ideas that have arisen while it was being developed.

7.1 Conclusions and main contributions

The research work can be summarized as the improvement of ultrafast mode-locking InN-based fiber lasers centered in the C-band of the spectrum, by presenting and testing new InN saturable absorbers based on highly accurate fabrication processes, that can potentially enhance not only the properties of the semiconductor material but also its laser performance. Subsequently, we improved the laser system by developing an all-fiber configuration with a handcrafted InN GRIN-to-SESAM coupling device. Furthermore, the fiber laser has potential applications in gas sensing and biomedical sensing, which we have validated.

This work began by presenting the fundamentals of light propagation in optical fibers and soliton generation required for a complete understanding of the pulsed-laser systems studied in this thesis. We also provided a full description of the effects of light-matter interaction, going from linear to other nonlinear phenomena commonly found in high-powered light pulses propagating in optical fibers, with a focus on saturable absorption, laying the foundations for the generation of mode-locked fiber lasers. Then, we included the state-of-the-art of ultrafast fiber lasers, focusing mainly on mode-locked fiber lasers. An in-depth description of the fiber laser employed in this thesis based on the use of InN saturable absorbers as the passive element was also presented after this introduction. The final section summarizes the sources of error in ultrafast passive mode-locked fiber lasers in terms of stability, optical power and time duration, and the strategies developed to counteract them.

The research work undertaken during the doctoral program is reported in chapters 5 and 6. In Chapter 5 we presented the main focus of the research, where we improved the fiber laser in terms of pulse duration and peak power. In the first work we presented, we focused on the enhancement of the InN saturable absorbers by considering the reduction of the residual doping concentration by the addition of a buffer layer, generating a decrease of dopants within the crystal lattice, and thus the defect density due to the Burstein-Moss effect. These effects reduce the energy bandgap of the material, approximating its emission to the operational wavelength (bandgap of the undoped material), enabling the fabrication of InN samples with higher quality and superior properties. A higher absorption and nonlinear response permitted obtaining the minimum pulsewidth and highest peak power achievable by this type of laser system. A simple method to reach the highest saturable absorber performance was then proposed, by adequately controlling the material deposition during the fabrication process, enhancing the nonlinear properties of the saturable absorber and thus improving the ultrashort laser pulse generation with a temporal duration as low as 134 fs and a peak power of 28 kW.

As part of our second work, we evaluated and discussed the current limits of the maximum peak power achievable by the fiber laser system. As an improvement,

we eliminated the free-space optical path where the InN sample was located by inserting the first proof-of-concept InN-based GRIN-to-fiber coupling device, ensuring a higher laser performance due to the reduction of the insertion losses. This alignment-free, compact, and turnkey laser design enhances the SESAM behavior, enabling the shortest pulse duration (92 fs) and highest peak power (74 kW) of this type of laser scheme. Finally, we examined the implications of insertion losses in further detail and ultrashort pulse laser generation during this chapter. We observed that by increasing the fiber length within the laser cavity, and thus reducing the repetition rate, a peak power of 1 MW at the output of the laser system is obtained while preserving the temporal duration of the optical pulse. A better control of the dispersion effects and noise components may improve the stability of the fiber laser system.

In Chapter 6, we demonstrated the potential of this type of fiber laser for rapid, highly accurate sensing applications. This involved specific alteration of the laser scheme, either by changing the optical fiber, the fiber laser set-up, or by developing application specific post-processing stages.

We were able to measure the absorption lines of HCN and CO molecules in a gas cell through the use of the fiber laser cavity based on the InN SESAM. We quantified this absorption spectrum by developing the supercontinuum generation of the ultrafast pulse produced at the output of the laser cavity, by propagating it through standard single-mode optical fibers, generating a temporal duration of 70 fs and more than 200 nm in the spectral domain. We were able to measure the vibro-rotational energy transitions of each compound with only 1 second of measurement. The results were developed in the IO-CSIC facilities and confirmed by comparison with the HITRAN database.

We also demonstrated measurements of Raman spectroscopy of biological samples in Chapter 6 by using a mode-locking fiber laser system. For that purpose, we developed an all-fiber dual comb laser as the light source for the Raman spectroscopic device, consisting of a 1 μ m pulse and a 1550 nm pulse. Additional broadening and compression stages, such as optical fibers and grating pairs respectively, were introduced for the generation of chirp pulses, essential in SF-CARS spectroscopy. This proof-of-concept laser scheme was developed in the University of Arizona laboratories, where an initial test of this assembly was evaluated by a Matlab simulation of the Raman absorption of biomolecules such as polystyrene and polyethylene with a resolution of 25 cm^{-1} and a spectral coverage of 2600-3450 cm^{-1} .

Finally, we reported estimations of the Raman response of biomolecules using the InN-based all-fiber laser as the initial laser source in the spectroscopic device. With this, a resolution below 25 cm^{-1} and a spectral coverage ranging from 180 cm^{-1} to 4350 cm^{-1} were obtained, denoting the feasibility of this laser system for spectroscopic applications.

Likewise, the results in this thesis were both published in scientific journals and discussed at appropriate conferences, fulfilling all the objectives initially set at the start of the doctoral work. Overall, the presented results carry important achievements in laser technology, and also in the field of spectroscopic fiber sensing.

7.2 Future perspectives

This dissertation offers clear paths for further exploration and investigation. As a result, the following open lines of research for improving the performance of the fiber laser have been identified:

- The improvements in residual doping and reduction of defect concentration within the InN thin film suggested in this thesis heavily impact the saturable absorber properties of the semiconductor. Additionally, the variation of the InN thickness demonstrated higher non-saturable absorption, enhancing the output laser performance. As such, there is a trade-off between the layer thickness and the maximum optical fluence tolerated by the material. While improved InN semiconductors with a layer thickness as low as 360 nm demonstrated a saturation fluence of $800 \mu\text{J}/\text{cm}^2$, the saturable absorber damage threshold level is still unreachable, motivating the study of the relation between the layer thickness and the maximum optical fluence.
- The selection of the material for the InN substrate is detrimental to the defect concentration of the semiconductor, and thus to the development of a high quality saturable absorber. Furthermore, the operation wavelength of the saturable absorber is influenced by the bandgap energy of the active material. The use of a material based on the ternary InGaN grown on GaN substrates as saturable absorber in the fiber laser cavity may change the emission wavelength towards the $1 \mu\text{m}$ range, essential in spectroscopic applications.
- Following the analysis of the fiber laser resonator cavity simulation, a future perspective is to develop an algorithm capable of evaluating the laser performance of the InN semiconductor taking into account its saturable absorber properties, closely related to the deposition control and fabrication process, as described in the previous chapters of this work.
- In relation to the development of the all-fiber based laser using a GRIN-to-SESAM coupling device, it would be interesting to evaluate the limitations of the UV-cured glue deposited in terms of thermal and strain resistance as well as the maximum power attainable by the fiber coupling device. Having this information would help in understanding the practical challenges of coupling devices in a proper in-field installation, validating the proposed laser system.
- The possibility to retrieve higher nonlinear absorption behavior from the InN semiconductor that generates an ultrafast laser performance by a simple, butt-coupling device opens the path for the development of new mechanical designs, enabling the tunability of the resonator cavity laser performance over different optical wavelengths, while correcting as well the intracavity insertion losses generated by the InN-to-GRIN device. The fiber laser community can benefit from these achievements, since the adaptable coupling device may enhance the optical power by several orders of magnitude, compared to other laser configurations, which could open the door for many high-power applications using standard optical fibers.

Conversely, the work presented in Chapter 6 opens the door to future perspectives for spectroscopic applications. In particular, we identify the following ideas for future research:

- In this thesis, we presented a first exploration of the gas sensing application of the InN-based fiber laser by using supercontinuum generation with standard SMFs and a maximum spectral bandwidth of 200 nm. The evident next step would be to evaluate the potential of the proposed broadening stage by using other fibers, such as HNLF or PCF among others, for applications where wider spectral bandwidths may affect the absorption region under study.
- With regard to the biological sensing application based on the Raman spectroscopic CARS technique, once we have conducted the numerical model for the simulation of the laser system, validating its feasibility and utility, a complete experimental development of the spectroscopic set-up must be implemented. A complete characterization of the temporal and spectral pulses, as well as its chirp values by a FROG device, is also demanded. As such, there is an implicit need for the generation of the 1 μm beam based on the use of the SC produced by highly nonlinear optical fibers, where a spectral bandwidth of more than 300 nm is still under study, in addition to the fulfillment of the chirp-matching condition with the 1550 nm pulse, by a careful selection of the dispersion and nonlinear effects essential for the spectral focusing technique. This is a key step in fully demonstrating the concept of CARS spectroscopic biological sensing employing all-fiber laser systems as light sources.
- Considering the resolution and spectral coverage, as well as the optical power provided in CARS systems based on ultrafast fiber laser generation, the measurements can be optimized by additional processing techniques. In this sense, we see the potential of developing an intelligent algorithm capable of correcting the sources of noise and mitigation strategies in the corresponding absorption region of interest.
- The presented results for CARS spectroscopy generated by the implementation of InN-based all-fiber technology is still in its early stages. Future developments may be able to improve resolutions and spectral coverages in similar structures, by selecting the appropriate fibers (dispersion and nonlinear effect contributions) and geometry (fiber length, resonator cavity, and central wavelengths). Additionally, the presented solution should be characterized experimentally to validate the proposed laser system. The improvements in sensitivity and spectral absorption range generated by the proposed system in this work due to the use of shorter pulses as excitation sources in the spectroscopic device may reduce the number of optical fibers and amplifiers in the fiber laser system, reducing its complexity and cost, desirable for commercial development.
- In the last few years, there has been a growing interest in the characterization of biomolecules by a non-invasive diagnostic tool able to measure in vivo processes for real-time monitoring with high accuracy and sensitivity. The SF-CARS technique in conjunction with an ultrafast fiber laser source could

represent a good solution for tracking molecular variations in biological samples, indispensable for disease diagnosis. Further experiments with the proposed fiber laser spectroscopic system with tunable optical wavelengths and resolution optimization should be tested in other spectral ranges to validate its use for real-time in vivo biological imaging.

7.3 Author's publications

Scientific Journals

- 2022 L. Monroy, J. Magnus, M. Gonzalez-Herraez, F. B. Naranjo, K. Kieu, "Spectral focusing technique simulation for CARS microscopy: evaluation of spectral resolution and spectral coverage," *submitted*
- 2022 L. Monroy, "¿Jugamos una partida de láser squash?," *Óptica Pura y Aplicada* 54(4). DOI: [10.7149/OPA.54.4.5442](https://doi.org/10.7149/OPA.54.4.5442)
- 2022 F. Gallazzi, I. Cáceres, L. Monroy, J. Nuño, C. Pulido, P. Corredera, F. B. Naranjo, M. González-Herráez, J. Ania Castañón, "Ultralong ring laser super-continuum sources using standard telecommunication fibre," *Optics and Laser Technology* 147, 107632. DOI: [10.1016/j.optlastec.2021.107632](https://doi.org/10.1016/j.optlastec.2021.107632)
- 2021 L. Monroy, M. Soriano-Amat, O. Esteban, E. Monroy, M. González-Herráez, F. Naranjo, "Performance enhancement of an ultrafast all-fiber laser based on InN saturable absorber using GRIN coupling," *Optics Express* 29(18), pp. 29357-29365. DOI: [10.1364/OE.430198](https://doi.org/10.1364/OE.430198)
- 2020 L. Monroy, M. Jiménez-Rodríguez, E. Monroy, M. González-Herráez, F. B. Naranjo, "High-Quality, InN-Based, Saturable Absorbers for Ultrafast Laser Development," *Applied Sciences* 10, 7832. DOI: [10.3390/app10217832](https://doi.org/10.3390/app10217832)
- 2019 L. Monroy, M. Jiménez-Rodríguez, P. Ruterana, E. Monroy, M. González-Herráez, and F.B. Naranjo, "Effect of the residual doping on the performance of InN epilayers as saturable absorbers for ultrafast lasers at 1.55 μ m," *Optical Materials Express* 9, 2785–2792. DOI: [10.1364/OME.9.002785](https://doi.org/10.1364/OME.9.002785)

International Conference Proceedings

- 2022 L. Monroy, J. Magnus, M. González-Herráez, F. B. Naranjo, K. Kieu, "Analysis of spectral coverage and resolution limitations in simulated SF-CARS microscopy," CLEO PacificRim 2022, Optical Society of America, Sapporo, Japan (Hybrid Format).
- 2021 L. Monroy, Ó. Esteban, E. Monroy, M. Gonzalez-Herraez, F. B. Naranjo, "High energy ultrafast all-fiber laser based on InN-GRIN saturable absorber", Advanced Photonics Congress, Montreal, Canada (Online).

- 2020 L. Monroy, M. González-Herráez, F. B. Naranjo, “Optimization of a passive ultrafast fiber laser based on saturable absorbers for gas sensing applications,” OSCINE, Valencia (Online).
- 2019 L. Monroy, E. Monroy, M. González Herráez, F.B. Naranjo, “Novel InN-based SESAMs with ultra-short time response,” 2019 Conference on Lasers and Electro-Optics Europe and European Quantum Electronics (CLEO/Europe-EQEC), Optical Society of America, Munich, Germany.
- 2018 M. Jiménez-Rodríguez, L. Monroy, E. Monroy, M. González-Herráez, F. B. Naranjo, “Study of Absorption Saturation in InN Thin Films through the Z-Scan Technique at 1.55 μ m,” Advanced Photonics Congress, Optical Society of America, Zurich, Switzerland.

National Conference Proceedings

- 2022 L. Monroy, M. González-Herráez, F. B. Naranjo, “High power ultrafast InN-based all fiber laser”, Ultrafast Science and Technology Spain (USTS), Universidad de Málaga.
- 2022 L. Monroy, J. Magnus, M. González-Herráez, K. Kieu, F. B. Naranjo, “Optimización de la resolución y ancho de banda de la técnica de spectral focusing en microscopía CARS”, XVI Congreso Nacional de Materiales, Universidad de Ciudad Real.
- 2021 L. Monroy, M. Soriano-Amat, Ó. Esteban, E. Monroy, M. González-Herráez; F. B. Naranjo. “Ultracompact mode-locked InN based fiber laser with ¡100 fs pulses”, XII Reunión Española de Optoelectrónica, OPTOEL’21 (Online).
- 2018 L. Monroy, M. Jiménez-Rodríguez, E. Monroy, M. González-Herráez, F. B. Naranjo, “Z-scan Characterization of InN layers at Telecom Wavelengths,” Congreso Nacional de Materiales, Universidad de Salamanca.

Book Chapters

- 2021 L. Monroy, O. Esteban, E. Monroy, M. González-Herráez, F. B. Naranjo. “Aplicación de láseres de pulsos ultracortos”. Octavas Jornadas de Jóvenes Investigadores de la Universidad de Alcalá, ISBN: 978-84-18254-50-5, 2021.
- 2021 L. Monroy, “InN SAs for Ultrafast Lasers”. Scholarly Community Encyclopedia MDPI, 2021. URL: <https://encyclopedia.pub/item/revision/9d11ff7f567ab6028c2dcdaff058ab01>.



Bibliography

- [1] Eugene Hecht. “*Optics*”. Addison Wesley, San Francisco (CA), third edition, 2002.
- [2] J Hecht. “*City of Light: The Story of Fiber Optics*”. Oxford University Press, first edition, 2004.
- [3] Anton A. Huurdeman. “*The Worldwide History of Telecommunications*”. John Wiley & Sons, first edition, 2003.
- [4] Alexander Graham Bell. “Improvement in telegraphy”, 1876. US Patent 174,465.
- [5] Ignace Urbain Jean Chappe. “*Histoire de la télégraphie*”. Ch. Richelet, 1824.
- [6] T. H. Maiman. “Stimulated optical radiation in Ruby”. *Nature*, 187(4736):493, 1960. DOI: [10.1038/187493a0](https://doi.org/10.1038/187493a0).
- [7] J. M. Dudley and J. R. Taylor. “*Supercontinuum Generation in Optical Fibers*”. Cambridge University Press, first edition, 2010. DOI: [10.1017/CBO9780511750465.002](https://doi.org/10.1017/CBO9780511750465.002).
- [8] K. O. Hill, D. C. Johnson, B. S. Kawasaki, and R. I. MacDonald. “CW threewave mixing in singlemode optical fibers”. *Journal of Applied Physics*, 49(10):5098–5106, 1978. DOI: [10.1063/1.324456](https://doi.org/10.1063/1.324456).
- [9] D. Welford and B.C. Johnson. “Real time monitoring of CW mode-locked dye laser pulses using a rapid-scanning autocorrelator”. *Optics Communications*, 45(2):101–104, 1983. DOI: [10.1016/0030-4018\(83\)90054-8](https://doi.org/10.1016/0030-4018(83)90054-8).
- [10] K. C. Kao and G. A. Hockham. “Dielectric-fibre surface waveguides for optical frequencies”. *Proceedings of the Institution of Electrical Engineers*, 113(7):1151–1158, 1966. DOI: [10.1049/ip-j.1986.0030](https://doi.org/10.1049/ip-j.1986.0030).
- [11] T. Miya, Y. Terunuma, T. Hosaka, and T. Miyashita. “Ultimate low-loss single-mode fibre at 1.55 μm ”. *Electronics Letters*, 15(4):106–108, 1979. DOI: [10.1049/el:19790077](https://doi.org/10.1049/el:19790077).
- [12] John M. Senior. “*Optical fiber communications: principles and practice*”. Pearson, London (UK), third edition, 2009.
- [13] G. Mahlke and P. Gossing. “*Fiber Optic Cables*”. Publicis MCD Corporate Publishing, 4 edition, 2001.

- [14] J. Arnaud. “Optical waveguide theory”. *Optical and Quantum Electronics*, 12(3):187–191, 1980. DOI: [10.1007/BF00620035](https://doi.org/10.1007/BF00620035).
- [15] E. Desurvire. “*Erbium-doped fiber amplifiers for new generations of optical communication systems*”, volume 2. Optica Publishing Group, 1991. DOI: [10.1201/b16404](https://doi.org/10.1201/b16404).
- [16] T. Li. “*Optical Fiber Communications: Fiber Fabrication*”, volume 1. Academic Press, San Diego, 1985.
- [17] Matej Komanec, Daniel Dousek, Dmytro Suslov, and Stanislav Zvanovec. “Hollow-core optical fibers”. *Radioengineering*, 29(3):417–430, 2020. DOI: [10.13164/re.2020.0417](https://doi.org/10.13164/re.2020.0417).
- [18] Kunimasa Saitoh and Shoichiro Matsuo. “Multicore fiber technology”. *Journal of Lightwave Technology*, 34(1):55–66, 2016. DOI: [10.1109/JLT.2015.2466444](https://doi.org/10.1109/JLT.2015.2466444).
- [19] David N. Payne, Arthur J. Barlow, and Jens J. Ramskov Hansen. “Development of low- and high-birefringence optical fibers”. *IEEE Transactions on Microwave Theory and Techniques*, 30(4):323–334, 1982. DOI: [10.1109/TMTT.1982.1131072](https://doi.org/10.1109/TMTT.1982.1131072).
- [20] Long Jin, Bai-Ou Guan, and Huifeng Wei. “Simplified hollow-core microstructured optical fiber for sensing applications”. In *Workshop on Specialty Optical Fibers and their Applications*, page W3.24. Optica Publishing Group, 2013. DOI: [10.1364/WSOF.2013.W3.24](https://doi.org/10.1364/WSOF.2013.W3.24).
- [21] E. G. Neumann. “*Single-Mode Fibers: Fundamentals*”, volume 14. Springer-Verlag, 1988. DOI: [10.1007/978-3-540-48173-7](https://doi.org/10.1007/978-3-540-48173-7).
- [22] R. P. Feynman. “*The Feynman Lectures on Physics*”, volume 2. Springer-Verlag, 1969. DOI: [10.1119/1.1972241](https://doi.org/10.1119/1.1972241).
- [23] Justin Peatross and Michael Ware. “*Physics of light and optics: A free online textbook*”. Brigham Young University, 2011. DOI: [10.1364/fio.2010.jwa64](https://doi.org/10.1364/fio.2010.jwa64).
- [24] Govind P. Agrawal. “*Nonlinear fiber optics*”. Academic Press, third edition, 2001. DOI: [10.3367/UFNr.0160.199005k.0151](https://doi.org/10.3367/UFNr.0160.199005k.0151).
- [25] Ajoy Ghatak and K. Thyagarajan. “*An Introduction to Fiber Optics*”. Cambridge University Press, 1998. DOI: [10.1017/CBO9781139174770](https://doi.org/10.1017/CBO9781139174770).
- [26] D. B. Keck, R. D. Maurer, and P. C. Schultz. “On the ultimate lower limit of attenuation in glass optical waveguides”. *Applied Physics Letters*, 22(7):307–309, 1973. DOI: [10.1063/1.1654649](https://doi.org/10.1063/1.1654649).
- [27] Andrew T. Young. “Rayleigh scattering”. *Applied Optics*, 20(4):533–535, Feb 1981. DOI: [10.1364/AO.20.000533](https://doi.org/10.1364/AO.20.000533).
- [28] Govind P. Agrawal. “*Fiber-Optic Communication Systems*”. John Wiley & Sons, first edition, 2002. DOI: [10.1002/0471221147](https://doi.org/10.1002/0471221147).

-
- [29] Shiva Kumar and M. Jamal Deen. “*Fiber Optic Coomunications: Fundamentals and Applications*”. John Wiley & Sons, first edition, 2014. DOI: [10.1017/CBO9781107415324.004](https://doi.org/10.1017/CBO9781107415324.004).
 - [30] Luc Thévenaz. “*Advanced Fiber Optics*”. Optica Publishing Group, 2011. DOI: [10.1201/b16404](https://doi.org/10.1201/b16404).
 - [31] Robert W. Boyd. “*Nonlinear Optics*”. Academic Press, third edition, 2013.
 - [32] R. H. Stolen and A. Ashkin. “Optical kerr effect in glass waveguide. *Applied Physics Letters*”, 22(6):294–296, 1973. DOI: [10.1063/1.1654644](https://doi.org/10.1063/1.1654644).
 - [33] R. H. Stolen and Chinlon Lin. “Self-phase-modulation in silica optical fibers”. *Phys. Rev. A*, 17:1448–1453, Apr 1978. DOI: [10.1103/PhysRevA.17.1448](https://doi.org/10.1103/PhysRevA.17.1448).
 - [34] B. E. A. Saleh and M. C. Teich. “*Fundamentals of Photonics*”. John Wiley & Sons, second edition, 2007. DOI: [10.1017/CBO9781107415324.004](https://doi.org/10.1017/CBO9781107415324.004).
 - [35] M. N. Islam, L. F. Mollenauer, R. H. Stolen, J. R. Simpson, and H. T. Shang. “Cross-phase modulation in optical fibers”. *Opt. Lett.*, 12(8):625–627, Aug 1987. DOI: [10.1364/OL.12.000625](https://doi.org/10.1364/OL.12.000625).
 - [36] J. Toulouse. “Optical nonlinearities in fibers: review, recent examples, and system applications”. *J. Lightwave Technol.*, 23(11):3625–3641, 2005. DOI: [10.1109/JLT.2005.855877](https://doi.org/10.1109/JLT.2005.855877).
 - [37] V. E. Zakharov and L. A. Ostrovsky. “Modulation instability: The beginning”. *Physica D: Nonlinear Phenomena*, 238(5):540–548, 2009. DOI: [10.1016/j.physd.2008.12.002](https://doi.org/10.1016/j.physd.2008.12.002).
 - [38] K. Tai, A. Hasegawa, and A. Tomita. “Observation of modulational instability in optical fibers”. *Phys. Rev. Lett.*, 56:135–138, Jan 1986. DOI: [10.1103/PhysRevLett.56.135](https://doi.org/10.1103/PhysRevLett.56.135).
 - [39] Sonia Martín-López. Generación de supercontinuo en fibras ópticas monomodo con fuentes de bombeo continuo. In *PhD Thesis, Universidad Complutense de Madrid*, 2006. ISBN: 978-84-669-2923-3.
 - [40] Govind P. Agrawal. “*Front Matter*”. Academic Press, fifth edition, 2013. DOI: [10.1016/b978-0-12-397023-7.00018-8](https://doi.org/10.1016/b978-0-12-397023-7.00018-8).
 - [41] N. J. Zabusky and M. D. Kruskal. “Interaction of solitons in a collisionless plasma and the recurrence of initial states”. *Physical Review Letters*, 15(6):240–243, 1965. DOI: [10.1103/PhysRevLett.15.240](https://doi.org/10.1103/PhysRevLett.15.240).
 - [42] Akira Hasegawa. “An historical review of application of optical solitons for high speed communications”. *Chaos: An Interdisciplinary Journal of Nonlinear Science*, 10(3):475–485, 2000. DOI: [10.1063/1.1286914](https://doi.org/10.1063/1.1286914).
 - [43] L. F. Mollenauer and J. P. Gordon. “*Solitons in Optical Fibers: Fundamentals and Applications*”. Academic Press, first edition, 2006.

- [44] P. Beaud, W. Hodel, B. Zysset, and H. Weber. “Ultrashort pulse propagation, pulse breakup, and fundamental soliton formation in a single-mode optical fiber”. *IEEE Journal of Quantum Electronics*, 23(11):1938–1946, 1987. DOI: [10.1109/JQE.1987.1073262](https://doi.org/10.1109/JQE.1987.1073262).
- [45] Mark J. Ablowitz, Theodoros P. Horikis, Sean D. Nixon, and Dimitri J. Frantzeskakis. “Dark solitons in mode-locked lasers”. *Optics Letters*, 36(6):793–795, 2011. DOI: [10.1364/OL.36.000793](https://doi.org/10.1364/OL.36.000793).
- [46] S. K. Turitsyn, B. G. Bale, and M. P. Fedoruk. “Dispersion-managed solitons in fibre systems and lasers”. *Physics Reports*, 521(4):135–203, 2012. DOI: [10.1016/j.physrep.2012.09.004](https://doi.org/10.1016/j.physrep.2012.09.004).
- [47] P. Grelu and N. Akhmediev. “Dissipative solitons for mode-locked lasers”. *Nature Photonics*, 6(2):84–92, 2012. DOI: [10.1038/nphoton.2011.345](https://doi.org/10.1038/nphoton.2011.345).
- [48] D. Anderson and M. Lisak. “Nonlinear asymmetric self-phase modulation and self-steepening of pulses in long optical waveguides”. *Phys. Rev. A*, 27:1393–1398, Mar 1983. DOI: [10.1103/PhysRevA.27.1393](https://doi.org/10.1103/PhysRevA.27.1393).
- [49] J. P. Gordon. “Theory of the soliton self-frequency shift”. *Optics Letters*, 11(10):662–664, 1986. DOI: [10.1364/OL.11.000662](https://doi.org/10.1364/OL.11.000662).
- [50] F. M. Mitschke and L. F. Mollenauer. “Discovery of the soliton self-frequency shift”. *Optics Letters*, 11(10):662–664, 1986. DOI: [10.1364/OL.11.000659](https://doi.org/10.1364/OL.11.000659).
- [51] G. P. Agrawal. “Effect of intrapulse stimulated Raman scattering on soliton-effect pulse compression in optical fibers”. *Optics Letters*, 15(4):224–226, 1990. DOI: [10.1364/OL.15.000224](https://doi.org/10.1364/OL.15.000224).
- [52] W. Jin, H. L. Ho, Y. C. Cao, J. Ju, and L. F. Qi. “Gas detection with micro- and nano-engineered optical fibers”. *Elsevier*, 19:741–759, 2013. DOI: [10.1016/j.yofte.2013.08.004](https://doi.org/10.1016/j.yofte.2013.08.004).
- [53] José Manuel Cabrera, Fernando J. López, and Fernando Agulló López. “*Óptica electromagnética: Vol. I Fundamentos*”. Addison-Wesley, 2^a edition, 1998.
- [54] Alonso Marcel and Edward J. Finn. “*Physics volume III: Quantum and Statistical Physics*”. Addison-Wesley, first edition, 1986.
- [55] María Luisa Calvo Padilla. “*Óptica Avanzada*”. Ariel Ciencia, first edition, 2002.
- [56] D. J. Griffiths. “*Introduction to Electrodynamics*”. Prentice Hall, first edition, 1999.
- [57] M. S. Dresselhaus. “*Solid state physics part II: Optical Properties of Solids*”. Wiley, 2001.
- [58] L. D. Landau, A. I. Akhiezer, and E. M. Lifshitz. “*General Physics: Mechanics and Molecular Physics*”. Pergamon, first edition, 1967. DOI: [10.1016/C2009-0-10924-8](https://doi.org/10.1016/C2009-0-10924-8).

-
- [59] P. A. Franken, A. E. Hill, C. W. Peters, and G. Weinreich. “Generation of optical harmonics”. *Phys. Rev. Lett.*, 7:118–119, Aug 1961. DOI: [10.1103/PhysRevLett.7.118](https://doi.org/10.1103/PhysRevLett.7.118).
 - [60] M. Bass, P. A. Franken, and J. F. Ward. “Optical rectification”. *Phys. Rev.*, 138:A534–A542, Apr 1965. DOI: [10.1103/PhysRev.138.A534](https://doi.org/10.1103/PhysRev.138.A534).
 - [61] T. F. Heinz, C. K. Chen, D. Ricard, and Y. R. Shen. “Spectroscopy of molecular monolayers by resonant second-harmonic generation”. *Phys. Rev. Lett.*, 48:478–481, Feb 1982. DOI: [10.1103/PhysRevLett.48.478](https://doi.org/10.1103/PhysRevLett.48.478).
 - [62] J. F. Nye. “*Physical properties of crystals : their representation by tensors and matrices*”. Clarendon Press, 1985. DOI: [10.1002/crat.2170211204](https://doi.org/10.1002/crat.2170211204).
 - [63] Meng Han, Günter Giese, and Josef F. Bille. “Second harmonic generation imaging of collagen fibrils in cornea and sclera”. *Opt. Express*, 13(15):5791–5797, 2005. DOI: [10.1364/OPEX.13.005791](https://doi.org/10.1364/OPEX.13.005791).
 - [64] Seong il Shin and Yong sik Lim. “Simple autocorrelation measurement by using a GaP photoconductive detector”. *OSA*, 20(3):435–440, 2016. DOI: [10.3807/JOSK.2016.20.3.435](https://doi.org/10.3807/JOSK.2016.20.3.435).
 - [65] Inrad Optics. “BBO nonlinear crystals. URL: [https://www.inradoptics.com/bbo#:~:text=Barium%20borate%20\(BBO\)%20is%20a,infrared%20to%20the%20deep%20ultraviolet](https://www.inradoptics.com/bbo#:~:text=Barium%20borate%20(BBO)%20is%20a,infrared%20to%20the%20deep%20ultraviolet).”
 - [66] P. D. Maker and R. W. Terhune. “Study of optical effects due to an induced polarization third order in the electric field strength”. *Phys. Rev.*, 148:990–990, 1966. DOI: [10.1103/PhysRev.148.990](https://doi.org/10.1103/PhysRev.148.990).
 - [67] R. Stolen. “Phase-matched-stimulated four-photon mixing in silica-fiber waveguides”. *IEEE Journal of Quantum Electronics*, 11(3):100–103, 1975. DOI: [10.1109/JQE.1975.1068571](https://doi.org/10.1109/JQE.1975.1068571).
 - [68] Kentaro Miyata, Nobuhiro Umemura, and Kiyoshi Kato. “Phase-matched pure $\chi(3)$ third-harmonic generation in noncentrosymmetric BiB₃O₆”. *Opt. Lett.*, 34(4):500–502, 2009. DOI: [10.1364/OL.34.000500](https://doi.org/10.1364/OL.34.000500).
 - [69] Jeff A. Squier, Michiel Müller, G. J. Brakenhoff, and Kent R. Wilson. “Third harmonic generation microscopy”. *Opt. Express*, 3(9):315–324, 1998. DOI: [10.1364/OE.3.000315](https://doi.org/10.1364/OE.3.000315).
 - [70] Raúl del Coso and Javier Solis. “Relation between nonlinear refractive index and third-order susceptibility in absorbing media”. *J. Opt. Soc. Am. B*, 21(3):640–644, 2004. DOI: [10.1364/JOSAB.21.000640](https://doi.org/10.1364/JOSAB.21.000640).
 - [71] E. Gavgiotaki, G. Filippidis, and V. Tsafas et al. “Third harmonic generation microscopy distinguishes malignant cell grade in human breast tissue biopsies”. *Sci Rep*, 10:11055, 2020. DOI: [10.1038/s41598-020-67857-y](https://doi.org/10.1038/s41598-020-67857-y).
 - [72] Bishnu P. Pal. “*Guided Wave Optical Components and Devices: Basics, Technology, and Applications*”. Academic Press, 2006. DOI: [10.1016/B978-0-12-088481-0.X5000-1](https://doi.org/10.1016/B978-0-12-088481-0.X5000-1).

- [73] A. M. Zheltikov and N. I. Koroteev. “Coherent four-wave mixing in excited and ionized gas media: four-photon spectrochronography, ellipsometry, and nonlinear-optical imaging of atoms and ions”. *Usp. Fiz. Nauk.*, 42:321–351, 1999. DOI: [10.1070/PU1999v042n04A](https://doi.org/10.1070/PU1999v042n04A).
- [74] T. Steffen and K. Duppen. “Time resolved four- and six-wave mixing in liquids. II. experiments”. *The Journal of Chemical Physics*, 106(10):3854–3864, 1997. DOI: [10.1063/1.473106](https://doi.org/10.1063/1.473106).
- [75] M. Yamane and Y. Asahara. “*Glasses for Photonics*”. Cambridge University Press, 2000. DOI: [10.1017/CBO9780511541308](https://doi.org/10.1017/CBO9780511541308).
- [76] R. K. Jain and M. B. Klein. “Degenerate four-wave mixing near the band gap of semiconductors”. *Applied Physics Letters*, 35(6):454–456, 1979. DOI: [10.1063/1.91158](https://doi.org/10.1063/1.91158).
- [77] Paras N. Prasad and David J. Williams. “*Introduction to nonlinear optical effects in molecules and polymers*”. John Wiley & Sons, 1991. DOI: [10.1002/pi.4990250317](https://doi.org/10.1002/pi.4990250317).
- [78] R. J. Gehr and R. W. Boyd. “Optical properties of nanostructured optical materials”. *Chemistry of Materials*, 8(8), 1996. DOI: [10.1021/cm9600788](https://doi.org/10.1021/cm9600788).
- [79] T. Gu, N. Petrone, J. F. McMillan, A. van der Zande, M. Yu, G. Q. Lo, D. L. Kwong, J. Hone, and C. W. Wong. “Regenerative oscillation and four-wave mixing in graphene optoelectronics”. *Nature Photonics*, 6(8):554–559, 2012. DOI: [10.1038/nphoton.2012.147](https://doi.org/10.1038/nphoton.2012.147).
- [80] E. Cumberbatch. “Self-focusing in non-linear optics”. *IMA Journal of Applied Mathematics*, 6(3):250–262, 1970. DOI: [10.1093/imamat/6.3.250](https://doi.org/10.1093/imamat/6.3.250).
- [81] Fibich Gadi and Alexander L. Gaeta. “Critical power for self-focusing in bulk media and in hollow waveguides”. *Opt. Lett.*, 25(5):335–337, Mar 2000. DOI: [10.1364/OL.25.000335](https://doi.org/10.1364/OL.25.000335).
- [82] G. Stibenz, N. Zhavoronkov, and G. Steinmeyer. “Self-compression of millijoule pulses to 7.8 fs duration in a white-light filament”. *Opt. Lett.*, 31(2):274–276, 2006. DOI: [10.1364/OL.31.000274](https://doi.org/10.1364/OL.31.000274).
- [83] G. Cerullo and S. De Silvestri. “Ultrafast optical parametric amplifiers”. *Review of Scientific Instruments*, 74(1):1–18, 2003. DOI: [10.1063/1.1523642](https://doi.org/10.1063/1.1523642).
- [84] Richard L. Sutherland. “*Handbook of nonlinear optics*”. CRC press, 2003.
- [85] Adam M. Larson. “Multiphoton microscopy”. *Nature Photonics*, 5(1), 2011. DOI: [10.1038/nphoton.an.2010.2](https://doi.org/10.1038/nphoton.an.2010.2).
- [86] Zhiwei Zheng, Chujun Zhao, Shunbin Lu, Yu Chen, Ying Li, Han Zhang, and Shuangchun Wen. “Microwave and optical saturable absorption in graphene”. *Opt. Express*, 20(21):23201–23214, 2012. DOI: [10.1364/OE.20.023201](https://doi.org/10.1364/OE.20.023201).

- [87] C. R. Giuliano and L. D. Hess. “Nonlinear absorption of light: optical saturation of electronic transitions in organic molecules with high intensity laser radiation”. *IEEE J. Quantum Electr.*, 3(8):358–367, 1967. DOI: [10.1109/JQE.1967.1074603](https://doi.org/10.1109/JQE.1967.1074603).
- [88] Thomas L. Paoli. “Saturable absorption effects in the self-pulsing (AlGa)As junction laser”. *Applied Physics Letters*, 34(10):652–655, 1979. DOI: [10.1063/1.90625](https://doi.org/10.1063/1.90625).
- [89] R. J. Tilley. “*Colour and the optical properties of materials: an exploration of the relationship between light, the optical properties of materials and colour*”. John Wiley & Sons, 1 edition, 2010. DOI: [10.1002/9780470974773](https://doi.org/10.1002/9780470974773).
- [90] Christian W. Freudiger, Wei Min, Brian G. Saar, Sijia Lu, Gary R. Holtom, Chengwei He, Jason C. Tsai, Jing X. Kang, and X. Sunney Xie. “Label-free biomedical imaging with high sensitivity by stimulated Raman scattering microscopy”. *Science*, 322(5909):1857–1861, 2008. DOI: [10.1126/science.1165758](https://doi.org/10.1126/science.1165758).
- [91] N. Bloembergen. “The stimulated Raman effect”. *American Journal of Physics*, 35(11):989–1023, 1967. DOI: [10.1119/1.1973774](https://doi.org/10.1119/1.1973774).
- [92] Richard C. Prince, Renee R. Frontiera, and Eric O. Potma. “Stimulated raman scattering: From bulk to nano”. *Chemical Reviews*, 117(7):5070–5094, 2017. DOI: [10.1021/acs.chemrev.6b00545](https://doi.org/10.1021/acs.chemrev.6b00545).
- [93] V. Ter-Mikirtychev. “*Fundamentals of fiber lasers and fiber amplifiers*”. Springer Series in Optical Sciences, 1 edition, 2014. DOI: [10.1007/978-3-319-02338-0](https://doi.org/10.1007/978-3-319-02338-0).
- [94] N. J. Doran and David Wood. “Nonlinear-optical loop mirror”. *Opt. Lett.*, 13(1):56–58, 1988. DOI: [10.1364/OL.13.000056](https://doi.org/10.1364/OL.13.000056).
- [95] O. H. Nam, K. H. Ha, J. S. Kwak, S. N. Lee, K. K. Choi, T. H. Chang, S. H. Chae, W. S. Lee, Y. J. Sung, H. S. Paek, J. H. Chae, T. Sakong, J. K. Son, H. Y. Ryu, Y. H. Kim, and Y. Park. “Characteristics of GaN-based laser diodes for post-DVD applications”. *Physica status solidi (a)*, 201(12):2717–2720, 2004. DOI: [10.1002/pssa.200405114](https://doi.org/10.1002/pssa.200405114).
- [96] R. Paschotta. “*Field Guide to Laser Pulse Generation*”. SPIE Press, 1 edition, 2008. DOI: [10.1117/3.800629](https://doi.org/10.1117/3.800629).
- [97] MKS Newport. “Methods for pulsed-laser operation”. URL: <https://www.newport.com/n/pulsed-laser-methods>.
- [98] Jean-Claude Diels and Wolfgang Rudolph. “*Ultrashort Laser Pulse Phenomena: Fundamentals, Techniques, and Applications on a Femtosecond Time Scale*”. Academic Press, 2 edition, 2006. DOI: [9780080466408](https://doi.org/9780080466408).
- [99] Thorlabs. “Pulsed lasers introduction to power and energy calculations”. URL: [thorlabs.com/images/tabimages/Laser_Pulses_Power_Energy_Equations.pdf](https://www.thorlabs.com/images/tabimages/Laser_Pulses_Power_Energy_Equations.pdf).

- [100] E. P. Ippen. “Principles of passive mode locking”. *Appl. Phys. B*, 58(159), 1994. DOI: [10.1007/BF01081309](https://doi.org/10.1007/BF01081309).
- [101] H. A. Haus. “Theory of mode locking with a fast saturable absorber”. *Journal of Applied Physics*, 46(7):3049–3058, 1975. DOI: [10.1063/1.321997](https://doi.org/10.1063/1.321997).
- [102] H. A. Haus. “Theory of mode locking with a slow saturable absorber”. *IEEE Journal of Quantum Electronics*, 11(9):736–746, 1975. DOI: [10.1109/JQE.1975.1068922](https://doi.org/10.1109/JQE.1975.1068922).
- [103] K. Tamura, J. Jacobson, E. P. Ippen, H. A. Haus, and J. G. Fujimoto. “Unidirectional ring resonators for self-starting passively mode-locked lasers”. *Opt. Lett.*, 18(3):220–222, 1993. DOI: [10.1364/OL.18.000220](https://doi.org/10.1364/OL.18.000220).
- [104] Ariel Gordon, Omri Gat, Baruch Fischer, and Franz X. Kärtner. “Self-starting of passive mode locking”. *Opt. Express*, 14(23):11142–11154, 2006. DOI: [10.1364/OE.14.011142](https://doi.org/10.1364/OE.14.011142).
- [105] Ursula Keller. “Recent developments in compact ultrafast lasers”. *Nature*, 424(6950):831–838, 2003. DOI: [10.1038/nature01938](https://doi.org/10.1038/nature01938).
- [106] Andrew M. Weiner. “*Ultrafast Optics*”. John Wiley & Sons, 1 edition, 2009. DOI: [10.1002/9780470473467](https://doi.org/10.1002/9780470473467).
- [107] K. S. Abedin et al. “154 GHz polarization-maintaining dispersion-managed actively modelocked fibre ring laser”. *Electron. Lett.*, 36(14):1185, 2000. DOI: [10.1049/el:20000891](https://doi.org/10.1049/el:20000891).
- [108] H. W. Loh, D. Atkinson, P. R. Morkel, M. Hopkinson, A. Rivers, A. J. Seeds, and D. N. Payne. “All-solid-state subpicosecond passively mode locked erbium-doped fiber laser”. *Applied Physics Letters*, 63(1):4–6, 1993. DOI: [10.1063/1.109747](https://doi.org/10.1063/1.109747).
- [109] Irl N. Duling. “All-fiber ring soliton laser mode locked with a nonlinear mirror”. *Opt. Lett.*, 16(8):539–541, 1991. DOI: [10.1364/OL.16.000539](https://doi.org/10.1364/OL.16.000539).
- [110] D. J. Richardson, R. I. Laming, D. N. Payne, M. W. Phillips, and V. J. Matsas. “320 fs soliton generation with passively mode-locked erbium fiber laser”. *Electronics Letters*, 27(9):730–732, 1991. DOI: [10.1049/el:19910454](https://doi.org/10.1049/el:19910454).
- [111] T. Tsun, M. Islam, and P. Chu. “High-energy femtosecond figure-eight fiber laser”. *Optics Communications*, 141(1):65–68, 1997. DOI: [10.1049/el:19910454](https://doi.org/10.1049/el:19910454).
- [112] K. Tamura, E. P. Ippen, H. A. Haus, and L. E. Nelson. “77-fs pulse generation from a stretched-pulse mode-locked all-fiber ring laser”. *Opt. Lett.*, 18(13):1080–1082, Jul 1993. DOI: [10.1364/OL.18.001080](https://doi.org/10.1364/OL.18.001080).
- [113] E.P. Ippen, C.V. Shank, and A. Dienes. “Passive mode locking of the cw dye laser”. *Applied Physics Letters*, 21(8):348–350, 1972. DOI: [10.1063/1.1654406](https://doi.org/10.1063/1.1654406).

- [114] M. Zirngibl, L.W. Stulz, J. Stone, J. Hugl, D. DiGiovanni, and P.B. Hansan. “1.2 ps pulses from passively mode-locked laser diode pumped er-doped fibre ring laser”. *Applied Physics Letters*, 27(19):1734 – 1735, 1991. DOI: [10.1049/el:19911079](https://doi.org/10.1049/el:19911079).
- [115] A. Cabasse, B. Ortaç, G. Martel, A. Hideur, and J. Limpert. “Dissipative solitons in a passively mode-locked er-doped fiber with strong normal dispersion”. *Opt. Express*, 16(23):19322–19329, Nov 2008. DOI: [10.1364/OE.16.019322](https://doi.org/10.1364/OE.16.019322).
- [116] Amélie Cabasse, Dmitry Gaponov, Khadime Ndao, Aghiad Khadour, Jean-Louis Oudar, and Gilles Martel. “130mW average power, 4.6nJ pulse energy, 10.2ps pulse duration from an Er3+ fiber oscillator passively mode locked by a resonant saturable absorber mirror”. *Opt. Lett.*, 36(14):2620–2622, Jul 2011. DOI: [10.1364/OL.36.002620](https://doi.org/10.1364/OL.36.002620).
- [117] D. Popa, Z. Sun, T. Hasan, W. B. Cho, F. Wang, F. Torrisi, and A. C. Ferrari. “74-fs nanotube-mode-locked fiber laser”. *Applied Physics Letters*, 101(15):153107, 2012. DOI: [10.1063/1.4757293](https://doi.org/10.1063/1.4757293).
- [118] W. Liu, L. Pang, H. Han, W. Tiang, H. Cheng, M. Lei, P. Yan, and Z. Wei. “70-fs mode-locked erbium-doped fiber laser with topological insulator”. *Scientific Reports*, 6(1), 2016. DOI: [10.1038/srep19997](https://doi.org/10.1038/srep19997).
- [119] W. Liu, L. Pang, H. Han, M. Liu, M. Lei, S. Fang, H. Teng, , and Z. Wei. “Tungsten disulfide saturable absorbers for 67 fs mode-locked erbium-doped fiber lasers”. *Opt. Express*, 25:2950–2959, 2017. DOI: [10.1364/OE.25.002950](https://doi.org/10.1364/OE.25.002950).
- [120] Xinxin Jin, Guohua Hu, Meng Zhang, Yuwei Hu, Tom Albrow-Owen, Richard C. T. Howe, Tien-Chun Wu, Qing Wu, Zheng Zheng, and Tawfique Hasan. “102 fs pulse generation from a long-term stable, inkjet-printed black phosphorus-mode-locked fiber laser”. *Opt. Express*, 26(10):12506–12513, 2018. DOI: [10.1364/OE.26.012506](https://doi.org/10.1364/OE.26.012506).
- [121] Robert I. Woodward and Edmund J. R. Kelleher. “2D saturable absorbers for fibre lasers”. *Applied Sciences*, 5(4):1440–1456, 2015. DOI: [10.3390/app5041440](https://doi.org/10.3390/app5041440).
- [122] Ananta R. Acharya. “Group III – nitride semiconductors: Preeminent materials for modern electronic and optoelectronic applications”. *Himalayan Physics*, 5:22–26, 2015. DOI: [10.3126/hj.v5i0.12818](https://doi.org/10.3126/hj.v5i0.12818).
- [123] Alan E. Willner, Robert L. Byer, Constance J. Chang-Hasnain, Stephen R. Forrest, Henry Kressel, Herwig Kogelnik, Guillermo J Tearney., Charles H. Townes, and Michalis N. Zervas. “Optics and photonics: Key enabling technologies”. *Proceedings of the IEEE*, 100(Special Centennial Issue):1604–1643, 2012. DOI: [10.1109/JPROC.2012.2190174](https://doi.org/10.1109/JPROC.2012.2190174).
- [124] Claude Weisbuch, Shuji Nakamura, Yuh-Renn Wu, and James S. Speck. Disorder effects in nitride semiconductors: impact on fundamental and device properties. *Nanophotonics*, 10(1):3–21, 2021. DOI: [10.1515/nanoph-2020-0590](https://doi.org/10.1515/nanoph-2020-0590).

- [125] Krishna Seshan. “*Handbook of Thin Film Deposition*”. William Andrew, 3 edition, 2012. DOI: [10.1016/C2009-0-64359-2](https://doi.org/10.1016/C2009-0-64359-2).
- [126] F. C. Frank and J. H. van der Merwe. “One-dimensional dislocations. I. static theory”. *Proceedings of the Royal Society A: Mathematical, Physical and Engineering Sciences*, 198(1053):205–216, 1949. DOI: [10.1098/rspa.1949.0095](https://doi.org/10.1098/rspa.1949.0095).
- [127] M. Volmer and A. Weber. “Nucleus formation in supersaturated systems”. *Z. Phys. Chem*, 119:277–301, 1926. URL: [https://www.scirp.org/\(S\(1z5mqp453edsnp55rrgjct55.\)\)/reference/referencespapers.aspx?referenceid=2331608](https://www.scirp.org/(S(1z5mqp453edsnp55rrgjct55.))/reference/referencespapers.aspx?referenceid=2331608).
- [128] I. N. Stranski and L. Krastanov. “Zur theorie der orientation ausscheidung von ionenkristallen aufeinander”. *Monatshefte für Chemie*, 71:351–364, 1938. DOI: [10.1007/BF01798103](https://doi.org/10.1007/BF01798103).
- [129] Marius Grundmann. “*The Physics of Semiconductors: An Introduction Including Nanophysics and Applications*”. Springer, 3 edition, 2010. DOI: [10.1007/978-3-319-23880-7](https://doi.org/10.1007/978-3-319-23880-7).
- [130] Neil W. Ashcroft and N. David Mermin. *Solid State Physics*. Brooks/Cole, 1976. ISBN : 9780030839931.
- [131] I. Vurgaftman, J. R. Meyer, and L. R. Ram-Mohan. “Band parameters for III–V compound semiconductors and their alloys”. *Journal of Applied Physics*, 89(11):5815–5875, 2001. DOI: [10.1063/1.1368156](https://doi.org/10.1063/1.1368156).
- [132] Arántzazu Núñez Cascajero. “Development of nitrides based on InN for sensor applications”. In *PhD Thesis, Universidad de Alcalá*, 2017. <https://ebuah.uah.es/dspace/handle/10017/38166?locale-attribute=es>.
- [133] Laura Monteagudo Lerma. “Development of III-nitride-based waveguides for application in all-optical integrated circuits at 1.55 μm ”. In *PhD Thesis, Universidad de Alcalá*, 2015. <https://ebuah.uah.es/dspace/handle/10017/28177>.
- [134] Pierre Carrier and Su-Huai Wei. “Theoretical study of the band-gap anomaly of InN”. *Journal of Applied Physics*, 97(3):033707, 2005. DOI: [10.1063/1.1849425](https://doi.org/10.1063/1.1849425).
- [135] Y. P. Varshni. “Temperature dependence of the energy gap in semiconductors”. *Physica*, 34(1):149–154, 1967. DOI: [10.1016/0031-8914\(67\)90062-6](https://doi.org/10.1016/0031-8914(67)90062-6).
- [136] T. L. Tansley and C. P. Foley. “Optical band gap of indium nitride”. *Journal of Applied Physics*, 59(9):3241–3244, 1986. DOI: [10.1063/1.336906](https://doi.org/10.1063/1.336906).
- [137] V. Yu. Davydov, A. A. Klochikhin, R. P. Seisyan, V. V. Emtsev, S. V. Ivanov, F. Bechstedt, J. Furthmüller, H. Harima, A. V. Mudryi, J. Aderhold, O. Semchinova, and J. Graul. “Absorption and emission of hexagonal InN. evidence of narrow fundamental band gap”. *physica status solidi (b)*, 229(3):r1–r3, 2002. DOI: [10.1002/1521-3951\(200202\)229:3;1::AID-PSSB99991;3.0.CO;2-O](https://doi.org/10.1002/1521-3951(200202)229:3;1::AID-PSSB99991;3.0.CO;2-O).

-
- [138] J. Wu, W. Walukiewicz, W. Shan, K. M. Yu, J. W. Ager, S. X. Li, E. E. Haller, Hai Lu, and William J. Schaff. “Temperature dependence of the fundamental band gap of InN”. *Journal of Applied Physics*, 94(7):4457–4460, 2003. DOI: [10.1063/1.1605815](https://doi.org/10.1063/1.1605815).
 - [139] Ananta R. Acharya. “Group iii – nitride semiconductors: Preeminent materials for modern electronic and optoelectronic applications”. *Himalayan Physics*, 5:22–26, 2015. DOI: [10.3126/hj.v5i0.12818](https://doi.org/10.3126/hj.v5i0.12818).
 - [140] N. Antoine-Vincent, F. Natali, M. Mihailovic, A. Vasson, J. Leymarie, P. Disseix, D. Byrne, F. Semond, and J. Massies. “Determination of the refractive indices of AlN, GaN, and $\text{Al}_x\text{Ga}_{1-x}\text{N}$ grown on (111) Si substrates”. *Journal of Applied Physics*, 93(9):5222–5226, 2003. DOI: [10.1063/1.1563293](https://doi.org/10.1063/1.1563293).
 - [141] M. Anani, H. Abid, Z. Chama, C. Mathieu, A. Sayede, and B. Khelifa. “ $\text{In}_x\text{Ga}_{1-x}\text{N}$ refractive index calculations”. *Microelectronics Journal*, 38(2):262–266, 2007. DOI: [10.1016/j.mejo.2006.11.001](https://doi.org/10.1016/j.mejo.2006.11.001).
 - [142] Marco Jiménez Rodríguez. “Development of passive ultrafast fiber lasers at telecom wavelengths using indium nitride as saturable absorber”. In *PhD Thesis, Universidad de Alcalá*, 2018. <https://dialnet.unirioja.es/servlet/tesis?codigo=251197>.
 - [143] J. Wu, W. Walukiewicz, S. Li, R. Armitage, J. Ho, E. Weber E.E. Haller, Hai Lu, William J. Schaff, A. Barcz, and R. Jakiela. “Effects of electron concentration on the optical absorption edge of InN”. *Applied Physics Letters*, 84(15), 2003. DOI: [10.1063/1.1704853](https://doi.org/10.1063/1.1704853).
 - [144] J. Tauc. “Optical properties and electronic structure of amorphous Ge and Si”. *Materials Research Bulletin*, 3(1):37–46, 1968. DOI: [10.1016/0025-5408\(68\)90023-8](https://doi.org/10.1016/0025-5408(68)90023-8).
 - [145] Marco Jiménez-Rodríguez, Laura Monteagudo-Lerma, Eva Monroy, Miguel González-Herráez, and Fernando B. Naranjo. “Widely power-tunable polarizationindependent ultrafast mode-locked fiber laser using bulk InN as saturable absorber”. *Optics Express*, 25(5):5366–5375, 2017. DOI: [10.1364/OE.25.005366](https://doi.org/10.1364/OE.25.005366).
 - [146] Michael E. Levinshtein, Sergey L. Rumyantsev, and Michael S. Shur. “*Properties of Advanced Semiconductor Materials: GaN, AlN, InN, BN, SiC, SiGe*”. Wiley, 1 edition, 2001. ISBN: [978-0-471-35827-5](https://www.wiley.com/9780471358275).
 - [147] Kung-Hsuan Lin, Gia-Wei Chern, Yin-Chieh Huang, Stacia Keller, Steven P. DenBaars, and Chi-Kuang Sun. “Observation of huge nonlinear absorption enhancement near exciton resonance in GaN”. *Applied Physics Letters*, 83(15):3087–3089, 2003. DOI: [10.1063/1.1619218](https://doi.org/10.1063/1.1619218).
 - [148] Meng Zhao, Chun-Hua Xu, Wei-Jie Hu, Wen-Jun Wang, Li-Wei Guo, and Xiao-Long Chen. “Observation of two-photon absorption and nonlinear refraction in AlN”. *Chinese Physics Letters*, 33(10):104201, oct 2016. DOI: [10.1088/0256-307x/33/10/104201](https://doi.org/10.1088/0256-307x/33/10/104201).

- [149] M. Haiml, R. Grange, and U. Keller. “Optical characterization of semiconductor saturable absorbers”. *Applied Physics B*, 79(3):331–339, 2004. DOI: [10.1007/s00340-004-1535-1](https://doi.org/10.1007/s00340-004-1535-1).
- [150] L. Nevou, J. Mangeney, M. Tchernycheva, F. H. Julien, F. Guillot, and E. Monroy. “Ultrafast relaxation and optical saturation of intraband absorption of GaN/AlN quantum dots”. *Applied Physics Letters*, 94(13):132104, 2009. DOI: [10.1063/1.3114424](https://doi.org/10.1063/1.3114424).
- [151] Souad Chouli, José M. Soto-Crespo, and Philippe Grelu. “Optical spectra beyond the amplifier bandwidth limitation in dispersion-managed mode-locked fiber lasers”. *Opt. Express*, 19(4):2959–2964, 2011. DOI: [10.1364/OE.19.002959](https://doi.org/10.1364/OE.19.002959).
- [152] Marco Jiménez-Rodríguez, Eva Monroy, Miguel González-Herráez, and Fernando B. Naranjo. “Ultrafast fiber laser using InN as saturable absorber mirror”. *J. Lightwave Technol.*, 36(11):2175–2182, 2018. DOI: <https://opg.optica.org/jlt/abstract.cfm?uri=jlt-36-11-2175>.
- [153] Laura Monroy, Marco Jiménez-Rodríguez, Eva Monroy, Miguel González-Herráez, and Fernando B. Naranjo. “High-quality, InN-based, saturable absorbers for ultrafast laser development”. *Applied Sciences*, 10(21), 2020. DOI: [10.3390/app10217832](https://doi.org/10.3390/app10217832).
- [154] Rick Trebino. *Frequency-Resolved Optical Gating: The Measurement of Ultrashort Laser Pulses*. Springer Science & Business Media, 2000.
- [155] C. Iaconis and I. A. Walmsley. “Spectral phase interferometry for direct electric-field reconstruction of ultrashort optical pulses”. *Opt. Lett.*, 23(10):792–794, 1998. DOI: [10.1364/OL.23.000792](https://doi.org/10.1364/OL.23.000792).
- [156] Jean-Claude M. Diels, Joel J. Fontaine, Ian C. McMichael, and Francesco Simoni. “Control and measurement of ultrashort pulse shapes (in amplitude and phase) with femtosecond accuracy”. *Appl. Opt.*, 24(9):1270–1282, 1985. DOI: [10.1364/AO.24.001270](https://doi.org/10.1364/AO.24.001270).
- [157] M. D. McCluskey and E. E. Haller. *Dopants and Defects in Semiconductors*. CRC Press, 2 edition, 2018.
- [158] V. Darakchieva, N. P. Barradas, M. Y. Xie, K. Lorenz, E. Alves, M. Schubert, P. O. Persson, F. Giuliani, F. Munnik, C. L. Hsiao, L. W. Tu, and W. J. Scha. “Role of impurities and dislocations for the unintentional n-type conductivity in InN”. *Physica B: Condens. Matter*, 404:4476–4481, 2009. DOI: [10.1016/j.physb.2009.09.042](https://doi.org/10.1016/j.physb.2009.09.042).
- [159] Ashraful Ghani Bhuiyan, Akihiro Hashimoto, and Akio Yamamoto. Indium nitride (inn): A review on growth, characterization, and properties. *Journal of Applied Physics*, 94(5):2779–2808, 2003. DOI: [10.1063/1.1595135](https://doi.org/10.1063/1.1595135).
- [160] L. Monroy, M. Jiménez-Rodríguez, P. Ruterana, E. Monroy, M. González-Herráez, and F. B. Naranjo. “Effect of the residual doping on the performance of InN epilayers as saturable absorbers for ultrafast lasers at 1.55 μ m”. *Opt. Mater. Express*, 9(7):2785–2792, 2019. DOI: [10.1364/OME.9.002785](https://doi.org/10.1364/OME.9.002785).

-
- [161] Francesca Gallazzi. “Ultralong continuous wave and ultrafast fibre lasers at telecommunication wavelengths”. In *PhD Thesis, Universidad de Alcalá*, 2020. <https://ebuah.uah.es/dspace/handle/10017/50850>.
 - [162] Bo Guo, Shi-Hao Wang, Zhi-Xin Wu, Ze-Xin Wang, Da-He Wang, Hao Huang, Feng Zhang, Yan-Qi Ge, and Han Zhang. “Sub-200 fs soliton mode-locked fiber laser based on bismuthene saturable absorber”. *Opt. Express*, 26(18):22750–22760, 2018. DOI: [10.1364/OE.26.022750](https://doi.org/10.1364/OE.26.022750).
 - [163] Qiaoliang Bao, Han Zhang, Yu Wang, Zhenhua Ni, Yongli Yan, Ze Xiang Shen, Kian Ping Loh, and Ding Yuan Tang. “Atomic-layer graphene as a saturable absorber for ultrafast pulsed lasers”. *Advanced Functional Materials*, 19(19):3077–3083, 2009. DOI: [10.1002/adfm.200901007](https://doi.org/10.1002/adfm.200901007).
 - [164] Wenjun Liu, Mengli Liu, Yuyi OuYang, Huanran Hou, Guoli Ma, Ming Lei, and Zhiyi Wei. “Tungsten diselenide for mode-locked Erbium-doped fiber lasers with short pulse duration”. *Nanotechnology*, 29:1–12, 2018. DOI: [10.1088/1361-6528/aaae40](https://doi.org/10.1088/1361-6528/aaae40).
 - [165] W. J. Liu, M. L. Liu, B. Liu, R. G. Quhe, M. Lei, S. B. Fang, H. Teng, and Z. Y. Wei. “Nonlinear optical properties of MoS₂-WS₂ heterostructure in fiber lasers”. *Opt. Express*, 27(5):6689–6699, 2019. DOI: [10.1364/OE.27.006689](https://doi.org/10.1364/OE.27.006689).
 - [166] Xiantao Jiang, Shunxiang Liu, Weiyuan Liang, Shaojuan Luo, and Zhiliang He et al. “Broadband nonlinear photonics in few-layer MXene Ti₃C₂T_x (T = F, O, or OH)”. *Laser & Photonics Reviews*, 12(2):1700229, 2017. DOI: [10.1002/lpor.201700229](https://doi.org/10.1002/lpor.201700229).
 - [167] L. Monroy, M. Soriano-Amat, Ó. Esteban, E. Monroy, M. González-Herráez, and F. B. Naranjo. “Performance enhancement of an ultrafast all-fiber laser based on an InN saturable absorber using GRIN coupling”. *Opt. Express*, 29(18):29357–29365, 2021. DOI: [10.1364/OE.430198](https://doi.org/10.1364/OE.430198).
 - [168] Amos Martinez, Mohammed Al Araithi, Artemiy Dmitriev, Petro Lutsyk, Shen Li, Chengbo Mou, Alexey Rozhin, Misha Sumetsky, and Sergei Turitsyn. “Low-loss saturable absorbers based on tapered fibers embedded in carbon nanotube/polymer composites”. *APL Photonics*, 2(12):126103, 2017. DOI: [10.1063/1.4996918](https://doi.org/10.1063/1.4996918).
 - [169] Junqing Zhao, Shuangchen Ruan, Peiguang Yan, Han Zhang, Yongqin Yu, Huifeng Wei, and Jie Luo. “Cladding-filled graphene in a photonic crystal fiber as a saturable absorber and its first application for ultrafast all-fiber laser”. *Optical Engineering*, 52(10):1 – 8, 2013. DOI: [10.1117/1.OE.52.10.106105](https://doi.org/10.1117/1.OE.52.10.106105).
 - [170] Seunghwan Ko, Junsu Lee, Joonhoi Koo, Beom Soo Joo, Minseon Gu, and Ju Han Lee. “Chemical wet etching of an optical fiber using a hydrogen fluoride-free solution for a saturable absorber based on the evanescent field interaction”. *J. Lightwave Technol.*, 34(16):3776–3784, 2016. DOI: <https://opg.optica.org/jlt/abstract.cfm?uri=jlt-34-16-3776>.

- [171] Francesca Gallazzi, Inés Cáceres, Laura Monroy, Javier Nuño, Concepción Pulido, Pedro Corredera, Fernando B. Naranjo, Miguel González-Herráez, and Juan Diego Ania Castañón. “Ultralong ring laser supercontinuum sources using standard telecommunication fibre”. *Optics & Laser Technology*, 147:107632, 2022. DOI: [10.1016/j.optlastec.2021.107632](https://doi.org/10.1016/j.optlastec.2021.107632).
- [172] Zuguang Guan. Laser remote sensing for environmental monitoring - from scandinavia to china. In *Renewable Energy and the Environment Optics and Photonics Congress*, page EW2C.3. Optica Publishing Group, 2012. DOI: [10.1364/E2.2012.EW2C.3](https://doi.org/10.1364/E2.2012.EW2C.3).
- [173] J. Laserna. Laser technology for environmental monitoring in the ocean. In *Renewable Energy and the Environment Optics and Photonics Congress*, page EW2C.1. Optica Publishing Group, 2012. DOI: [10.1364/E2.2012.EW2C.1](https://doi.org/10.1364/E2.2012.EW2C.1).
- [174] L. Monroy, J. Magnus, M. Gonzalez-Herraez, F. B. Naranjo, and K. Kieu. “Spectral focusing technique simulation for CARS microscopy: evaluation of spectral resolution and spectral coverage”. *submitted*, 2022.
- [175] Albert Schliesser, Markus Brehm, Fritz Keilmann, and Daniel van der Weide. “Frequency-comb infrared spectrometer for rapid, remote chemical sensing”. *Optics Express*, 13(22):9029–9038, 2005.
- [176] Cheng-Shane Chu, Yu-Lung Lo, and Ti-Wen Sung. “Review on recent developments of fluorescent oxygen and carbon dioxide optical fiber sensors”. *Photonic Sensors*, 1(3):234–250, 2011.
- [177] Jane Hodgkinson and Ralph P. Tatam. “Optical gas sensing: A review”. *Measurement Science and Technology*, 24(1), 2013.
- [178] R. R. Alfano and S. L. Shapiro. “Emission in the region 4000 to 7000 Å via four-photon coupling in glass”. *Phys. Rev. Lett.*, 24:584–587, 1970. DOI: [10.1103/PhysRevLett.24.584](https://doi.org/10.1103/PhysRevLett.24.584).
- [179] Feng Han, Chengli Wei, Jonathan Hu, Jindan Shi, and Xian Feng. Highly coherent visible supercontinuum generation in a micrometer-core borosilicate glass photonic crystal fiber. *J. Opt. Soc. Am. B*, 38(12):F145–F151, 2021. DOI: [10.1364/JOSAB.439304](https://doi.org/10.1364/JOSAB.439304).
- [180] J. M. Dudley and J. R. Taylor. “*Supercontinuum Generation in Optical Fibers*”. Cambridge University Press, 2010. DOI: [10.1017/CBO9780511750465](https://doi.org/10.1017/CBO9780511750465).
- [181] Jinendra K. Ranka, Robert S. Windeler, and Andrew J. Stentz. “Visible continuum generation in air-silica microstructure optical fibers with anomalous dispersion at 800 nm”. *Opt. Lett.*, 25(1):25–27, 2000. DOI: [10.1364/OL.25.000025](https://doi.org/10.1364/OL.25.000025).
- [182] Vincent Tombelaine, Christelle Lesvigne, Philippe Leproux, Ludovic Grossard, Vincent Couderc, Jean-Louis Auguste, Jean-Marc Blondy, Guillaume Huss, and Paul-Henri Pïoger. “Ultra wide band supercontinuum generation in air-silica holey fibers by SHG-induced modulation instabilities”. *Opt. Express*, 13(19):7399–7404, 2005. DOI: [10.1364/OPEX.13.007399](https://doi.org/10.1364/OPEX.13.007399).

-
- [183] J. C. Travers, M. H. Frosz, and J. M. Dudley. *Nonlinear fibre optics overview*, page 32–51. Cambridge University Press, 2010. DOI: [10.1017/CBO9780511750465](https://doi.org/10.1017/CBO9780511750465).
- [184] William C. Swann and Sarah L. Gilbert. “Line centers, pressure shift, and pressure broadening of 1530-1560 nm hydrogen cyanide wavelength calibration lines”. *J. Opt. Soc. Am. B*, 22(8):1749–1756, 2005. DOI: [10.1364/JOSAB.22.001749](https://doi.org/10.1364/JOSAB.22.001749).
- [185] W. C. Swann and S. L. Gilbert. “Pressure-induced shift and broadening of 1560–1630-nm carbon monoxide wavelength-calibration lines”. *J. Opt. Soc. Am. B*, 19(10):2461–2467, 2002. DOI: [10.1364/JOSAB.19.002461](https://doi.org/10.1364/JOSAB.19.002461).
- [186] Michael J. Thorpe, David Balslev-Clausen, Matthew S. Kirchner, and Jun Ye. “Cavity-enhanced optical frequency comb spectroscopy: application to human breath analysis”. *Opt. Express*, 16(4):2387–2397, 2008. DOI: [10.1364/OE.16.002387](https://doi.org/10.1364/OE.16.002387).
- [187] Scott A. Diddams, Leo Hollberg, and Vela Mbele. “Molecular fingerprinting with the resolved modes of a femtosecond laser frequency comb”. *Nature*, 445(7128):627–630, 2007.
- [188] Xuan Yang, Allan S.P. Chang, Bin Chen, Claire Gu, and Tiziana C. Bond. “High sensitivity gas sensing by Raman spectroscopy in photonic crystal fiber”. *Sensors & Actuators: B. Chemical*, 176:64–68, 2013.
- [189] Stuart D. Brorson and Hermann A. Haus. Geometrical limitations in grating pair pulse compression. *Appl. Opt.*, 27(1):23–25, Jan 1988. DOI: [10.1364/AO.27.000023](https://doi.org/10.1364/AO.27.000023).
- [190] Yukun Qin. “Development of all-fiber format laser sources for nonlinear microscopy and spectroscopy”. In *PhD Thesis, University of Arizona*, 2021. <https://www.optics.arizona.edu/news-events/events/dissertation-defense-yukun-qin-development-all-fiber-format-laser-sources-nonlinear>.
- [191] Khanh Kieu and Masud Mansuripur. “Femtosecond laser pulse generation with a fiber taper embedded in carbon nanotube/polymer composite”. *Opt. Lett.*, 32(15):2242–2244, 2007. DOI: [10.1364/OL.32.002242](https://doi.org/10.1364/OL.32.002242).
- [192] Yukun Qin, Yi-Hsin Ou, Benjamin Cromey, Orkhongua Batjargal, Jennifer K. Barton, and Khanh Kieu. “Watt-level all-fiber optical parametric chirped-pulse amplifier working at 1300 nm”. *Opt. Lett.*, 44(14):3422–3425, 2019. DOI: [10.1364/OL.44.003422](https://doi.org/10.1364/OL.44.003422).
- [193] Yukun Qin, Benjamin Cromey, Orkhongua Batjargal, and Khanh Kieu. “All-fiber single-cavity dual-comb for coherent anti-Stokes Raman scattering spectroscopy based on spectral focusing”. *Opt. Lett.*, 46(1):146–149, 2021. DOI: [10.1364/OL.413431](https://doi.org/10.1364/OL.413431).
- [194] Thomas Hellerer, Annika M.K. Enejder, and Andreas Zumbusch. “Spectral focusing: High spectral resolution spectroscopy with broad-bandwidth laser pulses”. *Applied Physics Letters*, 85(1):25–27, 2004. DOI: [10.1063/1.1768312](https://doi.org/10.1063/1.1768312).

- [195] Mojtaba Mohseni, Christoph Polzer, and Thomas Hellerer. “Resolution of spectral focusing in coherent Raman imaging”. *Opt. Express*, 26(8):10230–10241, 2018. DOI: [10.1364/OE.26.010230](https://doi.org/10.1364/OE.26.010230).
- [196] Ji-Xin Cheng, Lewis D. Book, and X. Sunney Xie. “Polarization coherent anti-Stokes Raman scattering microscopy”. *Opt. Lett.*, 26(17):1341–1343, 2001. DOI: [10.1364/OL.26.001341](https://doi.org/10.1364/OL.26.001341).
- [197] Ji-xin Cheng, Andreas Volkmer, Lewis D. Book, and X. Sunney Xie. “An ep-detected coherent anti-stokes raman scattering (E-CARS) microscope with high spectral resolution and high sensitivity”. *The Journal of Physical Chemistry B*, 105(7):1277–1280, 2001. DOI: [10.1021/jp003774a](https://doi.org/10.1021/jp003774a).
- [198] Esben Ravn Andresen, Pascal Berto, and Hervé Rigneault. “Stimulated raman scattering microscopy by spectral focusing and fiber-generated soliton as stokes pulse”. *Opt. Lett.*, 36(13):2387–2389, 2011. DOI: [10.1364/OL.36.002387](https://doi.org/10.1364/OL.36.002387).